

© 2011 by Youcai Wang. All rights reserved.

MEASUREMENT OF TARGET SINGLE-SPIN ASYMMETRY  
IN CHARGED KAON ELECTROPRODUCTION  
ON A TRANSVERSELY POLARIZED  $^3\text{He}$  TARGET

BY

YOUCAI WANG

DISSERTATION

Submitted in partial fulfillment of the requirements  
for the degree of Doctor of Philosophy in Physics  
in the Graduate College of the  
University of Illinois at Urbana-Champaign, 2011

Urbana, Illinois

Doctoral Committee:

Professor John D Stack, Chair  
Professor Alan M Nathan, Contingent Chair  
Professor Jen-Chieh Peng, Director of Dissertation Research  
Professor Scott S Willenbrock

# Abstract

The subject of quark transverse spin and quark transverse momentum distribution are two current research frontier in understanding the spin structure of the nucleons. The goal of the research reported in this dissertation is to extract new information on the quark transversity distribution and the novel transverse-momentum-dependent Sivers function in the neutron.

A semi-inclusive deep inelastic scattering experiment was performed at the Hall A of the Jefferson laboratory using 5.9 GeV electron beam and a transversely polarized  $^3\text{He}$  target. The scattered electrons and the produced hadrons (pions, kaons, and protons) were detected in coincidence with two large magnetic spectrometers.

By regularly flipping the spin direction of the transversely polarized target, the single-spin-asymmetry (SSA) of the semi-inclusive deep inelastic reaction  $^3\text{He}^\uparrow(e, e'h^\pm)X$  was measured over the kinematic range  $0.13 < x < 0.41$  and  $1.3 < Q^2 < 3.1$  (GeV) $^2$ .

The SSA contains several different azimuthal angular modulations which are convolutions of quark distribution functions in the nucleons and the quark fragmentation functions into hadrons.

It is from the extraction of the various “moments” of these azimuthal angular distributions (Collins moment and Sivers moment) that we obtain information on the quark transversity distribution and the novel T-odd Sivers function.

In this dissertation, I first introduced the theoretical background and experimental status of nucleon spins and the physics of SSA. I will then present the experimental setup and data collection of the JLab E06-010 experiment. Details of data analysis will be discussed next with emphasis on the kaon particle identification and the Ring-Imaging Cherenkov detector which are my major responsibilities in this experiment. Finally, results on the kaon Collins and Sivers moments extracted from the Maximum Likelihood method will be presented and interpreted. I will conclude with a discussion on the future prospects for this research.

*To Father and Mother.*

# Acknowledgments

When I was boarding on my exiled plane on the United Airlines from Shanghai to the USA on March 4, 2004, I told Eric Richardson, a State Department officer, then an officer at the Embassy of the United States in Beijing, China, that I would like to have a chance to study political science or law. Later, as a Visiting Scholar at the Fairbank Center in Harvard University, I sat in classes in the Law school only to find myself frustrated not fully understanding the lectures. Professor Jen-Chieh Peng, my current thesis advisor, then a member of the Committee on International Freedom of Scientists (CIFS) of the American Physical Society (APS), invited me to an APS meeting in Washington DC and encouraged me to study in the Physics Ph.D. program at the University of Illinois at Urbana-Champaign (UIUC). Professor Keh-Fei Liu at the University of Kentucky, Professor Lizhi Fang at the University of Arizona, and Professor Keqiang Xie recommended me to the program. Later, Professor Alan Nathan, then the Associate Head for graduate program of the Physics department, sent me an offer letter. I was very excited and accepted the offer.

The journey was not easy, but definitely rewarding. I feel myself owing so much to many people who trusted me, supported me and helped me during this period. My deepest appreciation goes to Professor Peng. He guided me through my preliminary exam and my research at the Jefferson National Laboratory. He spent numerous hours discussing with me on ideas to conduct data analysis. He also spent much time to help me revise my thesis. Without his patience, encouragement and great help, it is impossible for me to arrive here.

When I prepared for the qualifying examination, I took courses of electromagnetic field, quantum physics and statistical physics. I had been away from physics for more than 15 years, so these courses were very challenging for me. Professors Scott Willenbrock, Jon Thaler, and Michael Weissman encouraged me and helped me to complete these courses. Professor Scott Willenbrock always reassured me when I worried about my study. Professor John Stack has been very supportive during my study and research. When he became Associate Head for graduate program, he helped me find an English tutor to improve my conversation skills. I also want to thank them for having deep and interesting discussions with me in physics and sometimes in Chinese politics when I was on campus.

From 2007 to 2010, I participated in the experiment E06-010 at Hall A, Jefferson National Laboratory in Newport News, VA. I would like to thank the spokespersons of this experiment: Xiaodong Jiang, Jian-ping Chen, Haiyan Gao, Evaristo Cisbani, and Jen-Chieh Peng. Jian-ping always asked me lots of tough questions in the data analysis meetings and made me think more deeply and thoroughly. Xiaodong made me work harder on the preshower and aerogel detectors. Evaristo gave me lots of advices on making the Ring Imaging Cherenkov detector (RICH) work. He is also very instrumental in helping me with data analysis, not only in RICH detector, but also in maximum likelihood methods. He provided many guidance and comments on most of my presentations. He also enriched my life during the JLab research period and discussed with me on Chinese politics, democracy, and human rights; sometimes, he even helped revising my articles related to my political activities.

I want to thank Lingyan Zhu and Bogdan Wojtsekhowski, for their help in furnishing aerogel detector and enlightening discussion of data analysis. I want to thank Vincent Sulkosky for working on the HRS detectors. We worked on all HRS detectors except the RICH detector and I learnt a lot from him. I want to thank Alexandre Camsonne for working together on RICH detector, day and night. I also want to thank the Italian RICH group - Evaristo, Francesco Cusanno and Guido Maria Urciuoli for their hard work on the RICH detector during the experiment.

I want to thank all the collaborating scientists and the entire staff of JLab Hall A, and the many post-docs Yi Qiang, Brad Sawatzky, Bryan Moffit, Bo Zhao, and Patricia Solvignon and my graduate student colleagues: Qian Xin, Jin Huang, Kalyan Allada, Chiranjib Dutta, Yi Zhang, and Joe Katich. I also want to thank Yawei Zhang and Pengjia Zhu for helping me with SQL and Unix problems.

Once more, I would like to thank my dissertation committee members: Professor John Stack, Professor Jen-Chieh Peng, Professor Alan Nathan, and Professor Scott Willenbrock, for reviewing and commenting on my thesis.

I want to thank my colleagues of Chinese dissidents and China Democracy Party, Zhemin Yang, Gengsong Lv, Shuqing Chen, Liqun Chen, Tiancheng Wang, and Juntao Wang. They all encouraged me to complete the PhD program, especially when I was frustrated with my research progress. Some of them are in China and were still put into prisons now and then. They repeatedly urged me to complete the program, telling me that they don't have the opportunity to get a Ph.D degree in the U.S. I was always inspired by them.

Last but not least, I want to thank my parents and my brothers and sisters. They believe in me and are patient with me during this journey. I want to thank my wife and her parents, for taking care of my son William Yujiang Wang, who was born during my Ph.D program. My beloved wife, Jiangxia Hu, gave me lots of support in spirit and took care of my life. She also financially supported our family after our young

boy was born.

# Table of Contents

|   |           |
|---|-----------|
| List of Tables . . . . .  | ix        |
| List of Figures . . . . .   | x         |
| <b>Chapter 1 Introduction . . . . .</b>   | <b>1</b>  |
| <b>Chapter 2 Spin Structure of the Nucleons . . . . .</b>   | <b>8</b>  |
| 2.1 Deep Inelastic Scattering . . . . .   | 8         |
| 2.2 The DIS cross section . . . . .   | 9         |
| 2.3 The Quark Parton Model (QPM) and the QCD improved QPM . . . . .                                   | 14        |
| 2.4 The quark-quark correlation matrix . . . . .  | 17        |
| <b>Chapter 3 Transversity, Sivers Function, and Collins Function . . . . .</b>                        | <b>23</b> |
| 3.1 The Semi-Inclusive Deep Inelastic Scattering . . . . .  | 23        |
| 3.2 The Differential cross-section of SIDIS . . . . .   | 25        |
| 3.3 The Collins and Sivers azimuthal moments . . . . .  | 28        |
| 3.4 The transversity distribution function and the Sivers distribution function . . . . .             | 29        |
| 3.5 Other Related Function . . . . .  | 30        |
| 3.6 The HERMES and COMPASS results and theoretical prediction on Collins and Sivers moments . . . . . | 31        |
| <b>Chapter 4 Experimental Setup . . . . .</b>   | <b>38</b> |
| 4.1 Overview . . . . .  | 38        |
| 4.2 The Electron Accelerator . . . . .  | 39        |
| 4.3 Hall A . . . . .  | 40        |
| 4.4 Beamline . . . . .  | 40        |
| 4.4.1 Beam Energy Measurement Device . . . . .  | 40        |
| 4.4.2 Beam Current Measurement . . . . .  | 42        |
| 4.4.3 Raster and Beam Position Measurement . . . . .  | 44        |
| 4.5 The Polarized $^3\text{He}$ Target . . . . .  | 45        |
| 4.5.1 Principles . . . . .  | 46        |
| 4.5.2 The Target System . . . . .   | 49        |
| 4.5.3 Laser and Optical Fibers . . . . .  | 53        |
| 4.5.4 Polarimetry . . . . .   | 55        |
| 4.5.5 Target Spin Flip System . . . . .   | 62        |
| 4.6 The electron arm: BigBite spectrometer . . . . .  | 63        |
| 4.7 The hadron arm: the left HRS . . . . .  | 67        |
| 4.7.1 Overview of the Left High Resolution Spectrometer . . . . .                                     | 68        |
| 4.7.2 Vertical Drift Chambers . . . . .   | 70        |
| 4.7.3 Two Scintillator Planes S1 and S2m . . . . .  | 70        |
| 4.7.4 Gas Cherenkov Detector . . . . .  | 71        |
| 4.7.5 Aerogel Cherenkov Detector . . . . .  | 72        |
| 4.7.6 RICH Detector . . . . .   | 73        |



|                  |   |            |
|------------------|---|------------|
| 4.7.7            | Pion Rejectors . . . . .  | 76         |
| 4.8              | Trigger and Data Acquisition System . . . . .                                   | 77         |
| 4.8.1            | Trigger and Electronics for BigBite Spectrometer . . . . .                      | 79         |
| 4.8.2            | Trigger and Electronics for the left High Resolution Spectrometer . . . . .     | 83         |
| 4.8.3            | Coincidence Trigger . . . . .   | 83         |
| 4.8.4            | Scaler Setup . . . . .  | 84         |
| <b>Chapter 5</b> | <b>Data Analysis . . . . .</b>  | <b>90</b>  |
| 5.1              | Flow of the Data Analysis . . . . .   | 90         |
| 5.1.1            | Target Calibration . . . . .  | 90         |
| 5.1.2            | BigBite spectrometer calibration . . . . .                                      | 93         |
| 5.1.3            | High Resolution Spectrometer calibration . . . . .                              | 100        |
| 5.1.4            | Coincidence Time-of-Flight module . . . . .                                     | 112        |
| 5.1.5            | Data Quality Checks . . . . .   | 116        |
| 5.1.6            | Scaler Check and Deadtime Measurement . . . . .                                 | 119        |
| 5.2              | Select coincidence kaons and pions . . . . .                                    | 120        |
| 5.2.1            | Cut study for coincidence electrons in BigBite . . . . .                        | 121        |
| 5.2.2            | Contamination Study for Identifying DIS Electrons in BigBite . . . . .          | 125        |
| 5.2.3            | Cut study for coincidence kaons in left HRS with time of flight (TOF) . . . . . | 129        |
| 5.3              | The Maximum Likelihood Method . . . . .   | 141        |
| 5.3.1            | The least square method . . . . .   | 141        |
| 5.3.2            | The Maximum Likelihood Method . . . . .   | 142        |
| 5.4              | Numerical calculation for kaon Collins moment and Sivers moment . . . . .       | 154        |
| 5.4.1            | Coincidence Kaon Raw Asymmetry . . . . .  | 154        |
| 5.4.2            | Coincidence Kaon Collins moment and Sivers moment . . . . .                     | 154        |
| 5.4.3            | numerical calculation . . . . .   | 158        |
| 5.5              | Nitrogen Dilution Factor . . . . .  | 161        |
| 5.6              | Systematic Uncertainties . . . . .  | 163        |
| 5.7              | $^3\text{He}$ Results . . . . .   | 172        |
| 5.8              | Nuclear Correction: From $^3\text{He}$ to Neutron . . . . .                     | 173        |
| <b>Chapter 6</b> | <b>Results and Conclusion . . . . .</b>   | <b>179</b> |
| 6.1              | Pion Collins Moment and Sivers Moment . . . . .                                 | 179        |
| 6.2              | Kaon Collins and Sivers Moments . . . . .                                       | 180        |
| 6.3              | Conclusion . . . . .  | 181        |
|                  | <b>References . . . . .</b>   | <b>182</b> |
|                  | <b>Vita . . . . .</b>   | <b>187</b> |

# List of Tables

|      |   |     |
|------|---|-----|
| 4.1  | BCM calibration constants for both upstream and downstream signals determined during two different period measurements, the units are counts/ $\mu\text{A}$ . . . . .   | 44  |
| 4.2  | BCM offsets for both upstream and downstream determined during two different period measurements, the units are counts/ $\mu\text{A}$ . . . . .   | 44  |
| 4.3  | A few numbers from UVA and W/M database. $V_p$ is the volume of the pumping chamber, $V_t$ is the volume of the target chamber, $V_{tt}$ is the volume of the transfer tube. All the volumes are in $\text{cm}^3$ , the density is in amagats and the lifetime is in hours. . . . .   | 51  |
| 4.4  | Dimensions of the Helmholtz coils used in the experiment to produce the magnetic field to align the spins of the ${}^3\text{He}$ nuclei. The diameter is in meter and the resistance is in ohm. . . .   | 53  |
| 4.5  | Current settings for the three pairs of Helmholtz coils. $\vec{B}$ stands for the holding magnetic field direction, $I_S$ for current in the small coils, $I_L$ for current in the large coils and $I_V$ for current in the vertical coils. The units are in Ampere. . . . .  | 53  |
| 4.6  | Hall A HRS general characteristics. . . . .   | 68  |
| 4.7  | Various triggers constructed during E06-010 experiment. . . . .   | 86  |
| 5.1  | The Target Polarization Table . . . . .   | 92  |
| 5.2  | The cratemap of crate 14 for RICH detector . . . . .  | 109 |
| 5.3  | Pion contamination in the coincidence electron sample in BigBite with coincidence kaon and proton in left HRS. . . . .  | 126 |
| 5.4  | Photon induced electron contamination ratio in BigBite with to coincidence kaons and protons in left HRS. . . . .   | 128 |
| 5.5  | pion contamination in kaon . . . . .  | 138 |
| 5.6  | Total counts of coincidence hadrons . . . . .   | 141 |
| 5.7  | The filling densities of all three target cells. The “2% (relative)” represent the 2% of the listed density. . . . .  | 162 |
| 5.8  | Summary of the systematic uncertainties in the coincidence ${}^3\text{He}(e,e'\text{K}^\pm)\text{X}$ channel. Here “relative” represents the uncertainties are relative to the central value of the asymmetries. The “absolute” represents that the uncertainties are absolute, and presented in the unit of the statistical uncertainties. . . . . | 169 |
| 5.9  | Influences due to other angular momentum terms for $\text{K}^+$ . . . . .   | 170 |
| 5.10 | Influences due to other angular momentum terms for $\text{K}^-$ . . . . .   | 170 |
| 5.11 | Summary of the final systematic uncertainties in the coincidence ${}^3\text{He}(e,e'\text{K}^\pm)\text{X}$ channel. . .   | 170 |
| 5.12 | Sources of systematic uncertainties for $\text{K}^+/\text{K}^-$ due to incomplete acceptance . . . . .  | 172 |
| 5.13 | Final systematic uncertainties for $\text{K}^+/\text{K}^-$ . . . . .  | 172 |

# List of Figures

|      |   |    |
|------|---|----|
| 2.1  | Feynman diagram of deep inelastic scattering. Figure is from Ref. [35]. . . . .   | 8  |
| 2.2  | $F_2^{em}$ , i.e. $F_2$ due to $\gamma$ exchange, from HERA and fixed target experiments compared with the ZEUS NLO fit [31]. . . . .   | 12 |
| 2.3  | The spin-dependent structure function $xg_1$ of the proton, deuteron, and neutron (from $^3\text{He}$ target) measured in deep inelastic scattering of polarized electrons/positrons. This figure is reproduced from Ref. [34]. . . . .   | 14 |
| 2.4  | Comparison of the ZEUS fit with the global analyses CTEQ6M [33] and MRST2001 [32]. . . . .  | 16 |
| 2.5  | Handbag diagram for inclusive DIS . . . . .   | 17 |
| 2.6  | Diagram of the forbidden helicity flip amplitude. The helicities of the quarks and nucleons are labeled. . . . .  | 20 |
| 3.1  | Semi-Inclusive Deep Inelastic Scattering on polarized nucleon . . . . .   | 23 |
| 3.2  | The definition of $\phi_h$ and $\phi_S$ according to Trento convention . . . . .  | 25 |
| 3.3  | Leading-twist transverse momentum dependent quark distribution functions. This figure is extracted from [49]. . . . .   | 30 |
| 3.4  | Collins moments (upper panel) and Sivers moments (down panel) for charged pions (as labelled) as a function of $x$ , $z$ and $P_h$ . The error bands represent the systematic uncertainty due to acceptance and detector smearing effects and due to a possible contribution from the $\langle \cos\phi \rangle_{UU}$ moment in the spin-independent cross section. The figure is from [51]. . . . .  | 31 |
| 3.5  | Collins moments (left column) and Sivers moments (right column) for charged kaons (closed symbols, as labelled) and charged pions (open symbols, as labelled) as function of $x$ , $z$ and $P_{h\perp}$ . The error bands represent the maximal systematic uncertainty; the common overall 8.1% scaling uncertainty is due to the target polarisation uncertainty. The figure is from [60]. . . . .   | 32 |
| 3.6  | Collins asymmetry against $x$ , $z$ and $p_T^h$ for the “all” charged pions and kaons samples from the 2003–2004 Compass data, and the “all” $K_S^0$ ’s sample from the 2002–2004 data (left column). Sivers asymmetry against $x$ , $z$ and $p_T^h$ for the “all” charged pions and kaons samples from the 2003–2004 data, and “all” $K_S^0$ ’s sample from the 2002–2004 data (right column). The figure is from Ref. [60]. . . . .   | 33 |
| 3.7  | COMPASS proton data results of Collins moments for positive and negative hadrons. This figure is from [61]. . . . .   | 34 |
| 3.8  | COMPASS proton data results of Sivers moments for positive and negative hadrons. This figure is from [61]. . . . .  | 34 |
| 3.9  | The Sivers distribution functions for $u$ , $d$ and $s$ flavours as determined by our simultaneous fit of HERMES and COMPASS data. On the left panel, the first moment $x\Delta^N f^{(1)}(x)$ , $f_{1T}^{\perp(1)q}(x)$ of Ref. [131]) is shown as a function of $x$ for each flavour, as indicated. Similarly, on the right panel, the Sivers distribution $x\Delta^N f(x, k_t)$ is shown as a function of $k_t$ at a fixed value of $x$ for each flavour, as indicated. . . . . | 36 |
| 3.10 | The transversity distribution functions for $u$ and $d$ flavours as determined by our global fit; we also show the Soffer bound (highest or lowest lines) and the (wider) bands of our previous extraction [132] are also shown in this figure. The figure is from [131]. . . . .   | 37 |

|      |  |    |
|------|--|----|
| 3.11 | Predictions for the single spin asymmetry $A_{UT}^{\sin(\phi_h - \phi_S)}$ for pion and kaon production, which will be measured at JLab operating on a polarized $^3\text{He}$ (neutron) target, with a beam energy of 6 GeV. The figure is from Ref. [60]. . . . .  | 37 |
| 4.1  | The Jefferson Lab Accelerator. Fig. is from Ref. [66] . . . . .  | 39 |
| 4.2  | The overview of the HALL A. . . . .  | 40 |
| 4.3  | The Arc energy measurement was applied in this experiment E06-010 [68]. . . . .  | 41 |
| 4.4  | The configuration of BCMs in Hall A. Figure is from [66] . . . . .   | 42 |
| 4.5  | Three wave function states of $^3\text{He}$ . . . . .  | 46 |
| 4.6  | Energy Level diagram of $^{85}\text{Rb}$ . $\mathbf{I} = 5/2$ . The splittings are not to scale. . . . .   | 47 |
| 4.7  | Hybrid approach of Spin-Exchange Optical Pumping (SEOP) . . . . .  | 48 |
| 4.8  | Orientation of the hybrid cell in the Hall. . . . .  | 50 |
| 4.9  | Schematic diagram of the target ladder system. . . . .   | 52 |
| 4.10 | Left panel: Complete schematic of our Helmholtz coils system in the Hall. The RF coils and the pick up coils are also shown. Right panel: The real target setup. . . . .   | 53 |
| 4.11 | Schematic diagram of the optics setup. This setup was for the vertical pumping. For the transverse pumping, the big mirror MB2 was actually mounted on the oven. The rest of the setup was the same. . . . .   | 55 |
| 4.12 | A NMR frequency sweep signal fitted to the square root of a Lorentzian. . . . .  | 59 |
| 4.13 | EPR spectrum showing the $^3\text{He}$ spin states when they are anti-parallel ( $\vec{B} - \Delta\vec{B}$ ) and parallel ( $\vec{B} + \Delta\vec{B}$ ) to the holding field direction. . . . .  | 61 |
| 4.14 | Charged particle trajectories through the BigBite magnet. Positive particles with momentum less than 200 MeV/c and negative particles with momentum less than 220 MeV/c did not reach the detectors. The location of wire chambers, pre-shower, trigger scintillator planes and shower lead glass arrays are also indicated. . . . . | 63 |
| 4.15 | Simulation of particle trajectories. Most of the low-energy background particles can be shielded from hitting the Bigbite wire chambers by a 2 inch metal plate downstream of the target. . . . .  | 64 |
| 4.16 | Illustration of the Multi Wire Drift Chamber (MWDCs) plane orientations: u, v, and x. The corresponding second plane is shifted by half of the wire cell (0.5 cm), not indicated. . . . .  | 65 |
| 4.17 | Geometry of BigBite PreShower, Scintillator, and Shower detectors . . . . .  | 66 |
| 4.18 | Left panel: Overview of Hall A. Right panel: 4 magnet and Detector Package and Detector Hut of the left HRS. . . . .   | 67 |
| 4.19 | Diagram of the left HRS and its hut . . . . .  | 67 |
| 4.20 | Arrangement of the detectors in High Resolution Spectrometer during the E06-010 experiment. The figure is reproduced from [111] . . . . .  | 69 |
| 4.21 | Configuration of left HRS Wire Chambers, from [66] . . . . .   | 70 |
| 4.22 | Schematic diagram of RICH detector . . . . .   | 74 |
| 4.23 | Configuration of Pion Rejectors . . . . .  | 76 |
| 4.24 | Example of CODA configuration using read-out controllers. . . . .  | 78 |
| 4.25 | Total sum of preshower and shower detectors . . . . .  | 81 |
| 4.26 | BigBite spectrometer trigger logic diagram. . . . .  | 82 |
| 4.27 | Re-timing circuit for the BigBite trigger . . . . .  | 82 |
| 4.28 | Trigger logic for the left HRS. . . . .  | 84 |
| 4.29 | Schematic diagram of coincidence trigger setup between the two spectrometers . . . . .   | 85 |
| 4.30 | Coincidence timing between BigBite and HRS. . . . .  | 86 |
| 4.31 | Scaler setup and gating scheme using target spin and beam helicity. . . . .  | 87 |
| 4.32 | Beam helicity sequence during E06-010 experiment. . . . .  | 88 |
| 4.33 | Timing sequence for the target spin state [109]. . . . .   | 89 |
| 5.1  | Data analysis flow for the E06-010 experiment. . . . .   | 91 |
| 5.2  | online target polarization performance history. . . . .  | 92 |

|      |   |     |
|------|---|-----|
| 5.3  | $^3\text{He}$ target polarization measured by EPR when the target is in <i>transverse</i> direction. This plot is reproduced from [113]. . . . .  | 93  |
| 5.4  | $^3\text{He}$ target polarization measured by EPR when the target is in <i>vertical</i> direction. This plot is reproduced from [113]. . . . .  | 94  |
| 5.5  | Drift time spectrum for the 100th wire in the x plane of the third chamber [111]. . . . .   | 95  |
| 5.6  | The residual peak for the U-plane of the front chamber [111]. . . . .   | 96  |
| 5.7  | Reconstructed vertex for the multi-foil carbon target at a particle momentum of 1.2 GeV [111].  | 97  |
| 5.8  | A lead sieve slit plate with a thickness of 1.5". . . . .   | 98  |
| 5.9  | The left panel shows the reconstructed sieve pattern with first order optics model. The middle panel shows the sieve pattern after adding offsets. The right panel shows the sieve pattern after applying higher order corrections. The red points indicates where the sieve holes/slots are actually located [111]. . . . .  | 99  |
| 5.10 | Final momentum resolution achieved with two beam energies: left panel is for $E_0 = 1.23$ GeV and right panel is for $E_0 = 2.39$ GeV [111]. . . . .  | 100 |
| 5.11 | BigBite optics check: The left side top (bottom) panels show the reconstructed missing mass peak of the proton and other resonances for beam energies of 1.23 GeV (2.39 GeV). The right side panels show the momentum vs. scattering angle $\theta$ correlations at the beam energies of 1.23 GeV and 2.39 GeV [111]. . . . . | 101 |
| 5.12 | Momentum resolution for positive optics data at 1.23 GeV [111]. . . . .   | 102 |
| 5.13 | Preshower energy spectrum showing a clear separation between pions and electrons. The minimum ionizing pions peak around channel 180 and electron like events peak around channel 700. . . . .  | 103 |
| 5.14 | Reconstructed vertex $z_{react}$ for a multi-foil carbon target with a BeO target mounted in the front [114]. . . . .   | 104 |
| 5.15 | ADC sum of the gas Cherenkov detector. . . . .  | 105 |
| 5.16 | ADC sum of the Aerogel detector for the experiment. Left panel: negative polarity in LHRS. Right panel: positive polarity in LHRS. There are two high peaks at channel 0 and at single photo-electron peak channel 100 due to large number of proton events. . . . .  | 106 |
| 5.17 | The RICH detector should be rotated otherwise the Cherenkov light will be internally reflected.   | 108 |
| 5.18 | The 10th or 11th wire was broken, both of them were grounded. . . . .   | 108 |
| 5.19 | The timing and trigger for RICH. . . . .  | 111 |
| 5.20 | A ring for one event of a charged particle. . . . .   | 112 |
| 5.21 | A reconstructed RICH ring for many events in two and three dimensional plots. . . . .   | 113 |
| 5.22 | Left panel: separation of pions and kaons. Right panel: the reconstructed ring for charged pions. . . . .   | 114 |
| 5.23 | Energy divided by momentum for the two-layer lead-glass detector showing a clear separation between hadrons and electrons. . . . .  | 115 |
| 5.24 | Panel on the left (right) shows the timing resolution achieved by the single arm timing detectors in the HRS (BigBite spectrometer) [114]. . . . .  | 116 |
| 5.25 | Coincidence time-of-flight spectrum for $(e, e'\pi)$ where a clear separation between protons, kaons and pions is seen [114]. . . . .   | 117 |
| 5.26 | Preshower peak vs. run number before and after correction. . . . .  | 118 |
| 5.27 | Plot showing beam trip cuts for one run. The black points are excluded from the analysis [111].   | 121 |
| 5.28 | Vertical position (Position in X) vs the vertical slope (Slope in X) in the first chamber. The blue points are the negative charged particles in normal production runs. The red points are positive charged particles in normal production runs. The black region was neglected. Fig. is from [111]. . . . .                 | 123 |
| 5.29 | Reconstructed vertex is shown for electron-like events. The cut positions at $\pm 0.185\text{m}$ are for target events. The peaks at $\pm 0.2\text{m}$ are due to the BigBite target collimator. . . . .  | 124 |
| 5.30 | Energy deposited in the Preshower vs E/p. The separated electrons and pions are figured out in the plot. . . . .  | 125 |

|      |   |     |
|------|---|-----|
| 5.31 | Negative pion contamination to electron in coincidence channel (T5) in four x bins. The negative pion peak around channel 200 is convoluted by one Gaussian function with Landau function by exact fitting. . . . .   | 127 |
| 5.32 | Selected main regions in the 4 target variables in 2 dimensions separately: <i>ExTgtCor-L.dp</i> , <i>ExTgtCor-L.ph</i> , <i>ExTgtCor-L.ph</i> , and <i>L.tr.tg-y</i> , the 4 dimention phase space for the left HRS reconstructed optics. The figure is from J. Huang (MIT) [117]. . . . .   | 130 |
| 5.33 | Selected coincidence window between left HRS reaction vertex and BigBite reaction vertex, including some random coincidence background events in the coincidence window. . . . .  | 130 |
| 5.34 | The E/P spectrum showing hadrons separated from electrons with the pion rejectors in left HRS. This is the very first step to separate hadrons from electrons. Actually the gas Cherenkov can also clearly separate electrons from hadrons. $\pi^-$ is the dominant hadron when left HRS is in negative polarity. . . . .   | 131 |
| 5.35 | Gas Cherenkov spectrum. The red line is shown for the single photo-electron peak. left panel: for negative polarity in left HRS, right panel: for positive polarity in left HRS. In positive polarity, there are no peaks but only some background. . . . .   | 132 |
| 5.36 | Aerogel Cherenkov spectrum, the red line aligned at channel 100 is shown for the sigle photo-electron peak. left panel: for negative polarity in left HRS, right panel: for positive polarity in left HRS. In positive polarity, there is a huge single photon peak caused by the residual signal from proton. . . . .  | 133 |
| 5.37 | Time-of-flight (TOF) spectrum, the red line corresponds to the location of pion peak, the green line corresponds to the location of kaons, the blue line corresponds to the location of protons (if left HRS at positive polarity). Left panel: for negative polarity in the left HRS, a very small bump shows up at the kaon peak along with a huge pion peak. There is almost no event near the anti-proton peak. Right panel: for positive polarity in left HRS. One huge peak is for proton at left side and one huge peak is for $\pi^+$ at the right side. There is a small peak for $K^+$ . . . . .  | 134 |
| 5.38 | Time-of-flight(TOF) spectrum after applying the cuts for pions, the red line corresponds to the location of pion peak,the green line corresponds to the location of kaons, the blue line corresponds to the location of protons(if left HRS at positive polarity) . left panel:for negative polarity in the left HRS, there is no a very small bump shows up at the kaon peak along with a huge pion peak. right panel: for positive polarity in left HRS. One peak is still for proton at left side corresponding to blue line but it is greatly suppressed and far away from pion 6ns window, one huge peak is for $\pi^+$ corresponding to red line, there is no a small peak for $K^+$ corresponding to the the location of green line. . . . .                     | 135 |
| 5.39 | after applying cuts of $L.cer.asum_c < 250.$ & $L.a1.asum_c < 150.$ , there are still pion contamination in kaon especially in negative situation. . . . .  | 136 |
| 5.40 | The TOF spectra for various cuts on gas and aerogel Cherenkov together with two-gaussian fits to the pion and kaon peaks. The upper panel is for positive polarity in left HRS, the lower panel is for negative polarity in left HRS. There are nine small pad for figuring out the counts and contamination. The different cuts correspond to 1. $cer < 50$ & $a1 < 150$ , 2. $cer < 50$ & $a1 < 125$ , 3. $cer < 50$ & $a1 < 100$ , 4. $cer < 50$ & $a1 < 75$ , 5. $cer < 30$ & $a1 < 150$ , 6. $cer < 30$ & $a1 < 125$ , 7. $cer < 30$ & $a1 < 100$ , 8. $cer < 30$ & $a1 < 75$ , 9. $cer < 30$ & $a1 < 50$ . The combined cuts $cer < 30$ & $a1 < 125$ & $abs(CT.K.t) < 1$ . was selected to optimize the kaon counts with less than 3% pion contamination. . . . . | 137 |
| 5.41 | The cone angles measured by RICH versus TOF for events with negative HRS polarity. The TOF cuts applied for kaon events are shown as green curves. The blue box indicates the region of pion contamination. . . . .   | 138 |
| 5.42 | The TOF spectrum for negative LHRS polarity. The expected locations for $\pi^-$ , $K^-$ , $\bar{P}$ are indicated by red, green, and blue lines, respectively. The accidental coincidence events form a continuous background, and the 2ns beam structure is clearly visible. . . . .   | 140 |
| 5.43 | The TOF spectrum for positive LHRS polarity. The expected locations for $\pi^+$ , $K^+$ , $P$ are indicated by red, green, and blue lines, respectively. . . . .  | 140 |

|      |  |     |
|------|--|-----|
| 5.44 | Left panel: coincidence negative kaon raw asymmetry. Right panel: coincidence positive kaon raw asymmetry. Red means Transverse_in_plane, Blue: Vertical, Green: Total (include Vertical and Transverse), Pink: Total events in 1 bin. . . . .   | 154 |
| 5.45 | $\phi_h$ , $\phi_S$ and their combination $\phi_h + \phi_S$ , $\phi_h - \phi_S$ in vertical polarization target setting. Upleft panel: $\phi_h$ is around $\pm\pi$ , upright panel: $\phi_S$ is around $\pm\frac{\pi}{2}$ . Downleft panel: $\phi_h + \phi_S$ is around $\pm\frac{\pi}{2}$ or $\pm\frac{3\pi}{2}$ , downright panel: $\phi_h - \phi_S$ is around $\pm\frac{\pi}{2}$ or $\pm\frac{3\pi}{2}$ . . . . .   | 155 |
| 5.46 | $\phi_h$ , $\phi_S$ and their combination $\phi_h + \phi_S$ , $\phi_h - \phi_S$ in transverse_in_plane polarization target setting. Upleft panel: $\phi_h$ is around $\pm\pi$ , upright panel: $\phi_S$ is around 0 or $\pm\pi$ . Downleft panel: $\phi_h + \phi_S$ is around 0 or $\pm\pi$ , downright panel: $\phi_h - \phi_S$ is around 0 or $\pm\pi$ . . . . .   | 156 |
| 5.47 | Direct results from five situation, the target polarization does influence the results. Up panel: coincidence positive kaons, down panel: coincidence negative kaons. For the negative kaon, the Collins moment and Sivers moment are big number, especailly for the first bin: around -0.32 -0.34. . . . .  | 156 |
| 5.48 | The upleft panel is for $K^+$ Collins moment, the upright is for $K^+$ Sivers moment, the downleft is for $K^-$ Collins moment, the downright is for $K^-$ Sivers moment. The red line is my result, the blue is Xin's result, the cyan is MLE result of Xin's cut, yellow is MLE's result with my cut, green is for Cut $abs(CT.K.t) < 1.0$ , and the pink line has large uncertainty due to very small statistics. . . . .   | 157 |
| 5.49 | The upleft panel is for $K^+$ Collins moment, the upright is for $K^+$ Sivers moment, the downleft is for $K^-$ Collins moment, the downright is for $K^-$ Sivers moment. Under condition $abs(CT.K.t) < 1$ , the different results are obtained with different cut combination of gas Cherenkov and aerogel Cherenkov. . . . .  | 158 |
| 5.50 | The upleft panel is for $K^+$ Collins moment, the upright is for $K^+$ Sivers moment, the downleft is for $K^-$ Collins moment, the downright is for $K^-$ Sivers moment. Under condition $abs(CT.K.t) < 0.87$ , the different results are obtained with different cut combination of gas Cherenkov and aerogel Cherenkov. . . . .   | 159 |
| 5.51 | Result of kaon Collins moment and Sivers moment from numerical MLM analysis. Left up panel: Collins moment for $K^+$ , right up panel: Sivers moment for $K^+$ . Left down panel: Collins moment for $K^-$ , right down panel: Sivers moment for $K^-$ . The Sivers moment for $K^+$ is consistent with zero, and the Collins moment and Sivers moment are negative for $K^-$ . . . . .  | 160 |
| 5.52 | Collins moment versus Sivers moment for positive kaon. . . . .   | 160 |
| 5.53 | Collins moment versus Sivers moment for negative kaon. . . . .   | 161 |
| 5.54 | Positive kaon $1\sigma$ and $2\sigma$ Collins moment and Sivers moment contours for 4 bins. Aqua round point is the center point from numerical algorithm, the red round point is the central value from first order calculation. The pink and green curves are $1\sigma$ and $2\sigma$ Collins moment and Sivers moment contours from numerical algorithm, yet the red and blue curves are $1\sigma$ and $2\sigma$ contours from first order calculation. . . . .   | 162 |
| 5.55 | Negative kaon $1\sigma$ and $2\sigma$ Collins moment and Sivers moment contours for 4 bins. Aqua round point is the center point from numerical algorithm, the red round point is the central value from first order calculation. The pink and green curves are $1\sigma$ and $2\sigma$ Collins moment and Sivers moment contours from numerical algorithm, yet the red and blue curves are $1\sigma$ and $2\sigma$ contours from first order calculation. . . . .   | 163 |
| 5.56 | Collins moments and sivers Moments change under tof cut $abs(CT.K.t) < 1$ . condition combining with the other different gas Cherenkov cuts and aerogel Cherenkov cuts for Negative kaon. The left panel is for $K^-$ Collins moment, the right panel is for $K^-$ Sivers moment. Under condition $abs(CT.K.t) < 1.$ , the different results change with different cut combination of gas Cherenkov and aerogel Cherenkov. The fluctuation is reasonable enen for $K^-$ at first bin, the central values of Collins moment for $K^-$ at first bin are around -0.18 $\sim$ -0.22, the central values of Sivers moment for $K^-$ at first bin are around -0.18 $\sim$ -0.22. . . . . | 164 |

|      |   |     |
|------|---|-----|
| 5.57 | Collins moments and sivers Moments change under tof cut $abs(CT.K.t) < 0.87$ condition combining with the other different gas Cherenkov cuts and aerogel Cherenkov cuts for Negative kaon. The left panel is for $K^-$ Collins moment, the right panel is for $K^-$ Sivers moment. Under condition $abs(CT.K.t) < 0.87$ , the different results change with different cut combination of gas Cherenkov and aerogel Cherenkov. The fluctuation is reasonable enen for $K^-$ at first bin, the central values of Collins moment for $K^-$ at first bin are around $-0.20 \sim -0.23$ , the central values of Sivers moment for $K^-$ at first bin are around $-0.20 \sim -0.23$ . . . . . | 165 |
| 5.58 | A tight BigBite vertex cut was used to study the systematic uncertainties. . . . .  | 166 |
| 5.59 | The Collins moment and Sivers moment for coincidence pions. The values are relative small. . . . .  | 168 |
| 5.60 | The Collins and Sivers moments of random sub group negative pion on Transversely $^3\text{He}$ target are shown. The fluctuation is bigger, but it is reasonable for the total pion results. . . . .  | 171 |
| 5.61 | The Collins and Sivers moments of sub group negative kaon on transversely $^3\text{He}$ target are shown. The fluctuation is bigger, but it is reasonable for the total negative kaon results. . . . .  | 172 |
| 5.62 | The results of Collins and Sivers moments of kaon on transversely polarized $^3\text{He}$ target. The error bars represent the statistical uncertainties only. The systematic uncertainties are shown in the bottom. . . . .  | 173 |
| 5.63 | The two dimensional correlations between $Q^2$ vs $x$ , $p_t$ vs $x$ and $z$ vs $x$ , the left column is for $\pi^+$ , the middle column is for $K^+$ , the right column is for proton. The first row is for $Q^2$ vs $x$ , which has strong correlations. The second row is for $p_t$ vs $x$ , which shows some correlations, so it is worth showing Collins and Sivers moments as a function of $p_t$ , the third row is for $z$ vs $x$ , which shows some corrections. . . . .   | 174 |
| 5.64 | The two dimensional correlations between $Q^2$ vs $x$ , $p_t$ vs $x$ and $z$ vs $x$ , the left column is for $\pi^-$ , the middle column is for $K^-$ , the right column is for anti-proton. The first row is for $Q^2$ vs $x$ , which has strong correlations. The second row is for $p_t$ vs $x$ , which shows some correlations, so it is worth showing Collins and Sivers moments as a function of $p_t$ , the third row is for $z$ vs $x$ , which shows some corrections. . . . .  | 175 |
| 5.65 | Collins and Sivers moments of kaons versus $p_t$ . Upleft panel: Collins moment of $K^+$ , upright panel: Sivers moment of $K^+$ . Downleft panel: Collins of $K^-$ , downright panel: Sivers moment of $K^-$ . The Collins and Sivers moments of $K^-$ are negative, the Sivers moment of $K^+$ is consistent with zero. . . . .   | 176 |
| 5.66 | Collins and Sivers moments of kaons versus $z$ . Upleft panel: Collins moment of $K^+$ , upright panel: Sivers moment of $K^+$ . Downleft panel: Collins of $K^-$ , downright panel: Sivers moment of $K^-$ . The Collins and Sivers moments of $K^-$ are negative, the Sivers moment of $K^+$ is consistent with zero. . . . .   | 176 |
| 5.67 | The $^3\text{He}$ dilution factor for kaons from reference $H_2$ data. The top panel is for $K^-$ (assuming all bins to calculate the central value, and showing the statistical uncertainty for each bin), the bottom panel is for $K^+$ . . . . .   | 177 |
| 5.68 | Results of Collins and Sivers moments of kaon on transversely polarized “neutron” target. The error bars represent the statistical uncertainties only. The systematic uncertainties are shown in bottom. . . . .  | 177 |
| 5.69 | Comparison between the neutron Sivers moment data with theoretical predictions by Anselmino <i>et al.</i> [131]. The red curves are the central values of the prediction, and the green curves indicate the $1\sigma$ range. The data points with different colors correspond to analysis using different number of bins in $x$ . The top panel is for $K^+$ and the bottom panel is for $K^-$ . . . . .  | 178 |
| 6.1  | Final pion Collins moment and Sivers moment on neutron. Fig. is from [111] . . . . .  | 179 |
| 6.2  | Final kaon Collins moment and Sivers moment on $^3\text{He}$ . . . . .  | 180 |



# Chapter 1

## Introduction

In order to understand visible matter<sup>1</sup>, the protons, neutrons and electrons need to be investigated<sup>2</sup>. Electron is an elementary particle<sup>3</sup>. However proton and neutron (both called nucleon) are composite particles<sup>4</sup> and contain complex inner structures.

Proton and neutron are hadrons. In 1964, Gell-Mann [40] and Zweig [41] independently predicted that hadrons consist of fractionally charged quarks based on their proposed quark model. Within the quark model, three flavors of quarks, up (u), down (d), and strange (s), are introduced to categorize hadrons.

However, some particles, such as  $\Delta^{++}$  (three u quarks with the same spin orientation) and  $\Omega^-$  (three s quarks with the same spin orientation), cannot be explained by simple quark model. It was forbidden by the Pauli exclusion principle. An additional SU(3) gauge degree of freedom (later named color charge) was introduced by Han and Nambu [9] and Greenberg [10] to solve the paradox. Meanwhile, Han and Nambu [9] also introduced an octet of particles (gluons) as the mediator of the interaction between the quarks in SU(3) gauge group.

In 1969, Feynman proposed the parton model [39], to explain the data obtained in the electron deep inelastic scattering (DIS) experiments at SLAC [6] [7] [8]. The scaling behavior observed in the DIS cross sections was understood as a consequence of elastic scatterings of electrons off point-like spin-1/2 charged particles (called partons). The charged partons were found to carry  $\sim 50\%$  of the proton's momentum (in the infinite momentum frame), with neutral partons carrying the rest. This is the first confirmation of the existence of fractionally charged point-like spin-1/2 partons.

---

<sup>1</sup>There are dark matter and dark energy in the universe as well as visible matter. About 70% of the mass of the universe is believed to be composed of "dark energy", a mysterious substance or energy field that seems to permeate the universe, causing its expansion to speed up over time. Something like 25% is composed of "dark matter" - some sort of stuff that (like ordinary matter) clumps together under its own gravity, but is somehow invisible to us. Finally, the remaining 5% or so is ordinary matter - stars, planets, gas, dust, and all the rest. In this thesis, I will not discuss about dark matter and dark energy. [1]

<sup>2</sup>More than 99% of the visible matter is made up of proton, neutron and electron. Only a few percent from quark masses and the rest are from the kinetic energy and interactions of quarks and gluons. Such findings are confirmed with the lattice calculation [2].

<sup>3</sup>The basic quantities of electron such as mass ( $0.510998910(13) \text{ MeV}/c^2$ ), electric charge ( $-e$  or  $1.602176487(40)10^{19} \text{ C}$ ), magnetic moment ( $1.00115965218111 \text{ B}$ ) and spin(1/2) are all clear.

<sup>4</sup>Even though the total mass (proton: $938.272013(23) \text{ MeV}/c^2$ , neutron: $939.565560(81) \text{ MeV}/c^2$ ), electric charge (proton: $+1e$  or  $1.602176487(40)10^{19} \text{ C}$ , neutron:  $0e$  or  $0C$ ), magnetic moment (proton: $2.792847351(28) \mu_N$ , neutron: $1.9130427(5) \mu_N$ ) and spin (proton:  $1/2$ , neutron: $1/2$ ) are all clear.

The discovery of the partonic structures in the nucleons in DIS inspired the formulation of Quantum Chromodynamics (QCD) as the gauge field theory governing the strong interaction. According to QCD, a proton or neutron consists of three valence quarks surrounded by a “sea” of quark-antiquark pairs and gluons which are in a continuous state of flux. The gluons are the gauge bosons responsible for the color forces due to SU(3) local gauge invariance. Interactions between quarks and gluons led to the phenomenon of scaling violation, which was confirmed by subsequent DIS experiments. Later, through DIS experiments it was possible to link the partons to the quarks, and to discover the existence of electrically neutral constituents, the gluons, which lead into a dynamical theory of quarks and gluons-the QCD. As a matter of facts, the study of the evolution with the momentum transfer of DIS observables represents probably the most direct test of the perturbative aspects of QCD.

The three valence quarks are uud for proton, and udd for neutron. The proton and neutron are isospin partners just like the u and d quarks.<sup>5</sup> The nucleon “sea” is mainly composed of  $u\bar{u}$ ,  $d\bar{d}$ , and  $s\bar{s}$ . The s quark<sup>6</sup>, named strange quark, as well as u quark and d quark, are the three lighter quarks<sup>7</sup>. All the quarks are elementary particles and all with color charge. The gluons have no electric charge, no mass, with spin 1 and color charge.

QCD describes the strong interactions between quarks and gluons for hadrons, all hadrons are categorized into baryons (which consist of three quarks or three antiquarks, such as proton, antiproton, and neutron) and mesons (which contain one quark and one antiquark, such as pion and kaon). QCD is a non-abelian gauge theory with local SU(3) gauge group describing transformations of the quark color fields. Due to the non-abelian nature of QCD, the gluons, the mediators of the strong force, carry color charge and interact with themselves. This characteristic of the strong interaction leads to two famous phenomena of QCD: the asymptotic freedom<sup>8</sup> and the color confinement<sup>9</sup>.

Following extensive experimental efforts over the last several decades, the momentum distributions of various types (flavors) of quarks and antiquarks in the proton have been mapped out over a broad range of Bjorken- $x$  (fraction of proton’s momentum carried by a quark/antiquark) using electron, muon, and neutrino induced DIS reactions. These unpolarized quark distribution functions,  $f_1^q(x, Q^2)$ , where  $q$  denotes the quark flavor, are fundamental quantities describing QCD confinement of quarks inside a hadron. They have also provided crucial inputs for describing many important processes in high energy hadronic collisions.

---

<sup>5</sup>The u(d) quark has mass  $1.7 - 3.3 \text{ MeV}/c^2$  ( $4.1-5.8 \text{ MeV}/c^2$ ), electric charge  $+\frac{2}{3}e$  ( $-\frac{1}{3}e$ ), spin  $1/2$  ( $1/2$ ).

<sup>6</sup>S quark has mass  $101^{+29}_{-21} \text{ MeV}/c^2$ , electric charge  $-\frac{1}{3}e$ , and spin  $1/2$ .

<sup>7</sup>There are three heavier quarks, charm quark(c), bottom quark(b), and top quark(t), we will not discuss these three heavier quarks in this dissertation

<sup>8</sup>The asymptotic freedom describes the observation that the interaction between two color objects is weak at high energy–short distance, and strong at low energy–long distance.

<sup>9</sup>The color confinement refers to the observation that quarks/gluons cannot be sigilarly isolated or directly observed due to their color charge.

More recently, the quark helicity distributions,  $g_1^q(x, Q^2)$ , have been studied with DIS using longitudinally polarized beams and targets. The quark helicity distributions refer to the quark longitudinal polarization in a longitudinally polarized proton. A major puzzle revealed by the EMC collaboration [11] [36] at CERN in late 1980s indicated that only a small fraction of the proton's spin is carried by quarks. The remaining spin must reside in the gluon spin ( $\Delta G$ ) and the orbital angular momentum of the quarks and gluons ( $L_q$  and  $L_g$ ). As shown in the following equation:

$$s_z^N = \frac{1}{2} = \frac{1}{2}\Delta\Sigma + \Delta G + L_z^q + L_z^g \quad (1.1)$$

where:

$$\Delta\Sigma = (\Delta u_v + \Delta d_v + \Delta q_s) \quad (1.2)$$

is the contribution carried by the valence  $u$  quark, valence  $d$  quark, and sea quark spins. The valence quarks ( $\Delta q_v \equiv \Delta q - \Delta \bar{q}$ ) carry roughly the expected fraction ( $\simeq 60\%$ ) of the nucleon spin, while the (on average) negative helicity of sea quarks reduces this to about 30-35%<sup>10</sup>.

Many ongoing and future experiments are devoted to the measurements of  $\Delta G$ ,  $L_q$ , and  $L_g$  using a variety of beams and reactions.

In addition to the unpolarized quark distributions  $f_1^q(x, Q^2)$  and the helicity distributions  $g_1^q(x, Q^2)$ , a third type of quark distributions,  $h_1^q(x, Q^2)$ , is also required to fully describe the momentum and spin distributions of quarks in the nucleons. Unlike  $g_1^q(x, Q^2)$  which refers to the net helicity of a quark in a longitudinally polarized proton,  $h_1^q(x, Q^2)$  corresponds to the net transverse polarization of a quark in a transversely polarized proton [13] [14], i.e.

$$h_1^q(x, Q^2) = f_{\uparrow}^q(x, Q^2) - f_{\downarrow}^q(x, Q^2) \quad (1.3)$$

where  $f_{\uparrow}^q(x, Q^2)$  and  $f_{\downarrow}^q(x, Q^2)$  are the number densities of quarks with transverse spin parallel or anti-parallel to the transverse polarization direction of the proton. The unpolarized quark distributions can be expressed in terms of  $f_{\uparrow}^q(x, Q^2)$  and  $f_{\downarrow}^q(x, Q^2)$  as

$$f_1^q(x, Q^2) = f_{\uparrow}^q(x, Q^2) + f_{\downarrow}^q(x, Q^2) \quad (1.4)$$

---

<sup>10</sup>Longitudinal polarization function:[http://www.scholarpedia.org/article/Longitudinal\\_polarization\\_functions](http://www.scholarpedia.org/article/Longitudinal_polarization_functions).

In an analogous fashion, the helicity quark distributions can be expressed as

$$g_1^q(x, Q^2) = f_{\rightarrow}^q(x, Q^2) - f_{\leftarrow}^q(x, Q^2) \quad (1.5)$$

where  $f_{\rightarrow}^q(x, Q^2)$  and  $f_{\leftarrow}^q(x, Q^2)$  are the number densities of quarks with longitudinal spin parallel or anti-parallel to the longitudinal polarization of the proton. The differences between  $h_1^q(x, Q^2)$  and  $g_1^q(x, Q^2)$  are expected as a result of the relativistic motion of the quarks for which boosts and rotations do not commute. Similarly, the unpolarized quark distributions can also be expressed in terms of  $f_{\rightarrow}^q(x, Q^2)$  and  $f_{\leftarrow}^q(x, Q^2)$  as

$$f_1^q(x, Q^2) = f_{\rightarrow}^q(x, Q^2) + f_{\leftarrow}^q(x, Q^2) \quad (1.6)$$

Several model calculations on  $h_1^q(x, Q^2)$  based on chiral quark-soliton model [15] and quark-diquark model [16] have been performed. A measurement of the transversity distribution would provide much insight on the dynamics of quarks in the nucleon. The transversity distributions are difficult to measure, since they are chirally odd objects and therefore can not be measured in inclusive DIS which conserves chirality. As a result, very little is known experimentally for the quark transversity distributions. Fortunately, they may be accessible in semi-inclusive DIS (SIDIS), where the leading hadron formed by the quark knocked out by the incoming electron is also detected. One expects that SIDIS would provide additional information not available for inclusive DIS, since some properties (like the flavor and the transverse polarization) of the quark could be revealed by the nature of the measured hadrons. The question is, how can the hadrons in SIDIS reveal the transverse spin property of the quarks? This requires that the hadronization process be sensitive to the transverse spin of the quark.

In 1993, Collins [17] suggested that the transverse momentum of the hadron (relative to the axis defined along the quark momentum direction) could be correlated with the transverse spin direction of the quark. In other words, there could be a left-right asymmetry in the fragmentation of transversely polarized quark into a hadron. This transverse-spin dependent fragmentation function, called the Collins fragmentation function, is itself a chirally-odd object. The Collins function describes the correlation between quark's transverse spin and the hadron's transverse momentum and can be regarded as a "quark polarimeter" for detecting the transverse spin of the fragmenting quark. By combining two chirally-odd objects (transversity distribution function and Collins fragmentation function), the SIDIS can be used to extract the quark transversity distributions. The Collins function is time-reversal odd, since it corresponds to a term proportional to  $(\vec{k} \times \vec{p}_{h\perp}) \cdot \vec{s}_q$  in the quark fragmentation process ( $\vec{k}$  and  $\vec{s}_q$  are the momentum and the transverse spin of the fragmenting quark, and  $\vec{p}_{h\perp}$  is the transverse momentum of the hadron). The existence of this novel T-odd fragmentation function

requires interference of two amplitudes with different imaginary parts in the fragmentation process. Recent SIDIS experiment at HERMES [18], [19], [20], [50] and COMPASS [21], as well as data from BELLE [22], indicate that the Collins functions indeed exist and their magnitude is sufficiently large in order to extract information on the transversity distributions (see later). Any new experimental information on the Collins function is of interest not only for its connection to the extraction of quark transversity distributions in SIDIS, but also for understanding the nature of this novel T-odd fragmentation function.

An entirely different mechanism can also contribute to the azimuthal asymmetry in SIDIS. It was suggested by Sivers [23] that correlations between the transverse spin of the target nucleon and the transverse momentum of the quark could lead to single-spin asymmetries<sup>11</sup> in various processes. This correlation is expressed in terms of the ‘‘Sivers Function’’, which is an example of transverse-momentum-dependent (TMD) parton distribution functions. An interesting feature of the Sivers function is that it is related to the forward scattering amplitude of  $N_q^{\Rightarrow} \rightarrow N_q^{\Leftarrow}$  where the helicity of the target nucleon is flipped. The helicity flip of the nucleon must involve the orbital angular momentum of the unpolarized quark. Therefore, the Sivers function is connected to the orbital angular momentum of the quark. As a time-reversal odd object, the Sivers function requires initial/final state interactions via a soft gluon. As shown in references [24] [25] [26] [27] [28], such interactions are incorporated in a natural fashion by the gauge link that is required for a gauge-invariant definition of the TMD parton distribution. An unambiguous measurement of Sivers function would be very valuable for understanding the nature of the TMD parton distributions.

Several recent measurements at HERMES using longitudinally polarized hydrogen and deuterium targets have observed azimuthal asymmetries in SIDIS. However, separation of the Collins from the Sivers mechanism was not possible since both mechanisms have a common  $\sin\phi_h$  azimuthal behavior, where  $\phi_h$  is the azimuthal angle of the hadron. This difficulty is avoided when transversely polarized targets are used. The additional degree of freedom associated with the azimuthal angle  $\phi_S$  of the target nucleon polarization direction allows an unambiguous separation of these two mechanisms, namely, a  $\sin(\phi_h + \phi_S)$  and a  $\sin(\phi_h - \phi_S)$  mechanisms.

Both the HERMES [18] [19] [20] [50] and the COMPASS [21] experiments have recently reported first results from SIDIS data collected with transversely polarized targets. The HERMES experiment used 27.6 GeV positron beam bombarding a transversely polarized hydrogen gas target. The COMPASS experiment has also reported the measurement for 160 GeV/c muon beam incident on transversely polarized <sup>6</sup>LiD target. As discussed later, the HERMES experiment observed a striking pion-charge dependence of the Collins and Sivers effects on the polarized hydrogen target. In contrast, the COMPASS data on polarized <sup>6</sup>LiD target

---

<sup>11</sup>Which arises from final-state interaction with gluon exchange between the outgoing quark and the target spectator system in deep inelastic lepton-nucleon scattering at leading twist in perturbative QCD; i.e., the rescattering corrections are not power-law suppressed at large photon virtuality  $Q^2$  at fixed  $x_{bj}$ .

showed that both the Collins and the Sivers effects are consistent with zero<sup>12</sup>. These results suggest a strong and unexpected flavor dependence for both Collins and Sivers functions.

A measurement of the SIDIS using a transversely polarized  $^3\text{He}$  target, has been finished in HallA Jefferson Lab [29], and the result would provide very valuable new inputs for understanding the difference between the HERMES and the COMPASS results. A polarized  $^3\text{He}$  target is, to a good approximation, a polarized neutron target, since the two protons in a polarized  $^3\text{He}$  couple dominantly to a spin-zero state. Therefore, the JLab experiment probes the neutron quark structures, while the HERMES and COMPASS experiments measure the proton and deuteron quark structures. The measurement proposed at JLab could provide complementary information on the flavor structure of the Collins and Sivers function, as well as the first information on the transversity distributions of the neutrons.

When the accelerated electron beam scattering off the transversely polarized  $^3\text{He}$  target, the major final produced mesons are pions, meanwhile, there are some final produced mesons are kaons. For this experiment, the pion Collins and Sivers moments are the main Physics results to be extracted, meanwhile the kaon Collins and Sivers moments are also important physics attributes to be extracted even as by-product as experimental proposal. In this thesis, we will specifically discuss the detection of kaon Collins and Sivers moments, due to much less statistics of kaons than pions<sup>13</sup>, the final kaon Collins and Sivers moments will be only extracted at the  $^3\text{He}$  target instead of virtual “neutron” target.

The theory of the inner spin structure of the nucleon will be reviewed in Chapter 2 through inclusive DIS processes. The concept of factorization of the deep-inelastic scattering processes into distribution functions and fragmentation functions will be introduced. There are different notations of distribution and fragmentation functions in these fields, details about the chosen notation and further conventions will be given in the subsequent chapters. In Chapter 3, the Semi-Inclusive DIS (SIDIS) will be introduced then the Collins moment and the Sivers moment will be discussed. The chiral-odd transversity distribution function, the Sivers distribution function, the chiral-odd Collins fragmentation function and other related functions will also be discussed. In the last part of Chapter 3, the recent results from HERMES and COMPASS will be presented. In Chapter 4, the setup of the transversity experiment in JLab HALLA will be introduced including the incident Continuous Wave (CW) 5.89 GeV/c electron beam, the extended 40 cm long transversely polarized target and the spin-flipped system, the BigBite detector package to detect coincidence scattered electrons, the High Resolution Spectrometer (HRS) to detect kaons, pions and protons, and the data acquisition system including the main electronics for triggering and timing. In Chapter 5, the

---

<sup>12</sup>The COMPASS shows slightly nonzero result in 2009.

<sup>13</sup>The final coincidence positive kaons are about 5% of the final coincidence pions and the final coincidence negative kaons are about 1% of the final coincidence negative pions.

data analysis including detector calibration, target calibration, cuts studies will be addressed. The total number of kaon, pion, and proton events will be extracted. In this dissertation, the kaon Collins and Sivers moments will be extracted. Due to small kaon statistics, the maximum likelihood method (MLM) rather than Least Square Fit method will be used to extract the final kaon results. I will also introduce the numerical algorithm of MLM after using first order expansion which has analytical solution. Systematic uncertainties from target, detectors, cuts, and other angular modulation effects and the influence of incomplete acceptance due to small statistics will be estimated and the final kaon Collins and Sivers moments will be extracted. In Chapter 6, the final result of kaon Collins and Sivers moments as well as pion Collins and Sivers moments will be discussed and interpreted.

# Chapter 2

## Spin Structure of the Nucleons

With the evidence that the proton and the neutron are not elementary particles, the task of explaining the nucleon's spin in terms of its constituents is challenging. This provides a new frontier in hadron physics field in phenomenology, experiment and theory which is still very active and has had a crucial impact in our understanding of the internal structure of the nucleon.

From experimental side, the scattering polarized beams off polarized targets is a very successful tool to extract information about the spin of the inner structure of the nucleon. Inclusive Deep-Inelastic Scattering (DIS) was the first process in which point-like partons were identified inside the nucleon. Since then, measurement through DIS processes provides a variety of information on parton density distribution, parton helicity distribution, and related observables.

Furthermore, the semi-inclusive Deep-Inelastic Scattering (SIDIS) needs to be introduced in order to understand the topics of this thesis which are the transversity distribution functions, Sivers distribution functions and the Collins fragmentation functions. So I will first describe the DIS process in this chapter.

### 2.1 Deep Inelastic Scattering

The Inclusive Deep Inelastic Scattering (DIS) process is described in Fig. 2.1. The incident lepton (the

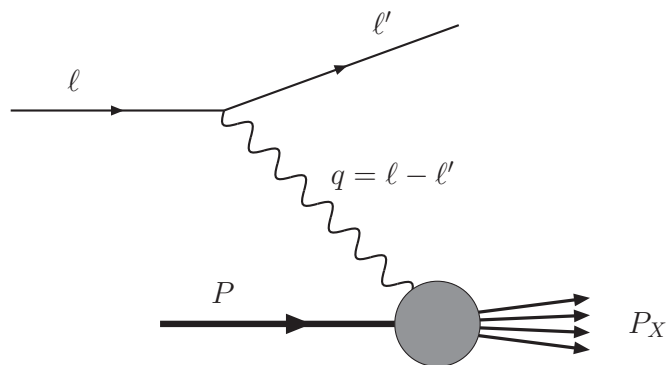


Figure 2.1: Feynman diagram of deep inelastic scattering. Figure is from Ref. [35]



accelerated electron beam in JLab Hall A) scatters off a nucleon  $N$  via the exchange of a virtual boson<sup>1</sup>. In DIS process, the momentum transfer is so large that the nucleon breaks and forms a hadronic final state  $X$ :

$$l(k) + N(P) \rightarrow l'(k') + X \quad (2.1)$$

where  $k = (E, \vec{p})$  and  $k' = (E', \vec{p}')$  are the momentum 4-vectors of the scattering lepton  $l$  and scattered lepton  $l'$ . Target momentum 4-vector is  $P \stackrel{lab}{=} (M, 0, 0, 0)$  in the lab frame, and  $M$  is the rest mass of the nucleon. The relevant kinematic variables for inclusive DIS process are summarised as follows:

$$\begin{aligned} \theta & \quad \text{polar scattering angle in the laboratory} \\ q = k - k' & \quad \text{four-momentum transfer to the target} \\ \nu = \frac{P \cdot q}{M} \stackrel{lab}{=} E - E' & \quad \text{energy transfer to the target} \\ y = \frac{P \cdot q}{P \cdot k} \stackrel{lab}{=} \frac{\nu}{E} & \quad \text{fractional energy transfer to the target} \\ Q^2 = -q^2 \approx 4EE' \sin^2 \frac{\theta}{2} & \quad \text{magnitude of momentum transfer squared} \\ W^2 = (P + q)^2 \stackrel{lab}{=} M^2 + 2M\nu - Q^2 & \quad \text{mass squared of the final state} \\ x = \frac{Q^2}{2P \cdot q} = \frac{Q^2}{2M\nu} & \quad \text{Bjorken scaling variable} \end{aligned}$$

$Q^2$  is a measure of the spatial resolution in the scattering process. In DIS processes,  $Q^2$  is large enough to resolve the constituents of the nucleon. The dimensionless Bjorken scaling variables  $x$  describes the inelasticity of the process. For elastic scattering process,  $W^2 = M^2$  and  $x = 1$ . For inelastic scattering process, the mass of the final state becomes larger than the nucleon mass and  $0 < x < 1$ . From the measurement of the  $k'$  of the scattered lepton, one can determine the values of  $x$  and  $Q^2$ .

## 2.2 The DIS cross section

The differential cross section for a scattered lepton which is detected with a solid angle  $d\Omega$  and in an energy range  $[E', E' + dE']$  can be written as [30]:

$$\frac{d^2\sigma}{d\Omega dE'} = \frac{\alpha^2}{2MQ^4} \frac{E'}{E} L_{\mu\nu} W^{\mu\nu} \quad (2.2)$$

where  $\alpha$  is the electromagnetic coupling constant.  $L_{\mu\nu}$  and  $W_{\mu\nu}$  are the leptonic and hadronic tensors, describing the interaction at the leptonic and hadronic vertices of the DIS process. They can be split into

---

<sup>1</sup>In JLab Hall A, this is predominantly electromagnetic interaction due to the low incident beam energy (6 GeV). The exchanged boson is photon. At much higher energies,  $Z^0$  boson exchange becomes important. Note that in JLab also weak interactions studied by high intensity beam and measuring the Parity Violation L-R asymmetry.

symmetric parts and antisymmetric parts under parity transformation, respectively:

$$L_{\mu\nu} = L_{\mu\nu}^{(S)} + iL_{\mu\nu}^{(A)}, \quad W_{\mu\nu} = W_{\mu\nu}^{(S)} + iW_{\mu\nu}^{(A)}, \quad (2.3)$$

where only the antisymmetric parts are spin-dependent. The DIS differential cross section becomes:

$$\frac{d^2\sigma}{d\Omega dE'} = \frac{\alpha^2}{2MQ^4} \frac{E'}{E} [L_{\mu\nu}^{(S)} W^{\mu\nu(S)} - L_{\mu\nu}^{(A)} W^{\mu\nu(A)}]. \quad (2.4)$$

The antisymmetric combinations of  $L_{\mu\nu}$  and  $W_{\mu\nu}$  do not appear due to the parity conservation of the electromagnetic interaction.

For leptonic tensor, after summation over all possible spin state  $s'$  of the final state lepton, the symmetric part

$$L_{\mu\nu}^{(S)}(k; k') = 2(k_\mu k'_\nu + k_\nu k'_\mu - g_{\mu\nu}(m^2 - k^\rho k'_\rho)) \quad (2.5)$$

is spin-independent while the antisymmetric part

$$L_{\mu\nu}^{(A)}(k, s; k') = 2m\epsilon_{\mu\nu\alpha\beta} s^\alpha (k^\beta - k'^\beta), \quad (2.6)$$

depends on the spin  $s$  of the incoming lepton. Here,  $\epsilon_{\mu\nu\alpha\beta}$  is the totally-antisymmetric Levi-Civita tensor (with  $\epsilon_{0123} = +1$ ) and  $m$  is the lepton mass.

Similarly but more complicated, the hadronic tensor can be decomposed into a symmetric and an antisymmetric part, the symmetric part is spin-independent and the antisymmetric part is dependent on the target nucleon spin  $S$ :

$$W_{\mu\nu}^{(S)}(q; P, S) = W_{\mu\nu}^{(S)}(q; P) + iW_{\mu\nu}^{(A)}(q; P, S). \quad (2.7)$$

where

$$\frac{1}{2M} W_{\mu\nu}^{(S)}(q; P) = (-g_{\mu\nu} + \frac{q_\mu q_\nu}{q^2}) W_1(P \cdot q, q^2) + \frac{1}{M^2} (P_\mu - \frac{P \cdot q}{q^2} q_\mu) (P_\nu - \frac{P \cdot q}{q^2} q_\nu) W_2(P \cdot q, q^2), \quad (2.8)$$

$$\frac{1}{2M} W_{\mu\nu}^{(A)}(q; P, S) = \epsilon_{\mu\nu\alpha\beta} q^\alpha \left\{ M S^\beta G_1(P \cdot q, q^2) + \frac{1}{M} [(P \cdot q) S^\beta - (S \cdot q) P^\beta] G_2(P \cdot q, q^2) \right\} \quad (2.9)$$

in which  $W_1$ ,  $W_2$ ,  $G_1$ ,  $G_2$  are Lorentz-invariant inelastic scalar form factors and are usually substituted by four dimensionless quantities dependent on the two DIS variables  $x$  and  $Q^2$ :

$$F_1(x, Q^2) \equiv M W_1(P \cdot q, q^2), \quad (2.10)$$

$$F_2(x, Q^2) \equiv \nu W_2(P \cdot q, q^2), \quad (2.11)$$

$$g_1(x, Q^2) \equiv \frac{(P \cdot q)^2}{\nu} G_1(P \cdot q, q^2), \quad (2.12)$$

$$g_2(x, Q^2) \equiv \nu(P \cdot q) G_2(P \cdot q, q^2). \quad (2.13)$$

$F_1$  and  $F_2$  are usually referred to as *unpolarized structure functions*, and  $g_1$ , and  $g_2$  are known as *polarized structure functions* dependent on spin. In the pQCD regime, all these structure functions cannot be predicted from first principles and can thus only be determined experimentally.

The symmetric and antisymmetric parts of the hadronic tensor can be rewritten in terms of these four structure functions according to:

$$W_{\mu\nu}^{(S)}(q; P) = 2 \left( -g_{\mu\nu} + \frac{q_\mu q_\nu}{q^2} \right) F_1(x, Q^2) + \frac{2}{P \cdot q} \left( P_\mu - \frac{P \cdot q}{q^2} q_\mu \right) \left( P_\nu - \frac{P \cdot q}{q^2} q_\nu \right) F_2(x, Q^2) \quad (2.14)$$

$$W_{\mu\nu}^{(A)}(q; P, S) = \epsilon_{\mu\nu\alpha\beta} \frac{2Mq^\alpha}{P \cdot q} \left[ S^\beta g_1(x, Q^2) + \left( S^\beta - \frac{S \cdot q}{P \cdot q} P^\beta \right) g_2(x, Q^2) \right] \quad (2.15)$$

Due to parity conservation of the electromagnetic interaction, only terms with the same symmetry can survive in the cross section. Therefore, the differential cross section can be obtained by replacing Eq. 2.2 as following:

$$\frac{d^2\sigma}{dE' d\Omega} = \frac{\alpha^2}{2MQ^4} \frac{E'}{E} [L_{\mu\nu}^{(S)} W^{\mu\nu(S)} - L_{\mu\nu}^{(A)} W^{\mu\nu(A)}]. \quad (2.16)$$

Same as Eq. 2.4.

The first part of Eq. 2.16 is the spin-independent cross section, after averaging over all spins in the initial state of the scattering process and summing over the spins in the final state, only the spin-independent symmetric parts of the leptonic and hadronic tensors contribute to the cross section, which can be expressed as Eq. 2.17:

$$\frac{d^2\sigma^{unpol}}{dE' d\Omega} = \frac{\alpha^2}{2MQ^4} \frac{E'}{E} L_{\mu\nu}^{(S)} W^{\mu\nu(S)} = \left( \frac{d^2\sigma}{dE' d\Omega} \right)_{Mott} \cdot \left[ \frac{2}{M} F_1(x, Q^2) \tan^2(\theta/2) + \frac{1}{\nu} F_2(x, Q^2) \right], \quad (2.17)$$

where

$$\left( \frac{d^2\sigma}{dE' d\Omega} \right)_{Mott} = \frac{4\alpha^2 E'^2}{Q^4} \cos^2(\theta/2) \quad (2.18)$$

is the Mott cross section, which describes the elastic scattering of a relativistic spin-1/2 particle off a spin-less point-like particle.  $F_2(x, Q^2)$  contains the unpolarized structure functions, which is the deviation due to the composite nature of the nucleon of the observed DIS cross section from the Mott cross section. Fig. 2.2 shows

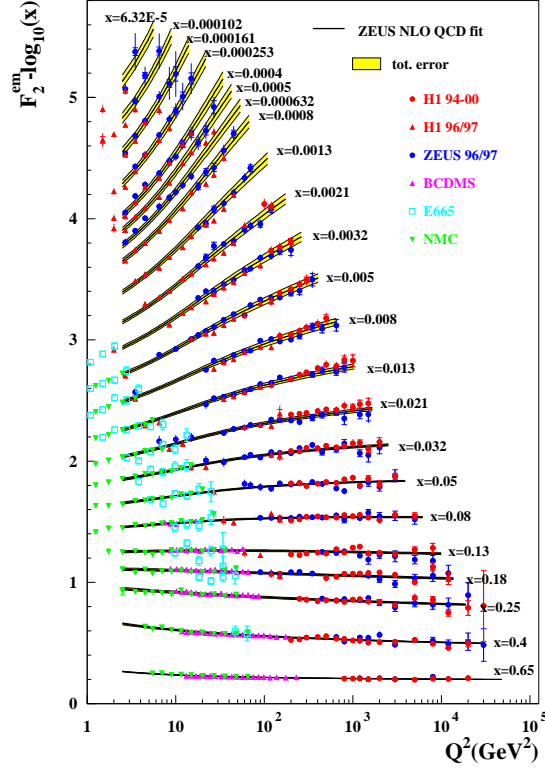


Figure 2.2:  $F_2^{em}$ , i.e.  $F_2$  due to  $\gamma$  exchange, from HERA and fixed target experiments compared with the ZEUS NLO fit [31].

a collection of data for the structure functions  $F_2$  as a function of  $Q^2$  for different  $x$ . The spin-independent DIS cross section Eq. 2.17 can be alternatively described in terms of the inclusive variables  $x$ ,  $y$  and  $Q^2$ :

$$\frac{d^2\sigma}{dx dQ^2} = \frac{4\pi\alpha^2}{xQ^4} [y^2 x F_1(x, Q^2) + (1-y) F_2(x, Q^2)] \quad (2.19)$$

The early deep-inelastic scattering experiments performed at SLAC showed that the unpolarized structure function  $F_1$  and  $F_2$  are approximately  $Q^2$ -independent in the large momentum transfer region:

$$F_{1,2}(x, Q^2) \approx F_{1,2}(x) \quad (Q^2 \gg M^2) \quad (2.20)$$

This phenomenon became known as *Bjorken scaling* or *scale invariance* because, in the so-called Bjorken limit

$$\lim_{Bj} = \begin{cases} Q^2 \rightarrow \infty \\ \nu \rightarrow \infty, \\ x = \frac{Q^2}{2M\nu} \quad \text{fixed} \end{cases} \quad (2.21)$$

Which means when  $Q^2$  and  $\nu$  approach infinity and for a fixed  $x$ , the  $F_{1,2}(x, Q^2)$  becomes  $F_{1,2}(x)$ . A  $Q^2$ -independence of the structure functions would imply that the incoming lepton detects the same structure independent of the spatial resolution. The observed scaling behavior could be successfully accounted for by considering scattering from point-like constituents within the proton, which is the first dynamical evidence of the quarks.

With the increased accuracy of the next generation DIS experiments and the broadening of the kinematic regions explored, a noticeable  $Q^2$ -dependence of the structure functions appeared (Fig. 2.2). Since a quark can radiate a hard gluon to gain large transverse momentum, and the gluons can split into  $q\bar{q}$  pairs and gluons can couple with other gluons, the violation of the Bjorken scaling, interpreted as the evidence of the dynamical structure of the proton, can be explained in the Quantum Chromodynamics (QCD) interaction, to be discussed later.

The second part of Eq. 2.16 is the spin-dependent cross section. When both the incident lepton beam and the target protons are longitudinally polarized, the antisymmetric (spin-dependent) parts of the leptonic and hadronic tensors contribute to the cross section. Since both the spin-independent and the spin-dependent parts of the cross section are non-vanishing in this situation, the only way to isolate the spin-dependent component consists in measuring the difference of the cross sections obtained with two opposite target spin states. From this difference, the net spin-dependent cross section is obtained as following:

$$\frac{d^3\sigma^{\leftarrow}}{dxdy} - \frac{d^3\sigma^{\rightarrow}}{dxdy} = \frac{4\alpha^2}{sxy} \left[ \left( 2 - y - \frac{\gamma^2 y^2}{2} \right) g_1(x, Q^2) - \gamma^2 y g_2(x, Q^2) \right], \quad (2.22)$$

where  $s = (P + k)^2$  denotes the squared center-of-mass energy and  $\gamma = (2Mx)/Q$ ,  $\rightarrow$  represents the longitudinal spin orientation of the incoming lepton, and  $\leftarrow, \Rightarrow$  denote the two different longitudinal spin states of the target nucleon.

Because  $\gamma^2 \sim 1/Q^2$  and  $g_2(x, Q^2)$  is small by itself, the cross section is dominated by the first term, containing the structure function  $g_1(x, Q^2)$ . In particular, if the target spin is collinear with the direction of the virtual photon, the contribution of  $g_2(x, Q^2)$  vanishes completely due to no effect of transverse component. However, because it is not possible to polarize the target nucleons with respect to the virtual photon direction, the non-vanishing contribution of the  $g_2(x, Q^2)$  structure function, which arises from the fact that the virtual photon direction has a transverse component with respect to the target spin, is taken into account. The  $g_1$  structure function is called parton helicity distribution and has been measured at SLAC, CERN, DESY, and JLab over the past two decades. Fig. 2.3 shows  $xg_1$  from different experiments for proton, deuteron and neutron.

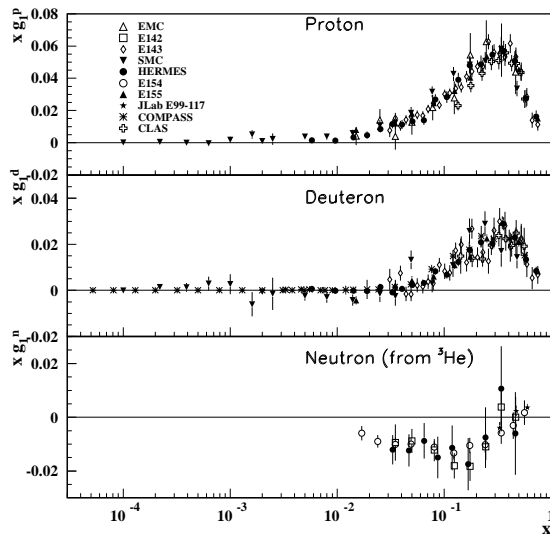


Figure 2.3: The spin-dependent structure function  $xg_1$  of the proton, deuteron, and neutron (from  $^3\text{He}$  target) measured in deep inelastic scattering of polarized electrons/positrons. This figure is reproduced from Ref. [34]

If the target is polarized transverse to the incoming lepton beam, the cross section in this case becomes:

$$\frac{d^3\sigma^{\rightarrow\downarrow}}{dx dy d\phi_S^l} - \frac{d^3\sigma^{\rightarrow\uparrow}}{dx dy d\phi_S^l} = \frac{4\alpha^2}{sxy} \sqrt{1-y-\frac{\gamma^2 y^2}{4}} [\gamma g_1(x, Q^2) + 2g_2(x, Q^2)] \cos \phi_S^l, \quad (2.23)$$

where  $\phi_S^l$  is the azimuthal angle of the target spin vector  $\vec{S}$  with respect to the lepton beam scattering plane. Neither  $g_1(x, Q^2)$  nor  $g_2(x, Q^2)$  dominates the cross section. The combination of measurements on longitudinally and transversely polarized targets can extract the  $g_2(x, Q^2)$ . First measurements of  $g_2(x, Q^2)$  were available in Ref. [36].

## 2.3 The Quark Parton Model (QPM) and the QCD improved QPM

The discovery of Bjorken Scaling [37] [38] [39] confirmed the existence of point-like components in protons and neutrons. Then, the Quark Parton Model (QPM) was developed to explain the Bjorken scaling. These partons were later recognized to be quarks, which had already been proposed by Gell-Mann [40] and Zweig [41] as basic constituents of the protons, neutrons and other hadrons.

The Quark Parton Model (QPM) is typically formulated in the infinite momentum frame, where  $\nu$  and

$Q^2$  go to infinity while  $x$  remains finite. In this special frame, the scattering can be viewed as the absorption of a virtual photon by one of the collinearly moving partons inside the nucleon. The struck parton carries only a fraction  $p_q = xP$  of the total momentum of the nucleon, where  $x$  is the Bjorken variable.

In the QPM, the nucleon is described in terms of the parton distribution functions (pdf)  $q_f(x)$ , which represents the probability density to find in the nucleon a quark  $f$  with fractional momentum  $x$ . The quantity  $q_f(x)dx$  represents the number of quarks with flavor  $f$  and fractional momentum in the range  $[x, x + dx]$ . If  $q_f^{\vec{\zeta}}$  and  $q_f^{\overleftarrow{\zeta}}$  are defined as the probability densities to find a quark of flavor  $f$  with fractional momentum  $x$  and spin parallel or anti-parallel, respectively, to the nucleon spin, there are relations between the spin-independent and spin-dependent parton distribution functions as:

$$q_f(x) = q_f^{\vec{\zeta}} + q_f^{\overleftarrow{\zeta}} \quad (2.24)$$

$$\Delta q_f(x) = q_f^{\vec{\zeta}} - q_f^{\overleftarrow{\zeta}} \quad (2.25)$$

where  $\Delta q_f(x)$  is the quark helicity distribution function.

Now, the spin-independent and spin-dependent structure functions can be interpreted within the QPM as the charge-weighted sum over the quark flavor  $f$  of the corresponding parton distribution functions:

$$F_1(x) = \frac{1}{2} \sum_f e_f^2 q_f(x) \quad (2.26)$$

$$g_1(x) = \frac{1}{2} \sum_f e_f^2 \Delta q_f(x) \quad (2.27)$$

$$g_2(x) = 0 \quad (2.28)$$

The resulting feature of  $q_f(x)$  is shown in Fig. 2.4, it is labeled by  $f$  instead of  $q_f$  in the Fig. 2.4.

Actually, the QPM model is too naïve to describe the internal structure of nucleon. In the late 1970s, a field theory for strong interaction, the QCD was developed whose basic fields are quarks interacting via electrically neutral vector gluons. QCD is the non-Abelian gauge theory of the strong interaction and part of the Standard Model. Quarks couple to the strong interaction through three different colours. And the field quanta of the strong interaction, i.e., the gluons, do carry colour charge, so they can interact with themselves. This causes a scale or energy dependence of the strong coupling ‘constant’  $\alpha_s$ :

$$\alpha_s(Q^2) = \frac{12\pi}{(33 - 2n_f) \ln(Q^2/\Lambda_{QCD}^2)} \quad (2.29)$$

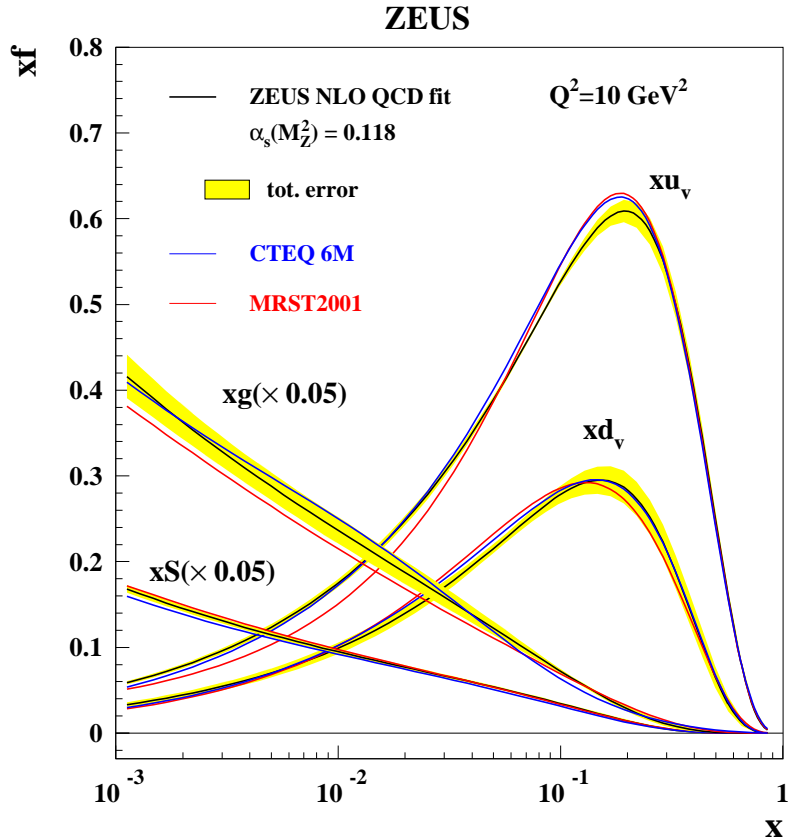


Figure 2.4: Comparison of the ZEUS fit with the global analyses CTEQ6M [33] and MRST2001 [32].

where  $n_f$  is the number of quark flavors. The QCD scale parameter  $\Lambda_{QCD}$  depends on  $n_f$  and the renormalization scheme. It is of the order of a couple of hundred MeV. Eq. 2.29 is only valid for  $Q^2 \gg \Lambda_{QCD}^2$  and shows that the coupling decreases with increasing  $Q^2$  and reaches zero for  $Q^2 \rightarrow \infty$ . This feature, which only appears in non-Abelian gauge theories, is called asymptotic freedom.

Due to the fact that quarks and gluons interact, gluons dress the quarks in the nucleon with a cloud of gluons and virtual quark-antiquark pairs, so-called sea quarks. With increasing  $Q^2$ , the wavelength of the virtual photon decreases and the resolution of the external probing current increases. The parton distribution functions and parton helicity distributions not only depend on  $x$  but also depend on  $Q^2$ . At low  $Q^2$ , a photon does not interact with the electrically neutral gluon. With sufficiently large  $Q^2$ , the gluon can be resolved in a quark-antiquark pair and the photon can interact with one of them.

In leading order perturbative QCD, the structure functions have the same form as in QPM except the pdfs also depend on  $Q^2$ :

$$F_1(x, Q^2) = \frac{1}{2} \sum_f e_f^2 q_f(x, Q^2), \quad (2.30)$$



$$g_1(x, Q^2) = \frac{1}{2} \sum_f e_f^2 \Delta q_f(x, Q^2), \quad (2.31)$$

In the QCD improved parton model the structure functions  $g_2(x, Q^2)$  does not vanish but appears from quark-gluon interactions.

## 2.4 The quark-quark correlation matrix

In the QCD improved parton model, the DIS can be described as the incoherent sum of elastic scattering on quasi-free constituents (quarks and antiquarks) of the nucleon. When a DIS process in which an initial state nucleon with momentum  $P$  and spin  $S$  is probed by a virtual photon carrying four momentum  $q$ , leading to a (not observed) final hadronic state  $X$  with momentum  $P_X$  and energy  $E_X$ , the hadronic tensor  $W_{\mu\nu}$  can be rewritten using a quantum field approach [42]:

$$W^{\mu\nu} = \frac{1}{2\pi} \sum_f e_f^2 \sum_X \int \frac{d^3 P_X}{(2\pi)^3 2E_X} \int \frac{d^4 p}{(2\pi)^4} \int \frac{d^4 k}{(2\pi)^4} \delta(k^2) \\ \times [\bar{u}_f(k) \gamma^\mu \phi_f(p; P, S)] * [\bar{u}_f(k) \gamma^\nu \phi_f(p; P, S)] \times (2\pi)^4 \delta^4(P - q - P_X) (2\pi)^4 \delta^4(p + q - k). \quad (2.32)$$

Here  $p$  and  $e_q$  are the four-momentum and the fractional electric charge of the soft quark struck by the virtual photon,  $u(\bar{u})$  is the spinor of the scattered quasi-free quark, carrying four-momentum  $k = p + q$ , and  $\gamma_\mu$  are the Dirac matrices. The matrix elements

$$\phi_i(p; P, S) = \langle X | \psi_i(0) | P, S \rangle, \quad (2.33)$$

of the quark fields  $\psi_i$  between the nucleon  $|P, S\rangle$  and its remnant  $|X\rangle$ , describes the emission of the soft quark from the nucleon. The Dirac delta functions represent momentum conservation.

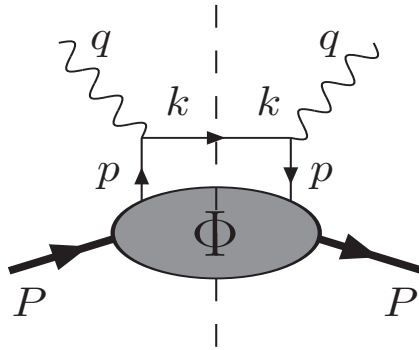


Figure 2.5: Handbag diagram for inclusive DIS

If we introduce the handbag diagram as Fig. 2.5, Eq. 2.32 can be rewritten in the following:

$$W_{\mu\nu} = \sum_q e_q^2 \int \frac{d^4 p}{(2\pi)^4} \delta((p+q)^2) \text{Tr}[\Phi \gamma_\mu (\not{p} + \not{q}) \gamma_\nu], \quad (2.34)$$

where  $\Phi$  is the *quark-quark correlation matrix (or quark-quark correlator)* with matrix element:

$$\Phi_{i,j}(p, P, S) = \sum_X \int \frac{d^3 P_X}{(2\pi)^3 2E_X} (2\pi)^4 \delta^4(P - p - P_X) \langle P, S | \psi_j(0) | X \rangle \langle X | \psi_i(0) | P, S \rangle. \quad (2.35)$$

where  $i$  and  $j$  are Dirac indices and summation over quark color is implicit. Using translational invariance, the completeness relation  $\sum_X |X\rangle \langle X| = 1$  and the identity

$$(2\pi)^4 \delta^4(P - p - P_X) \equiv \int d^4 \xi e^{i(P-p-P_X)\cdot\xi}, \quad (2.36)$$

The correlation matrix can be rewritten as a bilocal, bilinear operator acting on the initial nucleon state  $|P, S\rangle$ , intergrated over all possible separation  $\xi$  of the second quark spinor:

$$\Phi_{i,j}(p, P, S) = \int d^4 \xi e^{i p \cdot \xi} \langle P, S | \bar{\psi}_j(0) \psi_i(\xi) | P, S \rangle. \quad (2.37)$$

The correlation matrix can be decomposed in a basis of Dirac matrices:

$$\Gamma = 1, \gamma^\mu, \gamma^\mu \gamma_5, i\gamma_5, i\sigma^{\mu\nu} \gamma_5, \quad (2.38)$$

where  $\sigma^{\mu\nu} = \frac{i}{2}[\gamma^\mu, \gamma^\nu]$ , each selecting a different aspect of the nucleon inner structure [42]:

$$\Phi(p, P, S) = \frac{1}{2} \{ \mathcal{S} 1 + \mathcal{V}_\mu \gamma^\mu + \mathcal{A}_\mu \gamma_5 \gamma^\mu + i\mathcal{P}_5 \gamma_5 + i\mathcal{T}_{\mu\nu} \sigma^{\mu\nu} \gamma_5 \} \quad (2.39)$$

The scalar  $\mathcal{S}$ , vector  $\mathcal{V}_\mu$ , axial-vector  $\mathcal{A}_\mu$ , tensor  $\mathcal{T}_{\mu\nu}$ , and pseudo-scalar  $\mathcal{P}_5$  parameters depend on combinations of the quark momentum  $p$ , the nucleon momentum  $P$ , and the nucleon spin  $S$ .

The quantities above can be expanded according to powers of  $1/P^{+2}$ , where the leading order term is  $(1/P^+)^{-1} = P^+$ , and the next-to-leading term is  $(1/P^+)^0 = 1$ . The different powers correspond to the twist expansion according to [43], where the leading term is twist-two.

By neglecting transverse momentum of the quarks in the nucleon, only the vector, axial-vector, and tensor

---

<sup>2</sup>In order to understand the transverse components for specialty, the light cone coordinates are defined by  $(x^0, x^+, x^-, x^3)$ , where  $x^0$  is time component,  $x^3$  is z component, and  $x^+, x^-$  are combination of transverse components of  $x^1, x^2$  coordinates, in which  $x^+ \equiv \frac{1}{\sqrt{2}}(x^1 + x^2)$ , and  $x^- \equiv \frac{1}{\sqrt{2}}(x^1 - x^2)$ . Here  $P^+ = \frac{1}{\sqrt{2}}(P^1 + P^2)$ .

terms survive at leading order (= twist-two). They can be expressed by three real amplitudes  $A_i(p^2, p \cdot P)$  satisfying hermiticity and parity invariance.

$$\mathcal{V}^\mu = \frac{1}{2} \int d^4\xi d^{ip \cdot \xi} \langle P, S | \bar{\psi}(0) \gamma^\mu \psi(\xi) | P, S \rangle = A_1 P^\mu, \quad (2.40)$$

$$\mathcal{A}^\mu = \frac{1}{2} \int d^4\xi e^{ip \cdot \xi} \langle P, S | \bar{\psi}(0) \gamma^\mu \gamma_5 \psi(\xi) | P, S \rangle = \lambda_N A_2 P^\mu, \quad (2.41)$$

$$\mathcal{T}^{\mu\nu} = \frac{1}{2i} \int d^4\xi e^{ip \cdot \xi} \langle P, S | \bar{\psi}(0) \sigma^{\mu\nu} \gamma_5 \psi(\xi) | P, S \rangle = A_3 P^{[\mu} S_T^{\nu]} \quad (2.42)$$

where  $\lambda_N$  denotes the nucleon helicity and  $A_1 = \frac{1}{2P^+} \text{Tr}(\gamma^+ \Phi)$ ,  $\lambda_N A_2 = \frac{1}{2P^+} \text{Tr}(\gamma^+ \gamma_5 \Phi)$ , and  $S_T^i A_3 = \frac{1}{2P^+} \text{Tr}(\gamma^+ \gamma^i \gamma_5 \Phi)$ , in which  $S^\mu \approx \lambda_N P^\mu / M + S_T^\mu$  was applied.

Integrating the amplitudes  $A_i$  over  $p$  with the constraint  $x = \frac{p^+}{P^+}$ , three leading-twist parton distribution functions are obtained:

$$q(x) = \int \frac{d^4p}{(2\pi)^4} A_1(p^2, p \cdot P) \delta\left(x - \frac{p^+}{P^+}\right) \quad (2.43)$$

$$\Delta q(x) = \int \frac{d^4p}{(2\pi)^4} A_2(p^2, p \cdot P) \delta\left(x - \frac{p^+}{P^+}\right) \quad (2.44)$$

$$\delta q(x) = \int \frac{d^4p}{(2\pi)^4} A_3(p^2, p \cdot P) \delta\left(x - \frac{p^+}{P^+}\right) \quad (2.45)$$

These parton distribution functions provide a complete description of the momentum and spin distributions of the quarks within the nucleon at leading-twist level. The first two are the spin-independent distribution function  $q(x)$  (or  $f(x)$ ) and helicity distribution function  $\Delta q(x)$  (or  $g(x)$ ). As discussed earlier, these quantities have been measured with high accuracy by a number of experiments in past decades. The third parton distribution function ( $\delta q(x)$  or  $h(x)$ ), called *transversity*, is still poorly known experimentally.

In the helicity basis ( $|+\rangle$ ,  $|-\rangle$ ), there are 16 different amplitudes  $\mathcal{A}_{\Lambda\lambda, \Lambda'\lambda'}$ , where  $\lambda\lambda'$  ( $\Lambda\Lambda'$ ) represent quark (nucleon) helicity states. Imposing helicity conservation,  $\Lambda + \lambda = \Lambda' + \lambda'$ , only six amplitudes are not zero.

$$A_{++,++}, \quad A_{--,--}, \quad A_{+,-,+-}, \quad A_{-+,-+}, \quad A_{+-,-+}, \quad A_{-+,-+} \quad (2.46)$$

Parity invariance means:

$$A_{\Lambda\lambda, \Lambda'\lambda'} = A_{-\Lambda-\lambda, -\Lambda'-\lambda'} \quad (2.47)$$

hence,

$$A_{++,++} = A_{--,--}, \quad A_{+,-,+-} = A_{-+,-+}, \quad A_{+-,-+} = A_{-+,-+} \quad (2.48)$$

The time-reversal invariance can also be applied:

$$A_{\Lambda\lambda,\Lambda'\lambda'} = A_{\Lambda'\lambda',\Lambda\lambda} \quad (2.49)$$

However, this does not add further constraints. Finally, three independent amplitudes  $A_{++,+}$ ,  $A_{+-,+}$ ,  $A_{+,-,+}$  remain.

$A_{++,+}$ ,  $A_{+-,+}$  are diagonal in the helicity basis (the quark does not flip its helicity:  $\lambda = \lambda'$ ), however,  $A_{+,-,+}$  is off-diagonal (helicity flip:  $\lambda = -\lambda'$ ). Actually, these three quark-nucleon forward amplitudes are related to the three leading-twist quark distribution functions, as follows:

$$f_1(x) = f_+(x) + f_-(x) \sim \text{Im}(A_{++,+} + A_{+-,+}), \quad (2.50)$$

$$g_1(x) = f_+(x) - f_-(x) \sim \text{Im}(A_{++,+} - A_{+-,+}), \quad (2.51)$$

$$h_1(x) = f_\uparrow(x) - f_\downarrow(x) \sim \text{Im}(A_{+,-,+}). \quad (2.52)$$

As we discussed earlier, the first two are related to the two quark helicity conserving amplitudes and can therefore be diagonalized in the helicity basis. As a result, they can have a precise probabilistic interpretation in this helicity basis.

However,  $h(x)$ , being a quark helicity-odd amplitude, cannot be diagonalized in this helicity basis and therefore has no probabilistic interpretation in this helicity basis. In particular, since helicity and chirality coincide in the infinite momentum frame, where all masses can be neglected, transversity is a chiral-odd function. Since electromagnetic interaction conserves chirality, transversity can not be measured in inclusive DIS processes. Helicity is a conserved quantity for nearly massless particles, and for quark with mass  $m$ , it is suppressed by a factor of  $\frac{m^2}{Q^2}$ , as displayed in Fig 2.6.

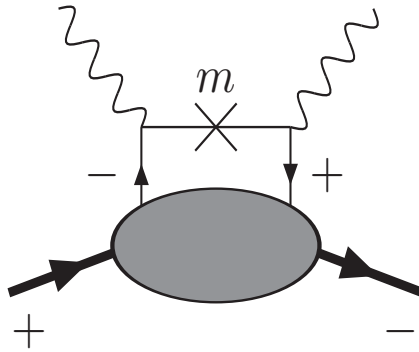


Figure 2.6: Diagram of the forbidden helicity flip amplitude. The helicities of the quarks and nucleons are labeled.

Alternatively, we can consider the transverse basis (with  $\uparrow$  directed along  $y$ )

$$|\uparrow\rangle = \frac{1}{\sqrt{2}}(|+\rangle + i|-\rangle), \quad (2.53)$$

$$|\downarrow\rangle = \frac{1}{\sqrt{2}}(|+\rangle - i|-\rangle). \quad (2.54)$$

In this basis, the distribution  $h(x)$  is related to a diagonal amplitude:

$$h_1(x) = f_\uparrow(x) - f_\downarrow(x) \sim \text{Im}(A_{\uparrow\uparrow,\uparrow\uparrow} - A_{\uparrow\downarrow,\uparrow\downarrow}). \quad (2.55)$$

Therefore,  $h_1(x)$  can clearly be interpreted as the difference between the probability to find a quark with spin polarized along the spin of a transversely polarized nucleon and the probability to find it polarized oppositely.

In addition, there are no such thing as leading-twist transverse polarization of gluons. The gluons have helicity  $\pm 1$  which lead to  $\Delta\Lambda = \pm 2$ , for vector boson exchange, helicity can not be changed by  $\pm 2$  unit.

From the equations  $q(x) = q^+(x) + q^-(x) = q^\uparrow(x) + q^\downarrow(x)$ , which leads to two inequalities:

$$|g(x)| \leq q(x), \quad |h(x)| \leq f(x). \quad (2.56)$$

There is a third inequality called the Soffer inequality [44]:

$$f(x) + g(x) \geq 2|h(x)|. \quad (2.57)$$

Due to chiral-odd property of transversity, it is difficult to measure transversity in DIS process, another chiral-odd term need to be present in a specific process to conserve chirality so that transversity can be measured.

One possibility is the polarized Drell-Yan process in proton-proton scattering. Here the transversity distribution of the quark from one of the two colliding protons can be measured in combination with that of the quark-antiquark from the other proton. Polarized Drell-Yan in proton-proton scattering is part of the RHIC Spin Program.

The other possibility is the semi-inclusive deep inelastic scattering (SIDIS) in which one of the final state hadrons is detected in coincidence with the scattered lepton. The presence of a chiral-odd fragmentation function in SIDIS will allow the extraction of the chiral-odd transversity distribution. The transversity experiment performed in JLab HallA is based on this SIDIS approach. In order to explain this clearly, I

would like to discuss it in the next Chapter.

# Chapter 3

## Transversity, Sivers Function, and Collins Function

### 3.1 The Semi-Inclusive Deep Inelastic Scattering

The Semi-Inclusive DIS (SIDIS) scattering, which can access the transversity, is to detect one or more produced hadrons in coincidence with the scattered lepton. Here, we only describe the situation where one produced meson (pion or kaon) is detected. The SIDIS is expressed by:

$$l(p) + N(P) \rightarrow l(p') + h(P_h) + X(P_X) \quad (3.1)$$

where  $l$ ,  $N$ ,  $h$ ,  $X$  denote the lepton, the nucleon target, the produced hadron and the undetected hadronic final state, respectively, and the quantities in parentheses denote their four momenta.

The Semi-Inclusive Deep Inelastic Scattering on a polarized target is shown schematically in Fig. 3.1.

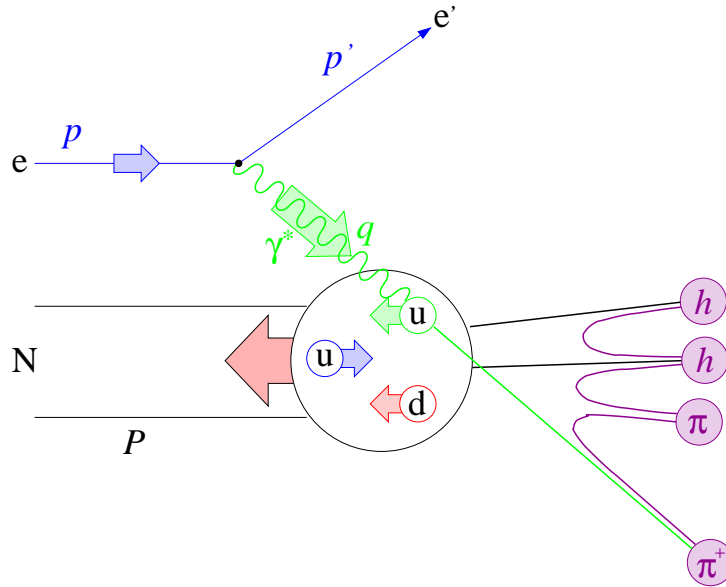


Figure 3.1: Semi-Inclusive Deep Inelastic Scattering on polarized nucleon

The scaling variable  $z$ , which refers to the fraction of the virtual photon energy carried by the produced

hadrons, is defined as:

$$z \equiv \frac{P \cdot P_h}{P \cdot q} \stackrel{lab}{=} \frac{E_h}{\nu}; \quad 0 \leq z \leq 1. \quad (3.2)$$

The process in which the final hadrons emerge from the deep inelastic scattering is called fragmentation (or hadronization) and cannot be treated using perturbative QCD since the strong coupling constant  $\alpha_s$  becomes too large at low energy, which is where fragmentation occurs.

In order to describe the semi-inclusive DIS, the *factorization theorem* is introduced, which states that the scattering of the photon off one of the nucleon can be divided into three parts: the hard scattering of the photon off one of the nucleon's constituents, the selection of these constituents according to their distribution within the nucleon, and the hadronization of the struck parton into the final state hadron. The cross section for a lepto-production of a hadron  $h$  can thus be factorised as:

$$\frac{d^3\sigma^h}{dx dQ^2 dz} = \sum_{a,b=q,\bar{q},g} d_a(x, Q^2) \otimes \sigma_{ab}(x, Q^2) \otimes F_b^h(z, Q^2), \quad (3.3)$$

where  $d_a(x, Q^2)$  is a parton distribution function, describing the distribution of the initial state parton  $a^1$  in the nucleon,  $\sigma_{ab}$  is the hard-scattering cross section (calculable from perturbation theory) for the process  $la \rightarrow l'b$  and  $F_b^h(z, Q^2)$  is a *fragmentation function*(FF), i.e. a function that describes the transition (fragmentation) from the final state parton  $b$  into a hadron  $h$  carrying a fractional energy  $z$ .

If only the three lightest quarks flavors ( $u, d, s$ ) are considered, the FFs can be divided into three categories: favorite ( $fav$ ), unfavorite ( $unfav$ ) and strange ( $s$ ), depending on the flavor of the fragmenting quark and on the quark content of the produced hadron such as charged pions as the following:

$$F_{fav}(z, Q^2) = F_u^{\pi^+}(z, Q^2) = F_u^{\pi^-}(z, Q^2) = F_d^{\pi^+}(z, Q^2) = F_d^{\pi^-}(z, Q^2), \quad (3.4)$$

$$F_{unfav}(z, Q^2) = F_u^{\pi^-}(z, Q^2) = F_u^{\pi^+}(z, Q^2) = F_d^{\pi^-}(z, Q^2) = F_d^{\pi^+}(z, Q^2), \quad (3.5)$$

$$F_s(z, Q^2) = F_s^{\pi^+}(z, Q^2) = F_s^{\pi^-}(z, Q^2) = F_s^{\pi^+}(z, Q^2) = F_s^{\pi^-}(z, Q^2). \quad (3.6)$$

There are similar expressions for charged kaons:

$$F_{fav}(z, Q^2) = F_u^{K^+}(z, Q^2) = F_s^{K^+}(z, Q^2) = F_u^{K^-}(z, Q^2) = F_s^{K^-}(z, Q^2), \quad (3.7)$$

$$F_{unfav}(z, Q^2) = F_s^{K^+}(z, Q^2) = F_u^{K^+}(z, Q^2) = F_s^{K^-}(z, Q^2) = F_u^{K^-}(z, Q^2), \quad (3.8)$$

$$F_{unfav}(z, Q^2) = F_d^{K^+}(z, Q^2) = F_d^{K^+}(z, Q^2) = F_d^{K^-}(z, Q^2) = F_d^{K^-}(z, Q^2) = F_s^{K^+}(z, Q^2). \quad (3.9)$$

---

<sup>1</sup>a and b are the same for electromagnetic interaction, a and b are different only for weak interaction.



The fragmentation functions are not calculable from first principles and have been historically derived from fits of data from  $e^+e^-$  experiments [45].

### 3.2 The Differential cross-section of SIDIS

The cross section of the one-hadron semi-inclusive electron-nucleon scattering is six fold differential:

$$d^6\sigma \equiv \frac{d^6\sigma}{dx dy dz d\phi_h d\phi_S dP_{h\perp}^2} = \frac{\alpha^2 y}{8zQ^4} 2MW^{\mu\nu} L_{\mu\nu}. \quad (3.10)$$

Where  $\phi_S$ ,  $\phi_h$  are the azimuthal angles which are defined according to the Trento convention [46] as shown in Fig. 3.2. The incident and scattered electrons define the lepton scattering plane, while the virtual photon and the detected hadron define the hadron production plane. The hadron azimuthal angle,  $\phi_h$ , is the angle between the lepton plane and the hadron plane, while  $\phi_S$  is the azimuthal angle of the target spin direction in the lepton plane.

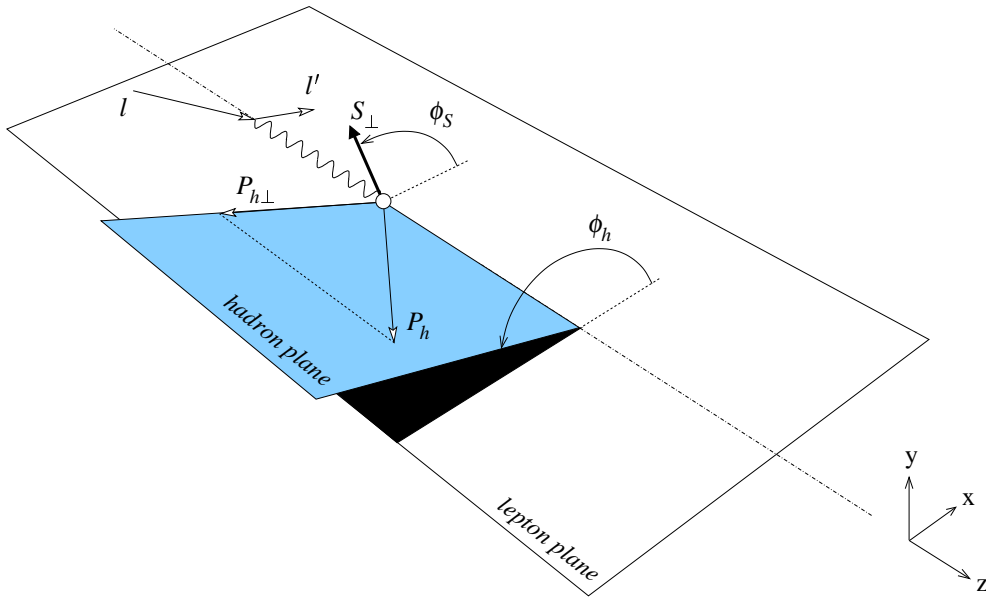


Figure 3.2: The definition of  $\phi_h$  and  $\phi_S$  according to Trento convention

Assuming single photon exchange, the electron-hadron cross section can be expressed in a model independent way through a set of structure functions, which in general depend on  $x$ ,  $Q^2$ ,  $z$  and  $P_{h\perp}^2$ , according to [122]:

$$\begin{aligned}
\frac{d^6\sigma}{dx dy dz d\phi_h d\phi_S dP_{h\perp}^2} &= \frac{\alpha^2}{xyQ^2} \frac{y^2}{2(1-\epsilon)} \left(1 + \frac{\gamma^2}{2x}\right) \left\{ F_{UU,T} + \epsilon F_{UU,L} \right. \\
&+ \sqrt{2\epsilon(1+\epsilon)} \cos\phi_h F_{UU}^{\cos\phi_h} + \epsilon \cos(2\phi_h) F_{UU}^{\cos(2\phi_h)} + \lambda_e \sqrt{2\epsilon(1-\epsilon)} \sin\phi_h F_{UU}^{\sin\phi_h} \\
&+ S_L \left[ \sqrt{2\epsilon(1+\epsilon)} \sin\phi_h F_{UL}^{\sin\phi_h} + \epsilon \sin(2\phi_h) F_{UL}^{\sin(2\phi_h)} \right] \\
&+ S_L \lambda_e \left[ \sqrt{1-\epsilon^2} F_{LL} + \sqrt{2\epsilon(1-\epsilon)} \cos\phi_h F_{LL}^{\cos\phi_h} \right] \\
&+ |S_T| \left[ \sin(\phi_h - \phi_S) (F_{UT,T}^{\sin(\phi_h - \phi_S)} + \epsilon F_{UT,L}^{\sin(\phi_h - \phi_S)}) \right] \\
&+ \epsilon \sin(\phi_h + \phi_S) F_{UT}^{\sin(\phi_h + \phi_S)} + \epsilon \sin(3\phi_h - \phi_S) F_{UT}^{\sin(3\phi_h - \phi_S)} \\
&+ \sqrt{2\epsilon(1+\epsilon)} \sin\phi_S F_{UT}^{\sin\phi_S} + \sqrt{2\epsilon(1+\epsilon)} \sin(2\phi_h - \phi_S) F_{UT}^{\sin(2\phi_h - \phi_S)} \\
&+ |S_T| \lambda_e \left[ \sqrt{1-\epsilon^2} \cos(\phi_h - \phi_S) F_{LT}^{\cos(\phi_h - \phi_S)} + \sqrt{2\epsilon(1-\epsilon)} \cos\phi_S F_{LT}^{\cos\phi_S} \right. \\
&\left. + \sqrt{2\epsilon(1-\epsilon)} \cos(2\phi_h - \phi_S) F_{LT}^{\cos(2\phi_h - \phi_S)} \right] \left. \right\}. \tag{3.11}
\end{aligned}$$

Where the first and second subscript  $U, L, T$  denoted the polarized direction which means Unpolarized ( $U$ ), Longitudinally polarized ( $L$ ), and Transversely polarized ( $T$ ), with respect to the photon direction, of beam and target, and the third subscript in  $F_{UU,T}, F_{UU,L}, F_{UU,T}^{\sin(\phi_h - \phi_S)}$  and  $F_{UU,L}^{\sin(\phi_h - \phi_S)}$  represents the polarization of the virtual photon. In addition,  $\lambda_e$  denotes the helicity state of the electron beam and

$$\epsilon = \frac{1 - y - \frac{\gamma^2 y^2}{4}}{1 - y + \frac{y^2}{2} + \frac{\gamma^2 y^2}{4}} \tag{3.12}$$

is the ratio of the longitudinal and the transverse photon fluxes.

In experiment with unpolarized beam and transversely polarized target, five terms are involved (terms with subscript  $UT$ ). In the leading twist, only three terms survive. They can be described as following:

$$F_{UT}^{\sin(\phi_h + \phi_S)} = \mathcal{C} \left[ -\frac{\hat{P}_{h\perp} \cdot \vec{k}_T}{M_h} h_1^q H_1^\perp \right], \tag{3.13}$$

$$F_{UT,T}^{\sin(\phi_h - \phi_S)} = \mathcal{C} \left[ -\frac{\hat{P}_{h\perp} \cdot \vec{p}_T}{M} f_{1T}^\perp D_1^q \right], \tag{3.14}$$

$$F_{UT}^{\sin(3\phi_h - \phi_S)} = \mathcal{C} \left[ \frac{2(\hat{P}_{h\perp} \cdot \vec{p}_T)(\vec{p}_T \cdot \vec{k}_T) + p_T^2(\hat{P}_{h\perp} \cdot \vec{k}_T) - 4(\hat{P}_{h\perp} \cdot \vec{p}_T)^2(\hat{P}_{h\perp} \cdot \vec{k}_T)}{2M^2 M_h} h_{1T}^\perp H_1^\perp \right] \tag{3.15}$$

Which contain Collins moment and Sivers moment and pretzelocity terms.

In the previous formula, we introduced the unit vector  $\hat{P}_{h\perp} = P_{h\perp}/|P_{h\perp}|$ , and the notation

$$\mathcal{C}[\mathcal{W}dF] = x \sum_{q,\bar{q}} e_q^2 \mathcal{I}[\mathcal{W}dF], \tag{3.16}$$

where

$$\mathcal{I}[\mathcal{W}dF] = \int d^2\vec{p}_T d^2\vec{k}_T \delta^2(\vec{p}_T - \vec{k}_T - \frac{\vec{P}_{h\perp}}{z}) \mathcal{W}(\vec{p}_T, \vec{k}_T) d_q(x, p_T^2) F_q(z, z^2 k_T^2) \quad (3.17)$$

is a convolution integral over the quark transverse momenta  $\vec{p}_T$  and  $\vec{k}_T$ , defined for any combination of a parton distribution function  $d(x, p_T^2)$  and a fragmentation function  $F(z, z^2 k_T^2)$  multiplied by a weight  $\mathcal{W}$ .

In experiment E06-010, based on unpolarized beam<sup>2</sup> and transversely polarized target with a net polarization of  $|S^T|$ , the differential cross section can be expressed as the sum of target spin-independent and target spin-dependent terms in the leading twist situation:

$$\frac{d\sigma^h}{dx dy dz_h d\phi_h} \equiv d\sigma^h = d\sigma_{UU} + d\sigma_{UT} = d\sigma_{UU} + d\sigma_{UT}^{Collins} + d\sigma_{UT}^{Sivers} + d\sigma_{UT}^{pretzelocity} \quad (3.18)$$

where each term can also be expressed as a convolution of a parton distribution function and a fragmentation function [48] as mentioned previously:

$$d\sigma_{UU} = \frac{4\pi\alpha^2 s}{Q^4} (1 - y - \frac{y^2}{2}) \Sigma_q e_q^2 [f_1^q \otimes D_1^q], \quad (3.19)$$

$$d\sigma_{UT}^{Collins} = \frac{4\pi\alpha^2 s}{Q^4} |S^T| (1 - y) \sin(\phi_h + \phi_S) \Sigma_q e_q^2 [h_1^q \otimes H_1^{\perp q}] \quad (3.20)$$

$$d\sigma_{UT}^{Sivers} = \frac{4\pi\alpha^2 s}{Q^4} |S^T| (1 - y + \frac{y^2}{2}) \sin(\phi_h - \phi_S) \Sigma_q e_q^2 [f_{1T}^{\perp q} \otimes D_1^q] \quad (3.21)$$

$$d\sigma_{UT}^{Pretzelocity} = \frac{4\pi\alpha^2 s}{Q^4} |S^T| \frac{1 - y}{2} \frac{P_{h\perp}^2}{6z^2 M_N^2} \sin(3\phi_h - \phi_S) \Sigma_q e_q^2 [h_{1T}^{\perp q} \otimes H_1^{\perp q}] \quad (3.22)$$

where  $h_1^q(x)$  is the *transversity distribution function*,  $H_1^{\perp(1)q}(z)$  is the *Collins fragmentation function*,  $f_1^{\perp(1)q}(x)$  is the *Sivers distribution function*,  $f_1^q(x)$  is the *unpolarization distribution function*, and  $D_1^q(z)$  is the *unpolarized fragmentation function*.

From the above equation, the transversity distribution function and the Sivers distribution function can be extracted by isolating the  $\sin(\phi_h + \phi_S)$  and the  $\sin(\phi_h - \phi_S)$  terms in the SIDIS cross section (often called the Collins moment and the Sivers moment, respectively).

---

<sup>2</sup>Actually, in JLab HALLA, the beam is longitudinally polarized. However, the helicity flip is very fast, and for transversity experiment we need not use this beam helicity information. So we will assume the unpolarized beam and the fast flip electron helicity actually decrease the systematic uncertainties for the final result. The beam helicity information can be used to extract double-spin asymmetry, a subject of another study.

### 3.3 The Collins and Sivers azimuthal moments

The differential cross section related to the Collins moment and Sivers moment can be deduced from Eq. 3.16 and can be written as:

$$d^{Collins} \sigma_{UT} = -\frac{2\alpha^2}{sxy^2} |\vec{S}_T| B(y) \sin(\phi_h + \phi_S) \sum_{q\bar{q}} e_q^2 \mathcal{I} \left[ \frac{\vec{k}_T \cdot \hat{P}_{h\perp}}{M_h} h_1^q(x, p_T^2) H_1^{\perp q}(z, z^2 k_T^2) \right], \quad (3.23)$$

where  $B(y) = \left(1 - y - \frac{y^2 \gamma^2}{4}\right) \frac{1}{1 + \gamma^2}$ , and the convolution integral of the product of the transversity distribution and the Collins fragmentation function is modulated by  $\sin(\phi_h + \phi_S)$ , and

$$d^{Sivers} \sigma_{UT} = -\frac{2\alpha^2}{sxy^2} |\vec{S}_T| A(y) \sin(\phi_h - \phi_S) \sum_{q\bar{q}} e_q^2 \mathcal{I} \left[ \frac{\vec{p}_T \cdot \hat{P}_{h\perp}}{M} f_{1T}^{\perp q}(x, p_T^2) D_1^q(z, z^2 k_T^2) \right], \quad (3.24)$$

where  $A(y) = \left(1 - y + \frac{y^2}{2} - \frac{y^2 \gamma^2}{4}\right) \frac{1}{1 + \gamma^2}$ , the convolution integral of the product of the Sivers distribution function and spin-independent fragmentation function is modulated by  $\sin(\phi_h - \phi_S)$ .

In order to separate the individual terms of the spin-dependent part of the cross section, cross section difference of opposite spin states is formed. In term of the experiment with unpolarized electron beam and transversely polarized target, the cross section difference is the following:

$$d^6 \sigma_{UT} \equiv \frac{1}{2} (d^6 \sigma_{U\uparrow} - d^6 \sigma_{U\downarrow}), \quad (3.25)$$

where  $\uparrow$  ( $\downarrow$ ) represent the polarization direction parallel (anti-parallel) to the direction specified by the angle  $\phi_S$ .

In particular, the Collins moment and the Sivers moment are modulated by  $\sin(\phi_h + \phi_S)$  and  $\sin(\phi_h - \phi_S)$  respectively. This can cause a *Single Spin Asymmetry* (SSA) which is defined as the difference in the count rate of produced hadrons in opposite target spin states divided by the sum. For example, for an unpolarized beam and a transversely polarized target,

$$A_{UT} = \frac{1}{\langle P \rangle} \frac{d^6 \sigma_{U\uparrow} - d^6 \sigma_{U\downarrow}}{d^6 \sigma_{U\uparrow} + d^6 \sigma_{U\downarrow}}, \quad (3.26)$$

where  $\langle P \rangle$  is the average target polarization and the arrows indicate opposite target polarization directions. This asymmetry is usually expressed as azimuthal moments, for example, for the Collins moment it reads,

$$\langle \sin(\phi_h + \phi_S) \rangle_{UT}^h = -|\vec{S}_T| \frac{\frac{1}{xy^2} B(y) \sum_{q\bar{q}} e_q^2 \int d^2 \vec{P}_{h\perp} \mathcal{I} \left[ \frac{\vec{k}_T \cdot \hat{P}_{h\perp}}{M_h} \delta q(x, p_T^2) H_1^{\perp q}(z, z^2 k_T^2) \right]}{2 \frac{1}{xy^2} A(y) \sum_{q\bar{q}} e_q^2 q(x) D_1^q(z)}, \quad (3.27)$$

and for the Siver moment it is,

$$\langle \sin(\phi_h - \phi_S) \rangle_{UT}^h = -|\vec{S}_T| \frac{\frac{1}{xy^2} A(y) \sum_{q\bar{q}} e_q^2 \int d^2 \vec{P}_{h\perp} \mathcal{I} \left[ \frac{\vec{p}_T \cdot \vec{P}_{h\perp}}{M_h} f_{1T}^{\perp q}(x, p_T^2) D_1^q(z, z^2 k_T^2) \right]}{2 \frac{1}{xy^2} A(y) \sum_{q\bar{q}} e_q^2 q(x) D_1^q(z)}. \quad (3.28)$$

Both these moments can be non-zero and these are also called as the *Collins effect* and the *Sivers effect*, respectively. Note that the kinematical term  $\frac{1}{xy^2} A(y)$  does not cancel because both the numerator and denominator are integrated separately over certain  $x$  and  $y$  ranges.

### 3.4 The transversity distribution function and the Sivers distribution function

The Collins moment, Eq. 3.27, contains the convolution of the chiral-odd transversity distribution function  $\delta q(x, p_T^2)$  and the chiral-odd Collins fragmentation function  $H_1^{\perp q}(z, z^2 k_T^2)$ . In the Sivers moment, Eq. 3.28, the convolution of the Sivers distribution function and the spin independent fragmentation function is involved. In order to evaluate these convolutions, assumptions should be made on the transverse momentum dependences of the distribution and fragmentation functions.

A usual assumption is the so-called *Gaussian ansatz* [122], according to which the transverse momentum  $\vec{p}_T$  and  $\vec{K}_T \equiv -z\vec{k}_T$ , which is the relation between the transverse momentum of the hadron with respect to the quark spin direction and the transverse momentum of the quark itself, follow a Gaussian distribution:

$$\delta q(x, p_T^2) \approx \frac{\delta q(x)}{\pi \langle p_T^2(x) \rangle} e^{-\frac{p_T^2}{\langle p_T^2(x) \rangle}} \quad (3.29)$$

$$H_{1T}^{\perp}(z, K_T^2) \approx \frac{H_{1T}^{\perp}(z)}{\pi \langle K_T^2(z) \rangle} e^{-\frac{K_T^2}{\langle K_T^2(z) \rangle}}, \quad (3.30)$$

where  $\langle p_T^2(x) \rangle = \frac{\int d^2 \vec{p}_T p_T^2 q(x, p_T^2)}{q(x)}$  and  $\langle K_T^2(z) \rangle = \frac{\int d^2 \vec{K}_T K_T^2 D_1(z, K_T^2)}{D_1(z)}$ .

Under this assumption, the distribution functions and fragmentation functions factorise and the integral can be calculated analytically as following:

$$\langle \sin(\phi_h + \phi_S) \rangle_{UT}^h = \frac{|\vec{S}_T|}{\sqrt{1+z^2 \langle p_T^2 \rangle / \langle K_T^2 \rangle}} \frac{\frac{1}{xy^2} B(y) \sum_{q\bar{q}} e_q^2 h_1^q(x) H_1^{\perp(1)q}(z)}{\frac{1}{xy^2} A(y) \sum_{q\bar{q}} e_q^2 q(x) D_1^q(z)}, \quad (3.31)$$

$$\langle \sin(\phi_h - \phi_S) \rangle_{UT}^h = -\frac{|\vec{S}_T|}{\sqrt{1+z^2 \langle p_T^2 \rangle / \langle K_T^2 \rangle}} \frac{\frac{1}{xy^2} A(y) \sum_{q\bar{q}} e_q^2 f_{1T}^{\perp(1)q}(x) D_1^q(z)}{\frac{1}{xy^2} A(y) \sum_{q\bar{q}} e_q^2 q(x) D_1^q(z)}. \quad (3.32)$$

From Collins moment with global fit of the Collins fragmentation function  $H_1^{\perp(1)q}(z)$ , the transversity

distribution function  $h_1^q(x)$  can be analytically solved, similarly, from Siverts moment with unpolarized fragmentation function  $D_1^q(z)$ , the Siverts distribution can be analytically solved.

### 3.5 Other Related Function

In addition to the four distribution functions (unpolarization distribution function  $f_1(x)$ , helicity distribution function  $g_1(x)$ , transversity distribution function  $h_1(x)$ , and siverts distribution function  $f_{1T}^\perp(x, p_T^2)$ ) we have discussed so far,

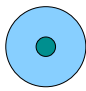
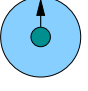
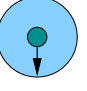
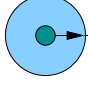
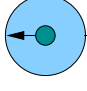
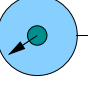
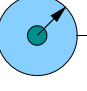
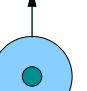
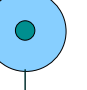
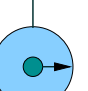
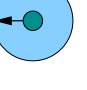
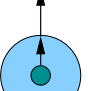
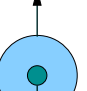
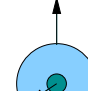
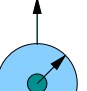
|         |          | quark  |   |  |
|---------|----------|--|---|--|
|         |          | <b>U</b>   | <b>L</b>  | <b>T</b>   |
| nucleon | <b>U</b> | q   |   | $h_1^\perp$  -   |
|         | <b>L</b> |  | $\Delta q$  -        | $h_{1L}^\perp$  -    |
|         | <b>T</b> | $f_{1T}^\perp$  -  | $g_{1T}^\perp$  -  | $\delta q$  - <br>$h_{1T}^\perp$  -  |

Figure 3.3: Leading-twist transverse momentum dependent quark distribution functions. This figure is extracted from [49].

there are four other distribution functions  $h_1^\perp(x, p_T^2)$ ,  $g_{1T}^\perp(x, p_T^2)$ ,  $h_{1L}^\perp(x, p_T^2)$ , and  $h_{1T}^\perp(x, p_T^2)$ , which all vanish after integrating over the quark intrinsic transverse momentum  $\vec{p}_T$ . All these eight distribution functions are leading-twist transverse momentum dependent quark distribution function shown in Fig. 3.3.

### 3.6 The HERMES and COMPASS results and theoretical prediction on Collins and Sivers moments

The first results for transversely target single-spin asymmetry (SSA) were reported by the HERMES Collaboration [50] [51]. With a transversely polarized proton target from semi-inclusive electroproduction of pions in DIS kinematics using a 27.5 GeV incident positron beam at the DESY storage ring, the SSA results were extracted. At that time, only pion results as shown in Fig. 3.4 were provided.

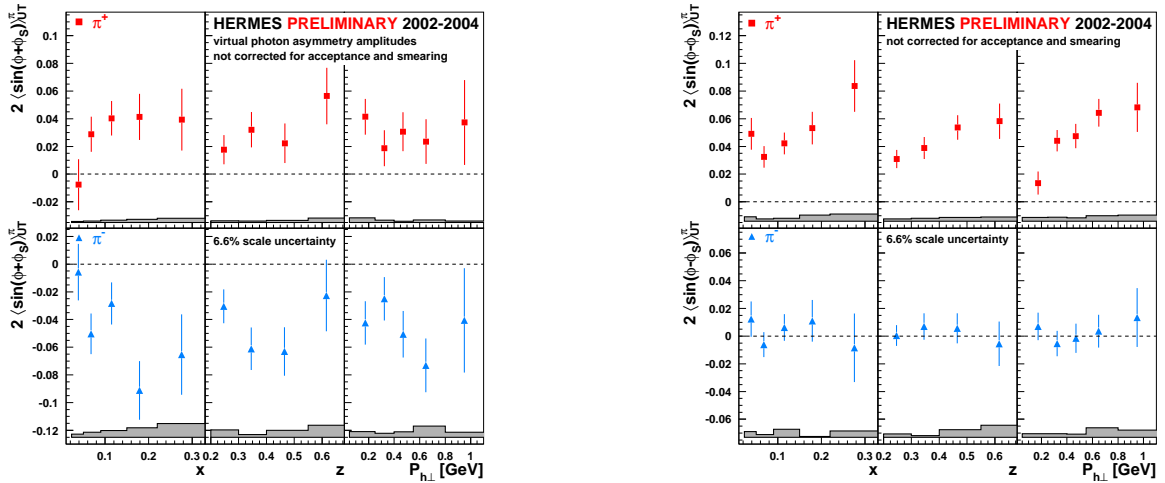


Figure 3.4: Collins moments (upper panel) and Sivers moments (down panel) for charged pions (as labelled) as a function of  $x$ ,  $z$  and  $P_{h\perp}$ . The error bands represent the systematic uncertainty due to acceptance and detector smearing effects and due to a possible contribution from the  $\langle \cos\phi \rangle_{UU}$  moment in the spin-independent cross section. The figure is from [51].

In Fig. 3.4, the non-zero  $\pi^+$  Collins moment and rather larger negative  $\pi^-$  Collins moment are shown. The Sivers moment for  $\pi^+$  case is large and positive, but the  $\pi^-$  Sivers moment is consistent with zero.

The COMPASS collaboration also reported first measurements [52] of the Collins and Sivers asymmetries of charged hadrons from semi-inclusive scattering of 160 GeV/c muons from a transversely polarized  ${}^6\text{LiD}$  target in the deep-inelastic kinematic region in the same year, 2005. At that time, the COMPASS did not separate pions, kaons from hadrons. Both the Collins asymmetry and Sivers asymmetry are consistent with zero [52].

Later, in 2007, the HERMES Collaboration shows new results of Collins and Sivers asymmetries, this time, the explicit kaon results [53] were included as well as pions.

In Fig. 3.5, the Collins and Sivers moments as a function of  $x$ ,  $z$  and  $P_{h\perp}$  are shown. Semi-inclusive DIS events were selected subject to the kinematic requirements  $Q^2 > 1\text{GeV}^2$ ,  $y < 0.95$ ,  $W^2 > 10\text{GeV}^2$ ,  $2\text{GeV} <$

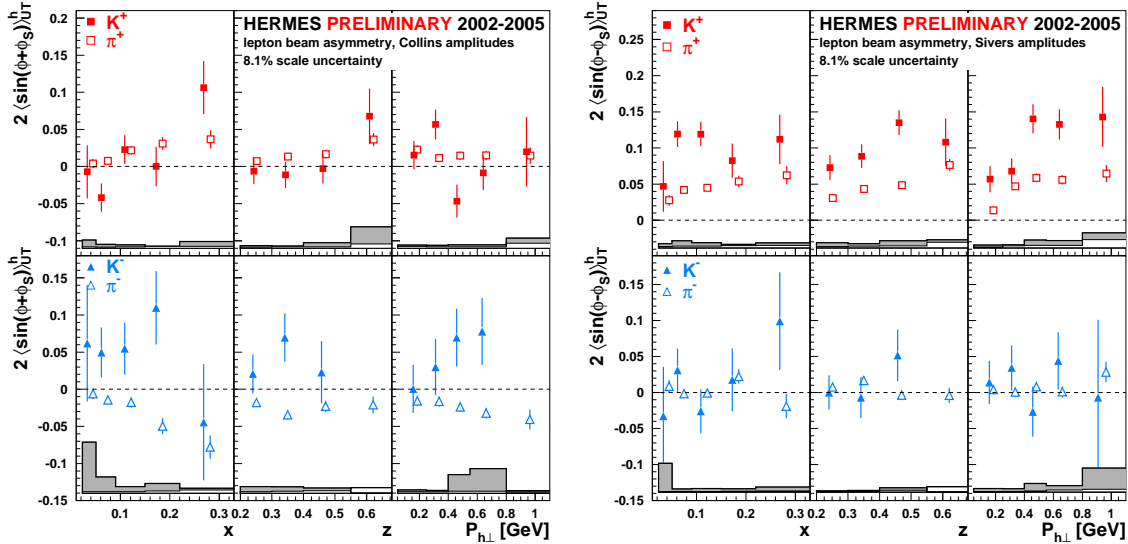


Figure 3.5: Collins moments (left column) and Sivers moments (right column) for charged kaons (closed symbols, as labelled) and charged pions (open symbols, as labelled) as function of  $x$ ,  $z$  and  $P_{h\perp}$ . The error bands represent the maximal systematic uncertainty; the common overall 8.1% scaling uncertainty is due to the target polarisation uncertainty. The figure is from [60].

$P_h < 15\text{GeV}$ ,  $0.2 < z < 0.7$  and  $\theta_{\gamma^*h} > 0.02\text{rad}$ , where  $\theta_{\gamma^*h}$  is the angle between the direction of the virtual photon and the hadron. The selected ranges in  $x$  and  $P_{h\perp}$  are  $0.023 < x < 0.4$  and  $0.05\text{GeV} < P_{h\perp} < 2\text{GeV}$ . These preliminary results are based on ten times more statistics than that in the publication [50] [51] and are consistent with the published result.

The Collins moment is positive for  $\pi^+$ , compatible with zero for  $\pi^0$ , and negative for  $\pi^-$ . Also, the magnitude of the  $\pi^-$  moment is comparable or larger than the one for  $\pi^+$ . This leads to the conclusion that the disfavoured Collins fragmentation function has a substantial magnitude with an opposite sign compared to the favoured Collins fragmentation function. For charged kaons no statistically significant non-zero Collins moments are found. However, the Collins moments for  $K^+$  are within statistical accuracy consistent with the  $\pi^+$  moments.

The significantly positive Sivers moments observed for  $\pi^+$ ,  $\pi^0$  and  $K^+$  imply a non-vanishing orbital angular momentum of the quarks inside the nucleon. As the magnitude of the  $K^+$  moment is larger than the one for  $\pi^+$ , the sea quark contribution to the Sivers mechanism appears to be important. Thus the orbital angular momentum of anti-quarks could be significant and highly flavour dependent. For  $\pi^-$  and  $K^-$  the Sivers moments are consistent with zero. Finally, the extracted Collins and Sivers moments for  $\pi^+$ ,  $\pi^0$ ,  $\pi^-$  are consistent with isospin symmetry.

In 2008, the COMPASS Collaboration reported new results of Collins and Sivers asymmetries in muon-deuteron DIS. This time, the hadrons are identified, Fig. 3.6 shows the new results, including kaons as well



as pions [54].

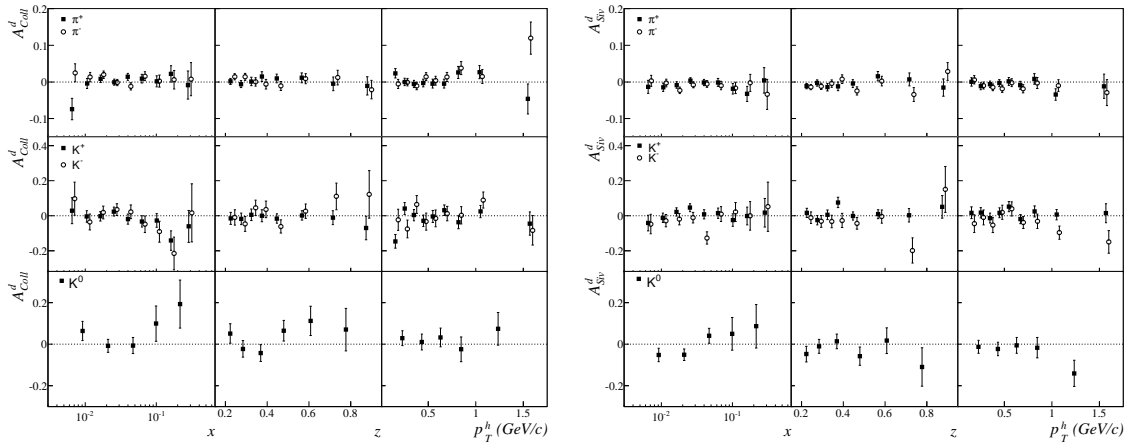


Figure 3.6: Collins asymmetry against  $x$ ,  $z$  and  $p_T^h$  for the “all” charged pions and kaons samples from the 2003–2004 COMPASS data, and the “all”  $K_S^0$ ’s sample from the 2002–2004 data (left column). Sivers asymmetry against  $x$ ,  $z$  and  $p_T^h$  for the “all” charged pions and kaons samples from the 2003–2004 data, and “all”  $K_S^0$ ’s sample from the 2002–2004 data (right column). The figure is from Ref. [60].

The final results for the Collins and Sivers asymmetries  $A_{Coll}$  and  $A_{Siv}$  for charged pions and charged and neutral kaons on the deuteron target vs. the three kinematic variables  $x$ ,  $z$  and  $p_T^h$  are given in Fig. 3.6. In the figures, the data points for negative hadrons, which are calculated in the same  $x$ -,  $z$ - and  $p_T$ -bin as for the positive hadrons, have been slightly shifted for graphical reasons.

All the measured asymmetries are small, a trend which was already observed in the published data of the non-identified hadrons. Small asymmetries are not a surprise, it was expected that transverse spin effects be small in the deuteron due to the opposite sign which was predicted for the u- and d-quark distributions, very much like in the helicity case.

The interpretation of the results on the deuteron can be done only in conjunction with corresponding proton data, measured by the HERMES Collaboration albeit at lower energy. Proton target data have been collected by COMPASS in 2007, Fig. 3.7, and Fig. 3.8 show the preliminary results of Collins moment and Sivers moment for positive and negative hadrons.

A simple analysis of the HERMES charged pion data and of the non-identified charged hadron data in COMPASS, assuming that all the hadrons are pions, led to the following conclusions [62] [63]:

1. the favoured and unfavoured Collins functions have about the same size and the COMPASS deuteron data are needed for the extraction of the d-quark transversity;
2. the null result for the Sivers asymmetry for the COMPASS data is a clear indication that the u- and d-quark Sivers distribution functions have about the same size and opposite sign.

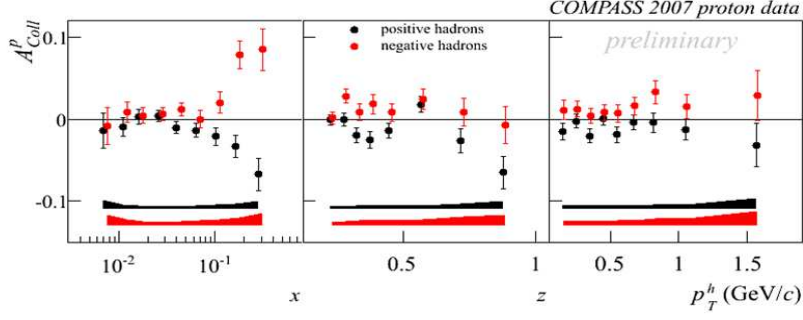


Figure 3.7: COMPASS proton data results of Collins moments for positive and negative hadrons. This figure is from [61]

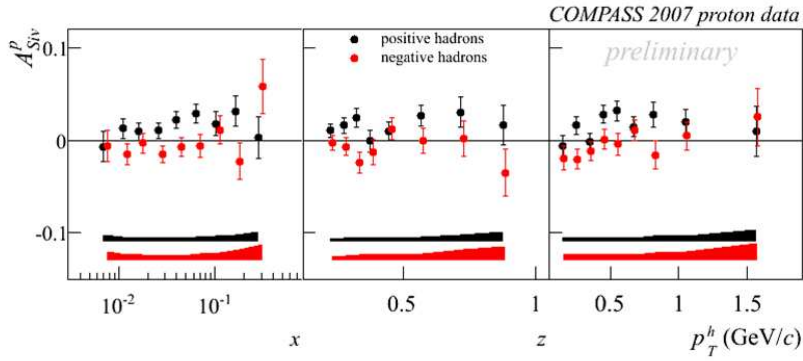


Figure 3.8: COMPASS proton data results of Sivers moments for positive and negative hadrons. This figure is from [61]

A first global analysis which combined the 2002–2004 HERMES pion Collins asymmetries, the COMPASS results for non-identified hadrons, and the BELLE data has recently allowed to extract the Collins functions and, for the first time, the transversity distributions for the u- and d-quark. Similar analyses can now be done including the present pion data which put more stringent constraints.

In summary, Sivers and transversity data from HERMES and COMPASS on proton and deuteron targets show:

- Large positive Sivers moment for  $K^+$  and small  $K^-$  Sivers moment observed for SIDIS on proton from HERMES, suggesting the valence nature of Sivers moment.
- $K^+$  Collins moment on proton is found to be positive and larger than  $\pi^+$ . In contrast,  $K^-$  Collins moment is found to be small. Since  $K^-$  does not have u or d as its valence quarks, this reflects the small transversity for sea quarks in the nucleon.

- $K^-$  and  $K^+$  Collins and Sivers moments on deuteron are all consistent with zero. The only exception is Collins moments at large  $x$  ( $x > 0.1$ ), where both  $K^+$  and  $K^-$  have positive values on the order of 0.1.
- Based on the HERMES and COMPASS data on proton and deuteron, one would naively expect the following for Collins and Sivers moments for  $K^+$  and  $K^-$  production on  $^3\text{He}$ :  
 $K^+$  Sivers: large and negative.  
 $K^-$  Sivers: small.  
 $K^+$  Collins: large and negative. At larger  $x$ , the magnitude is expected to be smaller.  
 $K^-$  Collins: small. At larger  $x$ , it might become slightly positive.
- Summary of prediction on the Collins and Sivers moments for kaons on  $^3\text{He}$  target, and compare with the above naive expectations (note that the global fits did not include some of the latest results from COMPASS and HERMES).
- It is therefore interesting to measure the  $K^+$  and  $K^-$  moments on transversely polarized  $^3\text{He}$  target.

Before the results of 2007 HERMES and 2008 COMPASS data were reported, lots of theoretical predictions were performed [55] [56] [136]. After these results released, M. Anselmino et al. performed a global fit to extract Sivers function based on SIDIS Data [131] and transversity and Collins functions from SIDIS and  $e^+e^-$  data [132]. The Sivers functions for  $u, \bar{u}, d, \bar{d}, s, \bar{s}$  are shown in Fig. 3.9. The transversity for  $u$  and  $d$  quarks are shown in Fig. 3.10.

Meanwhile, the predictions for the single spin asymmetry  $A_{UT}^{\sin(\phi_h - \phi_S)}$  for pion and kaon production which had been proposed at JLab E06-010, using a polarized  $^3\text{He}$  (neutron) target with a beam energy of 6 GeV, are shown in Fig. 3.11. The purpose of the JLab E06-010 experiment is to provide new data complementary to those obtained at HERMES and COMPASS. In the next chapter, we will discuss the experimental details of the JLab E06-010 experiment.

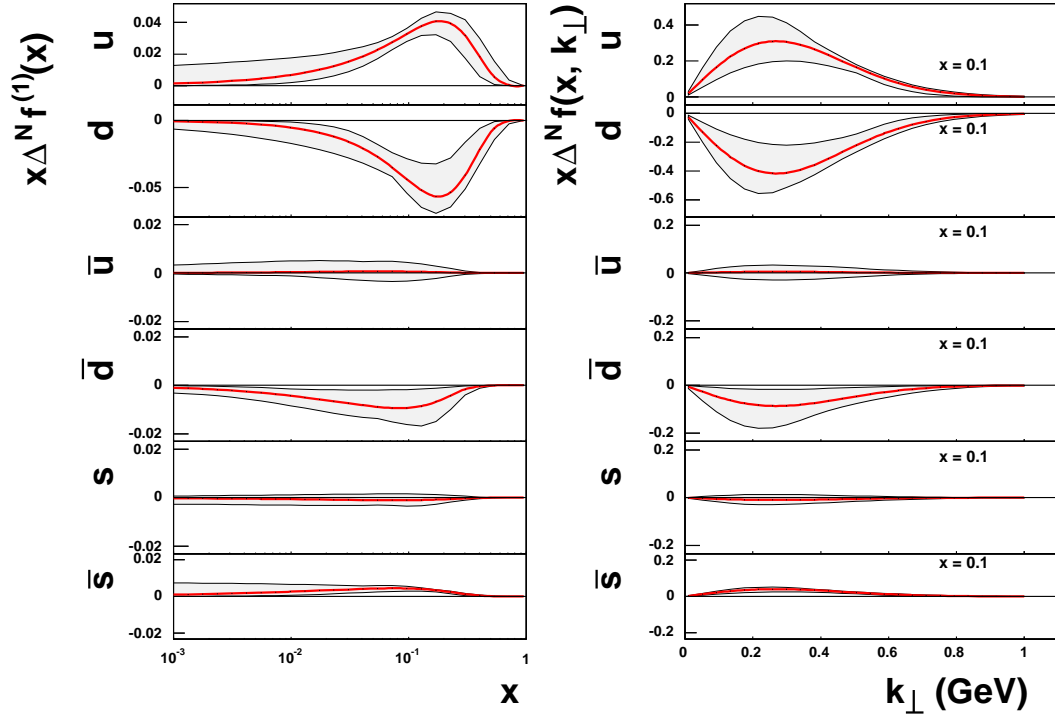


Figure 3.9: The Siverts distribution functions for  $u$ ,  $d$  and  $s$  flavours as determined by our simultaneous fit of HERMES and COMPASS data. On the left panel, the first moment  $x, \Delta^N f^{(1)}(x)$ ,  $f_{1T}^{\perp(1)q}(x)$  of Ref. [131] is shown as a function of  $x$  for each flavour, as indicated. Similarly, on the right panel, the Siverts distribution  $x \Delta^N f(x, k_t)$  is shown as a function of  $k_t$  at a fixed value of  $x$  for each flavour, as indicated.

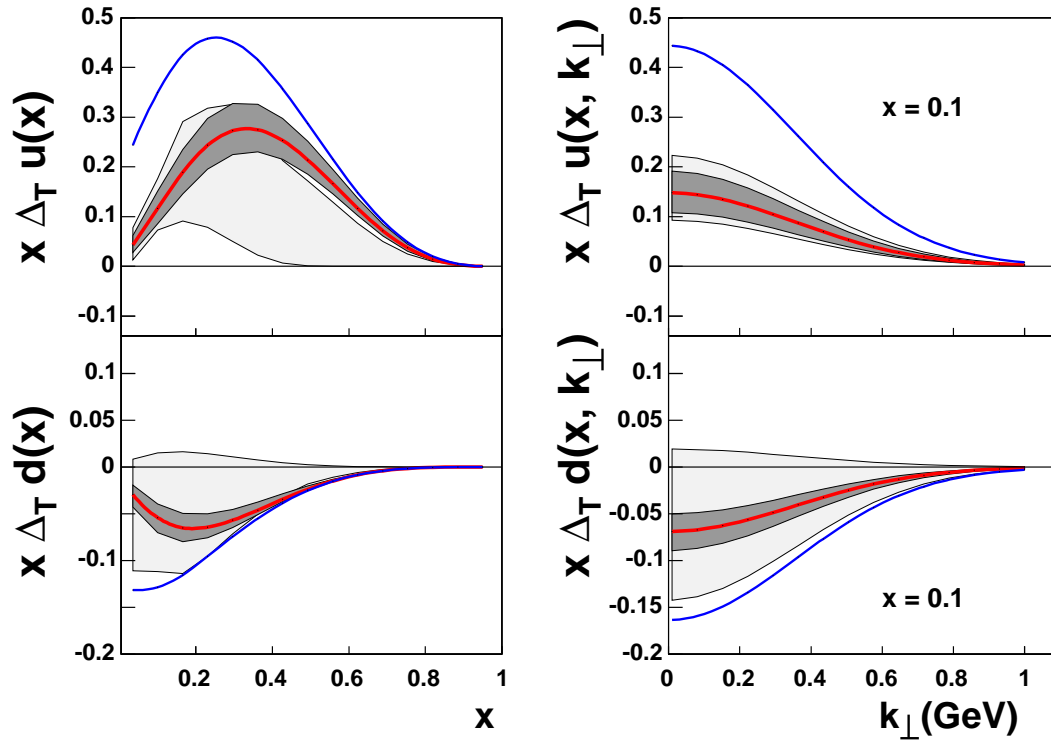


Figure 3.10: The transversity distribution functions for u and d flavours as determined by our global fit; we also show the Soffer bound (highest or lowest lines) and the (wider) bands of our previous extraction [132] are also shown in this figure. The figure is from [131].

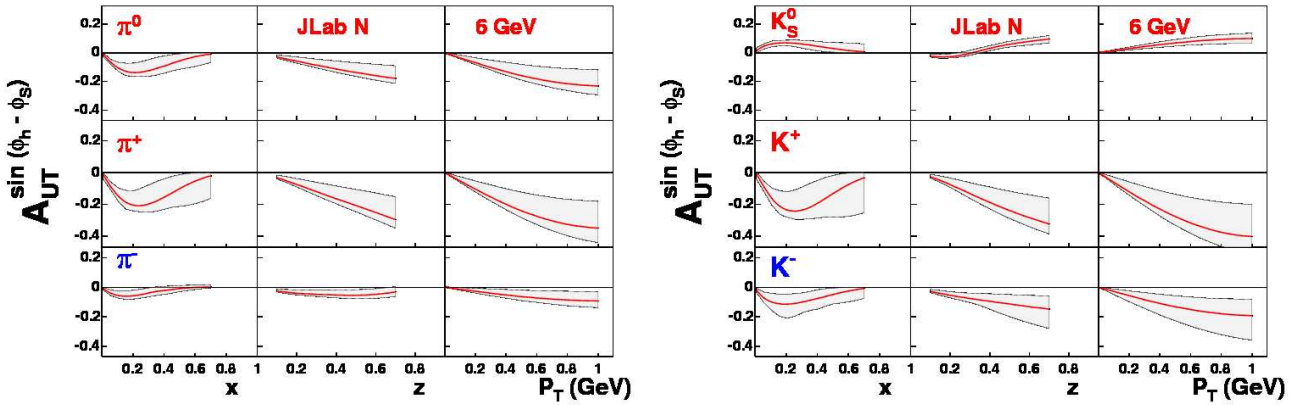


Figure 3.11: Predictions for the single spin asymmetry  $A_{UT}^{\sin(\phi_h - \phi_s)}$  for pion and kaon production, which will be measured at JLab operating on a polarized  $^3\text{He}$  (neutron) target, with a beam energy of 6 GeV. The figure is from Ref. [60]

# Chapter 4

## Experimental Setup

### 4.1 Overview

From nearly the end of October in 2008 until the beginning of February in 2009, the data of Experiment E06-010 were taken in Hall A of the Thomas Jefferson National Accelerator Facility (JLAB), which is located in Newport News, VA, USA. The target single-spin asymmetries(SSAs) of the neutron (extracted from  ${}^3\text{He}$ ) were measured in the valence quark region,  $x \sim 0.13 - 0.50$  at  $Q^2 \sim 1.0 - 3.2 \text{ GeV}^2$ , when a 5.89 GeV CW(Continuous Wave) electron beam was incident on a transversely polarized  ${}^3\text{He}$  target. The SIDIS kaon electroproduction  $e(n \uparrow, e' K^\pm)$  and pion electroproduction  $e(n \uparrow, e' \pi^\pm)$  reactions were measured.

The electrons were accelerated in the Jefferson Lab Accelerator, before scattering off the transversely polarized  ${}^3\text{He}$  target. The scattered electrons were detected on the right side at  $\sim 30$  degrees using the BigBite spectrometer. The distance between the front face of the magnet and the center of the target was 1.5m. The momentum coverage of the BigBite was from 0.6 to 2.5 GeV/c, and the solid angle was about 64 msr. The produced hadrons, such as  $\pi^\pm$ ,  $K^\pm$ , protons and antiproton were detected by the High Resolution Spectrometer(HRS) on the left side in coincidence with the scattered electrons detected in BigBite. The central momentum of the HRS was set at 2.35 GeV with the solid angle about 6msr, and the momentum coverage  $|\frac{\Delta p}{p}|$  was about 5%. The HRS was instrumented in the normal configuration with a pair of lead glass detector, a gas Cherenkov detector, an aerogel Cherenkov detector, and a Ring Imaging Cherenkov detector (RICH), in order to clearly identify  $K^\pm$ ,  $\pi^\pm$ , protons and antiprotons.

This Chapter will discuss the incident electron beam, the Hall A beamline components, the transversely polarized  ${}^3\text{He}$  target, the BigBite, and the HRS detector components. The data acquisition system will also be briefly discussed.

## 4.2 The Electron Accelerator

The electron accelerator consists of a polarized source, an injector, two linacs (the North Linac and the South Linac), two re-circulation arcs and extraction elements to send beam into the three experimental halls: A, B and C, as shown in Fig. 4.1.

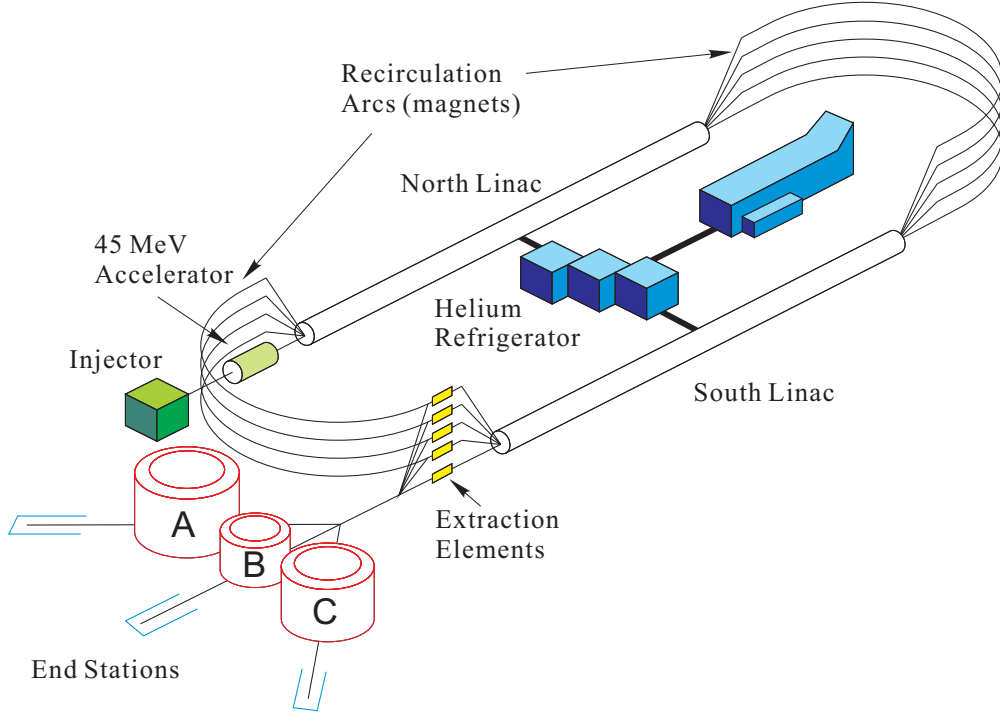


Figure 4.1: The Jefferson Lab Accelerator. Fig. is from Ref. [66]

The injector provides the polarized beams with up to  $200 \mu\text{A}$  current and up to 85% polarization which is produced by illuminating a strained superlattice gallium arsenide (GaAs) photocathode with circularly polarized photons. By tuning a left-handed circularly polarized laser (helicity  $-1$ , denoted as  $\sigma^-$ ) to proper frequency, electrons from the  $P_{\frac{3}{2}}$  ( $m = \frac{3}{2}$ ) state can be excited to the  $S_{\frac{1}{2}}$  ( $m = \frac{1}{2}$ ) level of the conduction band. Then the polarized electrons diffuse to the surface and escape into the surrounding vacuum, hence the electron beams are nearly 100% polarized (theoretically, practically 85%). The polarized beams were accelerated to 45 MeV with a radio frequency (SRF) chopping system at 499 MHz to develop a 3-beam. They were then longitudinally compressed in bunching section to form 2 picosecond bunches and injected into the North Linac. Both linacs are set identically and the superconducting RF cavities are phased to provide maximum acceleration. Each linac can gain from 400 to 600 MeV, therefore, after a maximum of 5 rounds, the energy of electron beam can range from 0.8 GeV (1 round) to 6.07 GeV maximum.

After passing through the South Linac, the beam can either circle around the west recirculation arc for

another round of acceleration, or be directed into a hall's transport channel using RF extraction. The 499 MHz RF cavities will extract every third bunch to a designated hall.

During this experiment, one-pass and two-pass beam were used for calibration data. The normal data were taken with a 5-pass beam of 5.89 GeV with 12  $\mu\text{A}$  to 14  $\mu\text{A}$  beam currents. Although polarized beams are not required for target single-spin asymmetry measurement, they were needed for a parasitic double-spin asymmetry measurement.

### 4.3 Hall A

Among the three experimental halls in JLab, Hall A is the largest one with diameter of 53m. Fig. 4.2 shows the overview of HALL A.

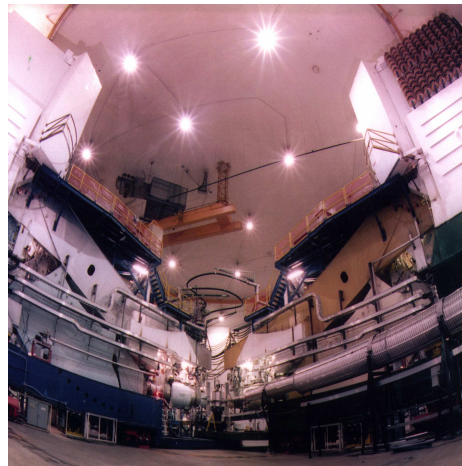


Figure 4.2: The overview of the HALL A.

### 4.4 Beamline

The Hall A beamline starts at the arc section (for beam energy measurement) and ends at the beam dump. It includes a beam energy measurement device, a Compton beam polarimeter, two beam current monitors (BCM), a raster, a Møller beam polarimeter, and several beam position monitors (BPM).

#### 4.4.1 Beam Energy Measurement Device

There are two methods to measure the beam energy. One is the eP measurement [88] utilizing the elastic  $P(e,e'P)$  reaction. The other is the Arc energy measurement [68].



During experiment E06010, the Arc energy measurement method was applied. Fig. 4.3 shows how it works. The method is based on the principle that an electron in a constant magnetic field moves in a circle.

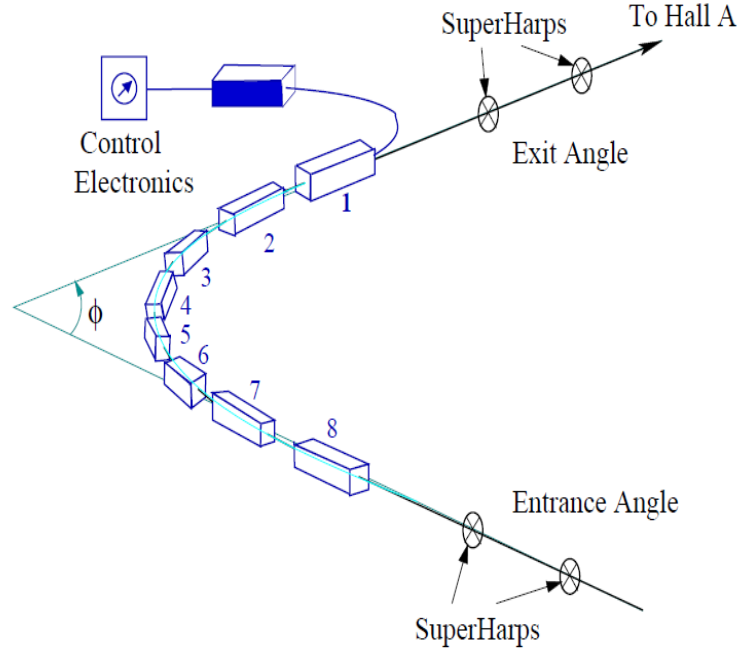


Figure 4.3: The Arc energy measurement was applied in this experiment E06-010 [68].

The radius depends on the magnitude of the magnetic field and of the electron's momentum. The electron energy is determined from the deflection angle of the beam in the 40m arc section of the beamline. The momentum of the electron ( $p$  in GeV/c) is related to the field integral of the eight dipoles and the bend angle  $\phi$  through the arc section by

$$p = c \frac{\int \vec{B} \cdot d\vec{l}}{\phi} \quad (4.1)$$

where  $c = 0.299792 \text{ GeV} \cdot \text{rad} \text{ T}^{-1} \text{ m}^{-1}$  is the speed of light. The nominal bend angle of beam in the arc section is  $\phi = 34.3^\circ$ , see Fig. 4.3.  $\vec{B}$  is the magnetic field, and  $d\vec{l}$  is the path length of the electron. The Arc energy measurement provides an absolute measurement to the  $2 \times 10^{-4}$  GeV level of accuracy. The SuperHarps (a set of wire scanner) installed at both the entrance and exit of the arc are used to determine the beam's position and the bend angle.

Before taking the production data, for calibration purposes, two lower beam energies, 1.2306 GeV and 2.3960 GeV, were used. Then, at the beginning of the experiment (Nov 17th, 2008), one full arc energy measurement was performed and the beam energy was determined to be  $E_{arc} = 5889.4 \pm 0.5(\text{stat.}) \pm 1.0(\text{sys.}) \text{ MeV}$ .

The beam energy is also monitored continuously online using the Tiefenback measurement [70]. This non-dispersive mode uses the relation between the field integral value and the set current in the eight dipoles of the arc section. The BPMs in the arc and the transfer functions for the Hall A beamline magnets provide the corrections. This method is accurate to  $\frac{\delta E_{beam}}{E_{beam}} \sim 5 \times 10^{-4}$ .

#### 4.4.2 Beam Current Measurement

The beam current is measured by the Beam Current Monitors (BCM) designed for stable, low noise, non-intercepting beam current measurements [71]. It contains an Unser monitor, two rf cavities, electronics and data acquisition, as illustrated in Fig. 4.4.

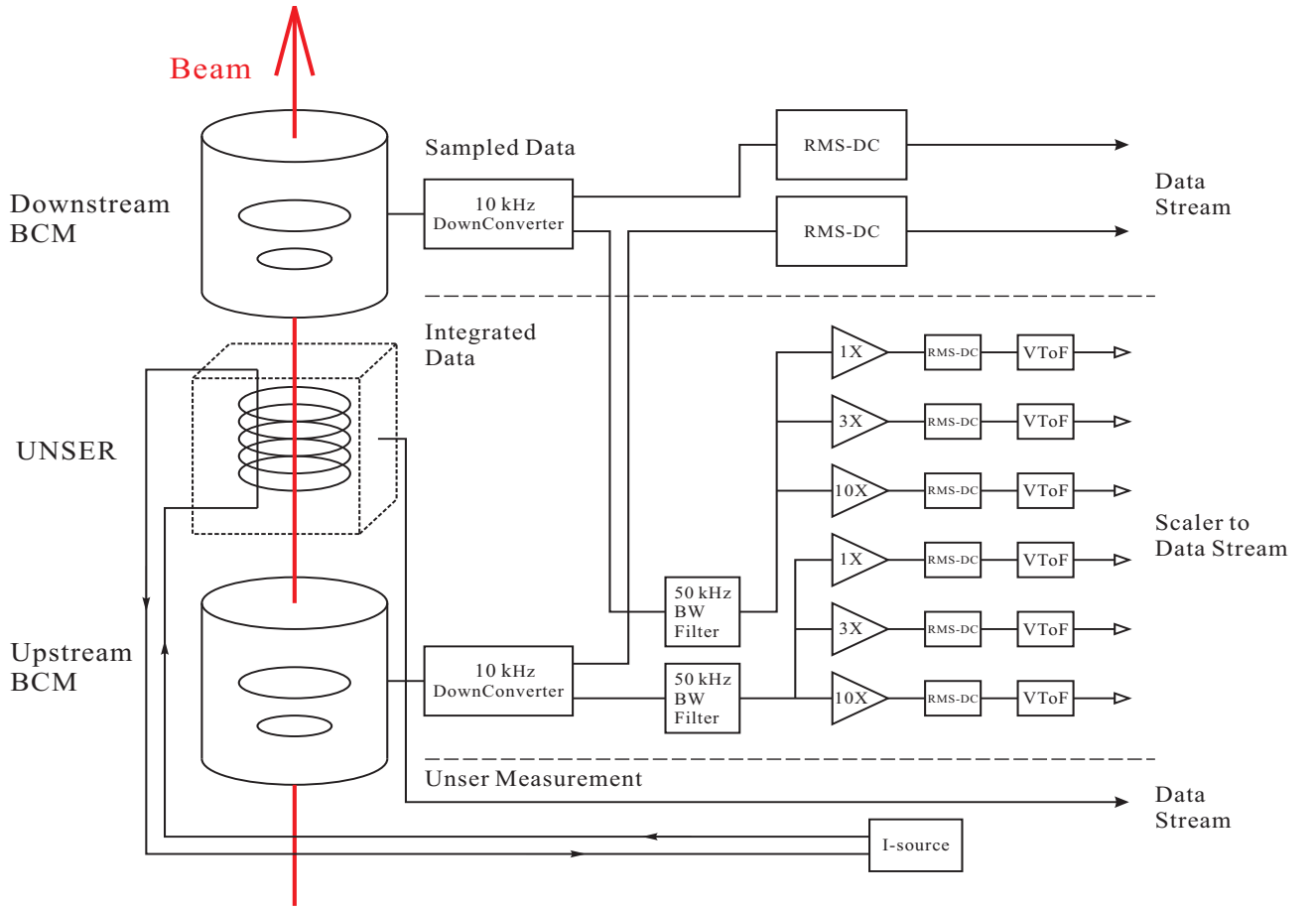


Figure 4.4: The configuration of BCMs in Hall A. Figure is from [66]

The cavities and the Unser monitor are enclosed in a box which is located 25m upstream of the target. The Unser monitor is a parametric current transformer designed for non-destructive beam current measurement and provides an absolute reference [72]. The monitor is calibrated by passing a known current through a

wire inside the beam pipe and has a nominal output of 4 mV/ $\mu$ A. However, the Unser monitor requires extensive magnetic shielding and temperature stabilization to reduce noise and drift, the Unser monitor's output signal drifts significantly on a time scale of several minutes, it cannot be used to continuously monitor the beam current. The drift is measured during the calibration runs and the net measured value is set to calibrate the two rf BCMs. The two resonant rf cavity monitors on either side of the Unser Monitor are stainless steel cylindrical high Q ( $\sim 3000$ ) waveguides tuned to the frequency of the beam (1.497 GHz) resulting in voltage levels at their outputs proportional to the beam current. Each of the rf output signals from the two cavities are split into two parts: to be sampled or integrated. The sampled signals processed by a high-precision digital multi-meter (DMM), HP3458A, and this device gives a digital output each second proportional to the RMS of beam current during that second. Signals from both cavities's and Unser's multimeter's are transported through GPIB ports and are recorded by the data logging process every 1-2 s. The integrated signals are sent to an RMS-DC converter and then to a voltage-to-frequency converter. These frequency signals are then fed to 200 MHz VME scalars and injected into the data stream along with other scaler information. The scalars accumulate during the run and each BCM scaler provides a number proportional to the time-integrated voltage level, which represents the total delivered beam charge. The RMS-to-DC output is linear for current from 5 to 200  $\mu$ A. A set of amplifiers has been introduced with gain factors of 1, 3, and 10 to lower currents at the expense of saturation at high currents. As a result, for both upstream BCM and downstream BCM, 6 BCMs ( $u_1, u_3, u_{10}, d_1, d_3, d_{10}$ ) are recorded in the data stream. The beam current and hence charge,  $Q_a = I_a t$ , are obtained from BCM scaler reading as follows:

$$I_a = \frac{N_a - f_a}{k_a}, \quad (4.2)$$

where  $a = 1, 3, 10$  is the gain factor,  $t$  is the time for each run (in seconds) and  $N_a$  is the BCM scaler reading for each gain factor. The calibration constant  $k_a$  and BCM offsets  $f_a$  are determined from calibration runs. For E06-010, the BCM calibration constant and BCM offset constant for the upstream and downstream cavities are given in table 4.1 and table 4.2 which are calibrated against the data provided by the accelerator group using the "OLO2" cavity to measure the beam current at the injector. For experiment E06-010, we use gain factor 3 for upstream  $u_3$  and downstream  $d_3$  to get the beam current measurement.

As we described in Sec. 4.2, the incident electron beam was polarized. For target single-spin asymmetries (SSA),  $n^\uparrow(e, e'K^\pm)$  reactions, the beam polarization is not required, all the beam helicities ( $H+$ ,  $H-$ ) will be summed up for the results. Due to the incomplete coverage kinematic in our experiment, the beam charge asymmetries will introduce an additional correction for the result of target single-spin asymmetries. The

Table 4.1: BCM calibration constants for both upstream and downstream signals determined during two different period measurements, the units are counts/ $\mu\text{A}$

| Date     | U1      | U3      | U10      | D1      | D3      | D10      |
|----------|---------|---------|----------|---------|---------|----------|
| Feb 2009 | 2101.87 | 6464.39 | 19718.30 | 2147.88 | 6645.89 | 20952.00 |
| Oct 2008 | 2077.56 | 6390.79 | -        | 2162.85 | 6696.15 | 21120.68 |

Table 4.2: BCM offsets for both upstream and downstream determined during two different period measurements, the units are counts/ $\mu\text{A}$

| Date     | U1     | U3     | U10    | D1     | D3     | D10    |
|----------|--------|--------|--------|--------|--------|--------|
| Feb 2009 | 395.80 | 453.40 | 770.52 | 154.58 | 133.32 | 293.46 |
| Oct 2008 | 369.84 | 406.98 | -      | 157.80 | 111.66 | 307.73 |

beam charge asymmetries, defined as

$$A_Q = \frac{Q^+ - Q^-}{Q^+ + Q^-}, \quad (4.3)$$

where  $Q^+ = I^+t^+$  ( $Q^- = I^-t^-$ ), and  $I^+(I^-)$  and  $t^+(t^-)$  are the beam intensity and pulses the time interval of  $H + (H-)$  pulses. During experiment E06-010, the beam charge asymmetry was minimized by the beam charge asymmetry feedback system [73]. It was implemented by running the parity data acquisition system [74]. The feedback system can limit the beam intensity asymmetries to a few ppm, however it is not reliable during beam trips, so the data during beam trips were discarded, as described in Chapter 5.

In order to avoid false asymmetry of beam helicity, the beam half-wave plate was inserted periodically during data-taking. The beam half-wave plate flips the helicity of the electron beam. It provides a powerful tool to check false asymmetry due to beam helicity.

### 4.4.3 Raster and Beam Position Measurement

In order to avoid overheating the target, the beam is rastered on the target with an amplitude of several millimeters at 25kHz by a pair of horizontal (X) and vertical (Y) air-core dipoles located 23 m upstream of the target. The triangle-wave raster pattern [75] was applied for achieving a very uniform rectangular density distribution of beam on the target by moving the beam with a time-varying dipole magnetic field whose waveform is triangular with very little dwell time at the peaks. In experiment E06-010, we used 3mmX3mm raster pattern.

Two beam position monitors (BPMa and BPMb) located 7.524m and 1.286m upstream of the target are used to determine the position and direction of the beam at the target location. The BPMs are composed of

a 4-wire antenna array of open ended thin wire striplines tuned to the fundamental RF frequency of 1.497 GHz of the beam. In order to determine the relative position of the beam, the standard difference-over-sum technique is used and it can determine the relative position of the beam to within 100 microns for currents above  $2\mu\text{A}$ . The absolute position of the BPMs can be calibrated with respect to the scanners (superharps) which are located adjacent to each of the BPMs. The superharps provide an invasive measurement of the beam position and consist of three wires oriented vertically and at  $45^\circ$ . The wires are scanned across the electron beam resulting in a shower of particles that are then detected. The superharps are routinely surveyed with respect to the Hall A coordinate system. The real beam position and direction at the target can be reconstructed using the BPM positions calculated from 8 BPM antennas' readout(2X4):

$$x, y_{target} = \frac{x, y_{BPMa} \cdot \Delta z_{BPMb} - x, y_{BPMb} \cdot z_{BPMa}}{z_{BPMb} - z_{BPMa}} \quad (4.4)$$

$$\vec{x}_{beam} = \frac{\vec{x}_{BPMb} - \vec{x}_{BPMa}}{|\vec{x}_{BPMb} - \vec{x}_{BPMa}|} \quad (4.5)$$

where  $\Delta = z_{BPM} - z_{target}$ .

The BPMs are slow in measuring the position of the beam and the delay is about a few microseconds. The raster magnets respond more quickly, and can be used to determine the positions directly. The calibration of raster involves finding the transformation coefficients and offsets for converting the raster currents to actual beam positions. This is done using the averaged beam position information from BPMs and raster currents recorded in the ADCs.

The position information from the BPMs are recorded into EPICS database based on the averaged position over 0.3 seconds and/or CODA data stream from each of the 8 BPM antennas (based on event-by-event information).

## 4.5 The Polarized $^3\text{He}$ Target

In order to understand the spin structure of neutron, neutron target is needed. However, the neutron's short half-life of  $885.7 \pm 0.8\text{s}$  [76] makes a neutron target impractical. Some alternative targets include deuterium and  $^3\text{He}$ .

The transversely polarized  $^3\text{He}$  target provides an effective neutron target, since in the ground state configuration, the wave function (Fig. 4.5) is dominated by the S-wave where two protons are paired and the lone neutron spin is aligned with the spin of the  $^3\text{He}$  nucleus. There are also  $S'$ -wave state and D-wave

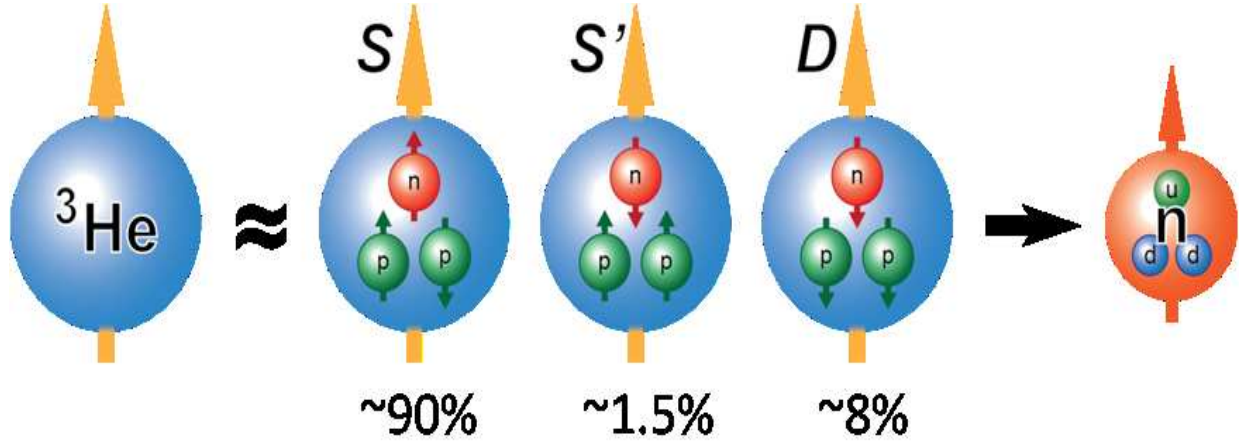


Figure 4.5: Three wave function states of  $^3\text{He}$

state. But almost  $\sim 90\%$  is S-wave state.

#### 4.5.1 Principles

Details about the Jefferson Lab polarized  $^3\text{He}$  target are available in Ref. [77].

There are two major methods to polarize  $^3\text{He}$ , one is based on the metastability-exchange optical pumping technique [78]. Usually it is used for internal targets. The second is based on spin exchange optical pumping (SEOP). This method are commonly used for high pressure gas targets, typically one to ten atmospheres. It was originally developed at SLAC [86] and has been used in JLab Hall A for several experiments since 1998 [80], including E06-010 experiment.

The Hall A standard polarized  $^3\text{He}$  target [80] used optically pumped Rubidium vapor to polarize Rb atoms first. Subsequently, the Rb polarization is transition to  $^3\text{He}$  nuclei via spin-exchange. Recently, Hall-A also adopted the K-Rb hybrid spin-exchange technique [87] which has achieved improved spin exchange efficiency and significantly shorter spin-up times.

We now describe the SEOP method. First, the optically pumped rubidium atoms are polarized.  $\text{Rb}(1s^2s^2 2p^63s^2 3p^63d^{10}4s^24p^65s)$  has a single electron in the outer shell ( $5S_{\frac{1}{2}}$ ), whose Hamiltonia in a magnetic field  $\vec{B}$  is the following:

$$\hat{H} = A_g \vec{I} \cdot \vec{S} + g_e \mu_B S_z B_z - \frac{\mu_I}{I} I_z B_z \quad (4.6)$$

where the first term is the coupling between the nuclear spin  $\vec{I}$  and electron spin  $\vec{S}$ , the second and third terms express the coupling between electron spin and nuclear spin with magnetic field  $B_z$  (along to z direction). The electron magnetic moment  $\mu_e = g_e \mu_B$  where  $g_e = 2.00232$ ,  $\mu_B = 0.57884 \times 10^{-11} \frac{\text{MeV}}{\text{T}}$ , the nuclear magnetic momentum  $\mu_I = 4.26426 \times 10^{-12} \frac{\text{MeV}}{\text{T}}$  for  $^{85}\text{Rb}$ , and the Rb atom's spin quantum number I ( $I=5/2$

for  $^{85}\text{Rb}$  and  $I=3/2$  for  $^{87}\text{Rb}$ ).

The  $^{85}\text{Rb}$  energy structure in weak magnetic field is shown in Fig. 4.6. In the process of optical pumping, Rb vapor is exposed to circularly polarized laser tuned to the  $5S_{1/2} \rightarrow 5P_{1/2}$  transition, known as the  $D_1$  transition. The photon wavelength of the  $D_1$  transition is roughly 794.8nm.

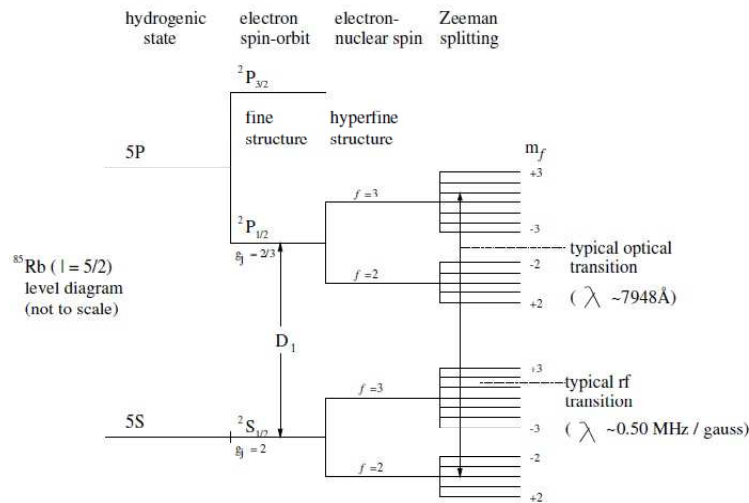


Figure 4.6: Energy Level diagram of  $^{85}\text{Rb}$ .  $I = 5/2$ . The splittings are not to scale.

A practical issue involves the photons emitted by the excited electrons when they decay back to the ground state. These photons are randomly polarized and thus would reduce the Rb polarization. A small amount (about 1%) of  $N_2$  is introduced to reduce this depolarization effect through a process called quenching, whereby the collisions between rubidium atoms and  $N_2$  allow the electrons to decay without emitting photons, through the excitation of  $N_2$  [83]. The amount of  $N_2$  is chosen to be about two orders of magnitude less in density than that of  $^3\text{He}$  but a few orders of magnitude more than the density of rubidium atoms. As a result, only about 5% of excited electrons decay by emitting photons.

The key process in spin-exchange optical pumping is the collisional transfer of polarization between optically pumped alkali-metal atoms and the nuclei of the inert gas atoms. Spin-dependent interactions,

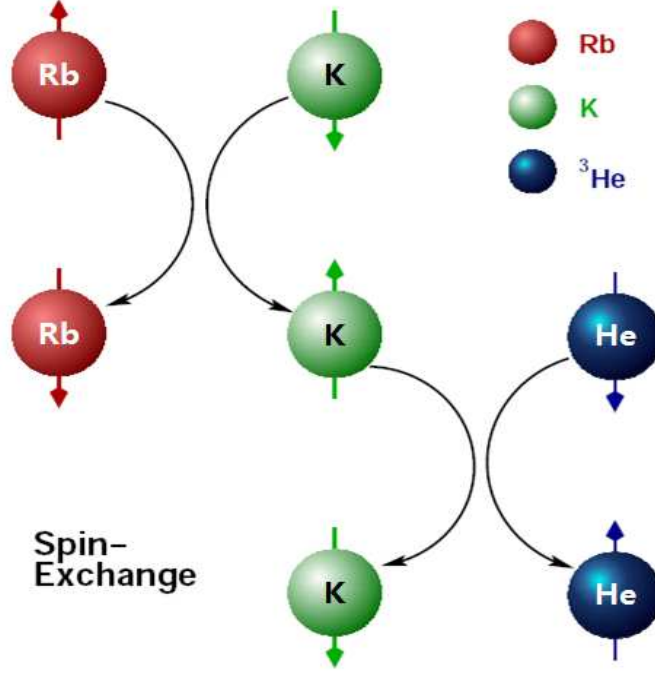


Figure 4.7: Hybrid approach of Spin-Exchange Optical Pumping (SEOP)

denoted by  $V_1(\vec{R})$  with  $R$  the interatomic separation, produce the spin transfer and relaxation in collisions. The spin-exchange process is dominated by two terms [85], as shown in Eq. 4.7.

$$V_1(\vec{R}) = \gamma(R)\vec{N} \cdot \vec{S} + A_b(R)\vec{I}_b \cdot \vec{S}. \quad (4.7)$$

The first term is the spin-rotation interaction between the electron spin  $\vec{S}$  and the rotational angular momentum  $\vec{N}$  of the <sup>3</sup>He-Rb system, the second term is the isotropic hyperfine interaction between  $\vec{S}$  and the inert gas nuclear spin  $\vec{I}_b$ .

The polarization of the rubidium vapor  $P_{Rb}$  is determined by the optical pumping rate ( $R$ ) and the spin destruction rate ( $\Gamma_{SD}$ ):

$$P_{Rb} = \frac{R}{R + \Gamma_{SD}}. \quad (4.8)$$

The optical pumping rate is defined as:

$$R = \int \Phi(\nu)\sigma(\nu)d\nu. \quad (4.9)$$

where  $\Phi(\nu)$  is the laser flux per unit frequency and  $\sigma(\nu)$  is the light absorption cross-section. The electron spin destruction rate  $\Gamma_{SD}$  is mainly determined by the spin-rotation interaction  $\gamma(R)\vec{N} \cdot \vec{S}$  during collisions



between Rb atoms and other gas molecules. The contribution from the randomly polarized photons emitted from the decay of excited electrons is small [86]. The destruction rate is

$$\Gamma_{SD} = k_{Rb-He}[{}^3He] + k_{Rb-Rb}[Rb] + k_{Rb-N_2}[N_2]. \quad (4.10)$$

where  $[{}^3He]$ ,  $[Rb]$ ,  $[N_2]$  are densities of each gas component.

The Hybrid Spin-Exchange Optical Pumping(HSEOP) [87] is introduced to further improve the efficiency of transferring the polarization to  ${}^3He$ . By adding vaporized potassium (K) to the pumping chamber, the Rb atom is polarized through normal optical pumping, then it transfers polarization to the potassium atom:



This equation shows how the Rb spin which was up before collision is transferred to the K spin.

The potential for the spin-exchange collision is written as follows

$$V(r) = V_o(r) + S_{Rb} \cdot S_K V_1(r), \quad (4.12)$$

where  $S_{Rb}$  and  $S_K$  are the spin operators of Rb and K atoms respectively. This potential is of the order of electron-volts because of the electrostatic nature of the spin-exchange interaction forces.

After K atoms are polarized, the spin-exchange collision between  ${}^3He$  and K atom will replace the spin-exchange collision between  ${}^3He$  and Rb due to higher efficiency transferring the polarization from K to  ${}^3He$ , and eventually polarizes  ${}^3He$  atoms.

### 4.5.2 The Target System

The target system for this experiment is considered the most complicated one in the history of polarized  ${}^3He$  experiments in HallA. The system mainly comprises of three pairs of Helmholtz coils, two pairs of RF coils, an oven with three pairs of pick up coils, a  ${}^3He$  cell, a target ladder with an empty target, a reference target and an optics target, and two pairs of target chamber pick up coils. A heater system together with an air flow system act as an integral part of the target system to maintain the desired temperature of 230°C inside the oven. Also there are two pairs of correction coils to correct for the field gradient prevailing in the target region.

#### ${}^3He$ cell

All the cells used in the experiment were hybrid cells. They were made at Princeton and filled at the

University of Virginia and the College of William and Mary. A schematic diagram of the cell dimensions as well as the orientation with respect to the Hall system is shown in Fig. 4.8 The main characteristics of the cells used in this experiment are summarized in Table 4.3.

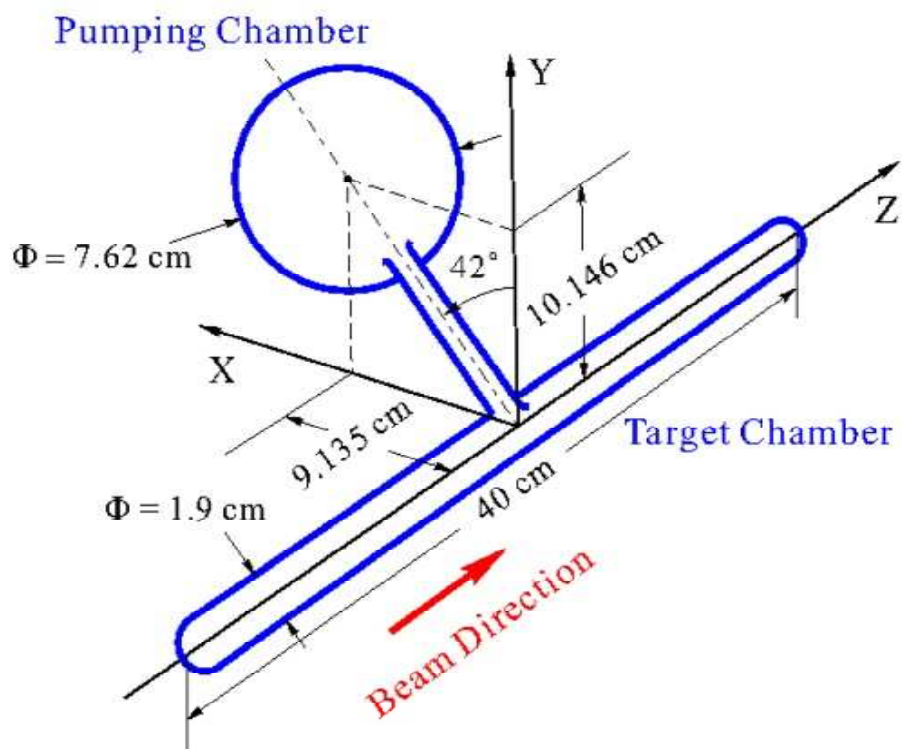


Figure 4.8: Orientation of the hybrid cell in the Hall.

As shown in Fig. 4.8, each of these cells has a pumping chamber of diameter 3 inch and a target chamber of diameter  $\sim 2$  cm. The pumping chamber and the target chamber are connected through a transfer tube of known length. All the quantities in Table 4.3 are measured at University of Virginia and College of William and Mary. In addition to those numbers, the material of the glass, the thickness of the cell window and the cell walls, the length of the transfer tube and the ratio  $K/Rb$  are few extremely important quantities for the polarimetry as well as other radiative correction analyses.

#### Target Ladder

Table 4.3: A few numbers from UVA and W/M database.  $V_p$  is the volume of the pumping chamber,  $V_t$  is the volume of the target chamber,  $V_{tt}$  is the volume of the transfer tube. All the volumes are in  $cm^3$ , the density is in amagats and the lifetime is in hours.

| Name    | Filled at | $V_p$  | $V_t$ | $V_{tt}$ | Fill Density | Lifetime(Raw/AFP corrected) |
|---------|-----------|--------|-------|----------|--------------|-----------------------------|
| Astral  | UVA       | 164.92 | 79.47 | 6.77     | 8.082        | 40/49                       |
| Maureen | W/M       | 180.75 | 89.05 | 4.15     | 7.23         | 26/29                       |

A target ladder is mounted on the oven which has five different target positions. The positions are shown in Fig. 4.9.

- **Polarized  $^3\text{He}$  target cell position**

This position was for our polarized  $^3\text{He}$  cell used for the main production in our experiment. The cell was glued to the bottom plate of the oven with RTV. This could be replaced by the water cell for calibration.

- **A solid BeO target inline with seven Carbon foils**

This position was for alignment of the beam on the target by tuning the beam and for optics calibration. The beryllium oxide (BeO) foil was used to make the beam spot easily visible so that a correct beam position on the target could be obtained.

- **A “hole” target**

This was just the center carbon foil but extended a bit more with a hole in it. This was also used for fine alignment.

- **An empty target position**

This position was mostly used for beam tuning and also during Moller measurement. It contained *no target* and thus this position allowed the incoming beam to pass without any obstacles in its path.

- **A reference cell position**

This position was for different calibration processes such as elastic calibration, the detector calibration, other background studies etc. The reference cell was filled with either nitrogen, hydrogen or Helium-3 in accordance with the purpose of the studies.

The target ladder could be moved vertically to different positions using a stepping-motor-driven motion control system. It had a limit switch at each position and the motion was controlled remotely via EPICS from the counting house. The pick up coil position shown in the schematic is the position between the two pairs of pick up coils. The target was lowered to this position to do the NMR measurements.

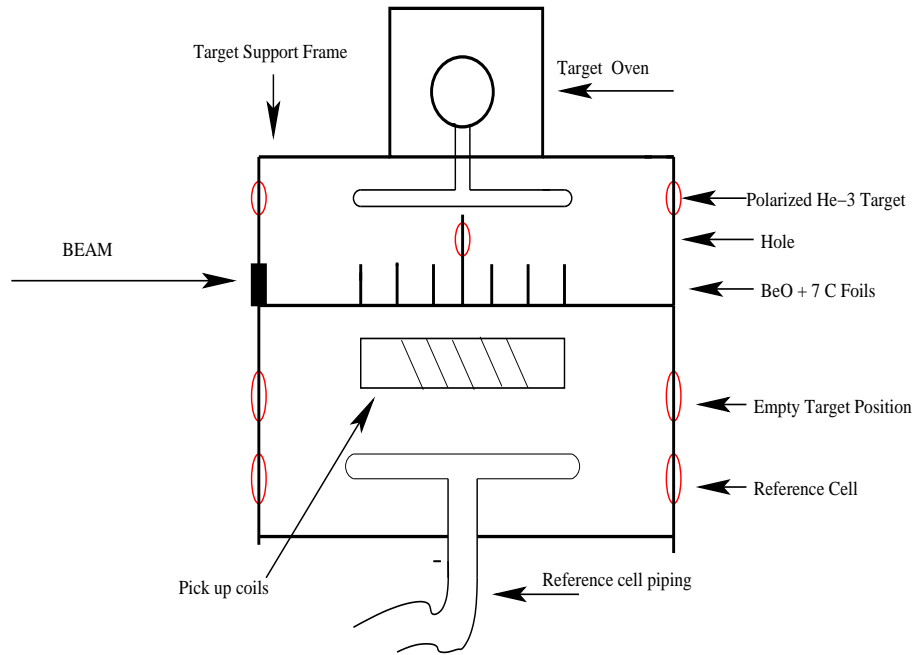


Figure 4.9: Schematic diagram of the target ladder system.

### Oven, Heater, and Airflow System

The oven had an inlet and an outlet for the circulation of the compressed air. Since the pumping chamber was in the oven and it had to be kept at  $230^{\circ}\text{C}$  for hybrid optical pumping, the air that came into the oven should be hot enough. In order to do that, the pressurized dry and filtered air provided by a compressor in the Hall was made to pass through two heaters. One of them was controlled by a variac in the Hall and the other one was by PID feedback electronic control chassis. The hot air in the oven was made to exit through an exhaust pipe. Both the inlet and the outlet are enclosed in a tube that supported the oven and wrapped with insulation material. A Resistive Temperature Device (RTD) was attached inside the oven to read the inside temperature and a thermocouple was inserted inside the insulation material near the second heater to measure the temperature of the hot air going into the oven. Throughout the experiment, our oven temperature was kept stable at  $230^{\circ}$  with a very good PID system.

### Helmholtz coils for Holding Field

Three pairs of Helmholtz coils were used in the experiment to produce the magnetic fields in three mutually perpendicular directions. Two pairs of horizontal Helmholtz coils were used to produce the desired magnetic field in two horizontal directions, *viz*, the longitudinal field along the beam direction and the transverse field perpendicular to the beam direction. The third pair of Helmholtz coils was the largest one which encompassed the other two and was used to produce the vertical field. The schematic diagram of

the Helmholtz coils system is shown in Fig. 4.10. Table 4.4 shows the basic characteristics of the three pairs of Helmholtz coils.

Table 4.4: Dimensions of the Helmholtz coils used in the experiment to produce the magnetic field to align the spins of the  $^3\text{He}$  nuclei. The diameter is in meter and the resistance is in ohm.

| Coil     | Inner diameter | Number of turns | Resistance |
|----------|----------------|-----------------|------------|
| Small    | 1.27           | 256             | 3          |
| Large    | 1.45           | 272             | 3          |
| Vertical | 1.83           | 355             | 4.4        |

The horizontal pairs of coils were powered by two KEPCO BOP 36-12D power supplies while an Agilent 6675A was used to power the vertical pair. The current settings for these three pairs of coils throughout the experiment were shown in Table 4.5.

Table 4.5: Current settings for the three pairs of Helmholtz coils.  $\vec{B}$  stands for the holding magnetic field direction,  $I_S$  for current in the small coils,  $I_L$  for current in the large coils and  $I_V$  for current in the vertical coils. The units are in Ampere.

| $\vec{B}$  | $I_S$ | $I_L$  | $I_V$    |
|------------|-------|--------|----------|
| Transverse | 6.234 | -4.621 | 0.712066 |
| Vertical   | 0.329 | -0.358 | 14.0927  |

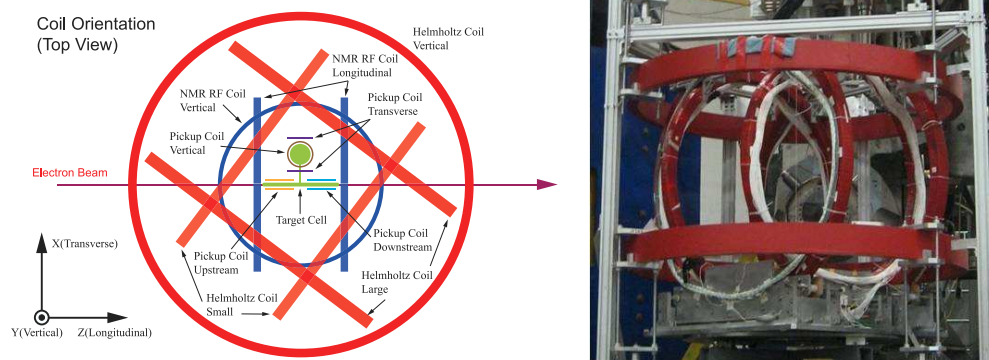


Figure 4.10: Left panel: Complete schematic of our Helmholtz coils system in the Hall. The RF coils and the pick up coils are also shown. Right panel: The real target setup.

### 4.5.3 Laser and Optical Fibers

During Experiment E06010, three COMET lasers were used on  $^3\text{He}$  cell instead of the FAP systems to provide the optical pumping. The difference between the COMET, sometimes referred to as Narrow Bandwidth

lasers, and the old FAP systems is that the COMET lasers have very narrow linewidth of wavelength ( $\sim 0.2$  nm) as compared to the 2 nm linewidth of the FAP systems. As a result, there is a dramatic increase in the absorption of the laser light by the hybrid cells and hence a large polarization could be achieved. With these COMET lasers, a maximum polarization of  $\sim 72\%$  was achieved and due to this high maximum polarization, in experiment E06-010, the polarization is  $\sim 65\%$ .

The lasers were installed and interlocked in the laser building behind the counting house. The fiber coming out of each COMET was connected to a 75 m long fiber that ran from the laser building to the Hall. Then the 75 m long fiber was connected to a 5 to 1 combiner. A 5 to 1 combiner has 5 separate fibers as input and one output combining all 5 fibers. In experiment E06010, three lasers were used at a time which means three 75 m fibers were connected to one the combiner and the output was the final input to the optics assembly in the optics enclosure. As a result, there was a power loss of  $\sim 6\%$  in the input assembly the optics.

### **Optics**

The laser light coming out of the 5 to 1 combiner had to be aligned so that a spot of roughly the same diameter of the  $^3\text{He}$  cell in the oven could be achieved. This was done with optics assembly where various optical components were placed and aligned accordingly. The unpolarized laser light was allowed to pass through all the optics components so that a “well defined” i.e. either left or right circularly polarized light is available at the output of the optics assembly. This circularly polarized light, when focussed to a spot of the cell diameter on the cell, was absorbed by the Rb atoms in the cell and thus the polarization of Rb and then the  $^3\text{He}$  started to grow. The alignment of the optics was quite essential in order to achieve a very high polarization of  $^3\text{He}$ . There were three optics lines in the optics enclosure in the Hall. The transverse and the vertical lines were for Experiment E06-010. The set up of the optics components is shown in Fig. 4.11.

The unpolarized laser light of 795nm from the combiner was incident on the first lens L1. The focal length of L1 was 75 mm. L1 focussed the three spots at its focal point. But after the focal point, the spots started to diverge again. Another lens L2 of focal length 750 mm was placed in such a way that the spots on the lens are reasonably separated and clearly visible. Then the beam splitter was used to separate S and P waves from the incident unpolarized light coming out of L2. The S wave was allowed to pass through the quarter wave plate Q1 and reflected back from the mirror M1 and pass through Q1 again. Thus after getting reflected from M1 and passing through Q1 twice, the S wave became P wave and passed through the beam splitter again. On the other hand, the P wave was allowed to incident on the mirror M2. Now both P waves passed through two quarter wave plates Q2 and Q3 so that the linearly polarized P waves

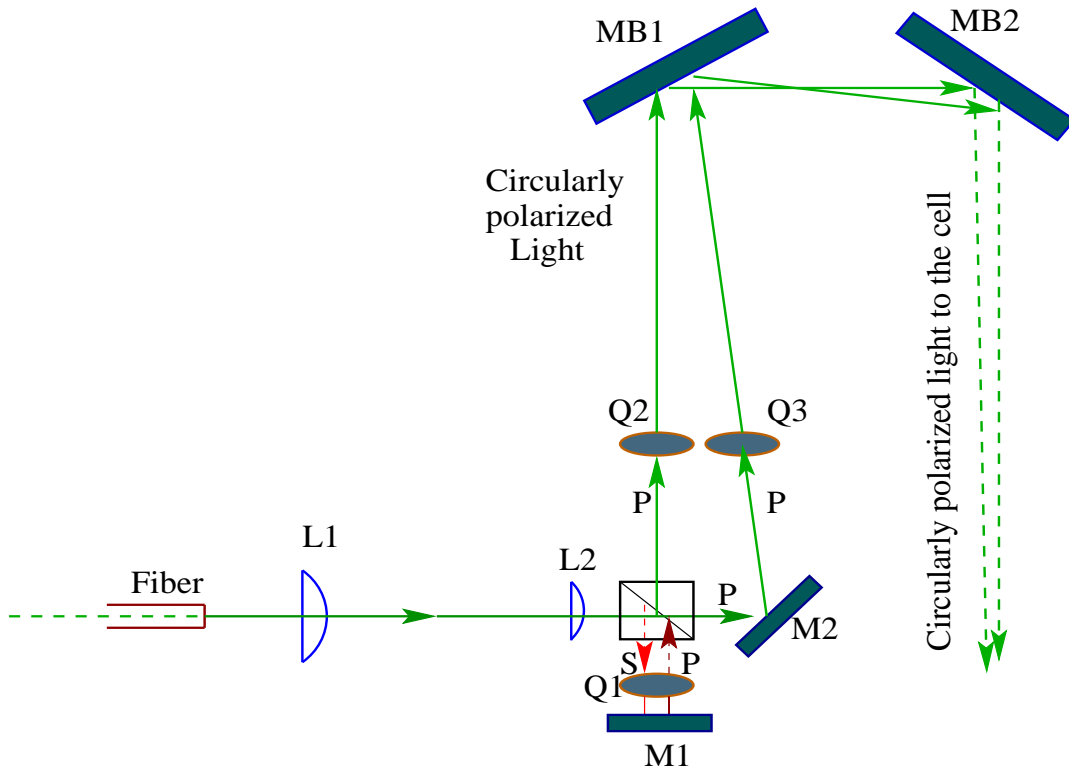


Figure 4.11: Schematic diagram of the optics setup. This setup was for the vertical pumping. For the transverse pumping, the big mirror MB2 was actually mounted on the oven. The rest of the setup was the same.

became circularly polarized. The quarter wave plates were calibrated before so that the linearly polarized P waves, when passed through them, would become circularly polarized (either left circularly polarized or right circularly polarized). The last two components in the path were two big mirrors MB1 and MB2. Each of them had a diameter of 6 inches. The two circularly polarized waves were then allowed to incident on MB1 at an angle of  $45^\circ$ . The reflected waves were again reflected at an angle of  $45^\circ$  on MB2. The relative orientation of the big mirrors was important in order to preserve the polarizations of both waves. The final spot size of the laser light on the cell was mostly influenced by L1. A simulation was done well before the experiment to determine the distances between the components and the focal lengths of the lenses used.

#### 4.5.4 Polarimetry

There are two polarimetry techniques to measure the polarization of  $^3\text{He}$ . One is Nuclear Magnetic Resonance (NMR), which was used frequently during this experiment. For each target spin flip in every 20 minutes, a corresponding NMR signal was generated and an instant polarization number was obtained. However NMR is a relative measurement and need to be calibrated. The other is Electron Paramagnetic Resonance (EPR),

which is an absolute measurement of polarization of  $^3\text{He}$ . The EPR was used to measure the polarization from time to time. Meanwhile a couple of water NMR measurements were performed to cross check the polarimetry. Based on the absolute measurement of EPR, the polarization of  $^3\text{He}$  being measured by NMR can be calibrated. Both methods will be discussed in the following subsections.

### NMR-AFP

Under a uniform static magnetic field together with another oscillating magnetic field, a nucleus of non-zero spin will exhibit a phenomenon called Nuclear Magnetic Resonance (NMR). The principle for this phenomenon is called Adiabatic Fast Passage (AFP), described as follows:

Consider a free particle with spin  $\vec{I}$  and magnetic moment  $\vec{M}$  in a magnetic field  $\vec{H}$ . The torque  $\vec{\tau}$  experienced by the particle is given by

$$\vec{\tau} = \vec{M} \times \vec{H}. \quad (4.13)$$

It is well known that the torque is the rate of change of angular momentum. It can be written as:

$$\vec{\tau} = \hbar \frac{d\vec{I}}{dt}. \quad (4.14)$$

And the magnetic moment  $\vec{M}$  can be written in terms of spin as

$$\vec{M} = \gamma \hbar \vec{I} \quad (4.15)$$

where  $\gamma$  is the gyro-magnetic ratio. Combining Eq. 4.13, Eq. 4.14 and Eq. 4.15,

$$\vec{M} \times \vec{H} = \hbar \frac{d\vec{I}}{dt} \quad (4.16)$$

$$\implies \vec{M} \times \vec{H} = \frac{1}{\gamma} \frac{d\vec{M}}{dt} \quad (4.17)$$

$$\implies \frac{d\vec{M}}{dt} = \gamma \vec{M} \times \vec{H} \quad (4.18)$$

which is effective in the inertial or laboratory frame of reference. To simplify, lets consider a rotating frame



of reference  $S'$  rotating with an angular velocity  $\vec{\omega}$  with respect to the laboratory frame. Then the relation of the rate of change of magnetic moment between these two frames can be written as

$$\frac{d\vec{M}}{dt} = \frac{\partial\vec{M}}{\partial t} + \vec{\omega} \times \vec{M} \quad (4.19)$$

where the term  $\frac{d\vec{M}}{dt}$  represents the rate of change in the laboratory frame and the term  $\frac{\partial\vec{M}}{\partial t}$  represents the rate of change in the rotating frame. Now combining Eq. 4.16 and Eq. 4.19, the motion of the magnetic moment in the rotating frame  $S'$  can be written as

$$\frac{\partial\vec{M}}{\partial t} = \gamma\vec{M} \times \vec{H} - \vec{\omega} \times \vec{M} \quad (4.20)$$

$$\implies \frac{\partial\vec{M}}{\partial t} = \gamma\vec{M} \times \left(\vec{H} + \frac{\vec{\omega}}{\gamma}\right) \quad (4.21)$$

Finally, in the rotating frame  $S'$ , the original holding field  $\vec{H}$  is replaced by an effective field  $\vec{H}_e$  given by

$$\vec{H}_e = \vec{H} + \frac{\vec{\omega}}{\gamma} \quad (4.22)$$

In Experiment E06010, there were two holding field configurations, i.e., the vertical and the transverse. In the vertical configuration, the holding field was kept constant along the vertical (perpendicular out of plane)  $\hat{i}$  direction with respect to the beam. Similarly, in the transverse configuration, the holding field was kept constant along the transverse (perpendicular in plane)  $\hat{j}$  direction with respect to the beam. Here only the vertical configuration is considered where the holding field  $\vec{H}_o$  was along x-axis. Now if a rotating frame with an angular velocity  $\vec{\omega} = -\gamma\vec{H}_o$  was selected, the effective field  $\vec{H}_e$  vanishes and hence magnetic moment becomes a constant of motion. This frequency is called the *Larmor frequency*. In order to measure NMR, an AFP need to be performed. An RF field was applied in the longitudinal z- direction (which was along the beam). The RF field can be described by  $\vec{H}_{rf} = H_{rf} \cos(\omega t)\hat{k} + H_{rf} \sin(\omega t)\hat{j}$ , the effective field in the rotating frame can be written as,

$$\vec{H}_e = \left(H_o + \frac{\omega}{\gamma}\right)\hat{i} + H_{rf}\hat{k} \quad (4.23)$$

where  $\omega$  is the frequency with which the rotating frame precesses. Note that  $\omega$  is not necessarily equal to the *Larmor frequency*.

During the measurement, the RF was swept from 77 kHz to 85 kHz through the resonance at  $\omega_o=81$  kHz and back. The sweep rate was 4kHz/sec to satisfy the AFP condition, which has two requirements. The change in the frequency and hence the passage of the spins through the resonance should be fast enough so that the spins don't have time to relax during the sweep (*fast condition*) and slow enough compared to  $\omega_o$  so that the spins can follow the sweep (*adiabatic condition*). The AFP conditions for the frequency sweep NMR can be expressed by:

$$\frac{|\gamma H_{rf}|}{T_2} \ll |\dot{\omega}| \ll \gamma^2 H_{rf}^2. \quad (4.24)$$

where  $T_2$  is the  $^3\text{He}$  spin relaxation time,  $\gamma=3.24$  kHz/G is the gyromagnetic ratio for  $^3\text{He}$ , and  $H_{rf}$  is the RF field. For field sweep NMR where the holding field is swept keeping the frequency constant, the usual AFP conditions can be satisfied with a sweep rate of 1.2 Gauss/s. In this case, the holding field is swept from 25 G to 32 G and then back with the resonance at 28 G which corresponds to a radio frequency of 81 kHz. During our experiment, field sweep NMR was done periodically as a part of our calibration for pumping chamber polarization and the target chamber polarization.

#### The Electronics and the measurement

Most of the NMR measurements done in the experiment were the frequency sweep NMR measurements in the pumping chamber and those were calibrated with the EPR measurements. Since the target spin was flipped once every 20 minutes, a frequency sweep NMR was also performed, so that polarization in the pumping chamber was monitored once every 20 minutes throughout the experiment. The advantage was that no extra NMR measurements were needed, unlike previous polarized  $^3\text{He}$  experiments.

A typical frequency sweep NMR signal is shown in Fig. 4.12. The height of the signal from the lock-in is proportional to the transverse component of the magnetization of  $^3\text{He}$  and hence the polarization. The signal is fitted to the square root of a Lorentzian.

$$S \propto \frac{\omega_1}{\sqrt{(\omega - \omega_o)^2 + \omega_1^2}} \quad (4.25)$$

where  $\omega_o$  is the Larmor frequency,  $\omega$  is the frequency of the RF field being swept and  $\omega_1$  is related to the

width of the peak and the magnitude of the RF field.

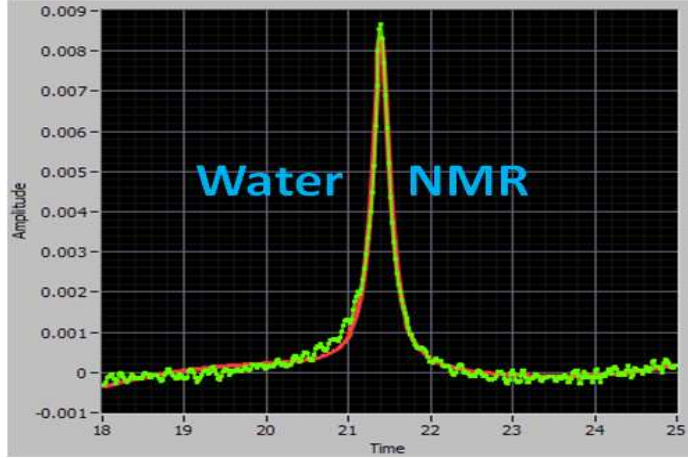


Figure 4.12: A NMR frequency sweep signal fitted to the square root of a Lorentzian.

## EPR measurement

### Theory

Electron Paramagnetic Resonance (EPR) measures the splitting of different energy levels of an atom in the presence of an external magnetic field due to Zeeman effect. Using EPR on the alkali present in the  $^3\text{He}$  cell, the absolute polarization of  $^3\text{He}$  can be extracted. The high pressure hybrid  $^3\text{He}$  cell contains some amount of Rb and K. The ratio of Rb to K in the cells used in the experiment was 5:1.

In principle, in the presence of a magnetic field  $\vec{B}$ , the  $F = 3$  state of Rb splits into seven sublevels  $M_F = -3, -2, \dots, 2, 3$ . The Zeeman splitting between  $F = 3, M_F = 3$  and  $F = 3, M_F = -2$  sublevels, described by the Electron-Paramagnetic Resonance frequency  $\mu_{EPR}$ , is proportional to the magnitude of the  $\vec{B}$  field. When  $^3\text{He}$  nuclei are polarized, their spins can generate a small magnetic field  $\vec{B}_{^3\text{He}}$ , in addition to the main holding field  $B_H = 25$  Gauss. The EPR measures this small component of the Zeeman splitting  $\delta\mu_{EPR}$ , which is proportional to the polarization of  $^3\text{He}$ . The EPR frequency can be decomposed as

$$\mu_{EPR} = \mu_0 \pm \delta\mu_{EPR}, \quad (4.26)$$

where  $\mu_0 \propto B_H$  and  $\delta\mu_{EPR} \propto B_{^3\text{He}} \propto P_{^3\text{He}}$ , with  $+(-)$  sign corresponds to the  $^3\text{He}$  spin being antiparallel (parallel) to the main holding field.

Since the measurement frequency shift  $\delta\mu_{EPR}$  is a small component compared to the main component  $\mu_0$  generated by the main holding field, during an EPR measurement the  $^3\text{He}$  spins are reversed by AFP. During a spin reversal the large component  $\mu_0$  cancel and the frequency shift  $\delta\mu_{EPR}$  is measured directly.

As described previously, in an external magnetic, the energy levels of the Rb and K atoms present in the

target chamber are split when the target is placed in a magnetic holding field. For Rb, the  $F=3$  ground state splits into seven sub-levels  $m_f = -3, -2, ..2, 3$ . Here  $F$  is the total angular momentum quantum number. The splitting corresponds to a frequency which is proportional to the holding field,  $\nu_0 = \gamma B_0$ , with  $\gamma = 0.466\text{MHz/G}$  for Rb atom. A shift in this frequency occurs due to the small effective magnetic fields created by the spin exchange mechanism of Rb-K and K- $^3\text{He}$ , and also due to the polarization of  $^3\text{He}$  nuclei itself. This shift in frequency is known as the EPR frequency shift ( $\Delta\nu_{EPR}$ ).

We can measure the contribution of  $^3\text{He}$  spins to the shift in the EPR frequency by reversing the direction of the  $^3\text{He}$  spins. This can be done by sweeping the RF field at AFP conditions at constant holding field. The shift in frequency due to  $^3\text{He}$  spins is of the order of few tens of kiloHertz in our case, and can easily be measured. The following equations (Eq. 4.27 to Eq. 4.29) show various contributions to the EPR frequency shift in two opposite states and how the difference in EPR frequency is related to only the  $^3\text{He}$  contribution.

$$\Delta\nu_+ = \Delta\nu_{He} + \Delta\nu_{SE} + \Delta\nu_B \quad (4.27)$$

$$\Delta\nu_- = -\Delta\nu_{He} + \Delta\nu_{SE} + \Delta\nu_B \quad (4.28)$$

$$\Delta\nu_+ - \Delta\nu_- = 2\Delta\nu_{He} \quad (4.29)$$

where  $\Delta\nu_{He}$  is contribution from  $^3\text{He}$  spins,  $\Delta\nu_{SE}$  is the spin-exchange contribution and  $\Delta\nu_B$  is the contribution from the holding field to the frequency splitting,  $\Delta\nu$ . This change in the frequency is related to the polarization of the  $^3\text{He}$  by the following equation [84]

$$\Delta\nu_{EPR} = \frac{8\pi}{3} \frac{d\nu_{EPR}}{dB} \kappa_o \mu_{He} \eta_{He} P, \quad (4.30)$$

where  $\kappa_o \equiv \kappa_o(T) = \kappa_{oo}(T_{ref}) + \kappa_{oT}(T - T_{ref})$  is a dimensionless quantity for spin-exchange that depends on the geometry and temperature of the cell.  $\frac{d\nu_{EPR}}{dB}$  can be calculated from the Breit-Rabi equation.  $P$  is the polarization of the  $^3\text{He}$  in the cell,  $\eta_{He}$  is the  $^3\text{He}$  density, and  $\mu_{He} = 6.706984 \times 10^{-14} \text{MeV/T}$ . The value of  $\kappa_{oT}$  is known at temperatures around  $170^\circ$ . This value is extrapolated to the operating temperature of  $255^\circ$ , resulting in large uncertainties. Therefore  $\kappa_{oT}$  presents the largest uncertainty in the polarization measurement using EPR.

In order to measure  $\Delta\nu_{EPR}$  of Rb, an RF field corresponding to the energy difference between  $m_F = -3$  to  $m_F = -2$  ground state sublevels has to be applied to the target. This increases the number of electrons in the  $m_F = -2$  sublevel. Since they absorb the photons from the circularly polarized laser light, these electrons get excited to the  $P_{1/2}$  state. As they decay back to the ground state ( $S_{1/2}$ ), there is an increase

in the number of photons emitted which can be detected by a photodiode. This is the  $D_1$  transition with a wavelength of 795 nm. Whereas the energy difference between  $S_{1/2}$  and  $P_{3/2}$  is called  $D_2$  (780 nm) transition. A thermal mixing between energy levels can cause electrons in the  $P_{1/2}$  state to mix with the  $P_{3/2}$  state and later decay back to  $S_{1/2}$  state as a  $D_2$  transition. This will release some  $D_2$  light. A  $D_2$  filter is used in front of the photodiode to separate  $D_2$  light from  $D_1$  light. For an EPR measurement, the  $^3\text{He}$  spins are flipped by sweeping the RF field (typically used for an NMR sweep) through resonance and measuring the change in the EPR frequency. A typical EPR spectrum is shown in Fig.4.13.

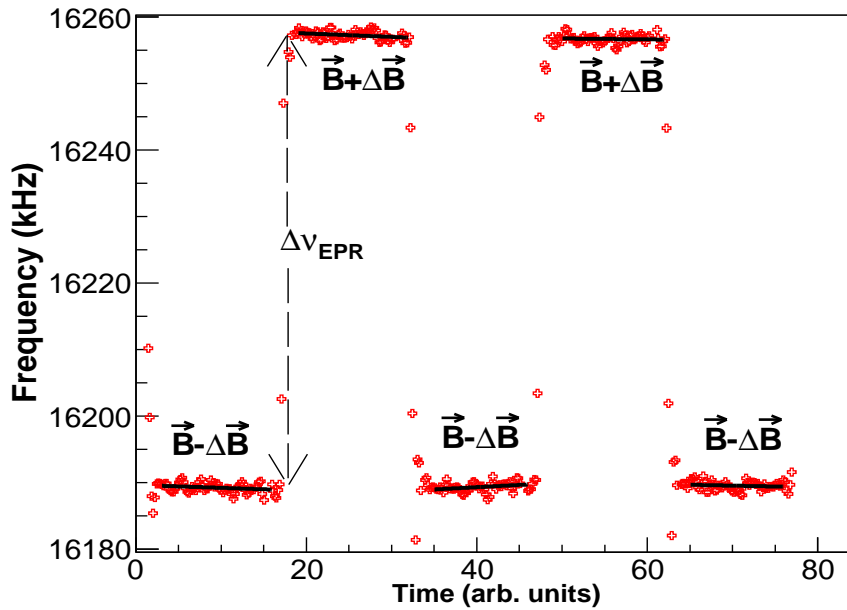


Figure 4.13: EPR spectrum showing the  $^3\text{He}$  spin states when they are anti-parallel ( $\vec{B} - \Delta\vec{B}$ ) and parallel ( $\vec{B} + \Delta\vec{B}$ ) to the holding field direction.

The extraction of the absolute polarization of  $^3\text{He}$  from EPR measurement can be done in two ways. The *Direct method* evaluates directly the absolute holding field at each frequency state and uses the magnetization of  $^3\text{He}$  to extract the polarization. The *Derivative method*, on the other hand, uses the frequency difference between the two states (original and flipped) of the  $^3\text{He}$  spins and the derivative of the frequency with respect to the holding field to calculate the polarization. Both method were used for the analysis to cross check the polarization number and they were quite consistent.

### 4.5.5 Target Spin Flip System

In this experiment, an automatic target spin-flip system was setup by Jin Huang (PhD student from MIT), the purpose of the automatic spin-flip system is to reduce the systematic uncertainties associated with the target and to get rid of any biases related to the DAQ. During Experiment E06-010, the spin of the  $^3\text{He}$  target was flipped once every 20 minute which had been tested to be balanced with the polarization loss during the target spin flip every time. The NMR signal generated was recorded during spin-flip, and the polarization of the target is measured by NMR during the experiment, so the polarization of the target is based on every spin state. Meanwhile, a spin-flip signal provided by the spin flip system to gate the scalers based on the target spin state. Then the accumulated charge and triggers provided by spin state based on target-spin gated scalers will be used for normalization of the experiment during the data analysis.

By rotating all the quarter wave plates, the polarization of the incoming lasers to the cell can be reversed when the  $^3\text{He}$  spins were flipped from one state to another by  $180^\circ$ . For every event, there is a marked target spin flag by the main DAQ system after the main DAQ received the spin state information which was sent by target spin state. During the spin flip, the NMR signal were collected and processed for confirming the spin state by the system.

The target spin flip consequence was controlled by the target spin flip system. The target spin flip system can acquire and record target spin state, output target spin related information into DAQ system therefore merge into event data stream, have a good interaction with human (Target Operator), and communicate with related target software/hardware.

All the quarter wave plates were monitored in each spin flip and can be seen in GUI during experiment E06010 in order to make sure the stability of the system.

### Measurement of Holding Field Direction

In order to find the right polarization for  $^3\text{He}$  target and the reference targets, the measurement of holding field direction should be carefully performed. In this experiment the  $^3\text{He}$  nuclei are polarized in two ways, one is in vertical (normal) direction, the other is in `transverse_in_plane` (sideways) direction with respect to the scattering plane which is determined by the vectors representing incoming and scattered lepton. The direction of the  $^3\text{He}$  spins was aligned with the magnetic field direction. Therefore it is mandatory to accurately measure the direction of the holding field generated by the Helmholtz coils in the target region.

There are two different methods to determine the direction of the magnetic field in the target region. One is for `transverse_in_plane` direction and one is for vertical direction respectively. In order to measure the `transverse_in_plane` field direction, a bar magnet was placed near the target region and the angles were

surveyed by the Jefferson Lab survey group. Using this information combined with the values of exact currents in the Helmholtz coils, the transverse\_in\_plane field direction was determined. In order to measure the vertical field direction, a vertical compass was designed and constructed. This is a flotation device, consisting a magnetic cylinder with an ability to float on air when pressurized air flows through the system. An optical encoder was attached to the cylinder to record the rotations. First, the compass assembly was placed in the target region and nitrogen gas was allowed to flow into the system so that the magnetic cylinder floats. Then the vertical field was turned on and values of the encoder readings were recorded. This procedure was repeated after rotating the entire assembly to  $180^\circ$ . Using this information the vertical field direction was determined [113].

## 4.6 The electron arm: BigBite spectrometer

In order to identify the coincidence scattered electrons and reach a large coverage of momentum and out-of-plane angles, the BigBite spectrometer was used and located at a related short drift distance of 1.50 m. Three sets of wire chambers were used to provide tracking information followed by a pre-shower, scintillator and shower assembly to provide trigger and particle identification for the electrons.

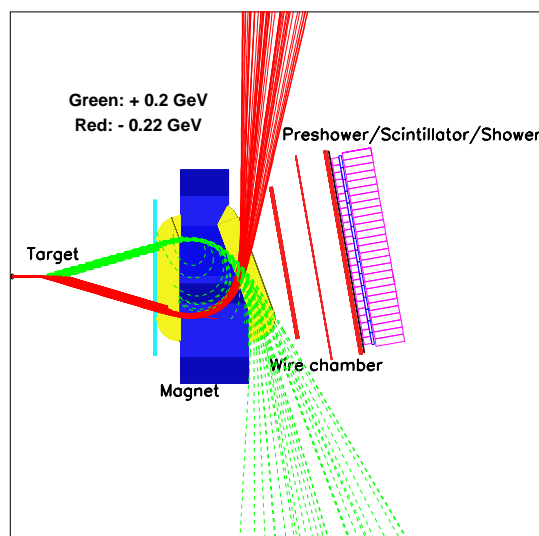


Figure 4.14: Charged particle trajectories through the BigBite magnet. Positive particles with momentum less than 200 MeV/c and negative particles with momentum less than 220 MeV/c did not reach the detectors. The location of wire chambers, pre-shower, trigger scintillator planes and shower lead glass arrays are also indicated.

The BigBite magnet dipole was installed before the three wire chambers to bend the incident particles passing through the BigBite collimator with different charges and different momentums in different directions and different trajectories. Using 710A current to energize the BigBite magnet, a 1.2 T magnetic field to

bend different particles in different trajectories, as shown Fig. 4.14. The momentum coverage was 0.6-2.5 GeV. The average solid angle acceptance was about 64 msr.

During Experiment E06010, a metal plate of 2 inch thickness was installed to shield background particles and the target from the fringe magnetic field from the BigBite magnet, as shown in Fig. 4.15. In addition, a short gas Cherenkov detector was installed for another experiment E06-014. The data taken from this short gas Cherenkov detector were not used in the analysis of this experiment. Finally, two target collimators were installed on the BigBite side to shield the high energy electrons/photons generated from the two endcaps of the target scattering chambers.

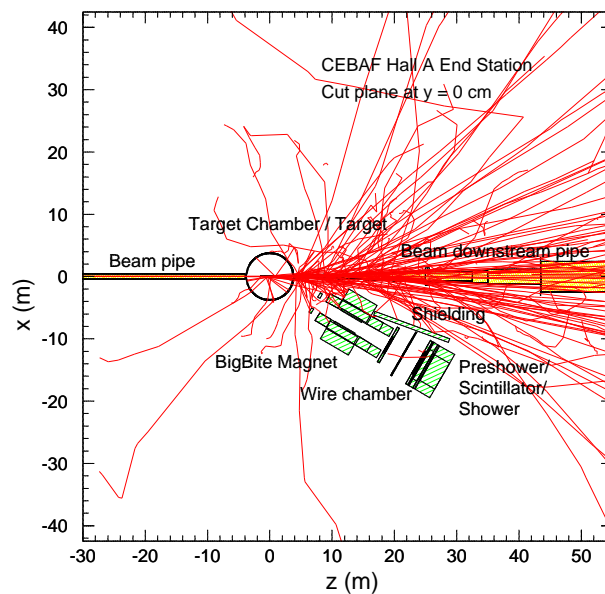


Figure 4.15: Simulation of particle trajectories. Most of the low-energy background particles can be shielded from hitting the Bigbite wire chambers by a 2 inch metal plate downstream of the target.

The coordinate systems relevant to the BigBite spectrometer are defined below.

- **Lab coordinate system:**

$z$  is along the beam direction

$y$  is against gravity

$x$  is to the left when looking in the beam direction

- **Magnet coordinate system:**

$x$  is to the right when facing the magnet

$y$  is against the gravity



$z$  is  $x \times y$

- **Detector coordinate system:** The origin is specified by the center of first wire chamber.

$x$  is pointing down from the center of the chamber

$z$  is the nominal direction of the particle passing through the detector

$y$  is  $z \times x$

The three sets (U-U', V-V' and X-X') of Multi Wire Drift Chambers (MWDCs) including 18 wire planes were used to provide tracking information for the charged particles entering the BigBite detector system. Each wire chamber consists of six wire planes, divided into three groups with orientations of  $u$  ( $+30^\circ$  with respect to the horizontal direction),  $v$  ( $-30^\circ$ ) and  $x$  ( $0^\circ$ ), as illustrated in Fig. 4.16. The distance between two adjacent wires in a single wire plane is 1 cm. The second plane, usually labeled with prime ( $u$ ,  $v$  and  $x$ ) is shifted by half of the wire cell (0.5 cm) to resolve the left and right ambiguities.

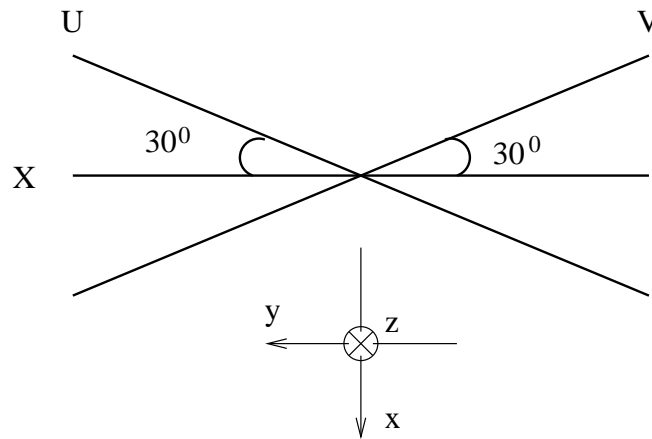


Figure 4.16: Illustration of the Multi Wire Drift Chamber (MWDCs) plane orientations:  $u$ ,  $v$ , and  $x$ . The corresponding second plane is shifted by half of the wire cell (0.5 cm), not indicated.

When a charged particle travels through the chamber, it ionizes the gas inside the chamber and leaves behind a track of electrons and ions along its trajectory. The gas supplied to the MWDCs is a 50%/50% argon-ethane ( $C_2H_6$ ) mixture with a flow rate of 10 liter/hour [88]. The ionization electrons accelerate toward the wires along the electric field. The time the electron takes to reach the wire is proportional to the distance traveled. Through the electronics read-out system, the trajectory of the traveled charged particle were precisely determined.

The BigBite scintillator plane was to provide the BigBite timing information and was installed in between the preshower and shower detectors, the scintillator consists of 13 plastic scintillator bars. Two PMTs are fixed to both sides of each scintillator bar in order to collect the signal. Each bar is 60 cm (length)  $\times$  17.5 cm (width)  $\times$  3.8 cm (thickness), as shown in Fig. 4.17.

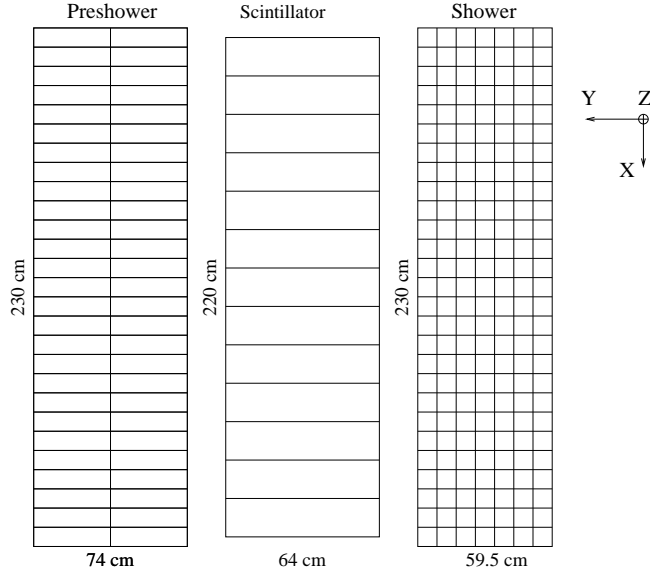


Figure 4.17: Geometry of BigBite PreShower, Scintillator, and Shower detectors

The BigBite scintillators provided an accurate timing information of the particles entering the BigBite, which is used together with the corresponding timing of the S2m scintillators to get the coincidence time-of-flight in the HRS. In other words the difference in the time of hit of a particle in the BigBite and the corresponding hit in the HRS gives the coincidence time-of-flight in the HRS. This is very crucial for the particle identification in the hadron spectrometer, as there is a slight difference (on the order of few ns) between different particles travelling 26 m in the HRS, before hitting the detector.

The preshower and shower detectors provide the electron particle identification (PID) in the BigBite. They also provide the trigger for the BigBite spectrometer. The preshower blocks are made of TF-5 lead-glass blocks, each measuring  $8.5 \text{ cm} \times 34 \text{ cm} \times 8.5 \text{ cm}$  in the X, Y, and Z directions, respectively. There are 54 preshower blocks arranged in two columns of 27 rows each. It has an active area of  $210 \times 74 \text{ cm}^2$ , with 8.5 cm (3 radiation lengths) along the particles direction. The shower blocks are made of TF-2 lead-glass material, each measuring  $8.5 \text{ cm} \times 8.5 \text{ cm} \times 34 \text{ cm}$  in the X, Y, and Z directions, respectively. It covers an active area of  $221 \times 85 \text{ cm}^2$ , with 34 cm (13 radiation lengths) along the particles direction. There are 189 shower blocks arranged in 7 columns of 27 rows each. Particles entering the lead-glass block generate electromagnetic showers and leave a large signal in the PMT, which is amplified and sent to the summing modules for making a trigger. The signals are also recorded in ADCs. The combined ADC information from both preshower and shower detectors gives the total energy deposited by the particle. The reconstructed energy has a resolution of about  $\Delta E/E = 8\%$ . The signal generated by electron is large compared to hadrons. Based on this difference in the response of the different particles in the detector, the hadrons and electrons

were cleanly separated.

## 4.7 The hadron arm: the left HRS

My major hardware efforts on Experiment E06-010 focus on the left HRS. With Vincent Sulkosky (Postdoctoral with JLab HallA) I worked on S1, S2m, gas Cherenkov detector. I also participated in the pion rejectors cabling and electronics, and on aerogel Cherenkov detector A1 with Bogdan Wojtsekhowski (staff scientist at JLab HallA). I have worked extensively on the RICH detector with Alexandre Camsonne (Postdoctoral with JLab HallA) and Evaristo et al. (Italian RICH group). Fig. 4.18 shows the left HRS, where I spent my efforts before and during the experiment E06-010.

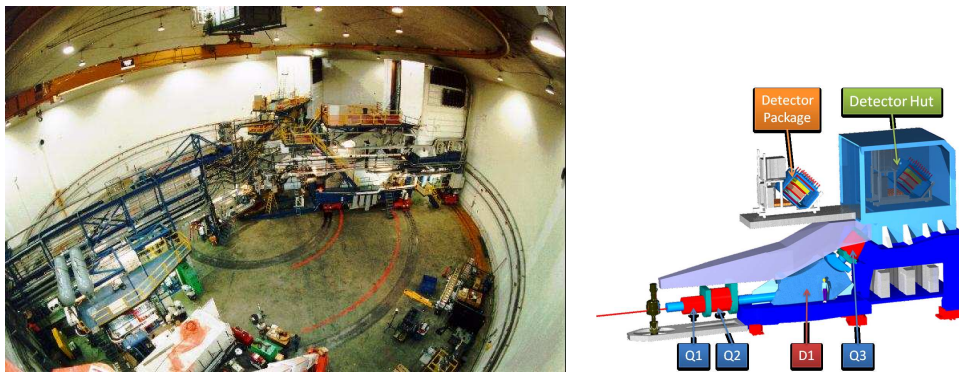


Figure 4.18: Left panel: Overview of Hall A. Right panel: 4 magnet and Detector Package and Detector Hut of the left HRS.

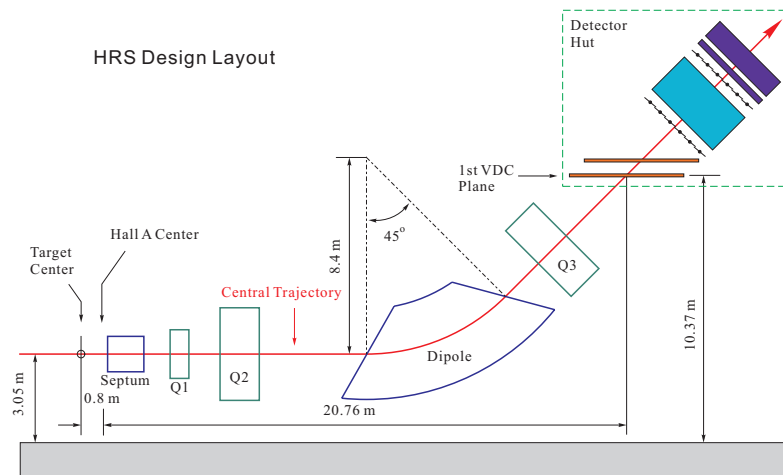


Figure 4.19: Diagram of the left HRS and its hut

### 4.7.1 Overview of the Left High Resolution Spectrometer

The left High Resolution Spectrometer (HRS) is part of the standard equipment in Hall A. There are two identical HRSs in the Hall. For this experiment, the left HRS was used for detecting the produced hadrons (for example, pions, kaons, and protons). The HRS consists of three quadrupole and one dipole magnets in a QQDQ configuration [88]. The layout of the magnets in the HRS is shown in Fig. 4.19. It focuses the charged particles within a small momentum and angular range to the detectors. The relative momentum resolution can reach up to  $2 \times 10^{-4}$  and the central momentum in the spectrometer is determined by the magnetic field of the dipole. In Experiment E06-010, the central momentum was set at 2.35 GeV in production runs. The configuration of detectors in the left HRS is shown in Fig. 4.20. The main characteristics of the spectrometers are shown in Table 4.7.1.

Table 4.6: Hall A HRS general characteristics.

|                                      |                      |
|--------------------------------------|----------------------|
| Momentum range $p$                   | $0.3 \sim 4.0$ GeV/c |
| Configuration                        | $QQD_nQ$             |
| Bending Angle                        | $45^\circ$           |
| Optical Length                       | 24.2 m               |
| Momentum Acceptance ( $\delta p/p$ ) | $\pm 4.5\%$          |
| Momentum Resolution                  | $1 \times 10^{-4}$   |
| Dispersion at the focus (D)          | 12.4 m               |
| Radial Linear Magnification (M)      | -2.5                 |
| D/M                                  | 5.0 m                |
| Angular Range                        | $6 \sim 12.5^\circ$  |
| Angular Acceptance Horizontal        | $\pm 25$ mrad        |
| Angular Acceptance Vertical          | $\pm 50$ mrad        |
| Solid Angle $\Delta\Omega$           | $\sim 6.7$ msr       |
| Angular Resolution Horizontal        | 1.5 mrad             |
| Angular Resolution Vertical          | 4.0 mrad             |
| Transverse Position Resolution       | 2.5 mm               |

The left HRS spectrometer needs to provide a trigger to activate the data-acquisition electronics, collecting tracking information (position and direction), coincidence determination, and identification of the out-going particles.

The detector package of the left HRS was used to detect and identify produced kaons, pions, and protons. It includes:

- a set of two Vertical Drift Chambers (VDCs) to provide tracking (position and direction) information,
- a scintillator plane S1 to provide the basic trigger,

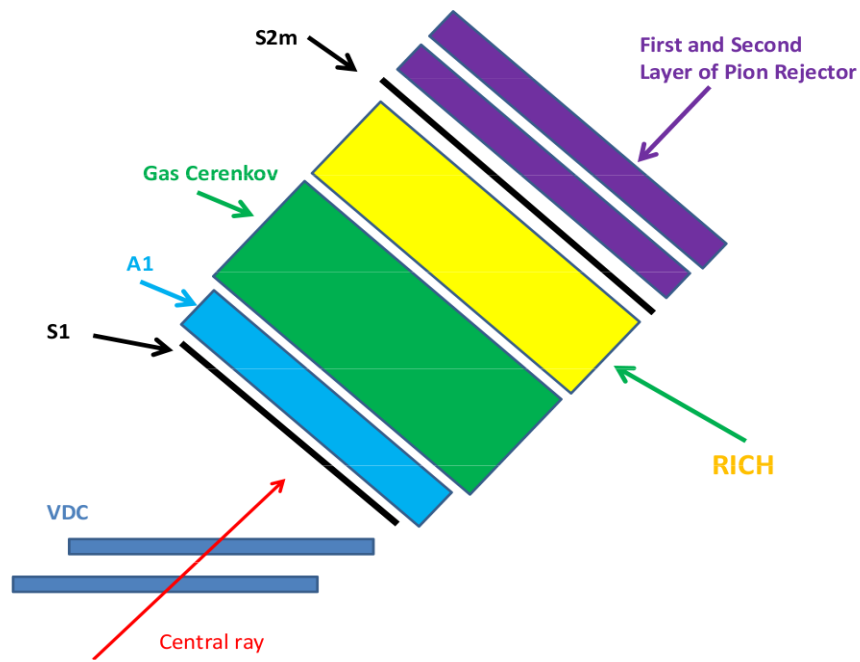


Figure 4.20: Arrangement of the detectors in High Resolution Spectrometer during the E06-010 experiment. The figure is reproduced from [111]

- an aerogel Cherenkov detector for particle identification (PID),
- a CO<sub>2</sub> gas Cherenkov detector for PID (to get rid of electrons),
- a ring imaging Cherenkov detector (RICH) for hadrons PID,
- a high resolution scintillator plane S2m to provide the trigger and precise timing information and the time-of-flight (TOF).
- a pair of lead glass pion rejectors for PID (to get rid of electrons).

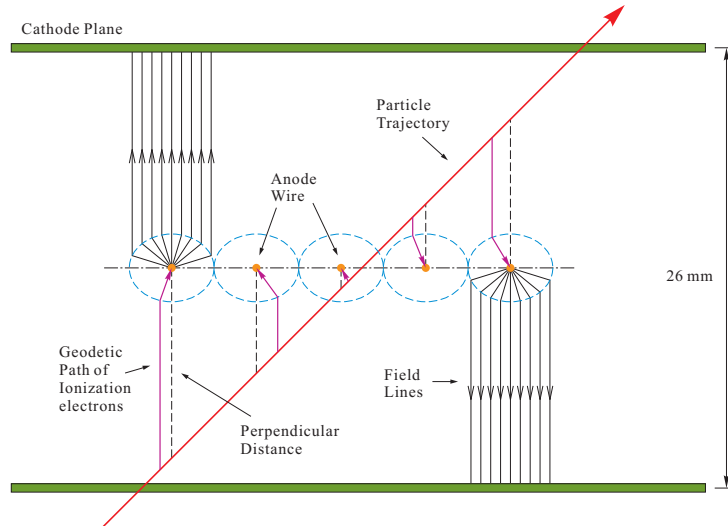


Figure 4.21: Configuration of left HRS Wire Chambers, from [66]

### 4.7.2 Vertical Drift Chambers

The two Vertical Drift Chambers (VDC) [89] [90] provide a precise measurement of the positions and angles of the out-going charged particles at the spectrometer focal plane. Each VDC is composed of two wire planes laid horizontally. The wires of one plane are perpendicular to those of the other plane, and are oriented at an angle of  $45^\circ$  with respect to the dispersive and non-dispersive (transverse) directions. The out-going particle trajectory travels across the wire planes at an angle of  $45^\circ$ , as shown in Fig. 4.21.

During Experiment E06-010, the VDC chambers have their cathode plane at about -4kV and the wires at ground. The gas supplied to the VDCs is a 62%/38% argon-ethane mixture, with a flow rate of 10 liters/hour [91]. The Hall A VDCs feature a five cell design, i.e. a typical  $45^\circ$  track will fire five wires as shown in Fig. 4.21. The fired wires are read out with Time-to-Digital converters (TDCs), which are started by the triggered wire and stopped by the event trigger supervisor. In this configuration, a smaller TDC signal corresponds to a longer drift time. With a  $50\mu\text{m}/\text{ns}$  drift velocity and time shift constants the distances of the track to each fired wire are precisely reconstructed. The position and angles of the track are then determined.

### 4.7.3 Two Scintillator Planes S1 and S2m

There are two trigger scintillator planes S1 and S2 in left HRS, separated by a distance of about 2 m. In Experiment E06-010, due to the requirement of precise timing information and coincidence time-of-flight (TOF), a high resolution trigger scintillator plane S2m [92] was installed in left HRS instead of the standard trigger scintillator plane S2. The S1 is composed of six overlapping paddles made of thin plastic scintillator

(5 mm BC408) to minimize hadron absorption. Each scintillator paddle has an active area of  $29.5 \times 35.5 \text{ cm}^2$  and is viewed by two photomultiplier tubes (PMTs) (Burle 8575). The S2m has sixteen counters: ( $43.2 \text{ cm} \times 5.1 \text{ cm} \times 14.0 \text{ cm}$ ). Each counter is viewed from both ends by a 5.1 cm photonis PMT XP2282B [93]. The sixteen paddles (fast plastic scintillator EJ-230) are arranged without overlap. The signal-path for S2m was designed so as to best preserve the timing of the pulses. The signals from each PMT were sent to a passive 90/10% splitter, with the greater portion sent to a P/S 706 discriminator on the detector frame and the lesser portion sent to the Fastbus ADCs. To form S2m's contribution to the trigger, the first discriminator output for each paddle's left- and right-side PMTs are logically AND'ed, and an OR over these results is performed. The right-side PMTs determine the timing of this trigger since their trigger-cables from the discriminator are 30 ns longer than those for the PMTs on the left side. The second output from the discriminator is sent through a NIM-ECL converter and an active ECL-delay module before being readout by Lecroy 1877A TDC modules set to 50 ps/channel.

In order to minimize the jitter of the trigger-gate timing, the gate for the spectrometer is "retimed" by forming a logical AND of the trigger from the Trigger Supervisor and the input of the local S2m-plane to the trigger. This gate is then used to control the TDC and ADC digitization and readout. A copy of this gate is also sent to the BigBite, where the relative timing between the gates of the left HRS and BigBite are measured by a TDC. This is performed for left HRS and BigBite, so there is a redundant readout of the relative timing of the gates.

The replacement of scintillator S2 by high resolution scintillator S2m is crucial to improve the intrinsic timing resolution of the trigger plane. It can also improve the signal pathway for measuring the relative timing of left HRS and BigBite.

#### 4.7.4 Gas Cherenkov Detector

The Gas Cherenkov detector is based on the Cherenkov effect [94,95]. It was installed in left HRS to get rid of electrons especially when left HRS was in negative polarity. The gas is  $\text{CO}_2$ , when at normal pressure, the refraction indice is  $n=1.00041$  which gives a threshold momentum  $\sim 17 \text{ MeV}/c$  for electrons and  $4.8 \text{ GeV}/c$  for pions. During Experiment E06-010, the central momentum was set at  $2.35 \text{ GeV}/c$ , so only electrons emit light and generate ADC signal.

The gas Cherenkov detector is made of 10 PMTs (type Burle 8854) and 10 mirrors [96]. The PMTs have a spherical entrance window of 129 mm of diameter. Only a spherical part of 110 mm of diameter is efficient to collect light reflected from the mirrors. The photocathode is made of Bialkali with a quantum efficiency of 22.5% at 385 nm and an extended response in the UV until 220 nm. Each mirror has a rectangular profile

built in an empty sphere of interior radius (reflective face) of 900 mm and thickness of 10 mm. The 10 mirrors are placed just before the output window and are grouped in two columns of 5 mirrors. Each mirror reflects the light onto a PMT placed at the side of the box. The mirrors of the same column are identical and the two columns are almost symmetrical. Positions and angles of the PMTs are not placed regularly like for the mirrors, but were adjusted by an optical study in order to maximise the collection of light coming from the particular envelope of particle which are detected by the HRS. PMTs are fixed and mirrors can be adjusted by hand. The light is converted to electronic signals by PMTs and fed to ADCs. The summed signal of all ten ADCs gives information about the total light emitted by the charged particle.

Though pions themselves in this momentum setting cannot produce any Cherenkov light directly, they can interact with the material they pass through and create lots of  $\delta$ -electrons [97]. These  $\delta$ -electrons can produce Cherenkov light and trigger the ADCs. Fortunately, these pion events can be removed with the selection of coincidence events between left HRS and BigBite which will be described later.

#### 4.7.5 Aerogel Cherenkov Detector

The Aerogel Cherenkov detector [98] is also a threshold Cherenkov detector. It is one of the crucial detectors to identify different hadron types. In Experiment E06-010, A1 was installed in the left HRS to identify pions, kaons, and protons. Before being installed, A1 had been tested using cosmic rays to replace bad PMTs in the EEL building. The refraction index of A1 is 1.015, hence pions can emit Cherenkov light (pion momentum threshold is at 0.8 GeV/c) but kaons cannot emit Cherenkov light (which requires kaon momentum higher than 2.8 GeV/c) during Experiment E06-010 when momentum was set at 2.35 GeV/c. Other relevant parameters [112] of A1 include the followings: radiator area is 32 cm  $\times$  170 cm, radiator thickness is 9 cm, diffusion reflector is 0.22  $\mu$ m Millipore paper, the PMT type is RCA 8854. The average number of photoelectrons (NPE) for  $\beta = 1$  particle is bigger than 6.

For A1, a diffusion technique of light collection was evaluated in Refs. [100–102]. In order to build aerogel detector with good performance, the following procedure has been performed:

- minimize the distance from aerogel to PMTs, e.g. to avoid if possible individual magnetic shield on PMT,
- minimize overall surface area of the diffusion (PMT) box,
- cover all “black” areas by Millipore, including outer edge of PMT,
- two layers of Millipore paper backed by white paper,



- detector made of two separable assemblies for PMTs and aerogel,
- vacuum lift for handling fragile aerogel material,
- tight packing of the aerogel blocks,
- avoid parasitic radiators in the path of particles.

The phenomenological expression for the average NPE. is

$$NPE = L \left(1 - \frac{1}{\beta^2 n^2}\right) \frac{\epsilon}{1 - \eta(1 - \epsilon)} \quad (4.31)$$

Where L is the effective thickness of the aerogel,  $\epsilon$  is the refraction of the light box covered by PMTs and  $\eta$  is the average reflectivity of the light box area.

The number of photons is related to the wavelength of the photons ( $\lambda$ ) and charge number of the material element ( $z$ ), as

$$\frac{d^2 N}{dz d\lambda} \propto \frac{z^2}{\lambda^2} \left(1 - \frac{1}{\beta^2 n^2(\lambda)}\right) \quad (4.32)$$

where n is the refractive index and  $\beta$  is the relativistic velocity  $\frac{v}{c}$ . Again, even though the kaons and protons cannot fire A1, the  $\delta$ -electrons they produced can fire A1. Fortunately the coincidence time-of-flight (TOF) can separate scattered electrons from  $\delta$ -electrons produced by kaons and protons.

#### 4.7.6 RICH Detector

The Hall A Ring Imaging Cherenkov (RICH) detector was mainly designed based on the ALICE-HMPID (High Momentum Particle Identification) RICH [103]. It was first installed in JLab Experiment E94-107 [104] and has been upgraded to extended the momentum range to about 3 GeV/c. The RICH has a proximity focusing geometry, The 300 nm thick CsI photocathode is obtained by vacuum evaporation.

Fig. 4.22 [105] shows the working principle of the RICH detector. The Cherenkov effect takes place in the liquid freon when a charged particle crosses it. The liquid radiator, 1.5 cm thick, is housed in a vessel made of NEOCERAM<sup>1</sup> on all sides but the exit window which is made of pure quartz, 0.5 cm thick. The use of a liquid radiator has been imposed by the momentum range (around 2 GeV/c) of the particles to be identified. The Cherenkov photons, emitted along a conic surface, are refracted by the freon-quartz-methane interfaces and strike a pad plane after traveling a proximity gap of 175 mm filled with methane.

---

<sup>1</sup>NEOCERAM is a glass-ceramic material with mechanical and thermal properties almost identical to quartz.

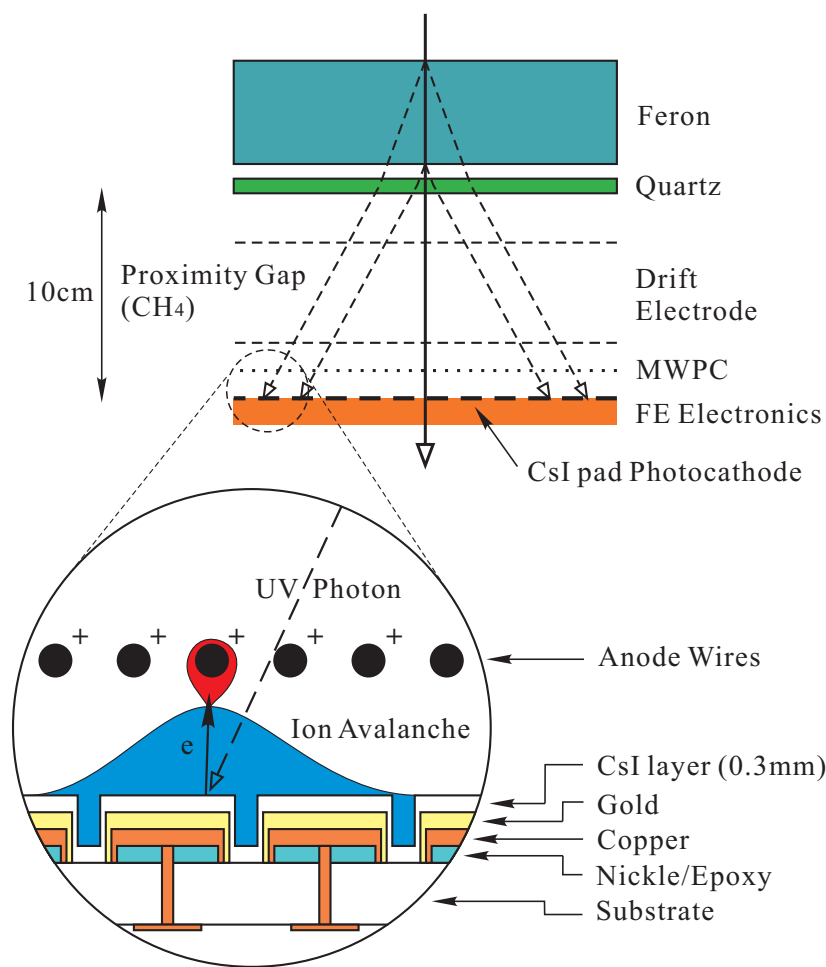


Figure 4.22: Schematic diagram of RICH detector

The pad plane is covered by a thin substrate of CsI which acts as photon converter. The emitted photoelectron is accelerated by an electrostatic field (2200V/2mm) between the pad plane and an anode wire plane in front of the pads, from a MWPC (Multi Wire Proportional Chamber). While the anode wires collect the electron avalanche, the counterpart ions are collected by clusters of pads, each of which is connected to the input channel of a multiplexed sample-and-hold electronics, housed on the back of the pad plane. At the end of this process, the clusters of pads hit by the photons should be scattered on a ring (ellipse) while one cluster coming from the ionized electrons of the charged particle track should be located in the central region of the ring. A drift electrode operated at 200V and located close to the quartz window, prevents electrons produced by ionization of the counting gas by charged particles in the proximity gap from reaching the MWPC.

The main components of the RICH are the liquid radiator, the gas system, the photon detector subsystem, and the readout electronics.

- The Liquid Radiator

A freon recirculating system provides a pure and stable liquid radiator; filtering and refilling stages keep the high solubility and volatility of the freon itself under control. The transparency of this radiator is very low for wavelengths below 160 nm and therefore cuts out those photons. The purity of the freon, one of the important parameters to control, is monitored continuously.

The  $C_6F_{14}$  radiator vessel represents a critical part in the detector design. The rather high perfluorohexane and silica glass densities, 1.68 g/cm<sup>3</sup> and 2.1 g/cm<sup>3</sup> respectively, and the need to avoid pollution from the material in contact with the liquid radiator that would affect the transparency in the 160-220 nm band, required careful investigation and optimization.

The liquid radiator container consists of a tray made of NEOCERAM closed by a UV-grade fused silica plate. Their thickness and size have been carefully optimized by investigating the best compromise between the detector total radiation length and the perfluorohexane hydrostatic pressure. NEOCERAM is a glass-ceramic material, thermally compatible with the fused silica (thermal coefficient  $0.5 \times 10^{-6} K^{-1}$ ). The vessel elements are glued together with Araldite AW106. The liquid radiator inlet and outlet are obtained by inserting two stainless steel pipes on the opposite edges of the NEOCERAM tray, the outlet always being at the highest location. To withstand the hydrostatic pressure, cylindrical spacers are glued to the NEOCERAM bottom plate on one side and the quartz window on the other side.

- The Gas System

The RICH detector has to be operated with pure methane to achieve the designed performances. A gas control system has been built, which controls the gas flow, and measures the purity of the gas. Main purpose of this system is to avoid any contamination with oxygen or moisture, that could eventually damage the CsI photocathode.

- The Photon Detector Subsystem

The photon detector is made of a MWPC, with one cathode plane replaced by a pad plane which allows the 2-dim localization of the photon hit. The CsI is evaporated onto the pad surface. At a distance of about 1 m from the pad plane four DC heated tungsten crucibles containing a measured amount of CsI powder are placed. The CsI photon converter enhances the photon-conversion quantum efficiency (QE).

- Readout Electronics

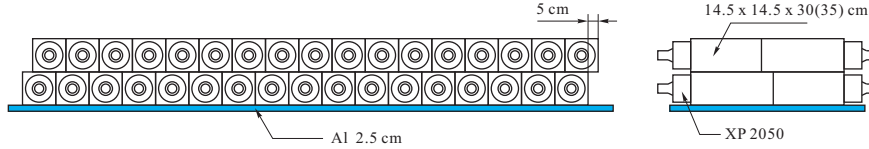


Figure 4.23: Configuration of Pion Rejectors

The set-up of the front-end and readout electronics on the RICH detector is as follows: The front-end is arranged in 40 rows, each consisting of 30 daisy-chained GASSIPLEX chips (one chip reads 16 channels) for a total of 19200 input channels, 480 per row. The charge content of these multiplexed analogue channels is converted by a 10 bit ADC when an experiment trigger is issued. The readout electronics consists of two types of CAEN VME modules: one V551 Sequencer and 20 V550 CRAMS two-channel FADC. When a trigger is asserted, the Sequencer provides at the same time the clock pulse to all the front-end rows and the related convert pulses, phase shifted, to the ADC modules V550. Each ADC channel is connected to a GASSIPLEX row of 480 input channels. The synchronised clock-convert pulses allow each analogue channel to be correctly converted and stored. The V550 CRAMS module is equipped with a zero-suppression circuit which prevents ADC values under a certain threshold, after pedestal subtraction, to be stored in the  $2\text{ K} \times 32$  bit memory locations. This ensures a readout time of  $197\ \mu\text{s}$  for 480 channels including CLEAR and T/H (Trigger/Hold) control signals.

At  $2.35\ \text{GeV}/c$  particle momentum, the expected Cherenkov angles for electrons, pions, kaons, and protons are  $0.680$ ,  $0.677$ ,  $0.652$ , and  $0.583$  rad, respectively. The Cherenkov angle resolution is about  $6\ \text{mrad}$  which gives a  $4\sigma$  separation of pion and kaon peaks at  $2.35\ \text{GeV}/c$  momentum.

#### 4.7.7 Pion Rejectors

The presence of a gas Cherenkov detector in left HRS during Experiment E06-010 means that the pion rejector is not essential for rejecting the electrons for negative polarity setting. However, it can still be combined with other detectors for final particle identification.

The two layers of pion rejectors, which are made of lead glass, are installed at the end of left HRS as the standard configuration of left HRS. The lead glass signal is linearly proportional to the energy of the particle [106]. For momentum around few ( $2.35$ )  $\text{GeV}/c$ , only electrons are able to develop electromagnetic showers, whereas hadronic showers usually do not occur due to the longer hadronic mean free path. Therefore, the particles can be identified according to the energy deposition in the pion rejector: low ADC signal for hadrons and high ADC signal for electrons.

The two layers of pion rejectors have the same geometry [107]. Each layer consists of 17 short blocks

and 17 long blocks of lead glass, forming a 2 (transverse)  $\times$  17 (dispersive) array. All lead glass are oriented transversely with respect to the direction of the particles. Short and long lead glass blocks are arranged interchangeably in the dispersive direction for each row. The gap between blocks of the first layer is covered by a lead glass block of the second layer, and vice versa, as shown in Fig. 4.23.

## 4.8 Trigger and Data Acquisition System

For the DAQ system of Experiment E06010, the triggers for the left HRS, the BigBite, and the coincidence between the left HRS and BigBite, are the three key elements. The scaler, which are used to normalize the experiment, will also be discussed in this section. The DAQ system consists of software and hardware as follows:

1. **The Trigger Supervisor(TS):** This is the key component to control the data acquisition. The TS connected the experiment specific triggering system and the read-out controllers (ROCs), which handle the event-by-event retrieval of the data recorded by the detectors. A 9U multi-functional VME board and several ECL inputs are the components of TS. The eight input channels allowed eight triggers, called T1 to T8. The TS maintained the “*system busy*” signal while a trigger was being processed, and it also accepted and prescaled multiple triggers. It generated a signal from the accepted triggers, for gating and timing of the front-end electronics (ADCs and TDCs), known as level-1 accept (L1A). By using a dedicated RS432 flat cable daisy-chained to all RICs in the configuration, the status of the ROCs was transmitted directly to the TS, and all RICs allowed the TS to monitor the ROCs that were busy. During this time no additional triggers are accepted until all ROCs are finished processing the data. This allows the TS to maintain synchronization between all ROCs [108].

2. **CODA (CEBAF Online Data Acquisition):** CODA is the standard data acquisition software toolkit developed at Jefferson Lab and used by experiments in all three Halls - A, B, and C. It provides several software tools for monitoring and recording data from the experiment. The main component of this system is called *RcServer* which is responsible for storing and initializing the chosen configuration. It also periodically checks the status of all the components and ensures that the recorded data are correct. Several CODA configurations can be created depending on the necessity of using various combinations of the ROCs. All the configurations and the status of the components involved are stored in a MiniSQL database server.

Fig. 4.24 shows the general flow for a simple CODA configuration. The L1A generated from the trigger supervisor causes the front-end electronics to digitize the detector signals and read out the crates. This is

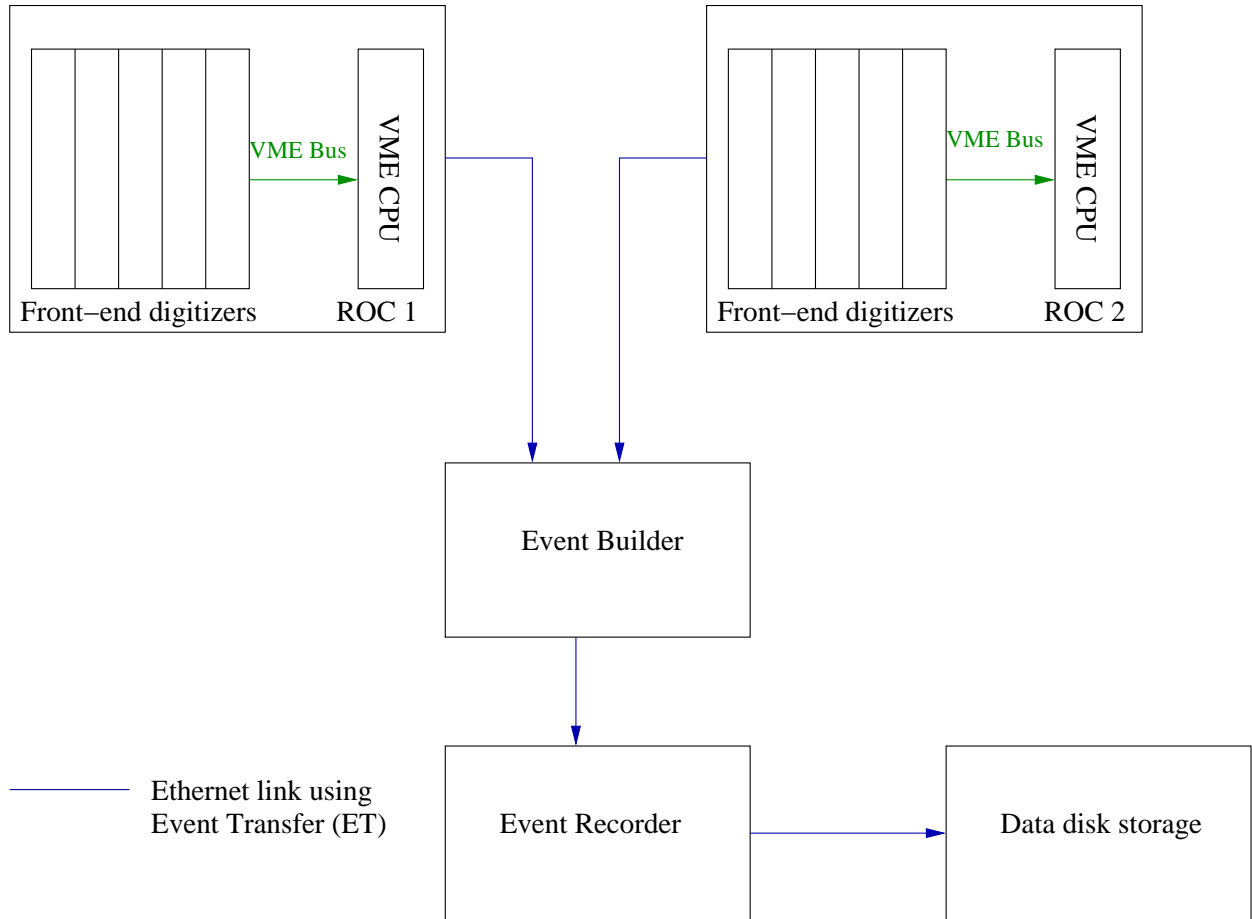


Figure 4.24: Example of CODA configuration using read-out controllers.

achieved by a set of C routines called CODA readout list (crl) which can be programmed by the user. Data from each crate is then transmitted to the Event Builder (EB). The Event Builder collects the data from different crates and sorts them into the structured CODA event. This constructed event is then recorded as a CODA file in the disk by the Event Recorder (ER). The transfer of the data from all the components takes place using the Event Transfer (ET) library.

3. **EPICS and slow controls:** The Experimental Physics and Industrial Control System (EPICS) provides information on the beam, magnets, power supplies, and various other instruments in the accelerator and in the Hall. The information such as beam position, beam current, beam energy, and magnet status, etc., are gathered and written to the CODA datastream once every few seconds. It was also used to retrieve target information such as target oven temperature from the polarized  $^3\text{He}$  target system. In addition, the slow controls were used to set/adjust high voltages of the photo-multiplier tubes on the detectors. A LeCroy 1458 high voltage mainframe was used over the ethernet connection to adjust the high voltages.

### 4.8.1 Trigger and Electronics for BigBite Spectrometer

The BigBite spectrometer was used in this experiment to detect the scattered electrons from DIS reactions, therefore the trigger was designed to select electrons entering the spectrometer. The two lead-glass detectors, preshower and shower, combined to form a full calorimeter to generate the trigger. In order to measure the total energy deposited by a particle in the lead-glass detector, a total hardware sum (TSUM) of the two overlapping rows of preshower ( $2 \times 2 = 4$  blocks) and shower ( $2 \times 7 = 14$  blocks) was formed (see Fig. 4.25). This is done by first summing the signals from two rows of preshower blocks using LeCroy 428F modules, and then summing the signals from two rows of shower blocks using custom built summing modules. The total sum signal (TSUM), combining the preshower signal amplified by five times with the shower signal amplified by ten times, then formed the BigBite trigger.

The TSUM signal is proportional to the total energy deposited by the particle in the calorimeter. This analogue signal then goes through a discriminator. The threshold of this discriminator is controlled remotely and can be adjusted according to the experiment's requirements. This BigBite trigger was known as T1. The detailed trigger logic can be found in Fig. 4.26.

Apart from the T1 trigger, there are other triggers constructed in the BigBite spectrometer for use in parasitic experiments. The T6 trigger was formed similar to T1 trigger, but with a higher threshold. The T7 trigger was formed with Cherenkov signals only, and T2 was formed with an overlap of Cherenkov, preshower and shower signals. The BigBite Cherenkov detector was not used for this experiment, as it was under commissioning and testing during the data-taking period of E06-010.

The BigBite detector signals were read out using both FASTBUS and VME electronics. The timing information from the individual wires in the drift chambers were read out using LeCroy 1877 TDCs. The scintillator time was recorded using F1 TDCs, which were designed at the Jefferson Lab. These are common-stop multihit TDCs with a resolution setting of either 120 ps or 60 ps. For this experiment it was set to 60 ps, since it is necessary to determine the coincidence time-of-flight of the particle in the HRS with high accuracy, in order to improve particle identification. LeCroy 1881 ADCs were used to read all the PMT signals in the calorimeters and scintillators. The ADC gate width was set to 240ns.

**Retiming in the BigBite** When multiple triggers, constructed in different spectrometers, are used in the trigger supervisor, it is necessary to keep the reference timing of the recorded TDC signal in a particular spectrometer constant with respect to the trigger generated in that spectrometer. To achieve this, a re-timing circuit was employed in the BigBite trigger setup to gate the ADCs and TDCs. Fig. 4.27 shows the re-timing circuit. The basic idea of the re-timing circuit in the BigBite spectrometer is that it makes sure

that the L1A generated by the TS has a corresponding T1 trigger by performing an AND logic between T1 and L1A. This way the reference time for the ADC and TDC gates is tied to the T1 trigger. Since the timing for the coincidence trigger (T5) is always given by the leading edge of the T1 trigger, this ensures that all the gates for the T5 trigger have a common reference time. If for some reason there is no T1 for a particular L1A (for example, if the accepted trigger is from the HRS) then a delayed copy of the L1A gives the timing for the gates (see the timing diagram in Fig. 4.27). The width of the T1 trigger was 40 ns and the timing for the ADC and TDC gates was tied to the leading edge of the T1 trigger.



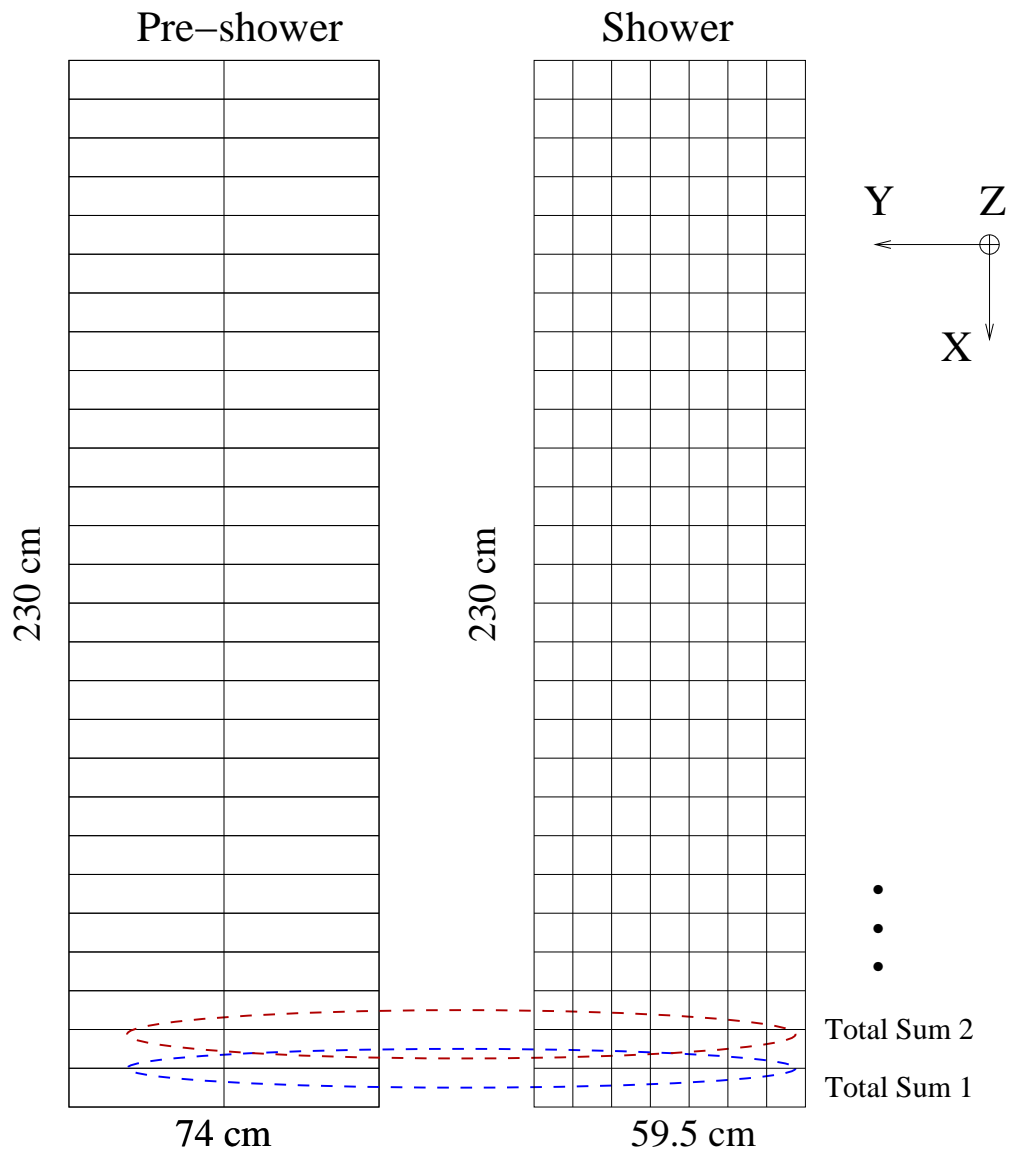


Figure 4.25: Total sum of preshower and shower detectors

BigBite Trigger Logic for Hall A Transversy (E06-010) Experiment

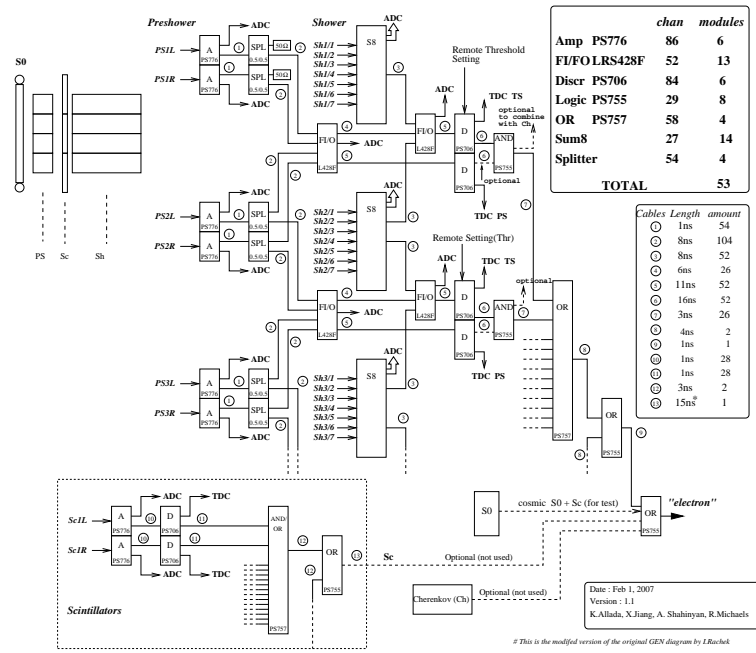


Figure 4.26: BigBite spectrometer trigger logic diagram.

Re-timing Circuit for the BigBite Trigger (E0-6010)

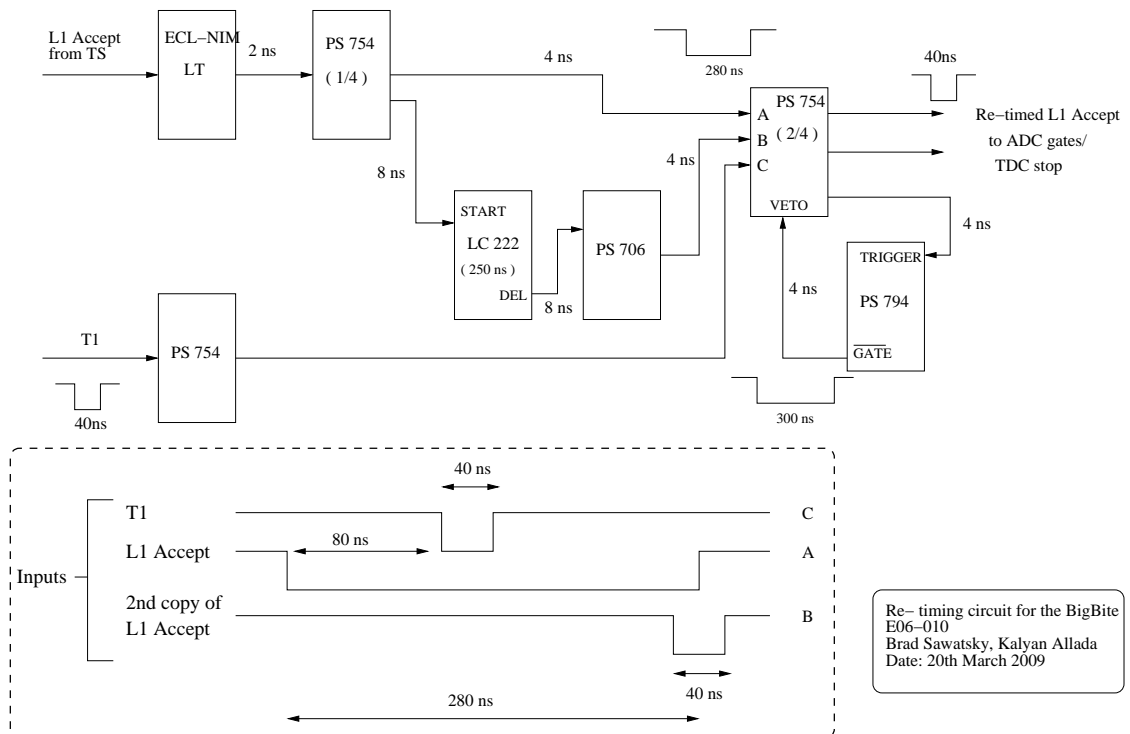


Figure 4.27: Re-timing circuit for the BigBite trigger

## 4.8.2 Trigger and Electronics for the left High Resolution Spectrometer

The left High Resolution Spectrometer (HRS) consists of several types of detectors (see section 4.7) used in the standard Hall A configuration. The RICH detector was added for kaons identification. The trigger diagram for the HRS is shown in Fig. 4.28. The main trigger is formed by requiring that both S1 and S2m scintillator planes have a hit, i.e., one paddle in S1 and one paddle in S2m have a hit on both sides (a total of four PMTs). In order to have a constant reference time, the timing of this trigger was tied to the leading edge of the right side PMT signal of the S2m scintillator paddles. This is usually known as T3 trigger in the spectrometer. A re-timing circuit was used to gate the ADCs and TDCs. The gates for ADCs and TDCs were generated using the L1A signal and the S2m PMT signals.

The signals from the detectors in the spectrometer were read out using FASTBUS electronics. The timing information from S1 and S2m scintillator planes were recorded using high resolution LeCroy 1875 TDCs with the resolution set to 50 ps. These are common-start single-hit TDCs. The signals from individual wires in the VDCs were recorded in common-stop multi-hit LeCroy 1877 TDCs which have a timing resolution of 0.5 ns. The timing information for other detectors like Aerogel (A1), gas Cherenkov, and the two-layer lead-glass detector were recorded using 1877 TDCs. The integrated charge of the signal coming out of the detector is recorded in ADCs. For this experiment LeCroy 1881 ADCs were used for all the detector signals in the spectrometer.

## 4.8.3 Coincidence Trigger

In this experiment scattered electrons were detected in the BigBite and hadrons were detected in the left HRS. A coincidence trigger (T5) between BigBite (T1) and HRS (T3) was constructed by overlapping individual triggers in time. A sketch of coincidence trigger setup between two arms is shown in Fig. 4.29.

In order to construct a coincidence trigger, two quantities should be known - the exact trigger formation time and the time-of-flight of particles, in both spectrometers. The trigger formation time was measured by injecting a fake electronic pulse at a point where a detector PMT signal goes into the trigger circuit, and measuring the time it takes to come out of the circuit. The exact time-of-flight of the particles in both spectrometers can be reconstructed from the kinematics (momentum) of the particle and the distance travelled in the spectrometers. Once these two quantities are known, appropriate cable delays are set in the individual triggers (T1 and T3) such that there is an overlap between them. A logic AND between T1 and T3 defines the T5 trigger. The schematic timing diagram is shown in Fig. 4.30. The timing of T5 is given by the leading edge of a T1 trigger. The cable delays are set such that T1 arrives 40 ns after T3. For this

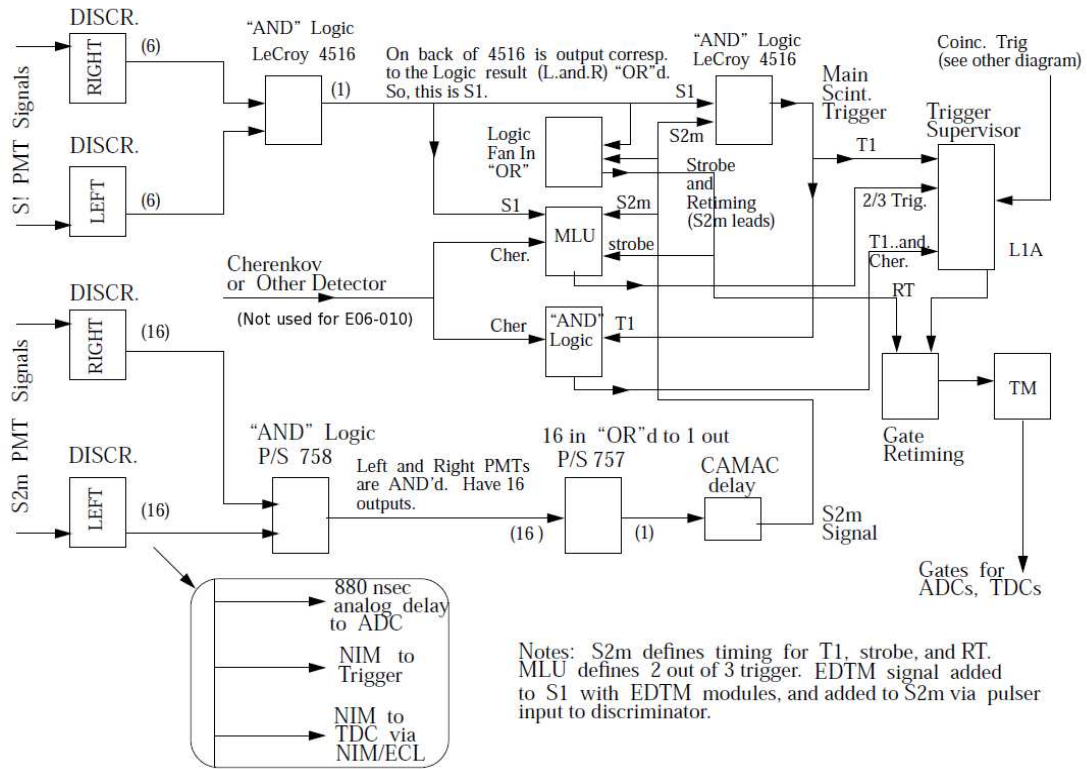


Figure 4.28: Trigger logic for the left HRS.

experiment the coincidence window was formed by T3 and the width was set to 140 ns. The width of T1 and T5 was set to 40 ns. During the commissioning of the experiment a full coincidence trigger was simulated using an electronic pulser with delays set close to the real experimental situation.

After the T5 signal is formed it is fed to the trigger supervisor (TS) which generates an L1A signal. This L1A signal is sent to both spectrometers where it is re-timed with the respective local trigger to form gates for TDCs and ADCs. Table 4.7 describes all the triggers that were used during the experiment E06-010.

#### 4.8.4 Scaler Setup

Scalers count raw signals generated from the PMTs on the detectors without any deadtime. They are used for getting information on the raw counts/rates for various triggers, which is needed to normalize the experimental data. Scalers are also used for counting the Beam Current Monitor(BCM) signal, which is basically a voltage signal converted to a frequency signal whose frequency is proportional to the beam current. This information from the scalers is very useful for real time monitoring of the trigger rates, beam current, and raw rates on the individual PMTs. Raw trigger counts are also used in the calculation of the

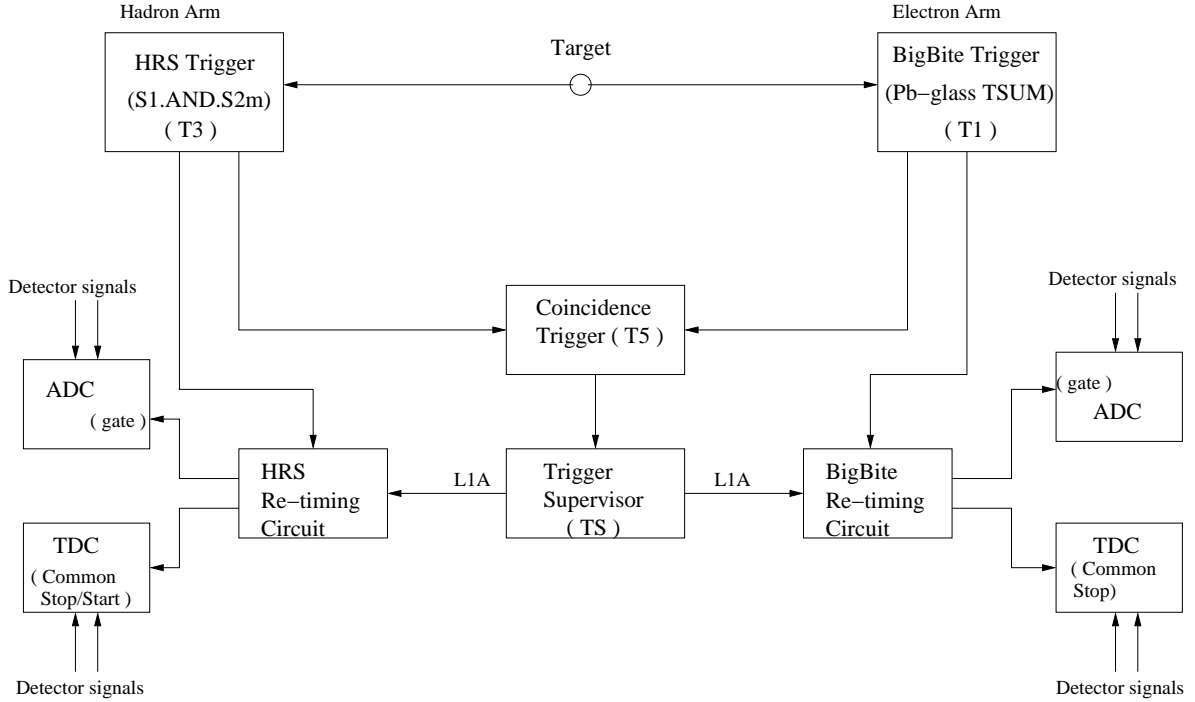


Figure 4.29: Schematic diagram of coincidence trigger setup between the two spectrometers

DAQ deadtime. Section 5.1.6 describes the deadtime measurement in detail.

The scaler setup is shown in Fig. 4.31. A set of five SIS38xx VME modules were used in 3800 mode. Each scaler has 32 input lines. The input signals, such as triggers, BCM signals, clock, etc., are daisy-chained using an RS432 flat cable. Therefore, all five scalers have copies of identical signals in their input lines. For the redundancy and cross-checking purposes, an identical scaler setup was constructed in both the spectrometers, BigBite and left HRS.

For this experiment the knowledge of beam helicity is not a requirement, since the measurement uses an unpolarized beam and a polarized target. Although this experiment depends only on the target spin, the scalers were gated using both target spin and beam helicity. This was done due to the considerations of other parasitic measurements which required both beam helicity and target spin gated scalers. Four scalers were gated with target-spin and helicity combinations: Tar+ Hel+, Tar+ Hel-, Tar- Hel+, Tar- Hel-, and one was ungated. On the top of this all five scalers were also gated with a *run gate*, which allowed the scalers to count only during the period of run-start and run-stop. The *run gate* can be obtained from the trigger supervisor.

The scaler gating scheme is shown in Fig. 4.31. It is formed by making a logical AND between three signals - run gate, target spin state, and beam helicity. Four gating signals were constructed separately using four combinations of target spin and beam helicity. These signals were then sent to the control bit on the

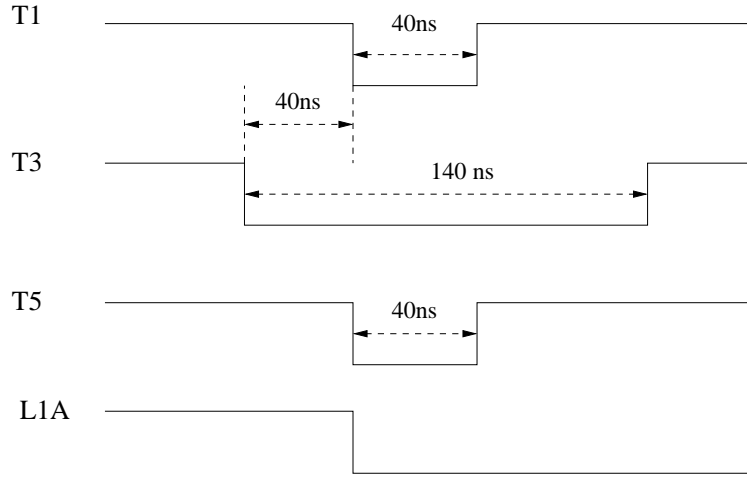


Figure 4.30: Coincidence timing between BigBite and HRS.

Table 4.7: Various triggers constructed during E06-010 experiment.

| Trigger type | Description  |
|--------------|--|
| 1            | Low threshold on BigBite lead-glass                  |
| 2            | BigBite gas Cherenkov singles                        |
| 3            | Left HRS singles (S1.AND.S2m)                        |
| 4            | Left HRS efficiency                                  |
| 5            | Coincidence between BigBite and Left HRS (T1.AND.T3) |
| 6            | High threshold on BigBite lead-glass                 |
| 7            | BigBite Cherenkov and lead-glass overlap             |
| 8            | 1024 Hz clock  |

SIS3800 scaler for gating purpose.

The beam helicity sequence is shown in Fig. 4.32. There are three relevant signals associated with the helicity:

- Quartet trigger (QRT) defines when a new random sequence of four helicity states has begun.
- The micro-pulse trigger (MPS) at 30Hz defines the periods when the helicity is valid.
- The helicity sequence has quartet structure (either  $+ - - +$  or  $- + + -$ ).

Scaler gating requires two helicity state signals, Hel+ and Hel-. These signals can be constructed using the MPS and helicity signals shown in Fig. 4.32. For example, the logical AND between the MPS and the helicity signals gives the Hel+ state, while the logical AND between the MPS and the inverse of helicity signals gives the Hel- state.

The target-spin timing sequence is shown in Fig. 4.33. There are two inputs for the formation of the target spin signals. An analogue NMR signal recorded in the lock-in amplifier, when the target is flipped and

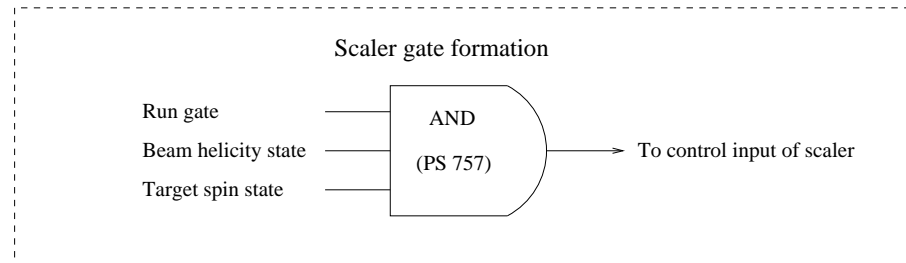
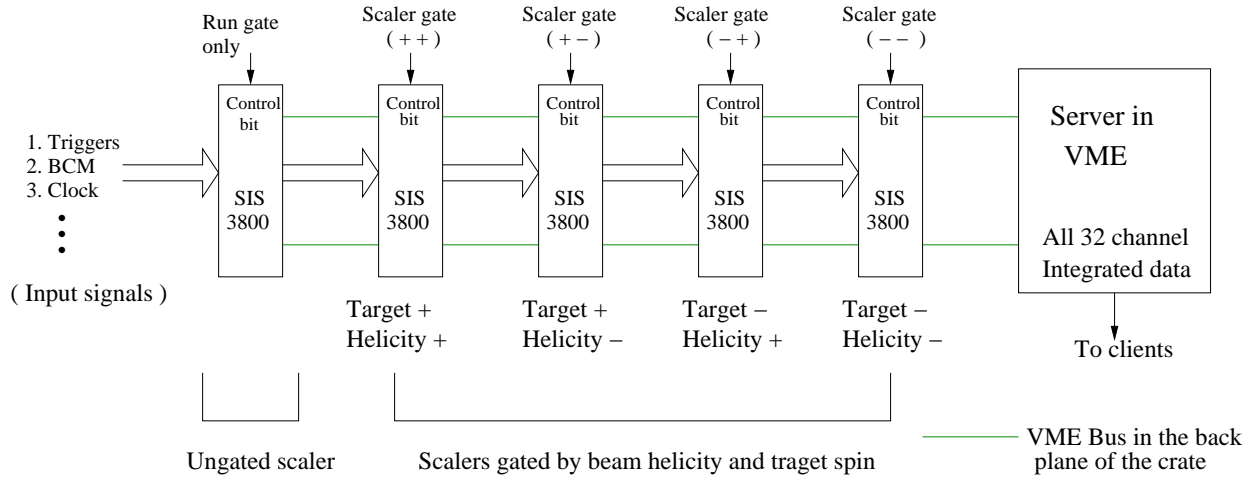


Figure 4.31: Scaler setup and gating scheme using target spin and beam helicity.

the status signal (TTL) from the function generator which provides the RF field to the NMR. Using these two signals, a NIM level target spin logic signal is constructed, one for each target state. The target spin-flip sequence is on a much longer time scale. A spin-flip happens every 20 minutes. There was an undefined period of about 5 seconds during the spin-flip.

The scalers were read out from the VME server. There are several clients that read scaler information, which included:

- Online GUI display of the real time trigger rates, raw PMT rates, and beam current during the experiment.
- Event type 140 (integrated data) which was inserted into the datastream using the Event Transfer (ET) functionality of CODA. This was done asynchronous to the CODA event.
- Scaler read out from the ROC in-synch with CODA events. This type of read out was done for every 100 CODA events.
- Event-by-event read out. Some of the most important signals like primary triggers and BCM signals

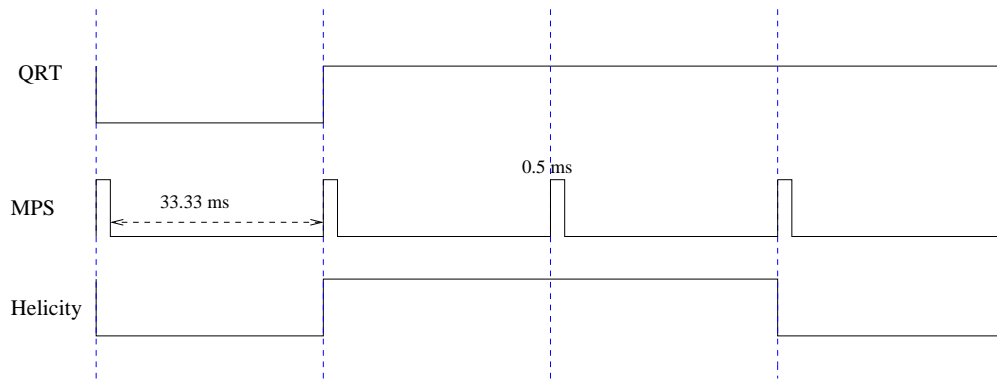


Figure 4.32: Beam helicity sequence during E06-010 experiment.

were read out every CODA event.

- Writing to a web based electronic log. At the end of each run the final reading of the scalers was written to an electronic log.



# Spin Flip Signal Timing Diagram

By Jin Huang <jinhuang@jlab.org>

68

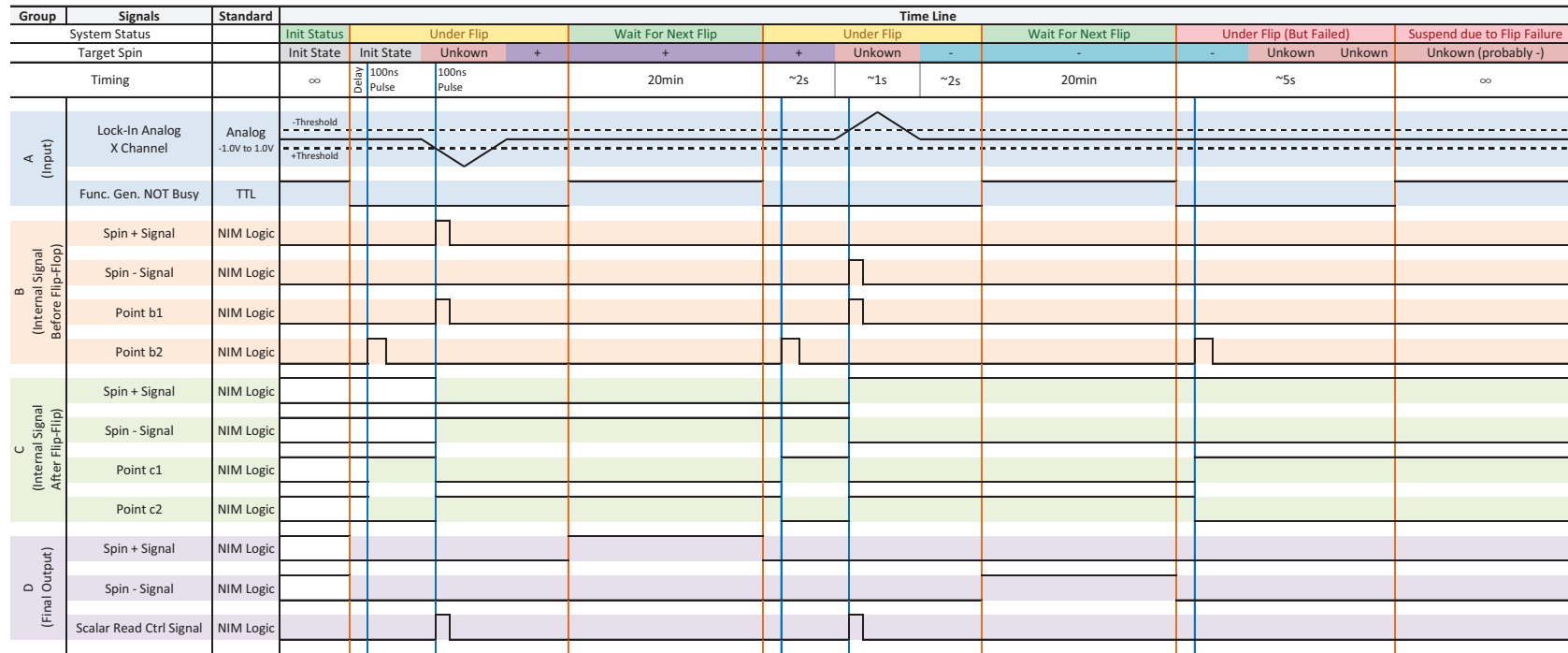


Figure 4.33: Timing sequence for the target spin state [109].

# Chapter 5

## Data Analysis

After completing the experiment setup and the DAQ systems, the experiment E06010 was performed from later Oct. 2008 to early Feb. 2009. The data were taken through the DAQ system and were stored into the tapes in ifarm at JLab: `/mss/halla/e06010/raw/`.

### 5.1 Flow of the Data Analysis

A general analysis flow diagram for E06-010 is shown in Fig 5.1. The raw data were first processed using the standard “Hall-A analyzer”. The Hall-A analyzer is an object oriented framework to decode and analyze the raw data. For this experiment, additional tools were developed for the BigBite optics and the coincidence TOF calculations. The raw data are decoded and filled into ROOT trees using a “run database”, which store the information of the run conditions. These tree variables were then used for detector calibration purposes. After completing detector calibration, the “pure” kaon and pion events will be retrieved with all the necessary variables, the pion Collins and Sivers moments will be extracted by “super local pairs” method based on “Least square fit method” and checked by Maximum Likelihood Method (MLM), the result is consistent for these two methods. Due to smaller statistics for coincidence kaon events, the kaon Collins and Sivers moments will be extracted by Maximum Likelihood Method which is a more precise method for small events. In this chapter, I will introduce the target and detector calibration first, then describe how to extract kaon Collins moment and Sivers moment by Maximum likelihood method from first order expansion and numerical calculation.

#### 5.1.1 Target Calibration

##### 1. Target Calibration and Polarization and Density Analysis

The polarized  $^3\text{He}$  target system is discussed in section 4.5. The online performance of target polarization is shown in Fig. 5.2.

During the experiment, the NMR signal was recorded based on spin state with spin-flip every 20 minutes.

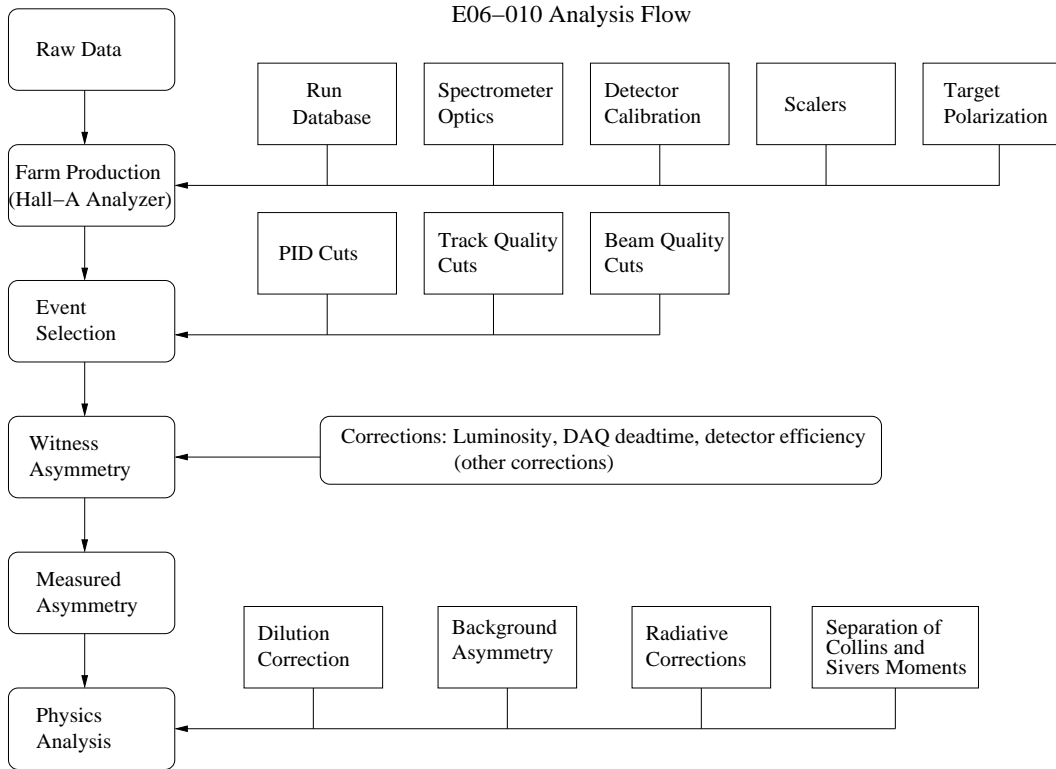


Figure 5.1: Data analysis flow for the E06-010 experiment.

An EPR measurement was performed once a week. The NMR measurement is a relative measurement and the EPR measurement is an absolute measurement of  $^3\text{He}$  target polarization. So the NMR measurement will be calibrated by the EPR measurement during target data analysis. The off-line target information is calibrated and analyzed by the target group, it includes target polarization, target density and target temperature.

The calibration of the NMR signals with an EPR measurements is discussed here. The procedure for measuring the target polarization using EPR is given in section 4.5. Fig. 5.2 shows the polarization results obtained from all the EPR measurements done during the experiment. Fig. 5.3 shows the target polarization measured at various times when the target spin was pointing in the “*transverse*” direction. Similarly, Fig. 5.4 shows the polarization when target spins were pointing in the “*vertical*” direction. The statistical uncertainty is about 2% for most of the measurements, but there were a few measurements with larger uncertainty mostly due to large statistical fluctuations in the alkali Zeeman splitting frequency.

2. NMR Calibration The calibration of the NMR signals involves performing an NMR AFP spin-flip followed by an EPR measurement and then another NMR measurement. Assuming that the signal heights of the first and second NMR are  $S_1$  and  $S_2$ , and the absolute polarization obtained by the EPR frequency shift for  $A \rightarrow B$  is  $P_1$  and for  $B \rightarrow A$  is  $P_2$ . Then, the proportionality constant between  $P_1$  and  $S_1$  gives the

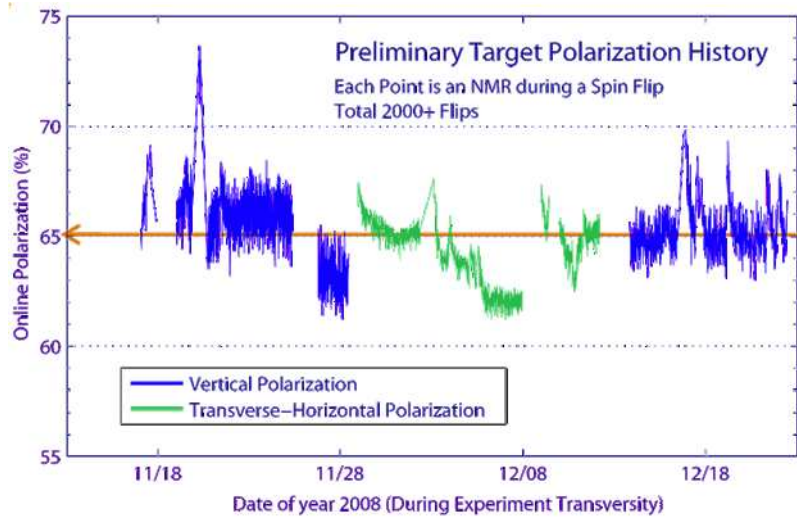


Figure 5.2: online target polarization performance history.

calibration between NMR and EPR,

$$P1 = c1 * S1. \quad (5.1)$$

Similarly, c2 can be determined from P2 and S2. The average of c1 and c2 is the overall calibration constant. This way every NMR signal can be calibrated to give the absolute target polarization.

The off-line target polarization table is as follows [110]:

Table 5.1: The Target Polarization Table

| flip ID | polarization |
|---------|--------------|
| 2060001 | 24.529       |
| 2060002 | 24.296       |
| 2080001 | 24.529       |
| ⋮       | ⋮            |
| 2690248 | 62.781       |
| 2690249 | 61.896       |
| 2690250 | 62.280       |
| ⋮       | ⋮            |
| 3080100 | 54.863       |
| 3080101 | 55.473       |
| 3080102 | 54.545       |

where spin flip ID is defined as `haPolHe3_Flip_Sequence_ID*10000+haPolHe3_Flip_Count`, both of which are EPICS variables in production root files. One pair of `haPolHe3_Flip_Sequence_ID` and `Flip_Count` makes one spin state, and the target polarization table shows the corresponding target polarization with the corresponding spin state. The first part in the table is not in production runs, and the average polarization is

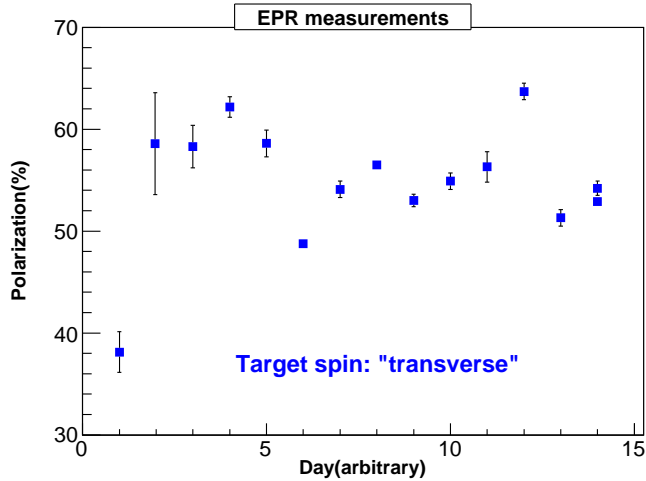


Figure 5.3:  $^3\text{He}$  target polarization measured by EPR when the target is in *transverse* direction. This plot is reproduced from [113].

about  $\sim 65\%$ .

### 5.1.2 BigBite spectrometer calibration

The BigBite spectrometer was used to identify coincidence scattered electrons in Experiment E06-010. The momentum and direction of the scattered electron need to be precisely extracted. Meanwhile, in order to get coincidence particles both in BigBite and LHRS, the timing information is also crucial to get the right coincidence time-of-flight, all the detectors need to be well calibrated in order to get precise momentum, angle, energy and timing information.

1. Multi-Wire Drift Chambers A set of multi-wire drift chambers (MWDCs) provided an accurate momentum reconstruction of the tracks of the particles passing through the BigBite spectrometer. In order to precisely reconstruct the tracks passing through the chambers, a number of calibration procedures had to be followed. The calibration steps included:

- $t_0$  calibration
- drift time to drift distance conversion
- determination of absolute wire position of individual wires.

The timing information of each wire in the MWDC was recorded in a TDC. This recorded time was the difference between the signal propagation from the wire to the TDC ( $t_{sig}$ ) and the signal from the BigBite trigger (provided by the calorimeter) to the TDC ( $t_{trig}$ ). As a particle hits the chamber, it produces an

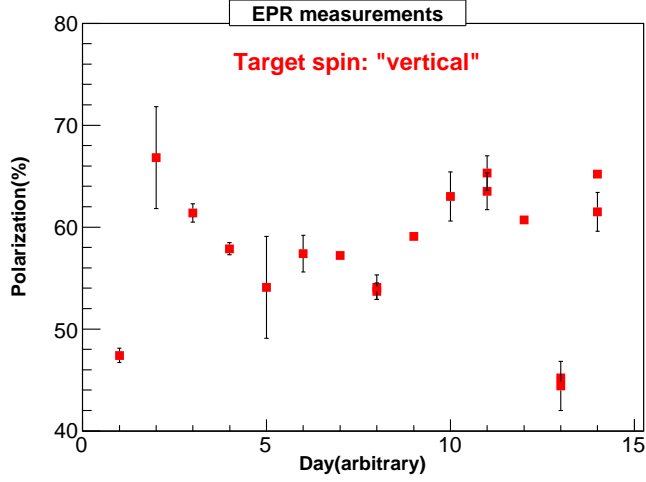


Figure 5.4:  $^3\text{He}$  target polarization measured by EPR when the target is in *vertical* direction. This plot is reproduced from [113].

ionization and the resultant electrons drift to certain distance before producing a signal on the wire:

$$t_{sig} = t_{drift} + t_{delay}^1 \quad (5.2)$$

where  $t_{drift}$  is the drift time of the electrons and  $t_{delay}^1$  is the propagation time of the signal from the wire to the TDC.  $t_{trig}$  is given by the following relation,

$$t_{trig} = t_{hit} + t_{path} + t_{delay}^2 + t_{tw} \quad (5.3)$$

where  $t_{hit}$  is the time of the hit, i.e., when the particle reaches the wire chamber.  $t_{path}$  is the time it takes for the particle to travel from the hit wire to the BigBite calorimeter, which provides the trigger.  $t_{delay}^2$  is the time for the signal to propagate from the calorimeter to the TDC.  $t_{tw}$  is the trigger time-walk effect that needs to be corrected.

Therefore, the recorded TDC time for individual wire (after correcting for the trigger time-walk effect) can be written as,

$$t_{sig} - t_{trig} - t_{tw} = t_{drift} - t_{hit} + t_{delay}^1 - t_{path} - t_{delay}^2 \quad (5.4)$$

which can be approximated to be

$$t_{sig} - t_{trig} - t_{tw} \approx t_{drift} - t_{hit} + t_0. \quad (5.5)$$

Here  $t_{path}$  is found to be the same for all types of particles within the momentum range of interest. The effect is less than 1 ns, which is comparable to the resolution of the recorded time in the TDC. The value of the  $t_0$  offset is determined for individual wire by identifying the rising edge of the drift time spectrum above the background events. Fig. 5.5 shows a drift time spectrum for one wire in x-plane. This procedure is repeated for all the wires in the three wire chambers.

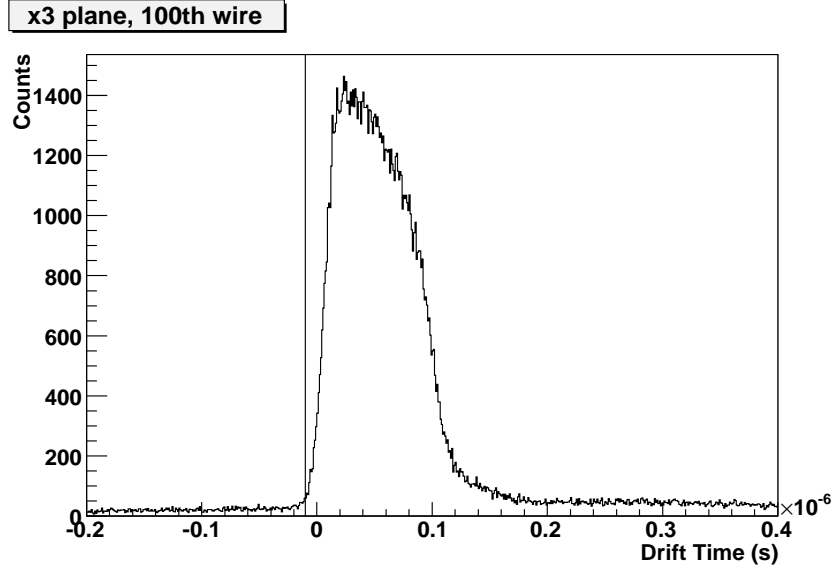


Figure 5.5: Drift time spectrum for the 100th wire in the x plane of the third chamber [111].

The reconstructed track provides the information on the position of the track in each wire plane. Using this information and the known position of the wire that got a hit, we can calculate the drift distance. This distance is plotted against the drift time and an empirical formula with several polynomials is fitted to the data (see Figure 5.5). This procedure yields the time to distance conversion function.

The chamber position was surveyed before the experiment. The overall chamber position is known from the survey report. The wire position of individual wire in the chamber is calibrated by recording the reading from the wirechamber construction report and comparing it with the position of the reconstructed track. The distance between the reconstructed track and the hit wire position is given by a quantity known as track residual, shown in Fig. 5.6. Each wire position can be shifted by the central value of the track residual spectrum. The resolution ( $\sigma$ ) of the residual peak after calibration was about  $180 \mu m$ .

## 2. BigBite Optics

The BigBite spectrometer optics was calibrated using two different beam energies:  $E_0 = 1.23$  GeV and  $E_0 = 2.39$  GeV. The momenta of the scattered particles from these two beam energy settings will cover the

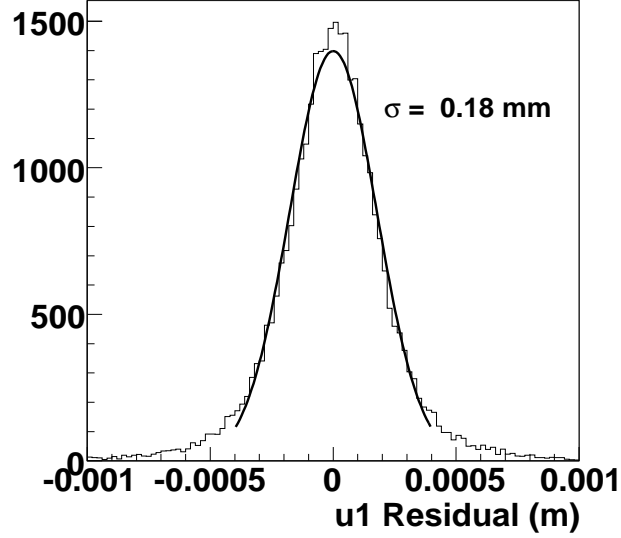


Figure 5.6: The residual peak for the U-plane of the front chamber [111].

range of momenta that we are interested in, i.e., 0.8 GeV to 2.2 GeV. In order to perform optics calibrations several steps needed to be followed.

The target, the BigBite magnet, the sieve slit and the chamber positions were surveyed and recorded. The survey report provided the position information. The position of the chamber can be calibrated using the data taken with the BigBite magnet turned off. When there is no field in the BigBite magnet the particles hit the detectors without bending, which can be used to directly get the kinematics of the scattered particles from the target.

Before the full vertex and angle reconstruction is performed, a first order optics calibration is done to calculate the particle's momentum and interaction vertex. In first order expansion the optics of the BigBite spectrometer is treated as a perfect dipole and a virtual bending plane is assumed in the middle of the magnet from which particles are bent. The angle between the momentum vector of the particle and the magnet field vector is given by

$$\cos \phi = \frac{\mathbf{B} \cdot \mathbf{p}}{|\mathbf{B}| \cdot |\mathbf{p}|} \quad (5.6)$$

where  $\phi$  is fixed. The naïve interaction vertex is constructed by looking at the intersection of the cone, formed by the fixed angle  $\phi$ , with the beam line. The vector connecting this naïve vertex and the mid point of the the bending plane determines the first order scattering angle.

### 3. Vertex Reconstruction



After the reconstruction of the first order vertex, higher order corrections are applied by looking at the dependence of  $\delta z$ , the difference between the reconstructed vertex and the expected vertex position of the multi-foil carbon target. Various tracking variables like track hit positions in the first chamber  $tr_x$  and  $tr_y$ , track direction  $tr_{xp}$  and  $tr_{yp}$ , and the positions of the bend points in the magnet coordinate system,  $bend_x$  and  $bend_y$  are used. Here  $tr_{xp}$  and  $tr_{yp}$  are defined as,

$$tr_{xp} = \frac{dtr_x}{dtr_z}, \quad tr_{yp} = \frac{dtr_y}{dtr_z}. \quad (5.7)$$

Since the BigBite spectrometer covers a wide range of momenta, a momentum dependent vertex correction needs to be added to the reconstructed vertex. For this, the first order momentum is used, based on Eq. ???. In addition to this, a fiducial volume cut is added in the magnetic mid-plane in order to exclude top and bottom regions of the magnet where the field is much weaker than in the central region. In the momentum range of 0.8-2.0 GeV the average resolution is about 0.8 cm. see Fig. 5.7.

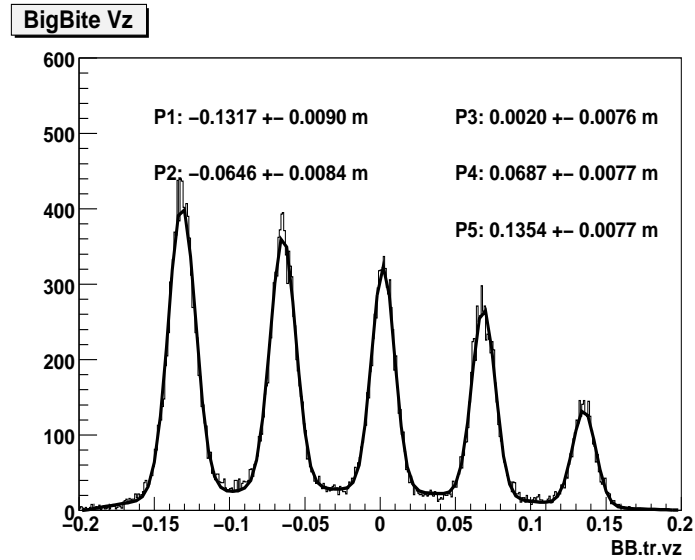


Figure 5.7: Reconstructed vertex for the multi-foil carbon target at a particle momentum of 1.2 GeV [111].

#### 4. Angle Reconstruction

A lead sieve plate with different patterns and a thickness of 1.5 inches, mounted in the front of the magnet, was used to reconstruct the scattering angle in the BigBite spectrometer. In first order the angle is reconstructed by connecting the reconstructed vertex with the middle point. Fig. 5.8 shows the real sieve plate and Fig. 5.9 shows the reconstructed sieve pattern. For higher order correction to the angle, a procedure similar to the one used for vertex reconstruction is adopted.



Figure 5.8: A lead sieve slit plate with a thickness of 1.5".

## 5. Momentum Reconstruction

The momentum calibration is done using elastic electrons scattered off a hydrogen target at two different beam energies: 1.23 and 2.39 GeV. Elastic electrons were selected by graphical cuts in the  $\delta p$  vs.  $bend_x$  plot where  $\delta p$  is the difference between first order reconstructed momentum and the expected momentum in elastic kinematics. Since the scattered electrons pass through various materials before hitting the chamber, energy loss effects are applied to both the beam and the scattered electrons. Using these events, a first order momentum is reconstructed and additional corrections were applied using a look-up table depending on the middle point position of the selected events. The corrections are given by,

$$p^{(1)} = z_0 \cdot p^{(0)} + z_1 + z_2 \cdot tr_x + z_3/\theta_{bend} \quad (5.8)$$

where the  $z_0$ ,  $z_1$ ,  $z_2$ , and  $z_3$  are functions of the middle point position  $bend_x$  and  $bend_y$ . Figure 5.10 shows the final resolution achieved using this procedure. An average resolution of 1% was obtained in the entire momentum range. Since the calibration was done at two momentum points, it is crucial to check the reliability of the optics in the range beyond these two points. This can be done by looking at the missing mass ( $W$ ) spectrum and identifying the resonances. In Fig. 5.11, the top (bottom) left panel shows the reconstructed missing mass spectrum for a beam energy of 1.23 (2.39) GeV where one can clearly see the  $\Delta(1232)$  and higher mass resonances at the right values of  $W$ . The right side panels show the momentum vs. scattered angle correlations from which clear elastic events can be identified. Similarly, for momenta beyond 2.36 GeV, hydrogen elastic events from a 5-pass beam energy of 5.892 GeV were used to check the optics quality.

BigBite is an open geometry spectrometer and both positive and negative particles can reach the detec-

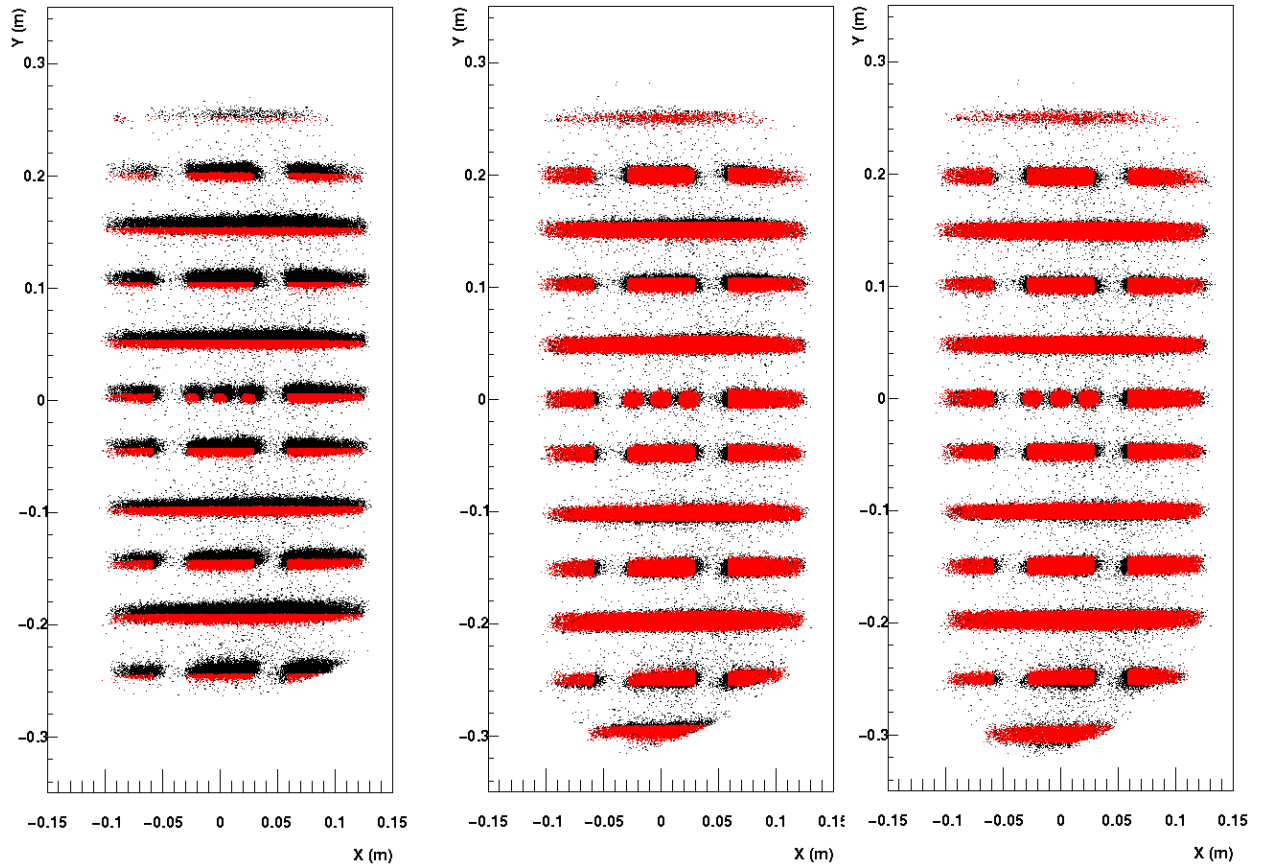


Figure 5.9: The left panel shows the reconstructed sieve pattern with first order optics model. The middle panel shows the sieve pattern after adding offsets. The right panel shows the sieve pattern after applying higher order corrections. The red points indicates where the sieve holes/slots are actually located [111].

tors, but they bend in opposite directions. Therefore it is necessary to calibrate the optics using the positive charged particles, too. A positive optics model was developed using the data taken by reversing the magnet polarity. Due to some practical issues, the runs were taken at  $45^\circ$  instead of the usual BigBite spectrometer setting of  $30^\circ$ . The positive mode optics developed at  $45^\circ$  was applied to  $30^\circ$  and checked against the negative mode optics for both  $30^\circ$  and  $45^\circ$ . The model gives a good description of the reconstructed momentum, vertex, and angle. Fig. 5.12 shows the momentum resolution achieved using positive optics.

## 6. Preshower and Shower

The BigBite calorimeter consists of a preshower detector and a shower detector, both made of lead-glass as described in Section 4.6. It was used for triggering the BigBite spectrometer and for particle identification of the scattered electrons. A detailed description of the BigBite trigger is given in Section 4.8.1. The total

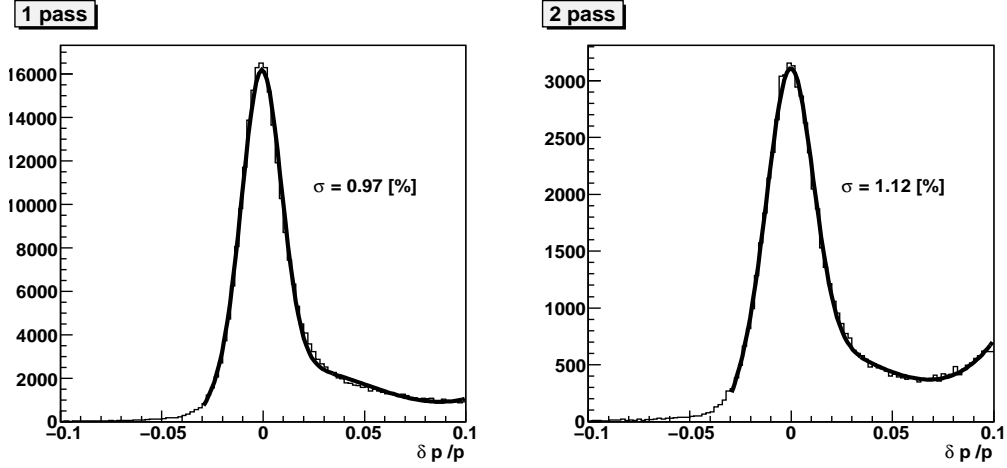


Figure 5.10: Final momentum resolution achieved with two beam energies: left panel is for  $E_0 = 1.23$  GeV and right panel is for  $E_0 = 2.39$  GeV [111].

energy of the detected particles is roughly proportional to the sum of the cluster amplitudes in both the preshower and shower detectors. In order to accurately measure this quantity, the detectors have to be calibrated to a known energy of the incident particle. For this experiment, the elastic reaction,  $H(e, e')X$ , on a  $H_2$  target was chosen with two different incident beam energies,  $E_0 = 1.23$  GeV and  $E_0 = 2.39$  GeV. Also, the preshower and shower detectors were initially gain matched with cosmic rays for a rough alignment of the ADC amplitudes by adjusting the high voltage on the PMTs. The calibration procedure used these two methods, utilizing cosmic rays and elastic events.

After Preshower and Shower systems were calibrated, the particle identification can be done by examining the signal in the preshower detector. Hadrons (in this case mostly pions) leave a small signal in the preshower detector due to minimum ionization whereas electrons leave a large signal in the preshower (Fig. 5.13). Electrons can be selected by placing a cut greater than channel 400 and hadrons can be selected by requiring that all the events generate a signal lower than channel 300.

### 5.1.3 High Resolution Spectrometer calibration

The left High Resolution Spectrometer (HRS) was used to detect the outgoing hadrons in coincidence with the electrons detected in the BigBite spectrometer. Unlike BigBite, which is an open geometry spectrometer, the HRS is a focusing spectrometer, where the magnet polarity can be changed to allow either positively or negatively charged particles to be focused on to the detectors. A brief description of the detector calibration procedures involved is given in this section.

1. Vertical Drift Chambers

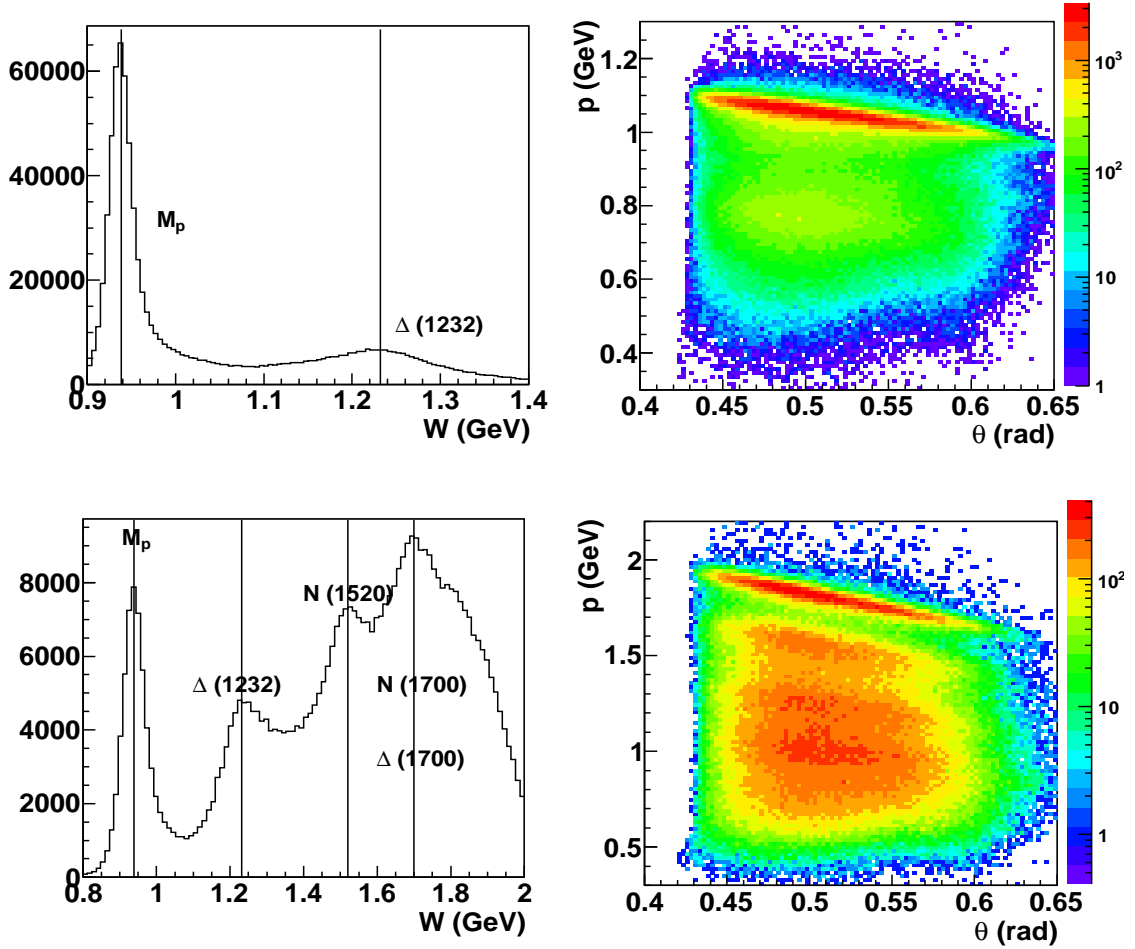


Figure 5.11: BigBite optics check: The left side top (bottom) panels show the reconstructed missing mass peak of the proton and other resonances for beam energies of 1.23 GeV (2.39 GeV). The right side panels show the momentum vs. scattering angle  $\theta$  correlations at the beam energies of 1.23 GeV and 2.39 GeV [111].

Vertical Drift Chamber (VDC) calibrations involve  $t_0$  (see Eq. 5.5) calibration and optimizing the optics calibrations for a good vertex and momentum reconstruction from a 40 cm long target. The calibration was performed with special elastic runs taken with different targets such as a 7-foil carbon target,  $^3\text{He}$ ,  $\text{N}_2$ , and  $\text{H}_2$  gas. The vertex calibration was done using the surveyed positions of the carbon foils along the target length. The positions of the reconstructed tracks from different carbon foils were aligned to the actual positions of the foils at the target. Fig. 5.14 shows the vertex reconstruction plot. All 7 foils are aligned to their actual position and an average resolution of 6 mm was achieved for  $z_{react}$ . The coincidence BigBite and HRS vertices agree at the level of 1 cm.

The out-of-plane angle ( $\theta_{tg}$ ) and the in-plane angle ( $\phi_{tg}$ ) were calibrated by minimizing the difference between the actual value and the reconstructed angle. Survey report provides the information on the actual

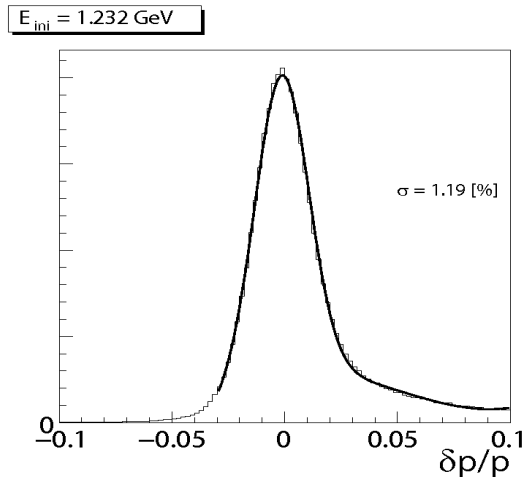


Figure 5.12: Momentum resolution for positive optics data at 1.23 GeV [111].

values of the angle.

The momentum of the outgoing particle was calibrated using the data taken with carbon target in elastic kinematics. A scan of the momentum was performed by moving the carbon elastic peak across the focal plane at  $p_0 = 0\%$ ,  $\pm 2\%$ , and  $\pm 4\%$ . An optimization of the momentum was done by choosing the specific ground state and a specific excited state of the carbon nucleus [116]. A resolution of about  $5 \times 10^{-4}$  was achieved using this procedure.

## 2. Gas Cherenkov Detector

A gas Cherenkov counter was used for particle identification. It was very useful for rejecting electrons, which was the primary background for the  $\pi^-$  and  $K^-$  detection in the negative polarity mode of the left HRS.

The calibration of the gas Cherenkov detector was performed by aligning the single photoelectron peak of each ADC spectrum to channel 200. This was done by fitting a Gaussian shape to the individual photoelectron peaks and scaling the mean value to channel 200. Then the sum of all 10 ADCs was constructed with the single photo-electron peak aligned at channel 200. Since pions and other hadrons peak around one specific channel (200) in the ADC spectrum, whereas electrons generate large signal in the ADC, one can separate the particles by cutting on the ADC value. Fig. 5.15 shows the ADC sum spectrum of the gas Cherenkov detector for a negative polarity run after pedestal subtraction. After performing a detailed cut efficiency study a cut on the ADC sum less than 250 channels was used in the pion analysis. This will reject the electrons with an efficiency of 99%. For kaon analysis, a cut study was performed and the gas Cherenkov cut was set at 30 channels. There are almost no electrons left, and the pion contamination in kaons is less

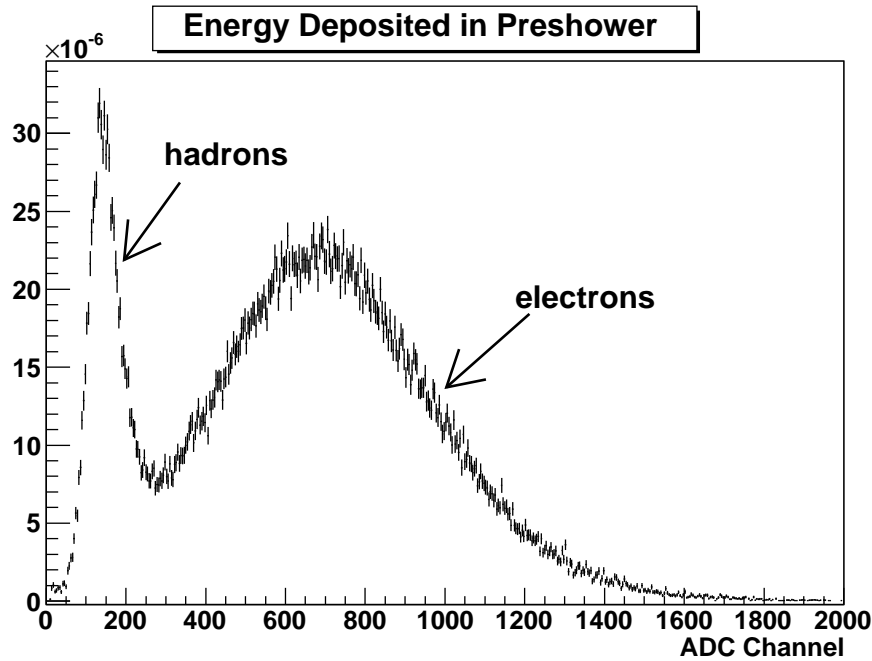


Figure 5.13: Preshower energy spectrum showing a clear separation between pions and electrons. The minimum ionizing pions peak around channel 180 and electron like events peak around channel 700.

than 5% even in negative polarity<sup>1</sup> mode when combining with information from aerogel, time-of-flight, and RICH detectors.

3. Aerogel Cherenkov Detector The aerogel Cherenkov detector can separate kaons and protons from pions since only pions can fire the aerogel detector.

Before being installed into left HRS, the aerogel detector was checked with cosmic rays, and the bad PMTs were replaced. Two scintillators were placed above and below the aerogel detector in four different positions to find and replace the bad PMTs.

After being installed into left HRS, during cosmic test and commissioning, the values of pedestals were determined using cosmic rays. Meanwhile the high voltage for each PMT could be adjusted to align the single photo-electron peak at around channel 100 for all 24 individual PMTs.

After the experiment, 12 major periods (six for positive polarity, six for negative polarity) were selected to align the single photo-electron peak to 100 channels for each individual PMT. The calibration coefficients are stored in the aerogel data base. Since the single photo-electron peak previously aligned at channel 100, the coefficients are all close to 1. The aerogel ADC sum spectra are shown in Fig. 5.16.

For positive polarity, the sharp peak at channel 100 is mainly due to  $\delta$  electrons which are produced by the protons interacting with material.

<sup>1</sup>In positive polarity at LHRS, using the combined cuts, the pion contamination in kaons is around 1%.

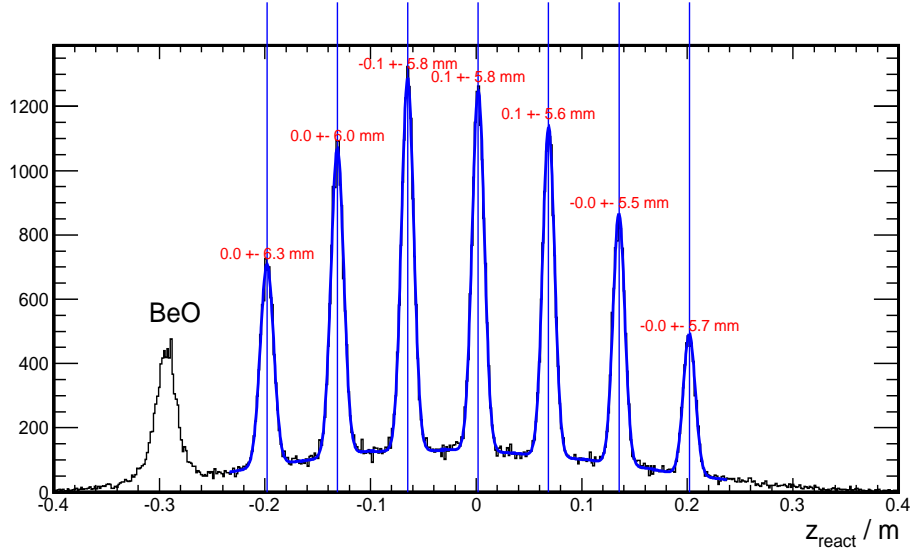


Figure 5.14: Reconstructed vertex  $z_{react}$  for a multi-foil carbon target with a BeO target mounted in the front [114].

The ADC spectrum of Aerogel (pedestal excluded) can be treated as a Poisson distribution convoluted with Gaussian distributions [112]. The Poisson distribution shows the probability of  $n$  photo-electrons collected by the PMTs and the Gaussian shapes stand for the response of PMTs to different number of photo-electrons (pedestal excluded<sup>2</sup>). Analytically, the spectrum shape can be expressed as the following:

$$Poisson(n, \mu) = \frac{e^{-\mu} \mu^n}{n!} \quad (5.9)$$

$$Gaus(x, n, \sigma) = \frac{1}{\sqrt{2\pi} \sqrt{n\sigma}} e^{-\frac{(x-nA_0)^2}{2n\sigma^2}} \quad (5.10)$$

$$A(x) = C \cdot \sum_n Poisson(n, \mu) \cdot Gaus(x, n, \sigma) \quad (5.11)$$

where  $C$ ,  $\mu$ ,  $\sigma$  are three free parameters:  $C$  is the amplitude factor,  $\mu$  is the average number of photo-electrons and  $\sigma$  is the width of single photo-electron response.  $A_0$  is the average amplitude of single photo-electron response ( $\sim 100$ ). The response width changes according to the number of collected photo-electron, and obeys basic statistics:

$$\sigma_n = C_\sigma \sqrt{n \cdot N} = \sqrt{n} \cdot C_\sigma \sqrt{N} = \sqrt{n} \cdot \sigma \quad (5.12)$$

where  $N$  is the total number of electrons collected by the PMT anode after amplification of a single photo-electron,  $C_\sigma$  is the coefficient of the single photo-electron response. The formula Eq. 5.9 was used to fit the aerogel ADC sum curve to confirm the alignment. The number of Cherenkov photons at a given

<sup>2</sup>In fact, pedestal strength follows the poissonian statistics as the other peaks, but it is generally not gaussian and in any case its sigma is generally different from the other peaks.



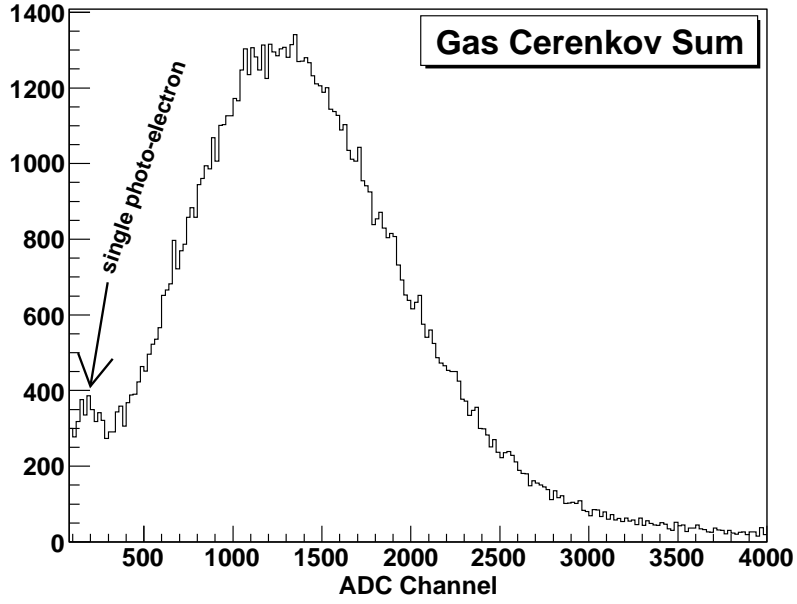


Figure 5.15: ADC sum of the gas Cerenkov detector.

wavelength depends on the particle speed, its charge, the radiator thickness and its refractive index according to:

$$\frac{d^2N}{dx d\lambda} \propto \frac{z^2}{\lambda^2} \left(1 - \frac{1}{\beta^2 n^2(\lambda)}\right), \quad (5.13)$$

where the average number of photo-electrons (N.P.E) is a function of incident particle's velocity. If the electrons were selected to fit the number of photo-electrons, the average N. P. E. was obtained:

$$N.P.E._{electron} = 6.15 \pm 0.23 \quad (5.14)$$

A cut on aerogel ADC sum  $> 150$  was selected to identify pions because pions can fire aerogel. The cut rejects more than 99% kaons. If a cut on aerogel ADC sum  $< 150$  is selected, it will reject 97% of the pions. Since the number of kaon events is only  $\sim 1\%$  of pion events for the negative polarity<sup>3</sup>, it is more complicated to select cuts to reject pion contamination for kaons. A detailed analysis will be described later. Using the combination of gas-Cherenkov detector, aerogel Cherenkov detector, RICH detector, and time-of-flight, the contamination of pions in negative coincidence kaons can be minimized to less than 5%<sup>4</sup>.

<sup>3</sup>In positive polarity, using the same final combined cuts, the total coincidence kaons are around 5% of the total coincidence pions, see later.

<sup>4</sup>Using the same cuts, the contamination of positive coincidence pions in positive coincidence kaons is around 1%.

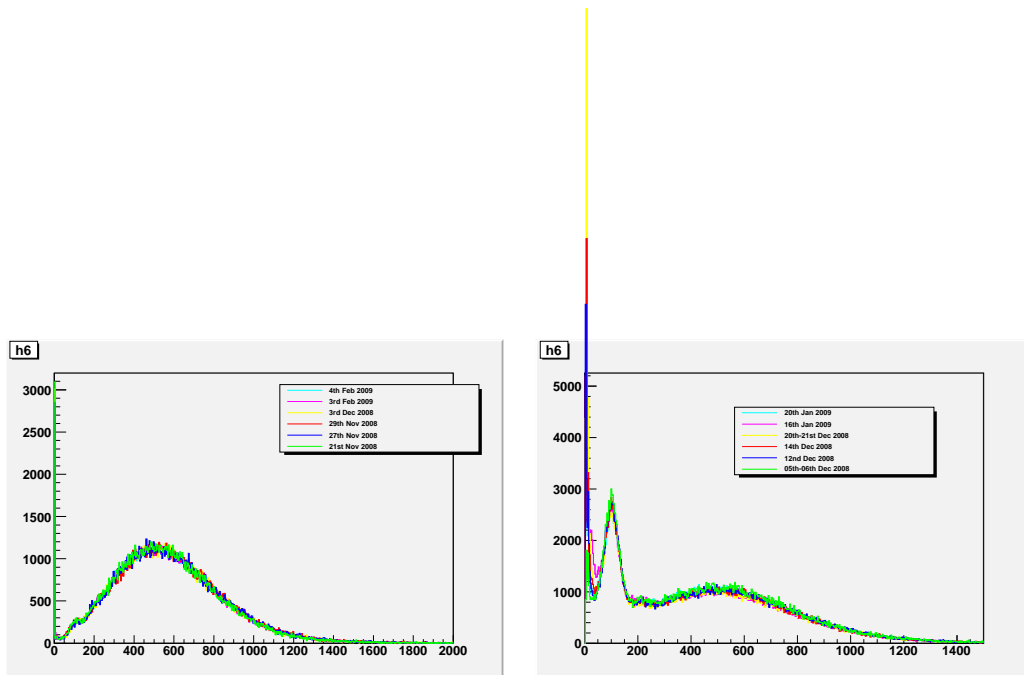


Figure 5.16: ADC sum of the Aerogel detector for the experiment. Left panel: negative polarity in LHRs. Right panel: positive polarity in LHRs. There are two high peaks at channel 0 and at single photo-electron peak channel 100 due to large number of proton events.

#### 4. RICH Detector

The RICH detector(see Sec. 4.7.6) is used to better identify kaons in combination with other detectors, such as gas Cherenkov detector, aerogel Cherenkov detector, and time-of-flight. Due to small production rate of coincidence kaons, the RICH detector was used to identify kaons and protons together with other detectors in this experiment.

Before installation, the RICH detector was checked with its own DAQ in the EEL building. One wire was broken during shipment from Italy to USA, it was opened under vacuum condition with special vacuum setup in the EEL building for repairment.

At first, the pedestal study was performed, including two procedures:

1. Scan of pedestal baseline

The baseline of the Gassiplex signals going to the positive output of the CRAM has been visualized on the oscilloscope and adjusted (in order to avoid saturation) by means of a screw in the receiving card of each gassiplex row. The threshold and pedestal were loaded into the CRAMs. This was done for all 40 ADCs.

2. Scan of pedestal Value (set in CRAMs):

The input signal is sampled by the ADC and its digital value is compared to a threshold value, if the signal is over threshold, the pedestal is subtracted and the result was stored in an output Buffer arranged in FIFO, which means (in C++):

$$ADC\_Value = (INPUT\_VALUE > THR)?(INPUT\_VALUE - PED) : noconversion.$$

In order to possibly detect the Cherenkov photons generated by cosmic muons going through in the quartz, the detector must be rotated (otherwise the Cherenkov will be internally reflected).

The optimal configuration should be the one represented in Fig.5.17, where C is the Cherenkov angle in quartz and the photon direction is perp. to the quartz window.

Baseline and pedestals were observed on the oscilloscope when tuning the pedestals. During pedestal study with cosmic ray, the front-end cards were checked one by one, defective cards (with more than 4% of broken or noisy channels) where replaced.

Few cards were replaced due to an high voltage trip at 2100 V (typical operating voltage). This trip has probably be caused by a broken wire that has required the opening of the RICH chamber in controlled dry nitrogen (in the dedicated glove box). Likely the broken wire was on one edge of the RICH MWPC and did not required its replacement. The broken wire was found in the second pad (starting from the High Voltage distribution side). Most of the broken wire was removed, and it was glued on the pad frame side with Mylar tape. Both wire 10th and 11th are grounded as shown in Fig. 5.18.

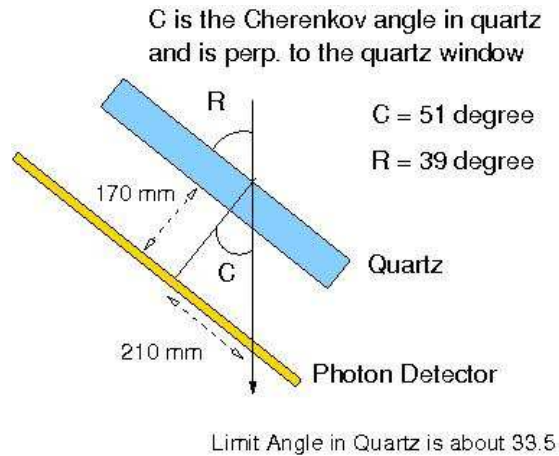


Figure 5.17: The RICH detector should be rotated otherwise the Cherenkov light will be internally reflected.

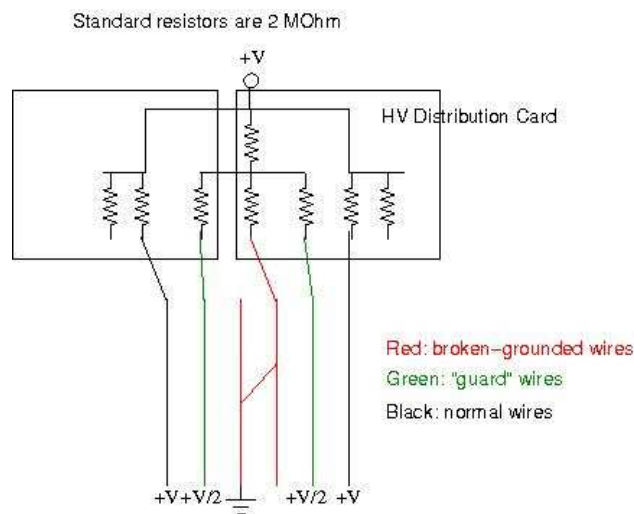


Figure 5.18: The 10th or 11th wire was broken, both of them were grounded.

After that, the corresponding resistors in card 0 and card 1 were removed, the resistors of the closest wires :9th and 12th were also removed. So wires 10th and 11th were grounded, and wires 9th and 12th were electrically floating. This fixing, that allowed safe operation up to 2400 V, did not influence noticeably the detector acceptance.

After checking the RICH detector with cosmic ray, the RICH detector was installed into Hall A LHRS between the gas Cherenkov detector and the S2M scintillator.

The 40 ADCs (20 VME modules) have been equally housed by 2 VME crates to balance the readout performance. In table 5.2 is shown the VME crate map of one of the two RICH crates.

The RICH front end electronics requires two voltage levels: -3.5V and 3.5V on the Gassiplex cards, actually they were set at about -4.0 V and + 3.8V to take into account drop along the long power lines.

Table 5.2: The cratemap of crate 14 for RICH detector

| ====   | Crate 14 | type  | vme        |            |       |       |  |
|--------|----------|-------|------------|------------|-------|-------|--|
| # slot | model    | clear | header     | mask       | nchan | ndata |  |
| 1      | 550      | 1     | 0xcd000000 | 0xffff0000 | 512   | 1024  |  |
| 2      | 550      | 1     | 0xcd010000 | 0xffff0000 | 512   | 1024  |  |
| 3      | 550      | 1     | 0xcd020000 | 0xffff0000 | 512   | 1024  |  |
| 4      | 550      | 1     | 0xcd030000 | 0xffff0000 | 512   | 1024  |  |
| 5      | 550      | 1     | 0xcd040000 | 0xffff0000 | 512   | 1024  |  |
| 6      | 550      | 1     | 0xcd050000 | 0xffff0000 | 512   | 1024  |  |
| 7      | 550      | 1     | 0xcd060000 | 0xffff0000 | 512   | 1024  |  |
| 8      | 550      | 1     | 0xcd070000 | 0xffff0000 | 512   | 1024  |  |
| 9      | 550      | 1     | 0xcd080000 | 0xffff0000 | 512   | 1024  |  |
| 10     | 550      | 1     | 0xcd090000 | 0xffff0000 | 512   | 1024  |  |
| 11     | 550      | 1     | 0xcd0a0000 | 0xffff0000 | 512   | 1024  |  |
| 12     | 550      | 1     | 0xcd0b0000 | 0xffff0000 | 512   | 1024  |  |
| 13     | 550      | 1     | 0xcd0c0000 | 0xffff0000 | 512   | 1024  |  |
| 14     | 550      | 1     | 0xcd0d0000 | 0xffff0000 | 512   | 1024  |  |
| 15     | 550      | 1     | 0xcd0e0000 | 0xffff0000 | 512   | 1024  |  |
| 16     | 550      | 1     | 0xcd0f0000 | 0xffff0000 | 512   | 1024  |  |
| 17     | 550      | 1     | 0xcd100000 | 0xffff0000 | 512   | 1024  |  |
| 18     | 550      | 1     | 0xcd110000 | 0xffff0000 | 512   | 1024  |  |
| 19     | 550      | 1     | 0xcd120000 | 0xffff0000 | 512   | 1024  |  |
| 20     | 550      | 1     | 0xcd130000 | 0xffff0000 | 512   | 1024  |  |

The readout speed of the RICH electronics is limited by the fact that groups of 480 channels (pads) are read out sequentially by each ADC, one by one. The frequency of the sequencer was about 1700 kHz, leading to a deadtime of  $720\mu\text{s}$ . The timing and trigger for RICH is shown in Fig. 5.19.

The pedestals and sparse readout single channel thresholds were estimated from dedicated short runs about twice per day; the thresholds were generally set as 3 pedestal RMS from the pedestal mean values.

The main RICH analysis procedure includes the following steps:

- identify noisy channels which are then masked
- adjust data base in order to fit the pion angle consistent with theoretical prediction with the fixed proximity gap
- solve specific problems (such as one ADC for  $y$  coordinate is inverted)
- reconstruct the Cherenkov angle and mip angle
- data quality checks and detector characterization (efficiency, rejection power)

The typical RICH event presents several hits, that can be generally classified into three groups:

- 1) some of the hits are distributed along a ring (ellipses) due to the Cherenkov photons;

- 2) a compact small spot of few hits caused by the MIPS of the charge particle (secondary electrons generated in the MWPC by the travelling charge particle);
- 3) hits of noise from various sources.

For example, a pion with momentum 2.35 GeV moves out through a reflective index 1.2863 gas will produce Cherenkov radiation, which satisfies:

$$\cos(\theta_{Cherenkov\_angle}) = 1/(n_{index} * \beta) \quad (5.15)$$

If we let  $c$  (velocity of light in vacuum) =1, Because momentum

$$P_{\pi} = m_{\pi} * v_{\pi} = m_{0,\pi} * v_{\pi} / \sqrt{(1 - v_{\pi} * v_{\pi})} \quad (5.16)$$

so

$$\beta_{\pi} \equiv v_{\pi} = P_{\pi} / \sqrt{(m_{0,\pi} * m_{0,\pi} + P_{\pi} * P_{\pi})} \quad (5.17)$$

For momentum  $P_{\pi} = 2.35$  GeV,  $m_{0,\pi} = 139.57$  MeV,  $\beta_{pi} = 0.99824$ . From  $\cos(\theta_{Cherenkovangle,\pi}) = 1/(n_{reflectiveindex} * \beta_{\pi})$ , then  $\theta_{\pi}$  (Cherenkov cone angle) =0.6781.

Similarly, for kaon, where  $m_{0,K} = 493.667$  MeV,  $\theta_K = 0.6528$ .

For proton, where  $m_{0,p} = 938.27$  MeV, then  $\theta_p = 0.5788$ .

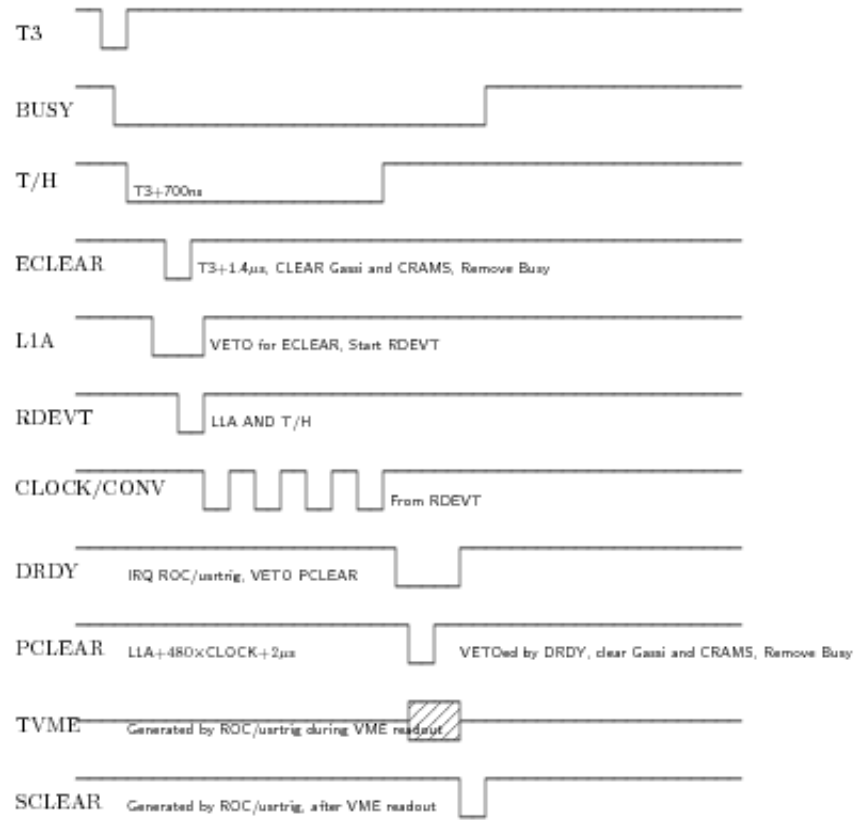


Figure 5.19: The timing and trigger for RICH.  
111

In data analysis, first, we need to reconstruct the coordinates and tune parameters to match the experiment result with theoretical calculation. And we also need to eliminate the noise and deal with other issues, such as large size events, eventually we still use Cherenkov cone angle and its deviation to identify pions, kaons, and protons.

For one specific event of a charged particle, the event display is shown in Fig. 5.20. One clear ring produced by a charged particle is shown in the plot. When many particles were reconstructed, the location

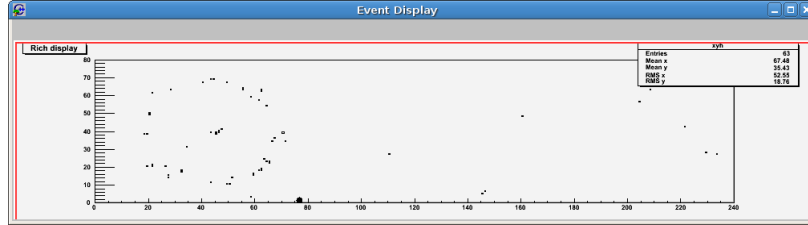


Figure 5.20: A ring for one event of a charged particle.

of the charged particles were aligned at a specific location, there is a clear “accumulated” ring shown in two dimensions and three dimensions in Fig. 5.21. The RICH ring is clearly visible above background.

Fig. 5.22 show  $\pi/K$  separation using the RICH. For pions, the Cherenkov angle is 0.6772 radian with  $\sigma_\pi \sim 0.00695$ . For kaons, the Cherenkov angle is about 0.6516 radian with  $\sigma_K \sim 0.0073$ . For protons, the Cherenkov angle is about 0.577 radian with  $\sigma_p \sim 0.0077$ .

## 5. Lead-glass Detector

In the lead-glass detector the hadrons only deposit ionization energies. but electrons leave large signals due to the electromagnetic showers. The calibration was performed by aligning the minimum ionization peak in each block to channel 100 in the ADC. An ADC sum of all the blocks in the two-layered lead-glass detector can be obtained afterwards. Fig. 5.23 shows the energy divided by momentum ( $E/p$ ) spectrum where a clear separation between hadrons and electrons is seen. A cut efficiency study was done and a cut on  $E/p < 0.65$  was applied to select hadrons.

### 5.1.4 Coincidence Time-of-Flight module

In this experiment two particles are detected in coincidence - a scattered electron in the BigBite spectrometer and a hadron in the left HRS. The path length of the particles traveling through the left HRS is about 25 m, we can calculate the coincidence time-of-flight (CTOF) of various particles. The CTOF will be different for different particles, due to differences in their masses with the same momentum  $\sim 2.35$  GeV/c. Ideally a sharp CTOF peak centered around zero was expected for a particular species of particle. The intrinsic timing resolution and momentum spread would broaden the CTOF peak.



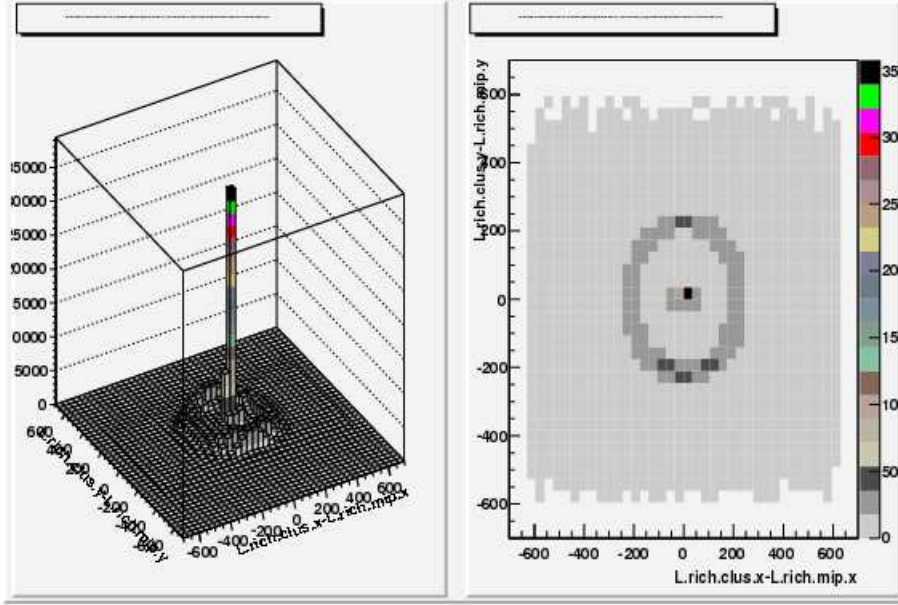


Figure 5.21: A reconstructed RICH ring for many events in two and three dimensional plots.

The coincidence time-of-flight information will reduce background and improve particle identification. In our case, the pion and proton peaks are separated by  $\sim +1.8$  ns and  $\sim -4.95$  ns, respectively, from the kaon peak. The coincidence TOF can be separated into three parts [116] [114].

$$t_{coin} = t_{HRS}^{RF} - t_{BB}^{RF} + \Delta t_{trigger} \quad (5.18)$$

where  $t_{coin}$  is the coincidence time,  $\Delta t_{trigger}$  is the time difference between two single arm triggers,  $t_{HRS}^{RF}$  is the time difference between the vertex reaction and the single arm trigger for the HRS. Similarly for BigBite it is  $t_{BB}^{RF}$ . Here  $t_{HRS/BB}^{RF}$  includes:

- Time-of-flight of the particle from reaction point to the scintillators.
- Detector response time including cable delays and processing by electronics.
- Difference in timing detector (BigBite Scintillator) signals and trigger signals (BigBite Calorimeter).

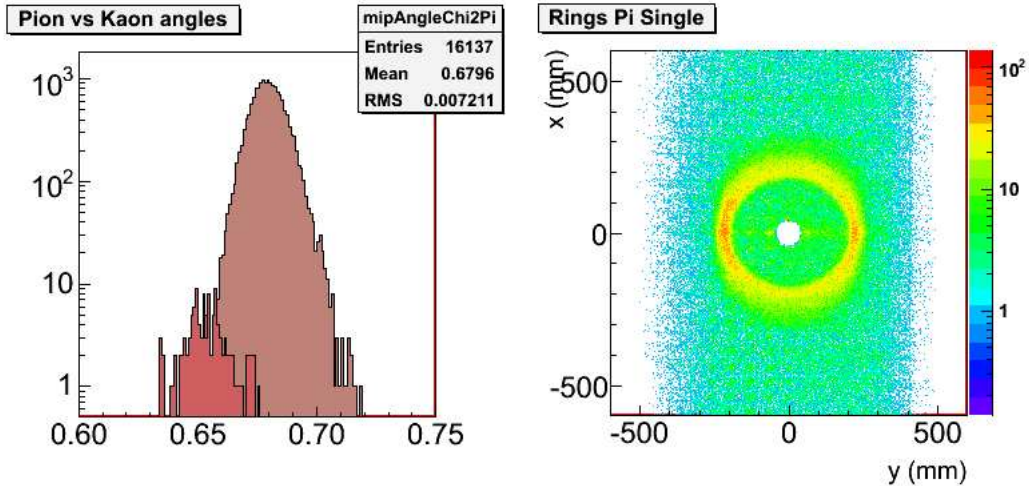


Figure 5.22: Left panel: separation of pions and kaons. Right panel: the reconstructed ring for charged pions.

These differences in time were recorded using high resolution (60 ps) TDCs.

$t_{HRS/BB}^{RF}$  is calibrated in individual spectrometers by using the beam radio frequency (RF) signal. The beam RF signal provides the timing for each beam bunch (each electron beam bunch is separated by 2 ns). This signal is recorded in the TDC ( $t_{RF}$ ). The difference of  $t_{HRS/BB}^{RF}$  and  $t_{RF}$  is minimized in both spectrometers separately before calculating the coincidence time. In the following section the calibration of the single arm timing detectors will be briefly described before showing the results of the coincidence TOF.

#### 1. HRS and BigBite Single Arm Timing Calibrations

The HRS timing was determined by the S2m scintillators. The goal was to reach below few hundred picoseconds resolution. Therefore it was necessary to perform various corrections on the scintillator timing, including pathlength correction, time-walk corrections, and scintillator timing offset correction. Fig. 5.24 shows the timing resolution of the S2m for pion-like events after all the corrections. A resolution of 140 ps was achieved for this detector.

In the BigBite spectrometer the scintillator plane was inserted between the preshower and shower counters. Therefore an electron coming from the target can induce a shower of secondary particles at the preshower which in turn can leave a signal in the scintillator, along with the primary electron. The calibration procedure involves two steps:

- Time-walk and bar offset corrections: This is done by choosing the events with a hit in two neighboring bars and minimizing the time difference between these two bars by applying time offset and time-walk

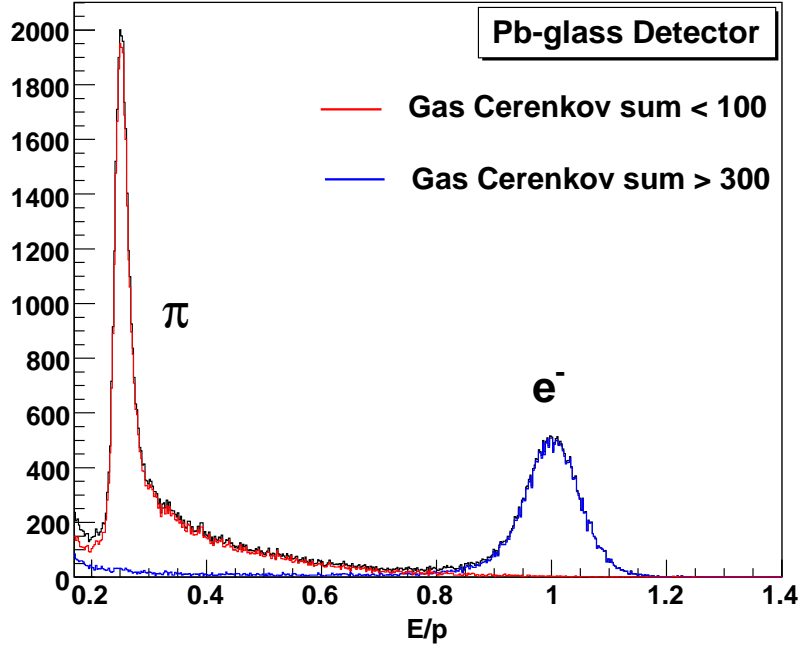


Figure 5.23: Energy divided by momentum for the two-layer lead-glass detector showing a clear separation between hadrons and electrons.

corrections. The following formula is used for correcting the time-walk effect on all the PMTs:

$$\Delta t_{tw} = -17.9 A_p^{-0.14} ns \quad (5.19)$$

where  $A_p$  is the pedestal subtracted amplitude measured in ADC channels.

- Pathlength calibration: This correction was done using the linear correlation between the pathlength difference and the tangent of the vertical track angle measured by the drift chambers,  $\theta_{MWDC}$ , as shown below.

$$\Delta L_{tw}/c = 1.4\theta_{MWDC} \quad (5.20)$$

Fig. 5.24 shows the resolution of RF time in the BigBite spectrometer which is about 270 ps.

## 2. Coincidence Time Between Two Arms

Once the RF time in the individual spectrometers is calibrated, the last term in Eq. 5.18 needs to be determined in order to calculate the coincidence time. For this experiment  $\Delta t_{trigger}$  was measured in a TDC with 60 ps resolution. A final coincidence time spectrum is shown in Fig. 5.25 calculated for the  $(e, e'\pi)$  reaction. A resolution of  $\sigma = 340$  ns was reached using this method.

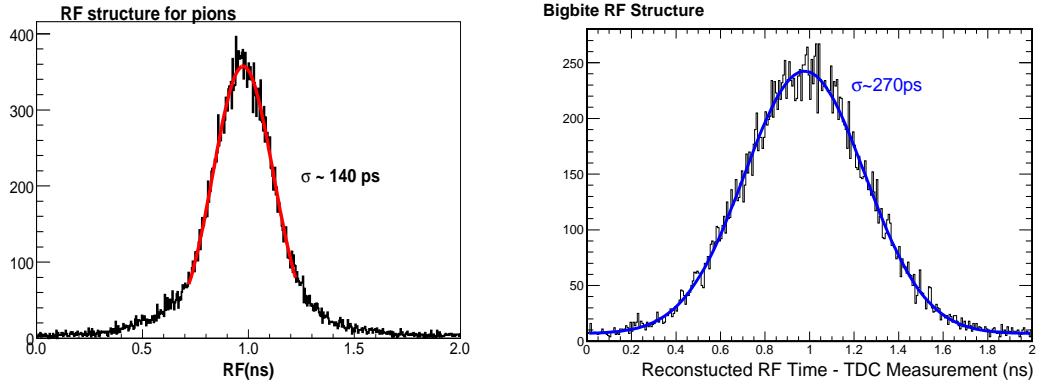


Figure 5.24: Panel on the left (right) shows the timing resolution achieved by the single arm timing detectors in the HRS (BigBite spectrometer) [114].

### 5.1.5 Data Quality Checks

#### 1. Problem related to flaky level-1 accept signal

During the running of this experiment, a very small portion of the data were affected due to intermittent double pulsing of the level-1 ‘accept’ (L1A) signal going to the left HRS DAQ. Since the level-1 accept signal was used for gating ADCs and TDCs, the events associated with a flaky gate signal were affected by this problem. These events were identified by doing various studies during the data analysis. Usually when a track passes through the detector, certain number of PMTs have signals, but it was found that for the problematic events almost all PMTs had signals. By looking at the distribution of number of PMTs that had a hit in a particular event, we could identify these kinds of problematic events. Also, by looking at the hit of the L1A signal in the TDC, one could identify the bad events. For every good event, the L1A signal had a hit in the TDC, but for a bad event, due to time-shift, there was no hit in the TDC. This way we could identify most of the bad events and assign them an event flag. These events were later cut away from the physics analysis.

#### 2. Radiation damage in the BigBite preshower and shower detectors

A gain drop had been observed for the BigBite lead-glass detector signals due to high radiation, especially for the preshower detector because of its closeness to the beam line. Due to radiation the lead-glass blocks change color and become less transparent, and over time this reduces the signals observed on the PMTs attached to the blocks. A position dependent correction was applied to the preshower and shower signals to fix this problem. For this correction the entire data set was divided into several run periods. Each run period was corrected by the slope of a linear fit to the preshower peak versus total accumulated charge.

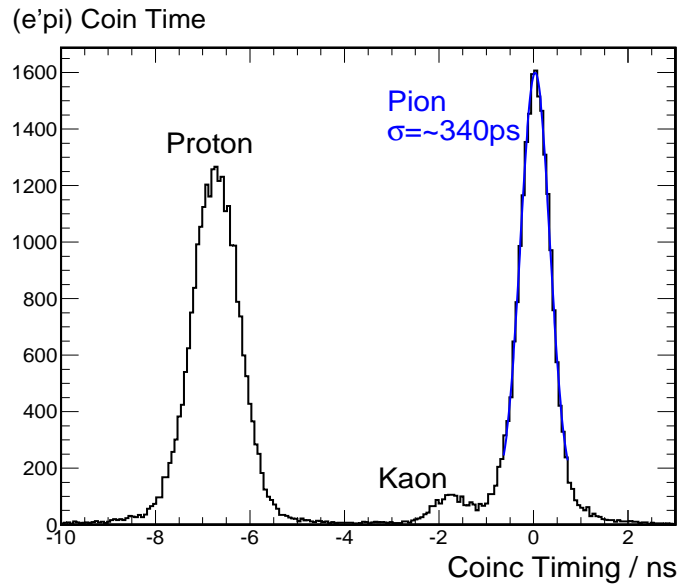


Figure 5.25: Coincidence time-of-flight spectrum for  $(e, e'\pi)$  where a clear separation between protons, kaons and pions is seen [114].

After this, a similar correction was applied to the shower signal by fitting a second order polynomial to the energy over momentum ( $E/p$ ) spectrum vs total accumulated charge. Fig. 5.26 shows the preshower peak value vs. run number. The top panel shows the data before the correction. There is a clear drop in the signal which was corrected as shown in the bottom panel.

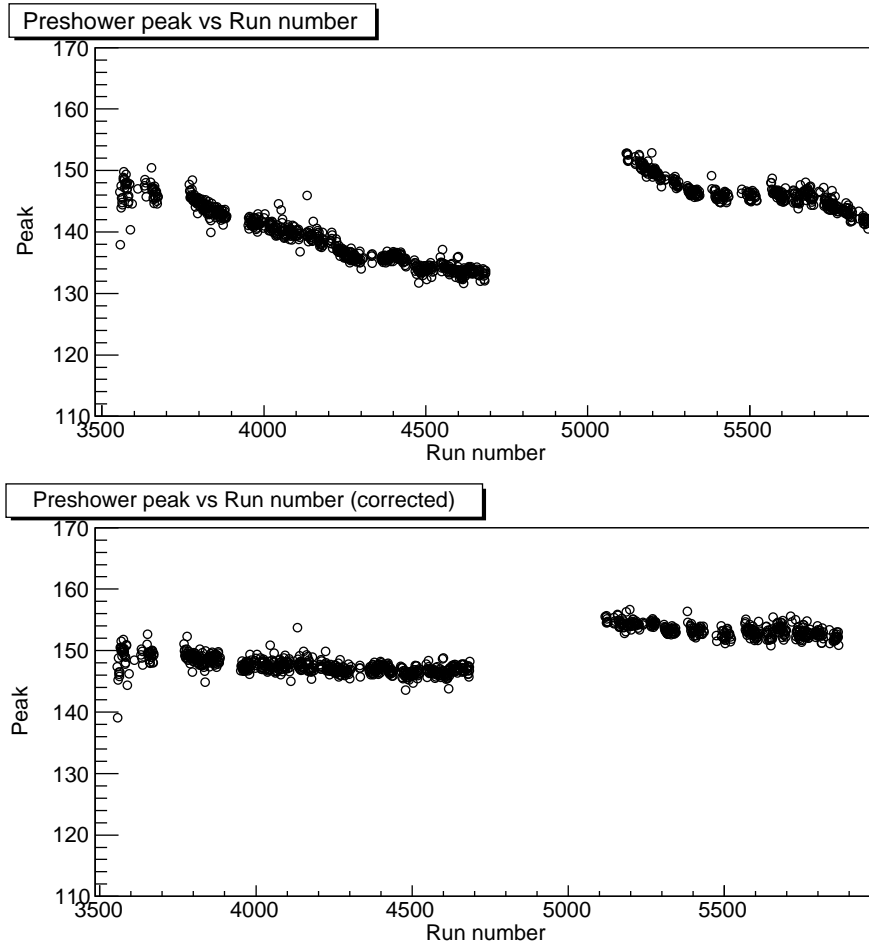


Figure 5.26: Preshower peak vs. run number before and after correction.

## 5.1.6 Scaler Check and Deadtime Measurement

### 1. Scaler Checks

The scaler setup for this experiment is discussed in Sec. 4.8.4. Scalers were used to record the signals from the Beam Current Monitors (BCMs), and the count raw and accepted triggers. A consistency check between two identical copies (one in the BigBite spectrometer and the other in the left HRS) of the scaler signals was done by M. Huang from Duke University. The goal was to find any possible hardware problems with the recorded signals. Although most of the gated scaler signals were found to be good, there were a few signals in the scaler with target spin and helicity combination of  $Tar - Hel-$ , which were found to be inconsistent between the left HRS and BigBite copies. Therefore ungated scalers, which are more reliable, were used to determine the target-spin dependent counts. This was done using the recorded target-spin state for every event in the datastream.

### 2. Deadtime Measurement

During the data acquisition some of the events were lost due to dead time in the DAQ system. This needs to be corrected in the analysis later. Dead time can be caused in two ways - one from the front-end electronics like discriminators or other logic modules which may lose some events in a high rate situation, called electronic dead time (EDT), and the other is due to the DAQ electronics, known as DAQ dead time. When an event occurs, the trigger supervisor accepts the trigger and sends an L1A signal to all the read-out controllers (ROCs) for retrieving the data from the ADCs and TDCs. The trigger supervisor maintains a *busy* state while all the ROCs are being read out. This *busy* state can last anywhere between 300  $\mu s$  to 500  $\mu s$ , depending on the kind of modules used. This waiting period causes a loss of events that occurred during this period. Typically DAQ deadtime is much longer than the electronic deadtime.

To measure the electronic deadtime, a pulser of 12.5 Hz was sent to the front-end trigger electronics which formed a fake trigger. Measuring the number of pulses recorded by the DAQ compared to the number of pulses sent gives an estimation of the electronic dead time. The DAQ deadtime is given by  $1 - LT$ , where  $LT$  is the livetime. The  $LT$  is measured by counting the number of events recorded ( $N_{rec}$ ) by a particular trigger divided by the total number of events ( $N_{tot}$ ) in this trigger (given by the scaler reading). If the triggers are prescaled, then the livetime is given by the following equation:

$$LT = \frac{ps \cdot N_{rec}^{data}}{N_{tot}^{scaler}}. \quad (5.21)$$

where  $ps$  is the prescale factor. In the E06-010 experiment no prescale factor was used, as the coincidence trigger rate was very low.

To correctly account for the livetime, fake EDT pulse counts have to be subtracted from the real trigger counts, both for the recorded counts in the TDC and raw scaler counts. Therefore the livetime reduces to:

$$LT = \frac{ps \cdot (N_{rec}^{data} - N_{EDT}^{data})}{N_{tot}^{scaler} - N_{EDT}^{scaler}}. \quad (5.22)$$

The livetime was typically greater than 85% during this experiment.

## 5.2 Select coincidence kaons and pions

Once all the detectors have been calibrated, the raw data were again decoded with the new calibrated information and this time the physics variables were filled into ROOT trees. Once the physics variables have been obtained, a number of data quality checks were done in order to exclude any bad data. This was done through a “skim” process where the previously generated ROOT trees had been reduced in size by keeping only the essential variables, and also removing any unwanted sections of the data. The following cuts have been implemented as data quality checks in the skimming process.

- **Beam trip cut:** For various reasons the electron beam in the accelerator trips several times during a run (which usually lasts for one hour). When the beam recovers from a trip, it slowly ramps to the set current value. Therefore it is essential to cut away the events within the beam-trip window (defined by a current threshold), since the beam charge monitors are not reliable with low beam current values. However, since the scalers are counting during this period, they have to be adjusted accordingly by identifying the counts before and after the beam-trip window and shifting them back for alignment with the real events. A typical run with a beam-trip is demonstrated in Fig 5.27. The red points are when there is acceptable beam and the black points indicate the periods which were excluded.
- **BigBite wire chamber trip cut:** A small deflection in the beam positions can result in beam hitting the glass wall and producing high rates at the chamber. When this happens the high voltage on the wire chambers trips due to the high currents. The events from the data during this kind of trips were identified and excluded from the physics analysis.
- **Other cuts:** Apart from the above mentioned data quality checks, there were other situations when a tiny fraction of the data is affected due to either DAQ problems or the problems related to the detectors. During the skimming process, all these run periods were identified and excluded.

Once the data files were reduced in size and all the necessary checks were performed, the event selection was done using the particle identification and quality cuts on the track reconstruction.



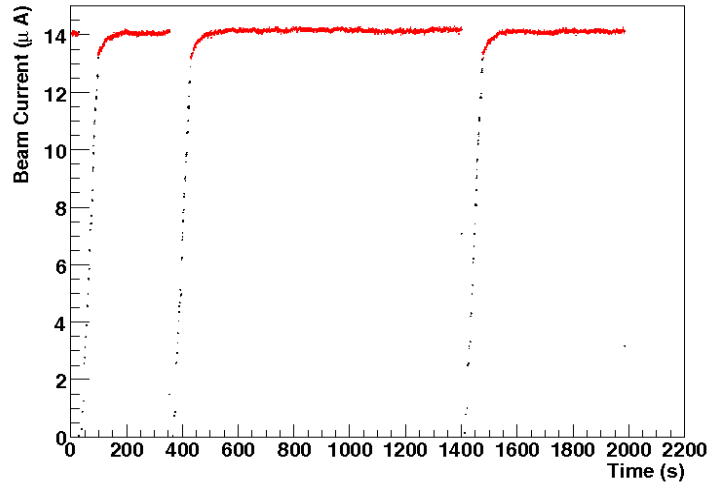


Figure 5.27: Plot showing beam trip cuts for one run. The black points are excluded from the analysis [111].

After detectors were calibrated and bad regions were cut away, the pure coincidence kaons, pions and protons need to be identified (in this thesis, the kaons are the focus), in order to get pure coincidence kaons, pions and protons, the coincidence electrons in Bigbite need to be selected and simultaneously the coincidence kaons, pions and protons need to be identified in left HRS. For selecting coincidence electrons in BigBite and identifying coincidence kaons, pions and protons in left HRS, the different cuts in BigBite and left HRS and the time-of-flight (TOF) between BigBite and left HRS need to be studied.

### 5.2.1 Cut study for coincidence electrons in BigBite

In BigBite side, there are five event categories which are called “electron-like events”, “positron-like events”, “negative-charged-hadron-like events”, “positive-charged-hadron-like events”, and “photon-like events”. All the events can be separated by the BigBite calorimeter system together with the reconstructed momentum information with Preshower, Shower energy deposit and charge type cut. For the purpose of SSA of coincidence kaon, the “electron-like events” are used to select good electrons, “the positron-like events” are used to identify the contamination of photon-induced electrons, and “the negative-charged-hadron-like events” are used to estimate the  $\pi^-$  contamination in selected coincidence T5 electrons.

The conditions for selecting coincidence electrons in Bigbite are as following, there are the same cuts and same procedure between BigBite with coincidence pions and with coincidence kaons and protons in left HRS. The coincidence electron’s cuts are contributed by X. Qian (Duke University) and K. Allada (University of Kentucky).

First, the coincidence events must be applied, the cut is

- The coincidence events cut:

$$(DL.evttypebits \& 1 < 5) == (1 < 5) \& \& Ndata.DL.edtpbb == 0. \quad (5.23)$$

where  $1 \& 5$  is algorithm symbol for choosing coincidence T5 event,  $Ndata.DL.edtpbb$  is the events which were man-made pulse for checking electronics.

then the real BigBite cuts for selecting coincidence electrons are applied as following:

- Track Quality Cut: The quality of the reconstructed track is defined as  $\chi^2/N_{dof}$ . Here  $N_{dof}$  is the number of degrees of freedom. A cut of 2.4 was applied to remove the reconstructed tracks at high  $\chi^2/N_{dof}$ . The false asymmetry which introduced by this cut estimated by comparing the mean value of  $\chi^2/N_{dof}$  in T5N (coincidence channel in LHRS negative polarity) to the mean value of  $\chi^2/N_{dof}$  in T5P (coincidence channel in LHRS positive polarity) was less than  $1.5 \times 10^{-4}$ .

$$BB.tr.chi[BB.ts.sh_flag_tr]/BB.tr.ndof[BB.ts.sh_flag_tr] < 2.4 \quad (5.24)$$

- Track Matching Cut:

The BigBite calorimeter provided the center position of the reconstructed shower cluster. For any charged particle, the position of the reconstructed cluster center (x and y) should match with the projected position from the reconstructed track on the shower. A coincidence electron tracking matching cut was applied.

- Optics Validity Cut:

The magnetic field is weaker at the very top and bottom of the BigBite magnet than that in the middle of the BigBite magnet. The optics reconstruction failed at the top and bottom regions. Therefore a 2-D graphic cut was used to exclude these two regions.

- Charge Type Cut: The charges of the particles were identified from the reconstructed tracks. Since the BigBite magnet provide a simple dipole field, the negatively charged particles are bent up and the positively charged particles are bent down. Therefore, they are clearly separated in the plot of vertical position (Position in X) and the vertical slope (Slope in X) in the first chamber, as illustrated in Fig. 5.28.

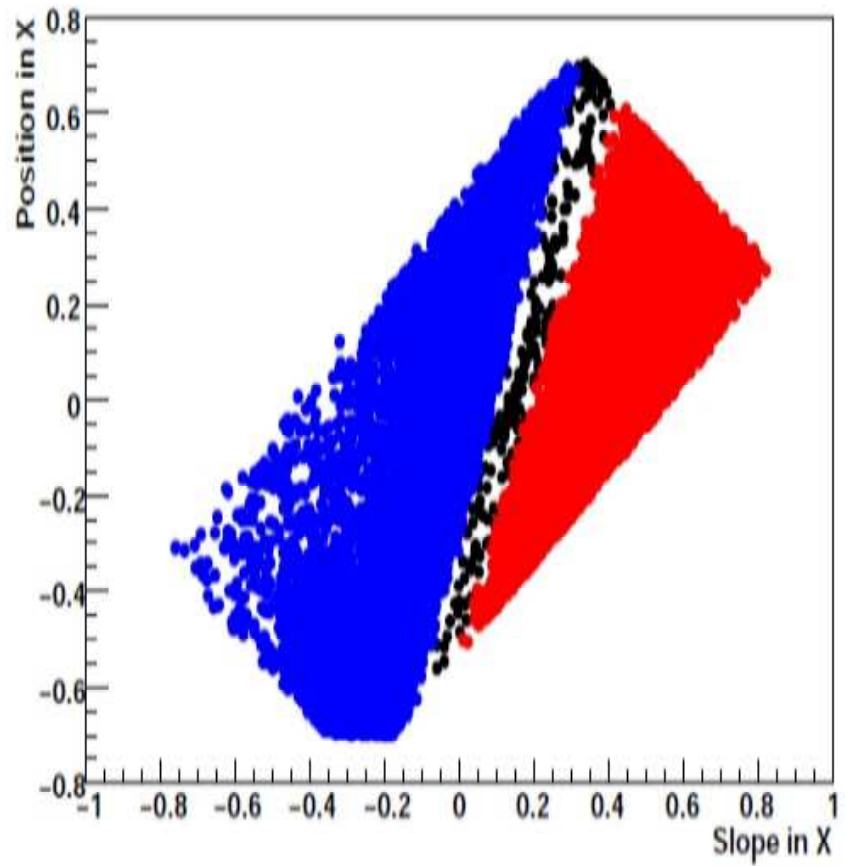


Figure 5.28: Vertical position (Position in X) vs the vertical slope (Slope in X) in the first chamber. The blue points are the negative charged particles in normal production runs. The red points are positive charged particles in normal production runs. The black region was neglected. Fig. is from [111].

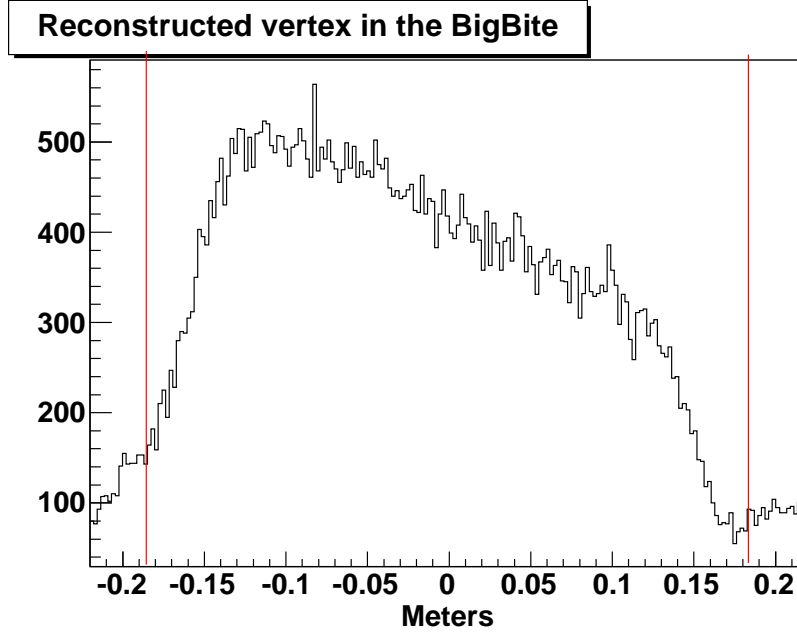


Figure 5.29: Reconstructed vertex is shown for electron-like events. The cut positions at  $\pm 0.185\text{m}$  are for target events. The peaks at  $\pm 0.2\text{m}$  are due to the BigBite target collimator.

Even though we only need to select coincidence electrons in BigBite, for the SIDIS events, we also need to understand the electron contamination from the decay of  $\pi^0$ . Therefore, the positron production also need to be studied in BigBite. Different charge type are shown in Fig. 5.28. During the experiment, the polarity of BigBite was changed to positive for reference runs. Studying both the reference positron runs and the normal production runs allows us to determine the electron contamination from decay of  $\pi^0$ .

– Interaction Vertex cut:

There are several different interaction vertex cuts for different trigger types T1, T6, T5. For coincidence events T5, the BigBite interaction vertex cut is  $(-0.185\text{m}, 0.185\text{m})$ , as in Fig. 5.29.

– Calorimeter PID cut:

The PID cut for electrons was selected with a 2-D cut on the energy deposited in preshower vs the  $E/p$ , the ratio of the total energy deposited in the Pre-Shower and Shower system to the reconstructed momentum. Fig. 5.30 shows a selected PID cut with T5 coincidence trigger. The electrons and pions are indicated in the plot. In order to select electron, the energy deposited in preshower was required to be larger than 200 MeV and the ratio of  $E/p$  was selected as  $\pm 20\%$  around 1 (from 0.8 to 1.2) as the plot shows.

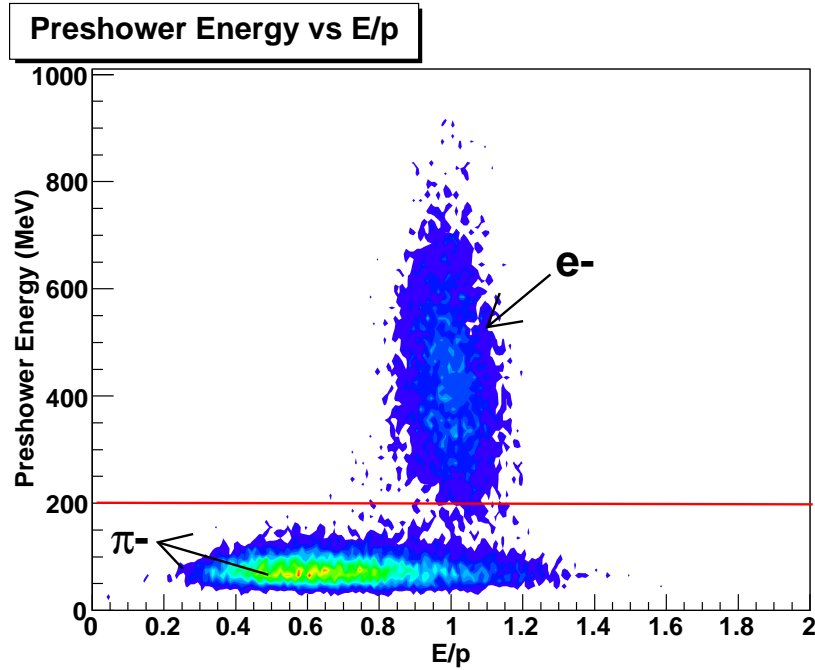


Figure 5.30: Energy deposited in the Preshower vs  $E/p$ . The separated electrons and pions are figured out in the plot.

- Position match cut: The center of the shower cluster was matched with the projected track position. A  $3\text{-}\sigma$  cut for the difference between the projected track position and the center of shower cluster, for both X and Y, was used as the standard cut.
- Particle momentum cut:

$$0.6 < p < 2.5\text{GeV} \quad (5.25)$$

In order to study contamination due to the  $\pi^0 \rightarrow 2\gamma$  followed by  $\gamma \rightarrow e^+e^-$ , the BigBite magnet polarity was changed to positive positron reference runs. Due to the short reference runs and the very small kaon production rate, it is not so useful for the kaon data. However it can also be viewed as a reference hint. In addition, the normal production runs can be used with positron events (when charge type cut changed to +1), the positron events roughly only need to change the charge type cut in production runs.

## 5.2.2 Contamination Study for Identifying DIS Electrons in BigBite

- Negative Pion Contamination

In the BigBite spectrometer, the main contamination to the electron sample was negative pions. Unlike the left HRS which has several detectors for identifying electrons, the BigBite depends entirely on the preshower and shower detector systems to identify the electrons. So there is no independent check for the pion contamination. Indeed, preshower is most effective in electron/pion separation, so we estimate the contamination by fitting the preshower energy deposition  $E_{preshower}$  spectrum. When selecting the coincidence electron in BigBite, the cut  $E_{preshower} < 0.2$  GeV (<400 channels) was selected to remove all the negative pions. Fig. 5.31 shows the negative pion peak around 200 channels modeled as Gaussian convoluted Landau function to find negative pion contamination.

The pion contamination  $f_{cont}$  was calculated by Eq. 5.26:

$$f_{cont} = \frac{\int_{400}^{\infty} f_{gl}(x) dx}{N_{ele}^{>400channels}}. \quad (5.26)$$

Where  $f_{gl}$  is the Gaussian function convoluted with Landau function obtained from the fitting procedure.  $x$  is the channel number of the preshower energy deposition.

Fig. 5.31 shows the result for pions in the HRS. For kaons and protons in the HRS, the same method was used to determine the pion contamination and the results are shown in Table 5.3.

Table 5.3: Pion contamination in the coincidence electron sample in BigBite with coincidence kaon and proton in left HRS.

| Hadrons type in left HRS                    | x1   | x2   | x3   | x4   |
|---|------|------|------|------|
| K <sup>+</sup> %                            | 2.05 | 2.65 | 1.89 | 1.21 |
| K <sup>-</sup> %                            | 0.75 | 0.90 | 0.81 | 1.27 |
| proton ( $wp > 1.6$ GeV && $wp < 10$ GeV) % | 2.62 | 2.88 | 1.47 | 1.28 |
| proton (no wp cut) %                        | 5.64 | 5.76 | 2.65 | 1.89 |

The negative pion contamination to coincidence electrons in BigBite for positive (negative) kaons in left HRS are all less than 3% (1.5%), if there are no wp cut, it will reach almost 6% for first bin and second bin in x.

## $\pi^-$ contamination (coincidence T5)

HRS positive

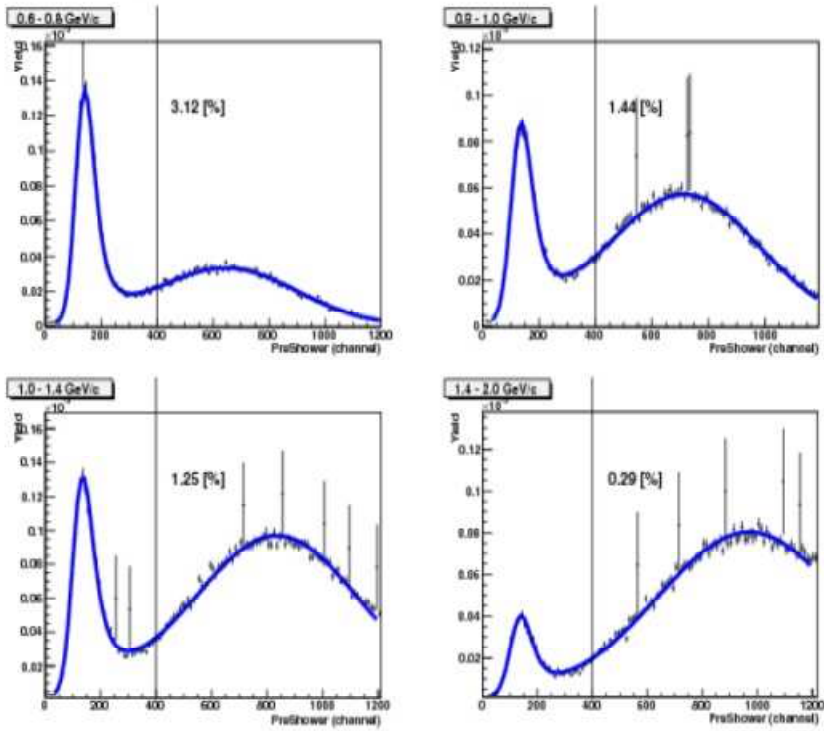


Figure 5.31: Negative pion contamination to electron in coincidence channel (T5) in four x bins. The negative pion peak around channel 200 is convoluted by one Gaussian function with Landau function by exact fitting.

The four x bins are scaled by: first bin ( $0.0622 \leq x < 0.1634$ ), second bin ( $0.1634 \leq x < 0.2162$ ), the third bin ( $0.2162 \leq x < 0.2866$ ), the fourth bin ( $0.2866 \leq x < 0.4978$ ).

- Photon Induced Electron Contamination

In experiment E06-010, there are many photon-like events, these high energy photon were dominated by the decay products of  $\pi^0$  produced in the collision. The lifetime of  $\pi^0$  is very short about  $8.4 \times 10^{-17}$ s [127]. It decays in two ways as Eq. 5.27 and Eq. 5.28:

$$\pi^0 \rightarrow 2\gamma \tag{5.27}$$

$$\pi^0 \rightarrow \gamma + e^+ + e^- \tag{5.28}$$

When photon interacts with material, it will also have certain probabilities to produce a pair of electron and positron. So there were electrons originated from  $\pi^0$  produced in target and ending up in the BigBite spectrometer. Such electrons, called “photon-induced” electrons, are a main contamination to the DIS electrons.

For each photon-induced electron, there is one corresponding photon-induced positron. The kinematics for both of them are expected to be the same. Therefore, through analyzing the photon-induced positrons, the photon-induced electrons can be estimated. There are two ways to analyze the photon-induced positrons, one is for the reference positrons runs, which the BigBite polarity was reversed with the same magnetic field strength. In this situation, the standard method for selecting electrons is directly used to select positrons. Then the positron yield can be compared to electron yield in four x bins to get the photo-induced electron ratio. This method is useful for coincidence electron in BigBite with coincidence pions in left HRS, but not for coincidence kaons due to the low statistics. Therefore, we used the second method which used all the production runs to identify positrons when the charge type cut changed to +1. The ratio between the photon-induced electrons and the scattered electron in BigBite with coincidence hadron in left HRS can be obtained. The result are listed in Table. 5.4.

Table 5.4: Photon induced electron contamination ratio in BigBite with to coincidence kaons and protons in left HRS.

| hadron type in left HRS                     | x1 | x2  | x3  | x4  |
|---|----|-----|-----|-----|
| $K^+$ %                                     | 16 | 3.7 | 0.6 | 0.2 |
| $K^-$ %                                     | 19 | 5.2 | 1.3 | 0.7 |
| proton % ( $wp > 1.6$ GeV && $wp < 10$ GeV) | 23 | 7.2 | 2.1 | 1.4 |
| proton % (no wp cut)                        | 22 | 6.7 | 1.8 | 1.3 |



### 5.2.3 Cut study for coincidence kaons in left HRS with time of flight (TOF)

The coincidence pions, kaons and protons were identified by left HRS detector package with time-of-flight (TOF). It is relatively easy to select pions because most electrons were rejected by the gas Cherenkov detector and the kaons and protons can be rejected by the aerogel Cherenkov detector. For the selected aerogel A1 [112] in the E06010, the index of refraction  $n=1.015$ , therefore, the kaons and protons cannot fire A1. Moreover, the coincidence time-of-flight (TOF) for protons is far away from pions.

Due to the low production rate for kaons, it is quite difficult to identify kaons from pions. The combination of gas Cherenkov, aerogel Cherenkov, RICH detector, and TOF information was used to identify kaons as well as protons. Before the combination method is introduced, the general cuts for kaons, protons, and pions are illustrated as follows:

#### 1. Single track and optics acceptance cut

Multi-track events are not well processed on left HRS side. To avoid confusion and technical difficulties, only single-track events are selected. Another cut is the optics acceptance cut “HRS\_RCut”. Fig. 5.32 shows the HRS optics cuts defined in the transversity Elog # 208. For skimmed root files, “HRS\_RCut” are implemented by a flag variable, “L.accep”.  $L.accep = 1$ : Inside the acceptance;  $L.accep = 0$ : outside the acceptance.

$$L.tr.n == 1 \&\& L.accep == 1 \tag{5.29}$$

#### 2. Coincidence vertex

The difference between the reaction vertices determined from the BigBite and the HRS is called coincidence vertex.

A  $3\sigma$  cut of coincidence vertex is applied, as shown in Fig. 5.33.

$$abs(ReactPt_z - BB.tr.vz[BB.ts.sh_flag_tr[]]) < 3. \times \sigma \tag{5.30}$$

where  $ReactPt_z$  and  $BB.tr.vz[]$  are vertex in left HRS and BigBite individually.  $BB.ts.sh_flag_tr[]$  is the flag of multiple tracks of the event corresponding to BigBite shower region.

#### 3. Coincidence Trigger Cut (Scalar)

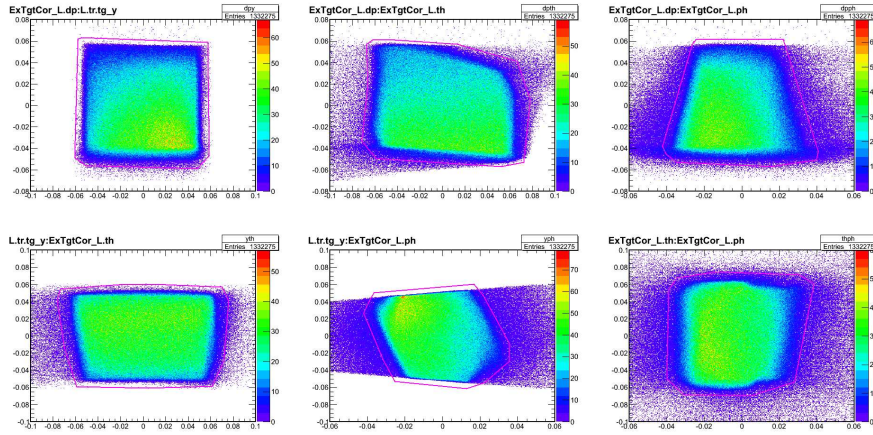


Figure 5.32: Selected main regions in the 4 target variables in 2 dimensions separately:  $ExTgtCor\_L.dp$ ,  $ExTgtCor\_L.ph$ ,  $ExTgtCor\_L.th$ , and  $L.tr.tg.y$ , the 4 dimensions phase space for the left HRS reconstructed optics. The figure is from J. Huang (MIT) [117].

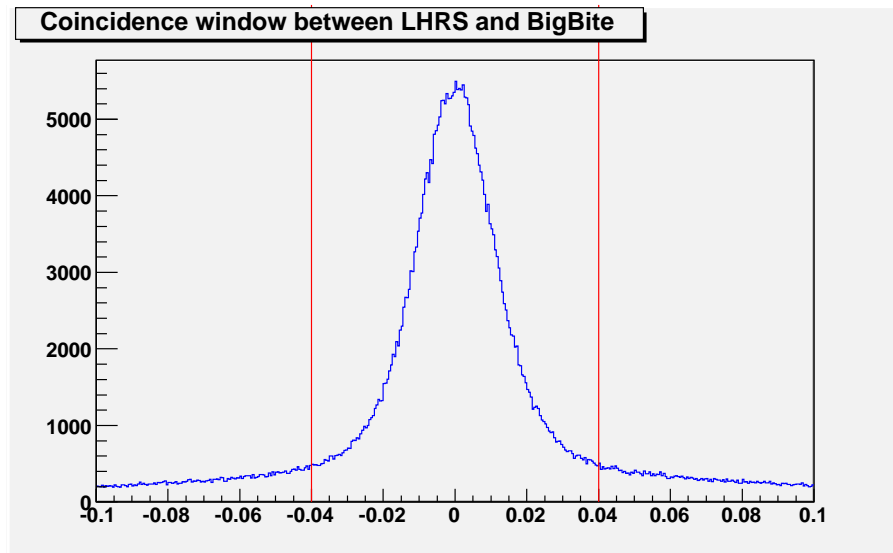


Figure 5.33: Selected coincidence window between left HRS reaction vertex and BigBite reaction vertex, including some random coincidence background events in the coincidence window.

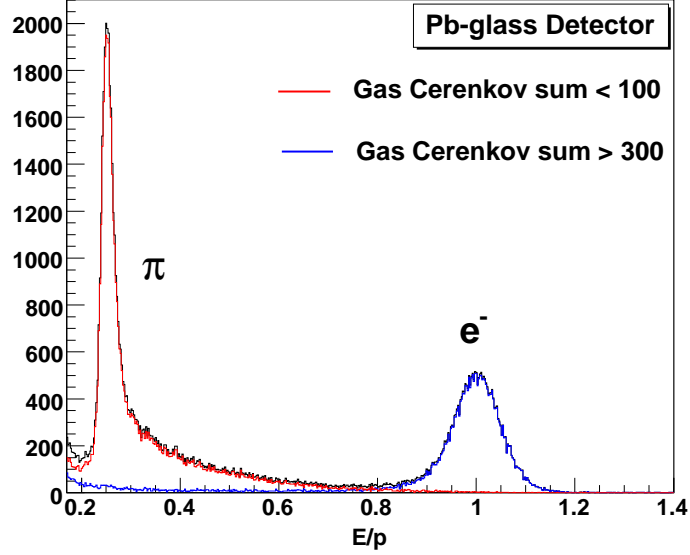


Figure 5.34: The E/P spectrum showing hadrons separated from electrons with the pion rejectors in left HRS. This is the very first step to separate hadrons from electrons. Actually the gas Cherenkov can also clearly separate electrons from hadrons.  $\pi^-$  is the dominant hadron when left HRS is in negative polarity.

Coincidence Trigger Cut is made by requiring the BigBite trigger T1 with left HRS T3 in the coincidence window.

$$(DL.evtypebits \ll 5) == (1 \ll 5) \quad (5.31)$$

Where DL.evtypebits is the event bits from specific trigger type. Obviously the same cut needs to be applied only once for both left HRS and BigBite arms .

4. Energy deposited in two layers of the pion rejector system:

Cut on the pion rejectors is also applied for all the hadrons. For hadrons, the ratio of the energy deposited in pion rejector layer 1 and layer 2 over particle momentum is less than 0.65, as shown in Fig. 5.34.

$$(L.prl2.e + L.prl1.e)/(1000. * ExTgtCor\_L.p) < 0.65 \quad (5.32)$$

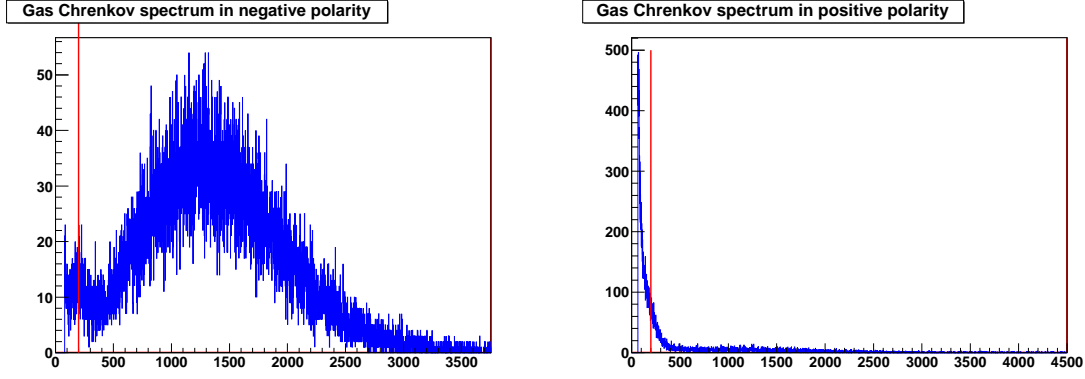


Figure 5.35: Gas Cherenkov spectrum. The red line is shown for the single photo-electron peak. left panel: for negative polarity in left HRS, right panel: for positive polarity in left HRS. In positive polarity, there are no peaks but only some background.

where  $L.prl1.e$ ,  $L.prl2.e$  are the energy deposited in pion rejector layer1 and layer 2 individually, and the variable  $ExtgtCor\_L.p$  is the momentum of the detected particle in LHRS measuring with the extended target.

5. The Track projections on the pion rejector 1:

$$L.prl1.trx > -1.5 \&\& L.prl1.trx < 1.0 \quad (5.33)$$

$$abs(L.prl1.try) < 0.22 \quad (5.34)$$

where  $L.prl1.trx$ ,  $L.prl1.try$  are the track projections in X, Y directions on the pion rejector layer 1, respectively.

Now the gas Cherenkov detector, the aerogel Cherenkov detector, and the RICH detector need to be used with TOF to identify coincidence kaons and protons.

Fig. 5.35 shows the gas Cherenkov spectrum. The red line is the channel 200 which was the location of the single photo-electrons peak. As described in Sec. 5.1.3, in negative polarity, there are a big main spectrum for electrons. For the positive polarity, there are no main peaks but some background. The cut for pion rejector energy deposited has been removed in order to see the main electron peak in negative polarity. To clearly see the single photon peak and main electron spectrum, a huge peak at channel less than 80 was cut away.

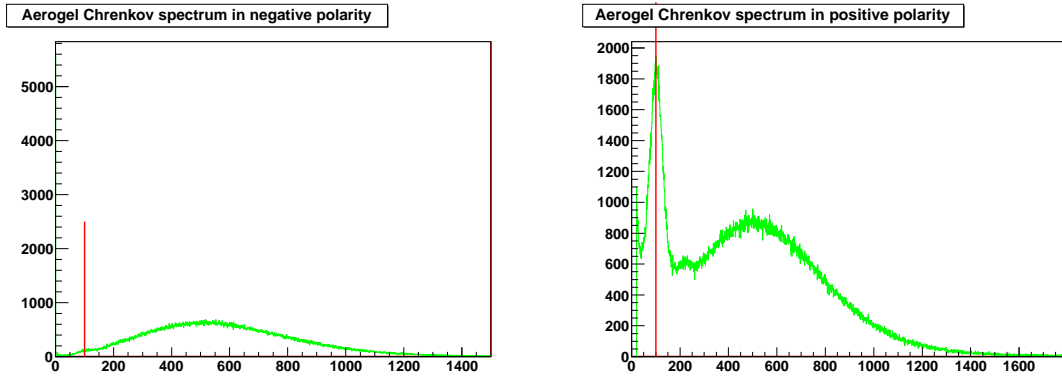


Figure 5.36: Aerogel Cherenkov spectrum, the red line aligned at channel 100 is shown for the single photo-electron peak. left panel: for negative polarity in left HRS, right panel: for positive polarity in left HRS. In positive polarity, there is a huge single photon peak caused by the residual signal from proton.

For pions, the gas cherenkov cut is:

$$L.cer.asum_c < 250. \quad (5.35)$$

Fig. 5.36 shows the aerogel Cherenkov spectrum. The red line at channel 100 is shown for the single photo-electron peak. left panel: for negative polarity in left HRS, right panel: for positive polarity in left HRS. In positive polarity, there is a huge single photon peak caused by the residual signal from proton.

For pion, the aerogel Cherenkov cut is:

$$L.a1.asum_c > 150. \quad (5.36)$$

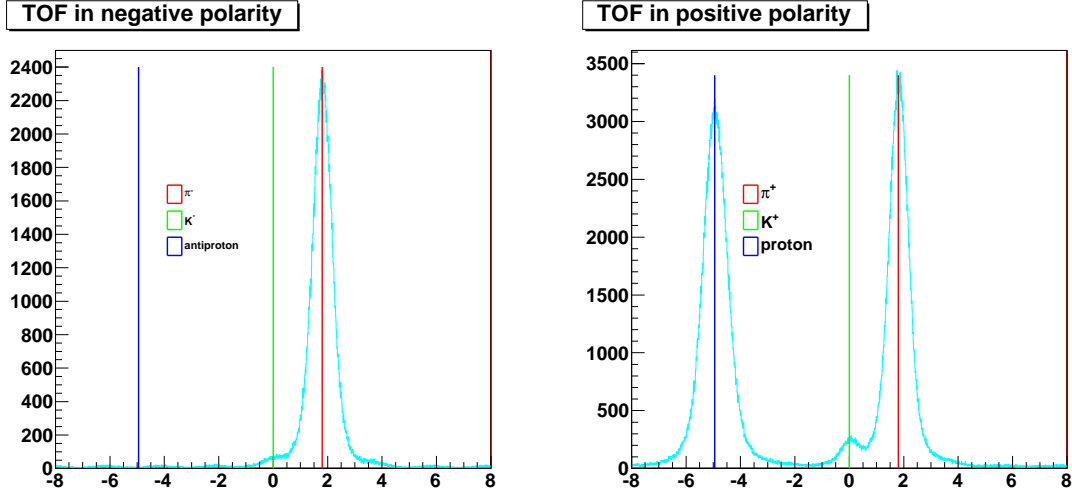


Figure 5.37: Time-of-flight (TOF) spectrum, the red line corresponds to the location of pion peak, the green line corresponds to the location of kaons, the blue line corresponds to the location of protons (if left HRS at positive polarity). Left panel: for negative polarity in the left HRS, a very small bump shows up at the kaon peak along with a huge pion peak. There is almost no event near the anti-proton peak. Right panel: for positive polarity in left HRS. One huge peak is for proton at left side and one huge peak is for  $\pi^+$  at the right side. There is a small peak for  $K^+$ .

Fig. 5.37 shows the TOF spectrum: the red line corresponds to the location of pion peak, the green line corresponds to the location of kaons, and the blue line for protons (if left HRS at positive polarity). For negative polarity in left HRS, a very small bump shows up at the kaon peak along with a huge pion peak. There is no anti-proton peak at the location of anti-proton. For positive polarity in left HRS, one huge peak is for proton at left side and one huge peak is for  $\pi^+$  at the right side. There is a small peak for  $K^+$ .

For identifying pions, we first applied the following cuts:

$$L.cer.asum_{\mathcal{L}} < 250 \&\& L.a1.asum_{\mathcal{L}} > 150 \&\& abs(CT.pi.t) < 3. \quad (5.37)$$

where  $CT.pi.t$  is the variable for coincidence time based on the pion location in TOF spectrum and  $abs$  is symbol for absolute value in mathematics.

After the selected cuts, the time of flight spectrum is shown as Fig. 5.38. The kaon peak is mostly excluded, although there is still a proton peak, it is small and far away from the pion peak. Using a 6ns TOF window for pion, the random proton background is greatly suppressed.

After applying the pion cuts as Eq. 5.37. The  $K^+$  contamination to coincidence  $\pi^+$  sample is less than 1%. For coincidence  $\pi^-$ , the  $K^-$  contamination is even less.

In order to identify coincidence kaons, it is more difficult because the kaon peak is in the tail of a huge pion peak. Even after applying aerogel Cherenkov cut to reject pions, many pions remain due to pion

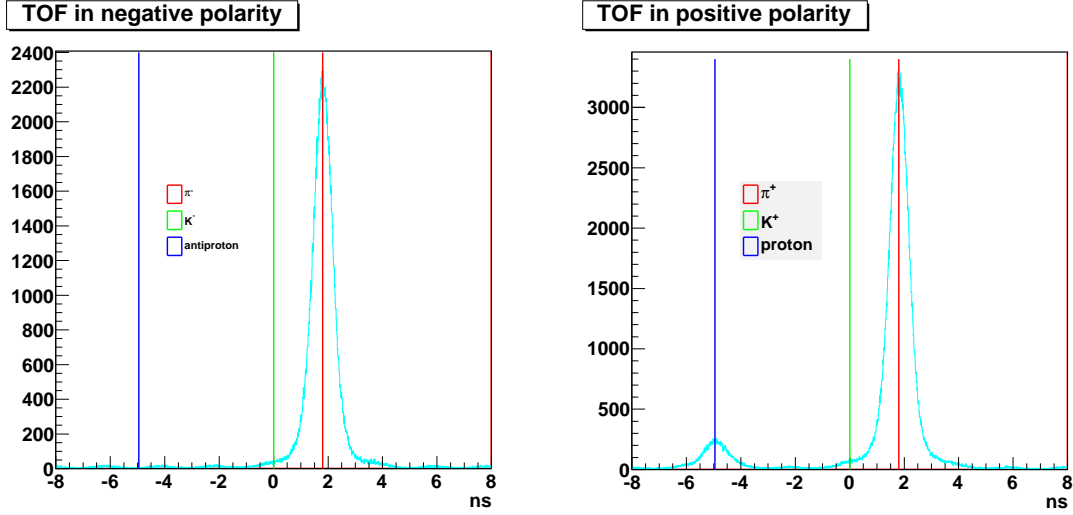


Figure 5.38: Time-of-flight(TOF) spectrum after applying the cuts for pions, the red line corresponds to the location of pion peak,the green line corresponds to the location of kaons, the blue line corresponds to the location of protons(if left HRS at positive polarity) . left panel:for negative polarity in the left HRS, there is no a very small bump shows up at the kaon peak along with a huge pion peak. right panel: for positive polarity in left HRS. One peak is still for proton at left side corresponding to blue line but it is greatly suppressed and far away from pion 6ns window, one huge peak is for  $\pi^+$  corresponding to red line, there is no a small peak for  $K^+$  corresponding to the the location of green line.

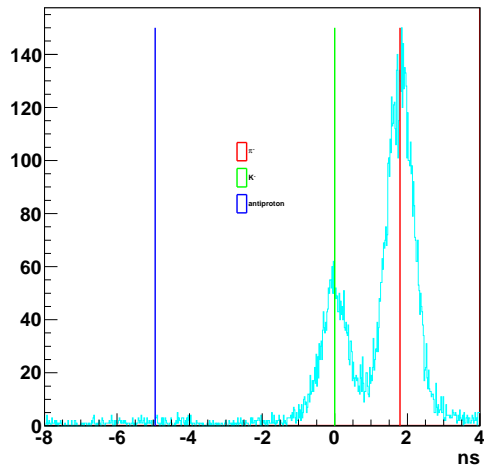
rejection inefficiency or “slow” pions. For example, if applying cut  $L.cer.asum_c < 250$  (excluding electrons) &&  $L.a1.asum_c < 150$  (excluding pions), many pions remain in kaon samples, as shown in Fig. 5.39. So more optimization is required to get pure kaons as well as protons.

We have obtained the TOF spectra using various cuts for the gas Cherenkov and the aerogel Cherenkov, as shown in Fig. 5.40. To maximize the kaon efficiency and minimize the pion contamination, we use the following cuts for kaons:

$$L.cer.asum_c < 30 \ \&\& \ L.a1.asum_c < 125 \ \&\& \ abs(CT.K.t) < 1. \quad (5.38)$$

Fig. 5.40 shows the two-gaussian fits to the pion and kaon peaks. From these fits, one can obtain the kaon counts and the pion contamination. The RICH detector provides additional information for determining the pion contamination, as discuss next.

TOF in negative polarity  $cer < 250$   $a1 < 150$



TOF in positive polarity  $cer < 250$   $a1 < 150$

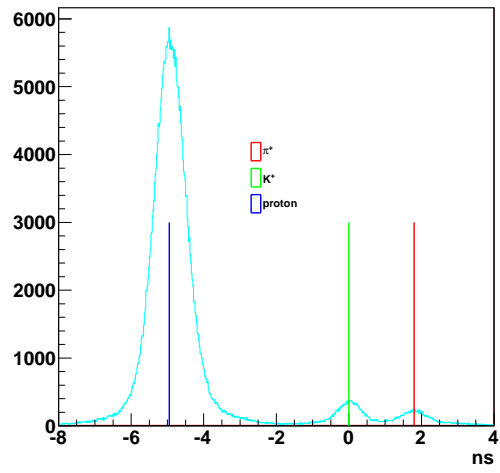


Figure 5.39: after applying cuts of  $L.cer.asum_c < 250$  &  $L.a1.asum_c < 150$ ., there are still pion contamination in kaon especially in negative situation.



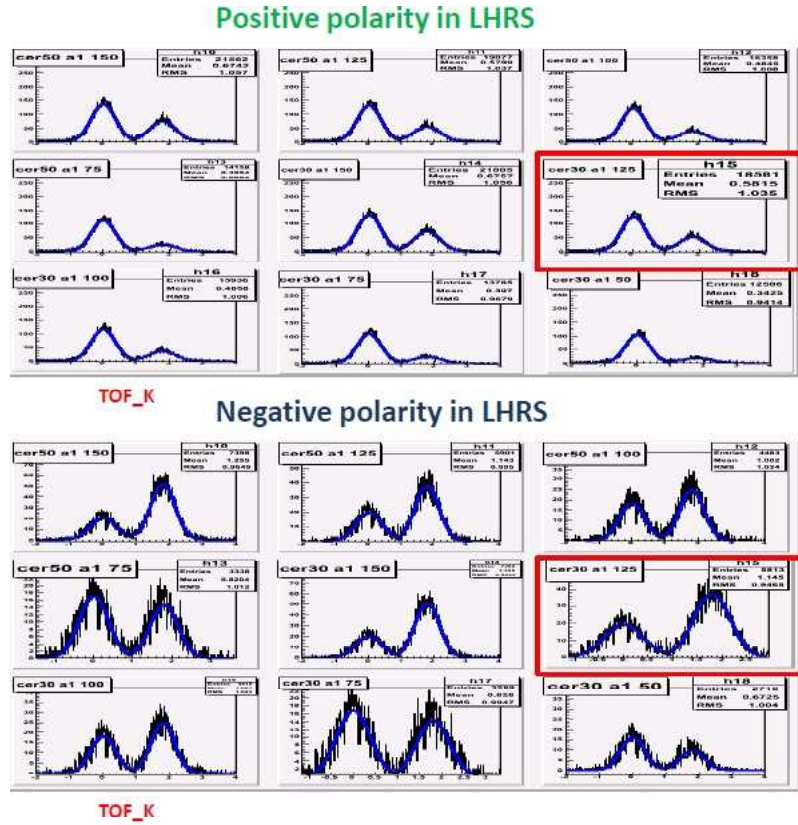


Figure 5.40: The TOF spectra for various cuts on gas and aerogel Cherenkov together with two-gaussian fits to the pion and kaon peaks. The upper panel is for positive polarity in left HRS, the lower panel is for negative polarity in left HRS. There are nine small pad for figuring out the counts and contamination. The different cuts correspond to 1.  $cer < 50 \& \& a1 < 150$ , 2.  $cer < 50 \& \& a1 < 125$ , 3.  $cer < 50 \& \& a1 < 100$ , 4.  $cer < 50 \& \& a1 < 75$ , 5.  $cer < 30 \& \& a1 < 150$ , 6.  $cer < 30 \& \& a1 < 125$ , 7.  $cer < 30 \& \& a1 < 100$ , 8.  $cer < 30 \& \& a1 < 75$ , 9.  $cer < 30 \& \& a1 < 50$ . The combined cuts  $cer < 30 \& \& a1 < 125 \& \& abs(CT.K.t) < 1$ . was selected to optimize the kaon counts with less than 3% pion contamination.

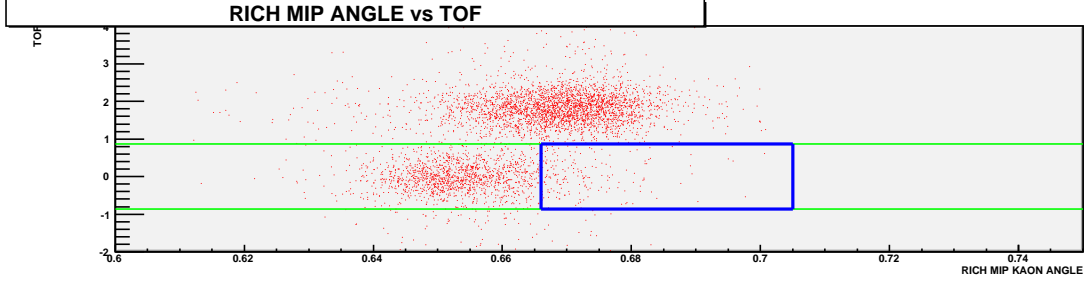


Figure 5.41: The cone angles measured by RICH versus TOF for events with negative HRS polarity. The TOF cuts applied for kaon events are shown as green curves. The blue box indicates the region of pion contamination.

The RICH detector was designed to identify pions, kaons and proton. Due to small statistics of kaons, RICH has been used to determine contamination of pions in kaons and to identify the antiprotons. When the gas Cherenkov, aerogel Cherenkov, TOF are combined with RICH, the final cuts for kaons are determined based on the criteria to maximize kaons with pion contamination less than 5%. The combined cuts are modified to  $cer < 30$  and  $a1 < 125$  and  $abs(CT.K.t) < 0.87$ .

Table 5.5 shows pion contamination in kaon with two different kaon TOF cut regions:  $abs(CT.K.t) < 1$ . and  $abs(CT.K.t) < 0.87$ , we applied  $abs(CT.K.t) < 0.87$  for the criteria pion contamination in kaon less than 5% when LHRS in negative polarity after applying all the other cuts.

Table 5.5: pion contamination in kaon

|                          | pion contamination | pure particles |
|--------------------------|--------------------|----------------|
| $K^+$ TOF_K(-1., 1.)     | 1.7%               | 98.3%          |
| $K^+$ TOF_K(-0.87, 0.87) | 0.9%               | 99.1%          |
| $K^-$ TOF_K(-1., 1.)     | 9.1%               | 90.9%          |
| $K^-$ TOF_K(-0.87, 0.87) | 4.2%               | 95.8%          |

Fig. 5.41 illustrates how the RICH information can be utilized to determine the pion contamination in the kaon events. In Fig. 5.41, the cone angle measured by the RICH is plotted versus the TOF. As shown by events in the blue box, some events which satisfy the TOF cut for kaons do not have the RICH angles expected for kaons. This allows us to determine the pion contamination in the kaon events. Similar procedure is also applied to the  $K^+$  and proton analysis.

The final cuts are follows:

Kaons:

$$L.cer.asum_c < 30 \& \& L.a1.asum_c < 125 \& \& abs(CT.K.t[BB.ts.sh_flag_tr]) < 0.87 \quad (5.39)$$

Protons:

$$L.cer.asum_{\mathcal{C}} < 30 \&\& L.a1.asum_{\mathcal{C}} < 150 \&\& abs(CT.p.t[BB.ts.sh\_flag\_tr]) < 3. \quad (5.40)$$

Pions:

$$L.cer.asum_{\mathcal{C}} < 250 \&\& L.a1.asum_{\mathcal{C}} > 150 \&\& abs(CT.pi.t[BB.ts.sh\_flag\_tr]) < 3. \quad (5.41)$$

where  $L.cer.asum_{\mathcal{C}}$ , and  $L.a1.asum_{\mathcal{C}}$  correspond to the adc sum of the gas Cherenkov detector, and the aerogel Cherenkov detector, respectively.  $CT.K.t[BB.ts.sh\_flag\_tr]$ ,  $CT.p.t[BB.ts.sh\_flag\_tr]$ , and  $CT.pi.t[BB.ts.sh\_flag\_tr]$  correspond to the time-of-flight of kaons, protons and pions between BigBite and LHRS.

In BigBite detector, not only the single-track events but also the multitrack events are selected. The majority coincidence events are due to single-track events. Using the above cuts for coincidence kaons, protons and pions, the fractions of single-track events in BigBite are 98.2% for  $K^+$ , 97.8% for  $\pi^+$ , 97.3% for proton, 97.7% for  $K^-$ , 98.5% for antiproton, and 97.8% for  $\pi^-$ . Since there are no reasons to exclude the multitrack coincidence events, the final events are based on the single-track events in LHRS in coincidence with single- or multi-track events in BigBite.

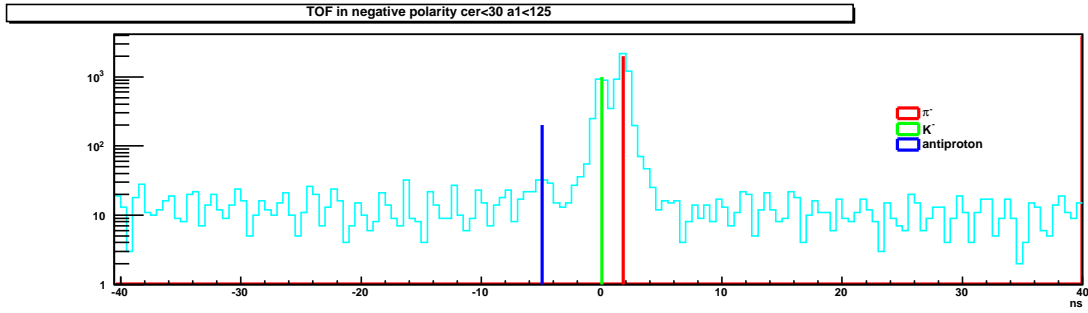


Figure 5.42: The TOF spectrum for negative LHRs polarity. The expected locations for  $\pi^-$ ,  $K^-$ ,  $\bar{P}$  are indicated by red, green, and blue lines, respectively. The accidental coincidence events form a continuous background, and the 2ns beam structure is clearly visible.

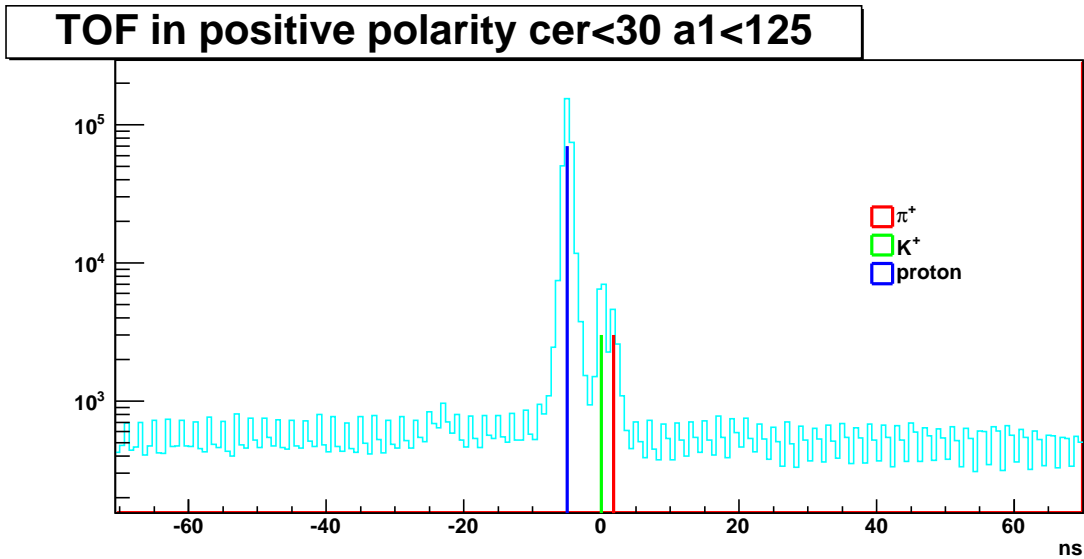


Figure 5.43: The TOF spectrum for positive LHRs polarity. The expected locations for  $\pi^+$ ,  $K^+$ ,  $P$  are indicated by red, green, and blue lines, respectively.

### Random coincidence background

Random coincidence between the BigBite and LHRs events are due to two separate interactions from two different electrons in the beam. Such random coincidences would produce a continuous background in the TOF spectrum, as shown in Fig. 5.42 and Fig. 5.43. The 2ns micro-structure is clearly visible in the TOF spectra and reflects the time structure of the electron beam.

For coincidence  $K^-$ , the random background is mainly caused by the pions (antiprotons are negligible). For coincidence  $K^+$ , the background is not only caused by the random pions, but mainly caused by protons. For pions and protons, due to their high production rates, the background is relatively small. It is very different for anti-protons, which has large background. With the final cuts, the background fractions are 2.7% for  $K^+$ , 0.4% for  $\pi^+$ , 0.4% for proton, and 0.4% for  $K^-$ , 0.5% for  $\pi^-$ , and 29.5% for anti-proton.

The accidental background was estimated from regions outside of the coincidence pion, proton, kaon peaks, and normalized according to the width of the kaon ( $2 \times 0.87 = 1.74 \text{ ns}$ ), pion ( $2 \times 3 \text{ ns} = 6 \text{ ns}$ ), and protons ( $2 \times 3 \text{ ns} = 6 \text{ ns}$ ) TOF windows.

**The demanded coincidence  $K^+$ ,  $K^-$ , pions and protons.**

After applying these cuts for kaons, pions and protons, the total counts of coincidence hadrons in LHRS are shown in table 5.6.

Table 5.6: Total counts of coincidence hadrons

|             | total coincidence event (up/down or left/right) |
|-------------|---|
| $K^+$       | 11789(5842/5921)                                |
| $\pi^+$     | 250865(124593/125795)                           |
| proton      | 259282(128747/130035)                           |
| $K^-$       | 2087(1066/1017)                                 |
| $\pi^-$     | 185844(93335/92150)                             |
| anti-proton | 131(43/88)                                      |

After selecting the kaon and proton events, we are ready to extract the Collins moment and Sivers moment. There are two methods which can be used, namely, the least square fit method [115] and the maximum likelihood method [115]. Due to small production rates of kaons, especially for  $K^-$ , it is not suitable to use the least squares fit method due to the limited statistics in certain azimuthal bins and non-Gaussian statistics. Therefore, the maximum likelihood method was used to extract the kaon Collins and Sivers moments.

## 5.3 The Maximum Likelihood Method

### 5.3.1 The least square method

In Semi-Inclusive DIS, the asymmetry  $A_{UT}^h(\phi_h, \phi_S)$  of the cross section in the unpolarized beam with transversely polarized target between the two opposite target transverse spin states with spin direction labelled in  $\phi_S$  and produced hadron direction labelled in  $\phi_h$  is given as:

$$A_{UT}^h(\phi_h, \phi_S) \propto \frac{\sigma^\uparrow - \sigma^\downarrow}{\sigma^\uparrow + \sigma^\downarrow} \quad (5.42)$$

$$= \frac{1}{\langle P_t \rangle} \frac{N_{h,norm}^\uparrow(\phi_h, \phi_S) - N_{h,norm}^\downarrow(\phi_h, \phi_S)}{N_{h,norm}^\uparrow(\phi_h, \phi_S) + N_{h,norm}^\downarrow(\phi_h, \phi_S)} \quad (5.43)$$

Where  $N_{h,norm}^{\uparrow(\downarrow)}$  is the luminosity-normalized SIDIS event yield for hadron type h and spin state up(down) or right(left), and  $\langle P_t \rangle$  represents the average target transverse polarization.

Further,

$$\frac{N_{h,norm}^{\uparrow}(\phi_h, \phi_S) - N_{h,norm}^{\downarrow}(\phi_h, \phi_S)}{N_{h,norm}^{\uparrow}(\phi_h, \phi_S) + N_{h,norm}^{\downarrow}(\phi_h, \phi_S)} = \frac{\frac{N_h^{\uparrow}(\phi_h, \phi_S)}{N_{DIS}^{\uparrow}} - \frac{N_h^{\downarrow}(\phi_h, \phi_S)}{N_{DIS}^{\downarrow}}}{\frac{N_h^{\uparrow}(\phi_h, \phi_S)}{N_{DIS}^{\uparrow}} + \frac{N_h^{\downarrow}(\phi_h, \phi_S)}{N_{DIS}^{\downarrow}}} \quad (5.44)$$

where  $N_{DIS}^{\uparrow(\downarrow)}$  is the total DIS yield for certain target spin state.

Then, the asymmetry  $A_{UT}^h(\phi_h, \phi_S)$  becomes:

$$A_{UT}^h(\phi_h, \phi_S) = \frac{1}{\langle P_t \rangle} \frac{N_h^{\uparrow}(\phi_h, \phi_S)N_{DIS}^{\downarrow} - N_h^{\downarrow}(\phi_h, \phi_S)N_{DIS}^{\uparrow}}{N_h^{\uparrow}(\phi_h, \phi_S)N_{DIS}^{\downarrow} + N_h^{\downarrow}(\phi_h, \phi_S)N_{DIS}^{\uparrow}} \quad (5.45)$$

From chapter 4, the asymmetry due to unpolarized beam scattered from transversely polarized target can be written as:

$$A_{UT}^h(\phi_h, \phi_S) = A_{UT}^{sin(\phi_h + \phi_S)} sin(\phi_h - \phi_S) + A_{UT}^{sin(\phi_h - \phi_S)} sin(\phi_h - \phi_S) + C. \quad (5.46)$$

Where C is the pretzelocity term written as  $A_{UT}^{sin(3\phi_h - \phi_S)} sin(3\phi_h - \phi_S)$ .

The Collins moment  $A_{UT}^{sin(\phi_h + \phi_S)}$  and Sivers moment  $A_{UT}^{sin(\phi_h - \phi_S)}$  can be extracted in a Least Square (LS) fit which makes use of the MIGRAD routine of the MINUIT [119] for the  $\chi^2$  minimization. The LS method was used to extract the pion Collins and Sivers moments for the experiment [111].

Owing to the low kaon statistics in Experiment E06010, the LS method is not suitable. When binned in the kinematic variables  $x, z, p_t$ , together with the azimuthal angles  $\phi_h$  and  $\phi_S$ , many bins have very low statistics and the result is not reliable [118].

### 5.3.2 The Maximum Likelihood Method

Maximum Likelihood Method(MLM) is also called Maximum Likelihood Estimator(MLE), which is used to estimate unknown parameters through maximizing the likelihood functions. In Experiment E06010, the maximum likelihood method is described in the proposal [120] and documented by Jin Huang and Yi Qiang [121] in detail. Due to the different conditions for kaons, I have modified the MLM analysis to include the effects from live-time, charge asymmetry, and target polarization.

Here, a long summary will be provided since the kaon Collins and Sivers moments are extracted using the Maximum Likelihood Method.

#### Input data.

In JLab HallA Experiment E06010, the SIDIS reaction  ${}^3He e^{\uparrow}(\vec{e}, e'\pi^{\pm}/K^{\pm})$  with polarized electron beam

and a transversely polarized  $^3He$  target, there are four target spin directions: vertical up/down (also called  $V\pm$ ) and transverse-in-plane with beam right/left (also called  $T\pm$ ). Each target spin state lasts for 20 minutes while beam helicity fast flips at a rate of 30 Hz. There are a total of roughly 3000 spin states during the experiment. Before performing the Maximum Likelihood Method for extracting kaon Collins and Sivers moments, the total charge, DAQ/electronics livetime of each spin state, target/beam polarization, target density and luminosity, and all the kinematics variable  $\phi_h, \phi_S, x, z, p_t, Q^2$  for each individual event had already been extracted.

#### Formula of MLM in Experiment E06010.

In order to extract parameters using MLM, a probability distribution function is defined. In SIDIS, the total yield [122] is simplified as

$$y(\phi_h, \phi_S) = \rho \cdot \sigma \cdot a_{T\pm/V\pm}(\phi_h, \phi_S) \left( 1 + S_T \sum_j \epsilon_j SSA_j(\phi_h, \phi_S) \right) \quad (5.47)$$

where  $\rho$  is the target density,  $\sigma$  is the cross-section of unpolarized beam with unpolarized target,  $a_{T\pm/V\pm}(\phi_h, \phi_S)$  is the acceptance for transverse\_in\_plane ( $\pm$ ) or vertical ( $\pm$ ) spin state,  $SSA_j(\phi_h, \phi_S)$  is the  $j^{th}$  azimuthal single spin angular modulation, for example  $\sin(\phi_h + \phi_S)$ ,  $\epsilon_j$  corresponds to the amplitude of  $SSA_j(\phi_h, \phi_S)$ .  $S_T$  is the transverse target polarization with respect to the  $\mathbf{q}$  vector. By performing the MLM, the  $\epsilon_j$  corresponding to Collins and Sivers moments can be extracted.

The probability of each event is:

$$f(\phi_h, \phi_S) = \rho \cdot \sigma \cdot a(\phi_h, \phi_S) \left( 1 + P \sum_j \epsilon_j A_j(\phi_h, \phi_S) \right) / Norm \quad (5.48)$$

where

$$Norm = \int_0^{2\pi} \int_0^{2\pi} \rho \cdot \sigma \cdot a(\phi_h, \phi_S) \left( 1 + P \sum_j \epsilon_j A_j(\phi_h, \phi_S) \right) d\phi_h d\phi_S \quad (5.49)$$

There are four spin states denoted by  $StateID \equiv i_{T\pm/V\pm}$ , which refers to vertical up/down and transverse\_in\_plane right/left event.

From Eq. 5.48, the probability distribution of each individual event is:

$$\begin{aligned} Pr(StateID \equiv i_{T\pm/V\pm}, \phi_h, \phi_S) &\equiv f_{i_{T\pm/V\pm}}(\phi_h, \phi_S) \\ &= \frac{\tilde{C}_{i_{T\pm/V\pm}}(\phi_h, \phi_S)}{Norm_{exp}} \left( 1 + P_{i_{T\pm/V\pm}} \sum_j \epsilon_j A_j(\phi_h, \phi_S) \right) \end{aligned} \quad (5.50)$$

where

$$\tilde{C}_{i_{T\pm}/V\pm} \equiv \tilde{L}_{i_{T\pm}/V\pm} \times LT_{i_{T\pm}/V\pm} / (\text{Units Conversion Constant}), \quad (5.51)$$

and the normalization function:

$$Norm_{exp} = \sum_{i_{T\pm}/V\pm} \int \int d\phi_h d\phi_S \tilde{C}_{i_{T\pm}/V\pm} a_{T\pm/V\pm}(\phi_h, \phi_S) \left( 1 + P_{i\pm} \sum_j \epsilon_j A_j(\phi_h, \phi_S) \right) \quad (5.52)$$

Here  $\sum_{i_{T\pm}/V\pm}$  is defined as sum over all spin states with state index  $i_{T\pm}/V\pm$ , while  $\sum_j$  is sum over all angular modulation term  $A_j(\phi_h, \phi_S)$ .

In order to simplify the formula, we define:

$$N_{\pm} \equiv \sum_{i_{\pm}} N_{i_{\pm}} \quad (5.53)$$

$$N \equiv N_+ + N_- \quad (5.54)$$

$$N_{P,\pm} \equiv \sum_{i_{\pm}} N_{i_{\pm}} P_{i_{\pm}} \quad (5.55)$$

$$N_{P^2,\pm} \equiv \sum_{i_{\pm}} N_{i_{\pm}} P_{i_{\pm}}^2 \quad (5.56)$$

$$\tilde{C}_{\pm} \equiv \sum_{i_{\pm}} \tilde{C}_{i_{\pm}} \quad (5.57)$$

$$\tilde{C}_{P,\pm} \equiv \sum_{i_{\pm}} \tilde{C}_{i_{\pm}} P_{i_{\pm}} \quad (5.58)$$

We also define several asymmetries, such as:

- effective charge asymmetry

$$A_C \equiv \frac{\tilde{C}_+ - \tilde{C}_-}{\tilde{C}_+ + \tilde{C}_-} \quad (5.59)$$

- effective polarized charge asymmetry

$$A_{CP} \equiv \frac{\tilde{C}_{P,+} - \tilde{C}_{P,-}}{\tilde{C}_{P,+} + \tilde{C}_{P,-}} \quad (5.60)$$

- raw event count asymmetry

$$A_{raw} \equiv \frac{N_+ - N_-}{N_+ + N_-} \quad (5.61)$$

In the case of single spin asymmetries on a transversely polarized target, there are five azimuthal terms [122],



- Three in leading twist:  $\sin(\phi_h + \phi_S)$ ,  $\sin(\phi_h - \phi_S)$ , and  $\sin(3\phi_h - \phi_S)$ ;
- Two in higher twist:  $\sin(\phi_S)$  and  $\sin(2\phi_h - \phi_S)$ .

(For kaons, the leading twist  $\sin(\phi_h + \phi_S)$  and  $\sin(\phi_h - \phi_S)$  are mainly considered.)

All five terms satisfy

$$A_i(\phi_h, \phi_S) = -A_i(\phi_h, \phi_S + \pi). \quad (5.62)$$

Even though in Experiment E06010 acceptance for plus and minus spin states are different for the same  $\phi_S$ , yet we have the identity:

$$a_{T+/V+}(\phi_h, \phi_S) = a_{T-/V-}(\phi_h, \phi_S + \pi) \quad (5.63)$$

Then the normalization function can be arranged into:

$$\begin{aligned}
Norm_{exp} &= \sum_{i_{T+/V+}} \int \int d\phi_h d\phi_S \tilde{C}_{i_{T+/V+}} a_{T+/V+}(\phi_h, \phi_S) \left(1 + P_{i_{T+/V+}} \sum_j \epsilon_j A_j(\phi_h, \phi_S)\right) \\
&+ \sum_{i_{T-/V-}} \int \int d\phi_h d\phi_S \tilde{C}_{i_{T-/V-}} a_{T-/V-}(\phi_h, \phi_S) \left(1 + P_{i_{T-/V-}} \sum_j \epsilon_j A_j(\phi_h, \phi_S)\right) \\
&= \sum_{i_{T+/V+}} \int \int d\phi_h d\phi_S \tilde{C}_{i_{T+/V+}} a_{T+/V+}(\phi_h, \phi_S) \left(1 + P_{i_{T+/V+}} \sum_j \epsilon_j A_j(\phi_h, \phi_S)\right) \\
&+ \sum_{i_{T-/V-}} \int \int d\phi_h d\phi_S \tilde{C}_{i_{T-/V-}} a_{T+/V+}(\phi_h, \phi_S + \pi) \left(1 - P_{i_{T-/V-}} \sum_j \epsilon_j A_j(\phi_h, \phi_S + \pi)\right) \\
&= \tilde{a}_T (\tilde{C}_{T+} + \tilde{C}_{T-}) + \tilde{a}_V (\tilde{C}_{V+} + \tilde{C}_{V-}) \\
&+ \tilde{a}_T (\tilde{C}_{P,T+} - \tilde{C}_{P,T-}) \sum_j \epsilon_j \tilde{a}_{T,j} + (\tilde{C}_{P,V+} - \tilde{C}_{P,V-}) \sum_j \epsilon_j \tilde{a}_{V,j} \\
&= \left(\tilde{a}_T (\tilde{C}_{T+} + \tilde{C}_{T-}) + \tilde{a}_V (\tilde{C}_{V+} + \tilde{C}_{V-})\right) \left(1 + \sum_j \epsilon_j A_{CP,j}\right), \quad (5.64)
\end{aligned}$$

where

$$\tilde{a}_{T/V} \equiv \int \int a_{T+/V+}(\phi_h, \phi_S) d\phi_h d\phi_S \quad (5.65)$$

$$\tilde{a}_{T/V,i} \equiv \int \int a_{T+/V+,i}(\phi_h, \phi_S) d\phi_h d\phi_S \quad (5.66)$$

$$A_{CP,i} \equiv \frac{\tilde{a}_{T,i} (\tilde{C}_{P,T+} - \tilde{C}_{P,T-}) + \tilde{a}_{V,i} (\tilde{C}_{P,V+} - \tilde{C}_{P,V-})}{\tilde{a}_T (\tilde{C}_{T+} + \tilde{C}_{T-}) + \tilde{a}_V (\tilde{C}_{V+} + \tilde{C}_{V-})} \quad (5.67)$$

therefore,  $\tilde{a}_{T/V}$  is the integrated acceptance,  $\tilde{a}_{T/V,i}$  is normalized  $A_i$  modulated acceptance, and  $A_{CP,i}$  is polarization and acceptance weighted effective charge asymmetry. In an ideal Transversity setup with instrument acceptance and efficiency symmetric relative to horizontal plane,  $\tilde{a}_{T,i} \rightarrow$  zero or the effect of transverse charge asymmetry is much smaller than that of vertical.

### Extract parameters and uncertainties with MLM

In order to use maximum likelihood method, the probability for each event is evaluated before multiplying these individual probabilities. Then the parameters are varied to maximize the total probability.

$$T_{prod} = \prod_{event} f_{i_{\pm}}(\phi_h, \phi_S) \quad (5.68)$$

Equivalently, we can form the log-likelihood function:

$$\begin{aligned} L(\epsilon_i) &\equiv \log \left( \prod_{event} f_{i_{\pm}}(\phi_h, \phi_S) \right) \\ &= \sum_{event} \log \left( 1 + P_{i_{T\pm/V\pm}} \sum_j \epsilon_j A_j(\phi_h, \phi_S) \right) - N \log Norm_{exp} + Const \end{aligned} \quad (5.69)$$

where  $\sum_{event}$  is summing over all events in both transvers\_in\_plane and vertical target states, while  $\sum_j$  sums over all angular modulations. In order to get the maximum probability, take the derivative of L with respect to parameter  $\epsilon_k$  and let it to zero:

$$\begin{aligned} 0 &= \frac{dL}{d\epsilon_k} \\ &= \frac{\sum_{event} P_{i_{T\pm/V\pm}} A_k(\phi_h, \phi_S)}{1 + P_{i_{T\pm/V\pm}} \sum_j \epsilon_j A_j(\phi_h, \phi_S)} - N \frac{A_{CP,k}}{1 + \sum_j \epsilon_j A_{CP,j}} \\ \xrightarrow{\text{1st expansion}} &\sum_{event} \left( P_{i_{T\pm/V\pm}} A_k - k(\phi_h, \phi_S) \left( 1 - P_{i_{T\pm/V\pm}} \sum_j \epsilon_j A_j(\phi_h, \phi_S) \right) \right) \\ &\quad - N A_{CP,k} \left( 1 - \sum_j \epsilon_j A_{CP,j} \right) + O \left( (N_+ - N_-) \sum_{mn} \epsilon_m \epsilon_n \text{terms} \right) + \dots \end{aligned} \quad (5.70)$$

Redefine:

$$\sum [PA_k] \equiv \sum_{event} P_{i_{T\pm/V\pm}} A_k(\phi_h, \phi_S) \quad (5.71)$$

$$\sum [P^2 A_j A_k] \equiv \sum_{event} P_{i_{T\pm/V\pm}}^2 A_j(\phi_h, \phi_S) A_k(\phi_h, \phi_S) \quad (5.72)$$

Replace Eq. 5.71 into Eq. 5.70, then

$$\begin{aligned}
0 &= \sum [PA_k] - \sum_j \epsilon_j \sum [P^2 A_j A_k] - NA_{CP,k} + NA_{CP,k} \sum_j \epsilon_j A_{CP,j} \\
&\quad + O\left((N_+ - N_-) \sum_{mn} \epsilon_m \epsilon_n \text{terms}\right)
\end{aligned} \tag{5.73}$$

Rearrange the equation, which corresponds to multiple equations with index k:

$$\sum_j \epsilon_j \left( \sum [P^2 A_j A_k] - NA_{CP,j} A_{CP,k} \right) = \sum [PA_k] - NA_{CP,k} + O\left((N_+ - N_-) \sum_{mn} \epsilon_m \epsilon_n \text{terms}\right) \tag{5.74}$$

Define the following matrices:

$$\mathbf{F} \equiv \begin{pmatrix} \sum [P^2 A_1 A_1] - NA_{CP,1} A_{CP,1} & \sum [P^2 A_1 A_2] - NA_{CP,1} A_{CP,2} & \dots \\ \sum [P^2 A_2 A_1] - NA_{CP,2} A_{CP,1} & \sum [P^2 A_2 A_2] - NA_{CP,2} A_{CP,2} & \dots \\ \vdots & \vdots & \ddots \end{pmatrix} \tag{5.75}$$

$$\mathbf{B} \equiv \begin{pmatrix} \sum [PA_1] - NA_{CP,1} \\ \sum [PA_2] - NA_{CP,2} \\ \vdots \end{pmatrix} \tag{5.76}$$

$$\epsilon \equiv \begin{pmatrix} \epsilon_1 \\ \epsilon_2 \\ \vdots \end{pmatrix} \tag{5.77}$$

Eq. 5.74 becomes:

$$\mathbf{F}\epsilon = \mathbf{B} + O\left(\frac{N_+ - N_-}{N} \sum_{mn} \epsilon_m \epsilon_n \text{terms}\right) \tag{5.78}$$

The results for  $\epsilon$  can be obtained as:

$$\epsilon = \mathbf{F}^{-1}\mathbf{B} + O\left(\frac{N_+ - N_-}{N} \sum_{mn} \epsilon_m \epsilon_n\right) \tag{5.79}$$

To evaluate its uncertainties, the second derivative of Eq. 5.69 need to be performed:

$$\begin{aligned}
\text{Log}(\epsilon_{jk}) &= -\frac{\partial^2 \log L}{\partial \epsilon_j \partial \epsilon_k} \\
&= -\frac{\partial^2}{\partial \epsilon_j \partial \epsilon_k} \left( \sum_{\text{event}} \log \left( 1 + P_{i_{T\pm/V\pm}} \sum_i \epsilon_i A_i(\phi_h, \phi_S) \right) - N \log \left( 1 + \sum_i \epsilon_i A_{CP,i} \right) \right) \\
&= -\frac{\partial}{\partial \epsilon_j} \left( \sum_{\text{event}} \frac{P_{i_{T\pm/V\pm}} A_k(\phi_h, \phi_S)}{1 + P_{i_{T\pm/V\pm}} \sum_i \epsilon_i A_i(\phi_h, \phi_S)} - N \frac{A_{CP,k}}{1 + \sum_i \epsilon_i \tilde{a}_i} \right) \\
&= \sum_{\text{event}} \frac{P_{i_{T\pm/V\pm}}^2 A_k(\phi_h, \phi_S) A_j(\phi_h, \phi_S)}{\left( 1 + P_{i_{T\pm/V\pm}} \sum_i \epsilon_i A_i(\phi_h, \phi_S) \right)^2} - N \frac{A_{CP,k} A_{CP,j}}{\left( 1 + A_{CP} \sum_i \epsilon_i \tilde{a}_i \right)^2} \\
&= \sum P^2 A_j A_k - N A_{CP,j} A_{CP,k} + O \left( N \sum_{ijk} A_{CP,i} A_{CP,j} A_{CP,k} \sum_i \epsilon_i \right) \tag{5.80}
\end{aligned}$$

The uncertainty matrix is given by

$$\mathbf{V} \begin{pmatrix} \epsilon_1 \\ \epsilon_2 \\ \vdots \end{pmatrix} = \begin{pmatrix} \sum [P^2 A_1 A_1] - N A_{CP,1}^2 A_{CP,1} & \sum [P^2 A_1 A_2] - N A_{CP,1} A_{CP,2} & \cdots \\ \sum [P^2 A_1 A_1] - N A_{CP,2}^2 A_{CP,1} & \sum [P^2 A_2 A_2] - N A_{CP,2} A_{CP,2} & \cdots \\ \vdots & \vdots & \ddots \end{pmatrix}^{-1} \tag{5.81}$$

$$+ O(1/N) \left( \sum_{ijk} A_{CP,i} A_{CP,j} A_{CP,k} \sum_i \epsilon_i \right) \tag{5.82}$$

or

$$\mathbf{V}(\epsilon) = \mathbf{F}^{-1} + O \left( \frac{\sum_{ijk} A_{CP,i} A_{CP,j} A_{CP,k} \sum_i \epsilon_i}{N} \right) \tag{5.83}$$

### SSA Acceptance Estimation

SSA acceptance is required for the results of SSA (Eq. 5.79 and Eq. 5.83). It appears in asymmetry correction term (Eq. 5.67), which takes a general form of

$$A_{CP} \sim \frac{\int \int \int a_{T\pm/V\pm}(\phi_h, \phi_S, \theta_S) A_i(\phi_h, \phi_S) d\phi_h d\phi_S d\theta_S}{\int \int \int a_{T\pm/V\pm}(\phi_h, \phi_S, \theta_S) d\phi_h d\phi_S d\theta_S} \times \frac{\tilde{C}_+ - \tilde{C}_-}{\tilde{C}_+ + \tilde{C}_-} \tag{5.84}$$

where  $A_i(\phi_h, \phi_S)$  is SIDIS angular modulation and  $\frac{\tilde{C}_+ - \tilde{C}_-}{\tilde{C}_+ + \tilde{C}_-}$  is asymmetry of effective charge.

If there are no asymmetry of effective charge between  $\pm$  states, acceptance will not affect the final result. If acceptance is symmetric,  $A_{CP} = 0$  independent of asymmetry of effective charge. In our experiment, the acceptance is different between two opposite spin states.

In real experiment, acceptance  $a_{T+}(\phi_h, \phi_S)$  is not necessarily equal to  $a_{V+}(\phi_h, \phi_S + \pi/2)$  (due to virtual

photon not exactly transverse to  $\vec{q}$ ), it is also reasonable to assume that

$$\int \int a_{V+}(\phi_h, \phi_S) d\phi_h d\phi_S = \int \int a_{T+}(\phi_h, \phi_S) d\phi_h d\phi_S \quad (5.85)$$

or

$$\tilde{a} \equiv \tilde{a}_T = \tilde{a}_V \quad (5.86)$$

So Eq. 5.67 will be simplified to

$$A_{CP,i} \equiv \frac{(\tilde{C}_{P,T+} - \tilde{C}_{P,T-})(\tilde{a}_{T,i}/\tilde{a}) + (\tilde{C}_{P,V+} - \tilde{C}_{P,V-})(\tilde{a}_{V,i}/\tilde{a})}{(\tilde{C}_{T+} + \tilde{C}_{T-}) + (\tilde{C}_{V+} + \tilde{C}_{V-})} \quad (5.87)$$

With  $a_+(\phi_h, \phi_S) = a_-(\phi_h, \phi_S + \pi)$  and  $A_i(\phi_h, \phi_S) = -A_i(\phi_h, \phi_S + \pi)$ ,

$$\begin{aligned} \frac{\tilde{a}_{T/V,i}}{\tilde{a}} &\equiv \frac{\int \int a_{T+/V+}(\phi_h, \phi_S) A_i(\phi_h, \phi_S) d\phi_h d\phi_S}{\int \int a_{T+/V+}(\phi_h, \phi_S) d\phi_h d\phi_S} \\ &= \frac{\int \int (y_{T+/V+}(\phi_h, \phi_S) + y_{T-/V-}(\phi_h, \phi_S + \pi)) A_i(\phi_h, \phi_S) d\phi_h d\phi_S}{\int \int (y_{T+/V+}(\phi_h, \phi_S) + y_{T-/V-}(\phi_h, \phi_S + \pi)) d\phi_h d\phi_S} \\ &= \frac{\int \int y_+(\phi_h, \phi_S) A_i(\phi_h, \phi_S) d\phi_h d\phi_S - \int \int y_-(\phi_h, \phi_S) A_i(\phi_h, \phi_S) d\phi_h d\phi_S}{\int \int y_+(\phi_h, \phi_S) + \int \int y_-(\phi_h, \phi_S) d\phi_h d\phi_S} \end{aligned} \quad (5.88)$$

$$(5.89)$$

We can estimate as follows;

$$\left( \frac{\tilde{a}_{T/V,i}}{\tilde{a}} \right) = \frac{\sum_{event, T+/V+} A_i(\phi_h, \phi_S) / \tilde{C}_{T+/V+} - \sum_{event, T-/V-} A_i(\phi_h, \phi_S) / \tilde{C}_{T-/V-}}{N_{T+/V+} / \tilde{C}_{T+/V+} + N_{T-/V-} / \tilde{C}_{T-/V-}} \quad (5.90)$$

where  $N/\tilde{C}_{T+/V+}$  are sums of event numbers or effective charges as defined in Eq. 5.53,  $\sum_{event, T\pm/V\pm}$  is defined as sum over events in a specific direction( $T \pm /V \pm$ ).

We consider the specific case, for two angular modulations,  $\sin(\phi_h + \phi_S)$  and  $\sin(\phi_h - \phi_S)$ .

With unpolarized beam on transversely polarized target, the probability distribution function can be formed as (ignore pretzelosity term):

$$f(\phi_h, \phi_S, P_t; A_{UT}^{sin(\phi_h \pm \phi_S)}) = (1 + P_t [A_{UT}^{sin(\phi_h + \phi_S)} \sin(\phi_h + \phi_S) + A_{UT}^{sin(\phi_h - \phi_S)} \sin(\phi_h - \phi_S)]) / Norm_{exp} \quad (5.91)$$

where  $P_t$  is the target transverse polarization corresponding to each event,  $Norm_{exp}$  is the normalization term which introduces the acceptance effect as previously deduced.  $A_{UT}^{sin(\phi_h + \phi_S)}$  and  $A_{UT}^{sin(\phi_h - \phi_S)}$  are Collins

angular modulation and Siverson angular modulation corresponding to  $\sin(\phi_h + \phi_S)$  and  $\sin(\phi_h - \phi_S)$  terms. Both of them need to be extracted for the kaon data set.

The total probability is

$$Tprob = \prod_{event} \left( \left( 1 + P_t [A_{UT}^{\sin(\phi_h + \phi_S)} \sin(\phi_h + \phi_S) + A_{UT}^{\sin(\phi_h - \phi_S)} \sin(\phi_h - \phi_S)] \right) / Norm_{exp} \right) \quad (5.92)$$

The logarithm of the total probability is:

$$\begin{aligned} & \log(Tprob) \\ = & \log \prod_{event} \left( \left( 1 + P_t [A_{UT}^{\sin(\phi_h + \phi_S)} \sin(\phi_h + \phi_S) + A_{UT}^{\sin(\phi_h - \phi_S)} \sin(\phi_h - \phi_S)] \right) - (Norm_{exp}) \right) \\ = & \sum_{event} \log \left( \left( 1 + P_t [A_{UT}^{\sin(\phi_h + \phi_S)} \sin(\phi_h + \phi_S) + A_{UT}^{\sin(\phi_h - \phi_S)} \sin(\phi_h - \phi_S)] \right) - N \log(Norm_{exp}) \right) \end{aligned} \quad (5.93)$$

In order to simplify the equation, we define:

$$a = A_{UT}^{\sin(\phi_h + \phi_S)} \quad (5.94)$$

$$b = A_{UT}^{\sin(\phi_h - \phi_S)} \quad (5.95)$$

In order to obtain Collins and Siverson moments to maximize the total probability, the partial derivative of “a” and “b” should be equal to zero.

$$0 = \sum_{event} \frac{P_t \sin(\phi_h + \phi_S)}{1 + P_t (a \sin(\phi_h + \phi_S) + b \sin(\phi_h - \phi_S))} - N \frac{\partial Norm_{exp} / \partial a}{Norm_{exp}} \quad (5.96)$$

$$0 = \sum_{event} \frac{P_t \sin(\phi_h - \phi_S)}{1 + P_t (a \sin(\phi_h + \phi_S) + b \sin(\phi_h - \phi_S))} - N \frac{\partial Norm_{exp} / \partial b}{Norm_{exp}} \quad (5.97)$$

Following the assumption that “a” and “b” are small, and the two terms  $\frac{\partial Norm_{exp} / \partial a}{Norm_{exp}}$  and  $\frac{\partial Norm_{exp} / \partial b}{Norm_{exp}}$  can be obtained from Eq. 5.67, Eq. 5.85, Eq. 5.87, Eq. 5.88.

$$\begin{aligned} 0 = & \sum_{event} P_t \sin(\phi_h + \phi_S) (1 - P_t (a \sin(\phi_h + \phi_S) + b \sin(\phi_h - \phi_S))) \\ & - N A_{CP,a} (1 - (a A_{CP,a} + b A_{CP,b})) + O((N_+ - N_-)(a^2 + a \times b + b^2)) \end{aligned} \quad (5.98)$$

$$\begin{aligned}
0 = & \sum_{event} P_t \sin(\phi_h - \phi_S) (1 - P_t (a \sin(\phi_h + \phi_S) + b \sin(\phi_h - \phi_S))) \\
& - N A_{CP,b} (1 - (a A_{CP,a} + b A_{CP,b})) + O((N_+ - N_-)(a^2 + a \times b + b^2))
\end{aligned} \tag{5.99}$$

Rearrange these equations and drop 2nd order terms,

$$\begin{aligned}
& a \left( \sum_{event} P_t^2 \sin(\phi_h + \phi_S) \sin(\phi_h + \phi_S) - N A_{CP,a} A_{CP,a} \right) \\
& + b \left( \sum_{event} P_t^2 \sin(\phi_h + \phi_S) \sin(\phi_h - \phi_S) - N A_{CP,a} A_{CP,b} \right) \\
& = \sum_{event} P_t \sin(\phi_h + \phi_S) - N A_{CP,a}
\end{aligned} \tag{5.100}$$

$$\begin{aligned}
& a \left( \sum_{event} P_t^2 \sin(\phi_h + \phi_S) \sin(\phi_h - \phi_S) - N A_{CP,a} A_{CP,b} \right) \\
& + b \left( \sum_{event} P_t^2 \sin(\phi_h - \phi_S) \sin(\phi_h - \phi_S) - N A_{CP,b} A_{CP,b} \right) \\
& = \sum_{event} P_t \sin(\phi_h - \phi_S) - N A_{CP,b}
\end{aligned} \tag{5.101}$$

where  $P_t$  is transverse target polarization,  $A_{CP,a}$ ,  $A_{CP,b}$  is polarization and acceptance weighted effective charge asymmetry corresponding to  $\sin(\phi_h + \phi_S)$ ,  $\sin(\phi_h - \phi_S)$  angular modulation.

The ‘‘a’’ and ‘‘b’’ can be solved in the following way:

$$\begin{aligned}
a = & \left( \left( \sum_{event} P_t \sin(\phi_h + \phi_S) - N A_{CP,a} \right) \right. \\
& \left( \sum_{event} P_t^2 \sin(\phi_h - \phi_S) \sin(\phi_h - \phi_S) \right. \\
& \left. - N A_{CP,b} A_{CP,b} \right) - \left( \sum_{event} P_t \sin(\phi_h - \phi_S) - N A_{CP,b} \right) \\
& \left. \left( \sum_{event} P_t^2 \sin(\phi_h + \phi_S) \sin(\phi_h - \phi_S) - N A_{CP,a} A_{CP,b} \right) \right) \\
& \div \left( \left( \sum_{event} P_t^2 \sin(\phi_h + \phi_S) \sin(\phi_h + \phi_S) - N A_{CP,a} A_{CP,a} \right) \right. \\
& \left( \sum_{event} P_t^2 \sin(\phi_h - \phi_S) \sin(\phi_h - \phi_S) - N A_{CP,b} A_{CP,b} \right) \\
& \left. - \left( \sum_{event} P_t^2 \sin(\phi_h + \phi_S) \sin(\phi_h - \phi_S) - N A_{CP,a} A_{CP,b} \right) \right. \\
& \left. \left. \left( \sum_{event} P_t^2 \sin(\phi_h + \phi_S) \sin(\phi_h - \phi_S) \right) \right) \right)
\end{aligned} \tag{5.102}$$

and

$$\begin{aligned}
b = & \left( \left( \sum_{event} P_t \sin(\phi_h - \phi_S) - NA_{CP,b} \right) \right. \\
& \left( \sum_{event} P_t^2 \sin(\phi_h + \phi_S) \sin(\phi_h + \phi_S) - NA_{CP,a} A_{CP,a} \right) \\
& - \left( \sum_{event} P_t \sin(\phi_h + \phi_S) - NA_{CP,a} \right) \\
& \left. \left( \sum_{event} P_t^2 \sin(\phi_h + \phi_S) \sin(\phi_h - \phi_S) - NA_{CP,a} A_{CP,b} \right) \right) \\
& \div \left( \left( \sum_{event} P_t^2 \sin(\phi_h + \phi_S) \sin(\phi_h + \phi_S) - NA_{CP,a} A_{CP,a} \right) \right. \\
& \left( \sum_{event} P_t^2 \sin(\phi_h - \phi_S) \sin(\phi_h - \phi_S) - NA_{CP,b} A_{CP,b} \right) \\
& - \left( \sum_{event} P_t^2 \sin(\phi_h + \phi_S) \sin(\phi_h - \phi_S) - NA_{CP,a} A_{CP,b} \right) \\
& \left. \left( \sum_{event} P_t^2 \sin(\phi_h + \phi_S) \sin(\phi_h - \phi_S) \right) \right) \quad (5.103)
\end{aligned}$$

The uncertainties of “a” and “b” are also deduced from second partial derivatives of the total probability:

$$\begin{aligned}
\sigma_a = & \left( \frac{\sum_{event} P_t^2 \sin(\phi_h - \phi_S) \sin(\phi_h - \phi_S) - NA_{CP,b} A_{CP,b}}{\sum_{event} P_t^2 \sin(\phi_h - \phi_S) \sin(\phi_h - \phi_S) - NA_{CP,b} A_{CP,b}} \right)^{\frac{1}{2}} \\
& \times \left( \left( \sum_{event} P_t^2 \sin(\phi_h + \phi_S) \sin(\phi_h + \phi_S) - NA_{CP,a} A_{CP,a} \right) \right. \\
& \left. - \left( \sum_{event} P_t^2 \sin(\phi_h + \phi_S) \sin(\phi_h - \phi_S) - NA_{CP,a} A_{CP,b} \right) \right)^{\frac{1}{2}} \\
& \times \left( \sum_{event} P_t^2 \sin(\phi_h + \phi_S) \sin(\phi_h - \phi_S) - NA_{CP,a} A_{CP,b} \right)^{\frac{1}{2}} \quad (5.104)
\end{aligned}$$

$$\begin{aligned}
\sigma_b = & \left( \frac{\sum_{event} P_t^2 \sin(\phi_h + \phi_S) \sin(\phi_h + \phi_S) - NA_{CP,a} A_{CP,a}}{\sum_{event} P_t^2 \sin(\phi_h + \phi_S) \sin(\phi_h + \phi_S) - NA_{CP,a} A_{CP,a}} \right)^{\frac{1}{2}} \\
& \times \left( \left( \sum_{event} P_t^2 \sin(\phi_h - \phi_S) \sin(\phi_h - \phi_S) - NA_{CP,b} A_{CP,b} \right) \right. \\
& \left. - \left( \sum_{event} P_t^2 \sin(\phi_h - \phi_S) \sin(\phi_h + \phi_S) - NA_{CP,b} A_{CP,a} \right) \right)^{\frac{1}{2}}
\end{aligned}$$



$$\times \left( \sum_{event} P_t^2 \sin(\phi_h - \phi_S) \sin(\phi_h + \phi_S) - N A_{CP,a} A_{CP,b} \right)^{\frac{1}{2}} \quad (5.105)$$

From Eq. 5.102, Eq. 5.103, Eq. 5.104, and Eq. 5.105, the Collins moment and Sivers moment and its uncertainties can all be extracted.

### **Lifetime Correction, Charge Asymmetry and Acceptance Correction, Target polarization correction**

For Eq. 5.102, Eq. 5.103, Eq. 5.104, and Eq. 5.105, the lifetime correction, target polarization correction and charge asymmetry and acceptance correction have been already introduced. Actually all these corrections can be introduced step by step in practice, and it is obviously seen that the correction of acceptance is due to charge asymmetry.

### **Conclusion and Discussion**

The maximum likelihood method includes some assumptions. One assumption is that the angular modulations should be small, otherwise, it need to be solved numerically.

In my analysis, I first used the least square method to get the kaon result from E06010 proposal [123]. Then I learned that the maximum likelihood method is more suitable, due to the low statistics of kaons in E06010. I then adopted the maximum likelihood method to extract kaon Collins and Sivers moments. As Jin Huang, et al. mentioned in their detailed deduction, the MLM has the following benefits:

- As cross check of existing local-pair angular-binned-fitting method developed [124] for the pion analysis.
- High statistics is required for angular-binned-fitting method to be unbiased (in an extreme example, bin fitting method would break down if statistical expectation of count in each bin is less than 1). Therefore, there are practical difficulties for channels with very low statistics (eg.  $(e,e'K^-)$ ). On the other hand, MLM does not have this problem as long as total counts are high.
- For angular modulation extraction, part of angle information will be lost during binning process, while MLM would access preserve all the information.

## 5.4 Numerical calculation for kaon Collins moment and Sivers moment

### 5.4.1 Coincidence Kaon Raw Asymmetry

For coincidence kaons and protons in LHRS, all variables such as electron momentum, spin state,  $x_{bj}$ ,  $y$ ,  $z$ ,  $p_t$ ,  $w$ ,  $w'$ ,  $Q^2$ , and  $\phi_h, \phi_S$  can be extracted [125]. All these events also contain such as run number, event number, gas cherenkov sum, aerogel cherenkov sum, rich mip angle, etc. Meanwhile, the beam charge, livetime were calculated for each run and polarization calculated for each spin state using the polarization table generated from the Epics variable haPolHe3\_Flip\_Sequence\_ID and haPolHe3\_Flip\_Count. Using all these information, the raw asymmetries of coincidence kaons are shown in Fig. 5.44.

The target single spin asymmetry is proportional to  $\sin(\phi_h + \phi_S)$  and  $\sin(\phi_h - \phi_S)$ . For Vertical setting,  $\phi_h \pm \phi_S$  are around  $\pm\pi/2$ , and for Transverse\_in\_plane setting,  $\phi_h \pm \phi_S$  are around  $\pm\pi$ , see Figs 5.45 and 5.46. Therefore, the raw asymmetry of the data with vertical setting should be larger than that of the Transver\_in\_plane setting. This is consistent results shown in Fig. 5.44. If the raw asymmetry is not equal to zero, it means that either or both of Collins moment and Sivers moment are not zero.

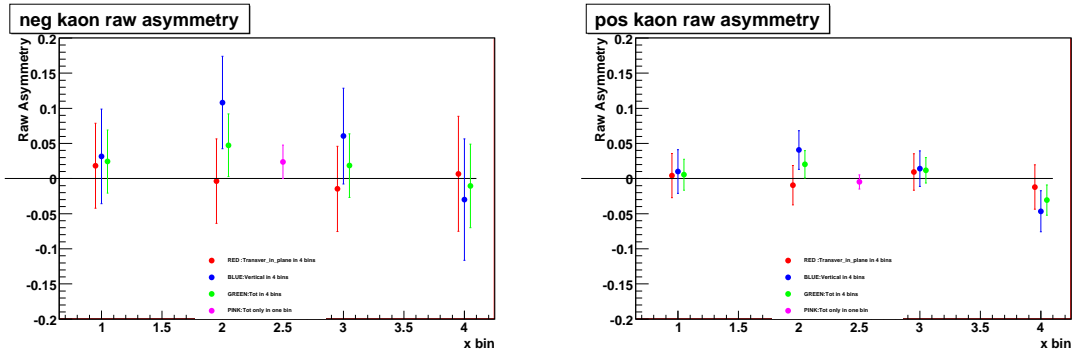


Figure 5.44: Left panel: coincidence negative kaon raw asymmetry. Right panel: coincidence positive kaon raw asymmetry. Red means Transverse\_in\_plane, Blue: Vertical, Green: Total (include Vertical and Transverse), Pink: Total events in 1 bin.

### 5.4.2 Coincidence Kaon Collins moment and Sivers moment

To extract coincidence kaon Collins moment and Sivers moment and their statistic uncertainties using maximum likelihood method is straight forward according to formula Eq. 5.102, Eq. 5.103, Eq. 5.104, and Eq. 5.105. Actually, I modified these formula to extract Collins and Sivers moment for five situations: (1) directly use all the identified coincidence kaons' information, (2) for all the identified coincidence kaons, the total beam charge had been already included in the first order solution. Then, consider the livetime

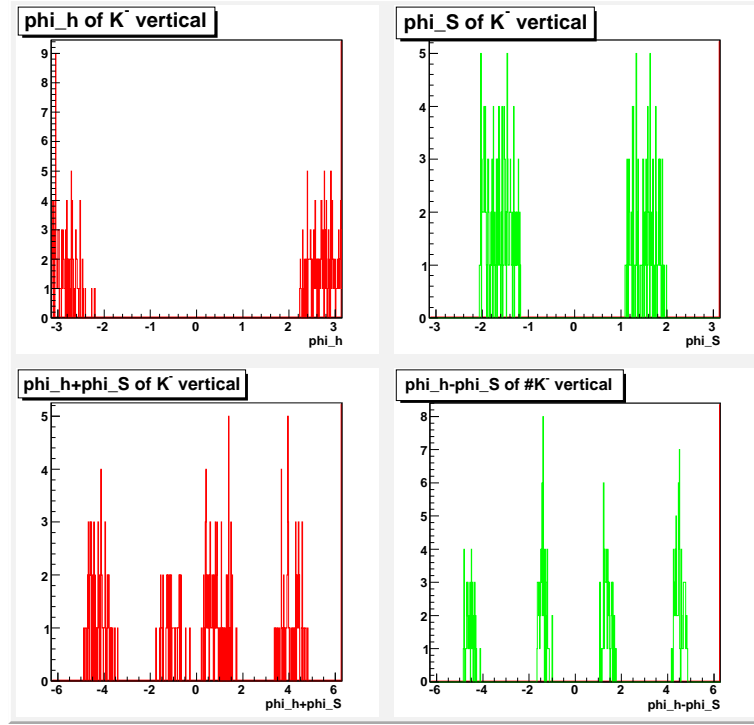


Figure 5.45:  $\phi_h$ ,  $\phi_S$  and their combination  $\phi_h + \phi_S$ ,  $\phi_h - \phi_S$  in vertical polarization target setting. Upleft panel:  $\phi_h$  is around  $\pm\pi$ , upright panel:  $\phi_S$  is around  $\pm\frac{\pi}{2}$ . Downleft panel:  $\phi_h + \phi_S$  is around  $\pm\frac{\pi}{2}$  or  $\pm\frac{3\pi}{2}$ , downright panel:  $\phi_h - \phi_S$  is around  $\pm\frac{\pi}{2}$  or  $\pm\frac{3\pi}{2}$ .

correction. (3) merge target polarization with identified coincidence hadrons. (4) merge livetime correction with target polarization. (5) Due to beam charge asymmetry and asymmetric acceptance, merge all these factors together to obtain the final results shown in Fig. 5.47. Only (5) is the final result for kaon Collins moment and Sivers moment.

In Fig. 5.47, the black points only consider the raw events and the red points include the livetime correction. The pink points include the target polarization and the green points include both the livetime and target polarization. Finally the cyan points include the effects due to charge asymmetry and acceptance asymmetry. The cyan points are the final direct Collins moment and Sivers moment results for positive and negative coincidence kaons in transversely polarized  $^3\text{He}$  target.

Meanwhile, Jin got kaon results of Collins and Sivers moments also based on the maximum likelihood, but different cuts. Xin also used the “pair and local pair” method to get the kaon results of Collins and Sivers moments with the cut  $L.cer.aeum_c < 250$  &  $L.a1.asum_c < 150$  &  $abs(CT.K.t[]) < 1.0$ . Fig. 5.48 compares these results. Obviously, the two different procedures with the same Maximum Likelihood Method have the similar results, but different cuts on gas cherenkov, aerogel cherenkov and time-of-flight give slightly different results.

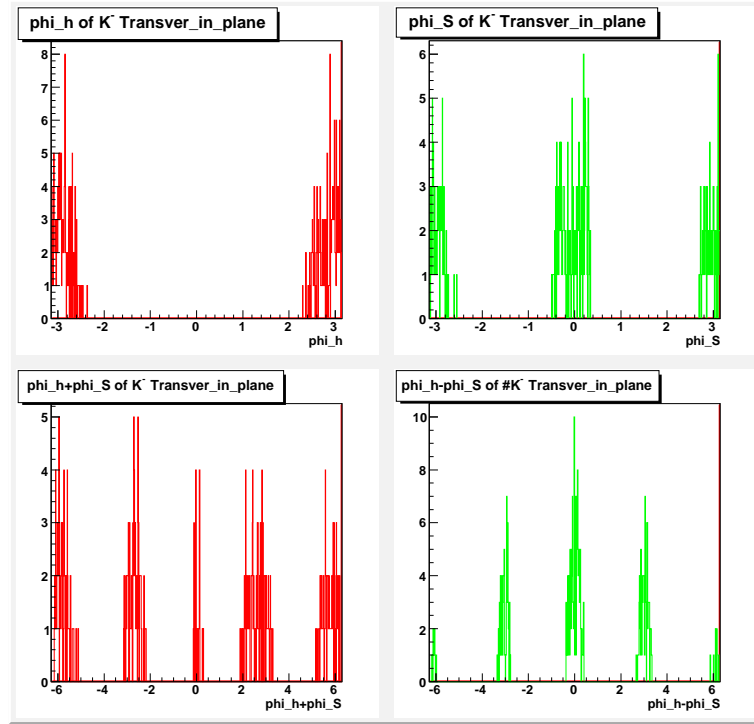


Figure 5.46:  $\phi_h$ ,  $\phi_S$  and their combination  $\phi_h + \phi_S$ ,  $\phi_h - \phi_S$  in transverse\_in\_plane polarization target setting. Upleft panel:  $\phi_h$  is around  $\pm\pi$ , upright panel:  $\phi_S$  is around 0 or  $\pm\pi$ . Downleft panel:  $\phi_h + \phi_S$  is around 0 or  $\pm\pi$ , downright panel:  $\phi_h - \phi_S$  is around 0 or  $\pm\pi$ .

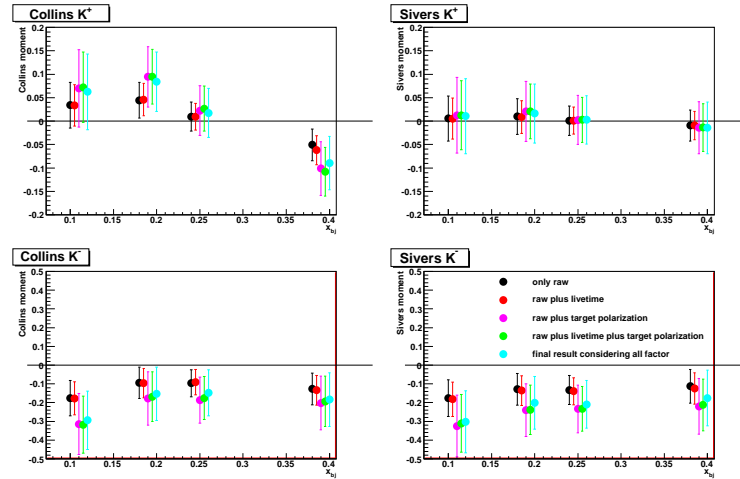


Figure 5.47: Direct results from five situation, the target polarization does influence the results. Up panel: coincidence positive kaons, down panel: coincidence negative kaons. For the negative kaon, the Collins moment and Sivers moment are big number, especially for the first bin: around -0.32 -0.34.

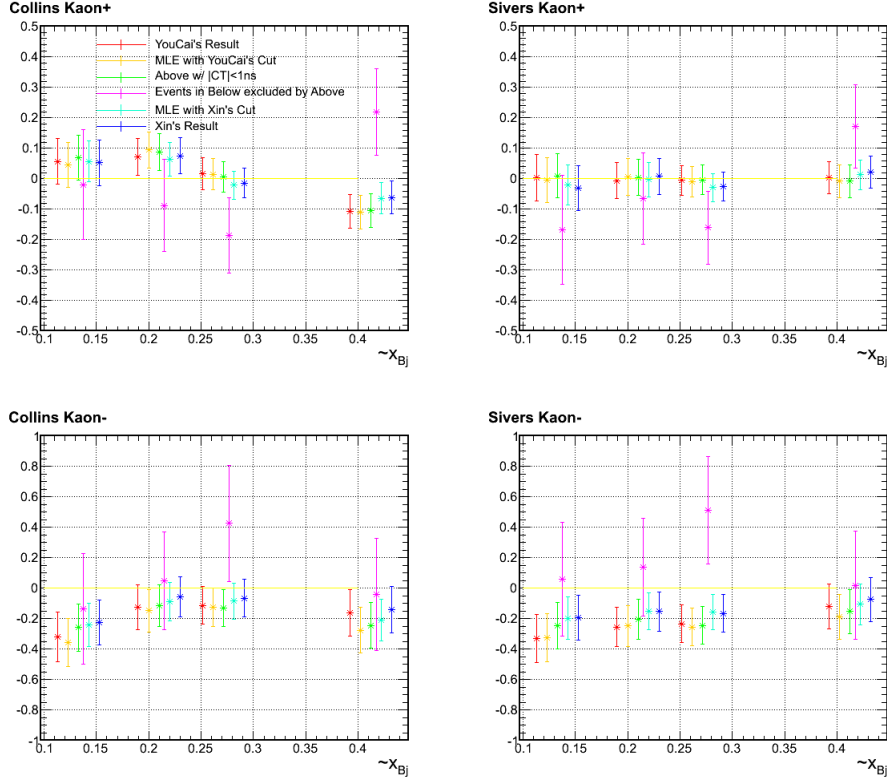


Figure 5.48: The upleft panel is for  $K^+$  Collins moment, the upright is for  $K^+$  Sivers moment, the downleft is for  $K^-$  Collins moment, the downright is for  $K^-$  Sivers moment. The red line is my result, the blue is Xin's result, the cyan is MLE result of Xin's cut, yellow is MLE's result with my cut, green is for Cut  $abs(CT.K.t) < 1.0$ , and the pink line has large uncertainty due to very small statistics.

Fig. 5.48 shows the different results with different cuts and methods. The red line is my result with the cut  $L.cer.asum_c < 30$ .  $\&\& L.a1.asum_c < 125$ .  $\&\& abs(CT.K.t) < 0.87$ . The blue line is Xin's result with cut  $L.cer.asum_c < 250$ .  $\&\& L.a1.asum_c < 150$ .  $\&\& abs(CT.K.t) < 1$ . The cyan line is the result of MLE with cut  $L.cer.asum_c < 250$ .  $\&\& L.a1.asum_c < 150$ .  $\&\& abs(CT.K.t) < 1$ . The yellow line is the result of MLE with cut  $L.cer.asum_c < 30$ .  $\&\& L.a1.asum_c < 125$ .  $\&\& abs(CT.K.t) < 0.87$ . The green line is the result of MLE with cut  $L.cer.asum_c < 30$ .  $\&\& L.a1.asum_c < 125$   $\&\& abs(CT.K.t) < 1$ . The pink line has big error bar because few events survive the tight cut  $L.cer.asum_c < 30$ .  $\&\& L.a1.asum_c < 125$ .  $\&\& abs(CT.K.t) < 1$ . and  $L.cer.asum_c < 250$ .  $\&\& L.a1.asum_c < 150$ .  $\&\& abs(CT.K.t) < 1$ .

In order to see subtle change between different cuts, I differentiate cuts with gas Cherenkov, aerogel Cherenkov and time-of-flight, the results are shown in Fig. 5.49 and Fig. 5.50.

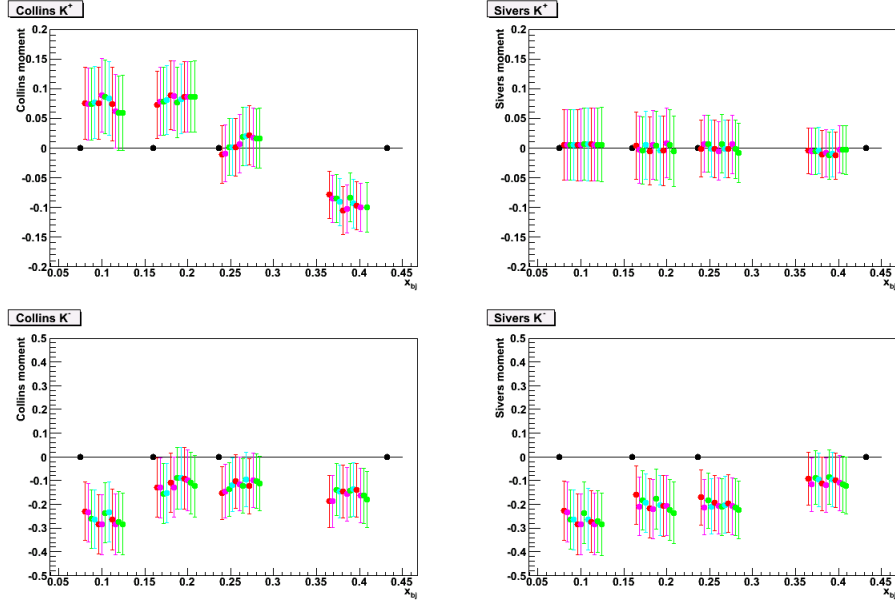


Figure 5.49: The upleft panel is for  $K^+$  Collins moment, the upright is for  $K^+$  Sivers moment, the downleft is for  $K^-$  Collins moment, the downright is for  $K^-$  Sivers moment. Under condition  $abs(CT.K.t) < 1$ , the different results are obtained with different cut combination of gas Cherenkov and aerogel Cherenkov.

Fig. 5.49 and Fig. 5.50 are for two different tof conditions:  $abs(CT.K.t) < 1$ ,  $abs(CT.K.t) < 0.87$ . Under condition  $abs(CT.K.t) < 1$ , the central values of Collins moment for  $K^-$  at first bin are around  $-0.22 \sim -0.28$ , the central values of Sivers moment for  $K^-$  at first bin are around  $-0.22 \sim -0.28$ , under condition  $abs(CT.K.t) < 0.87$ , the central values of Collins moment for  $K^-$  at first bin are around  $-0.27 \sim -0.32$ , the central values of Sivers moment for  $K^-$  at first bin are around  $-0.27 \sim -0.34$ . These are relatively small variations, showing the stability of the results relative to the cuts.

### 5.4.3 numerical calculation

When applying formula Eq. 5.102, Eq. 5.103, Eq. 5.104, Eq. 5.105, we assume that the Collins and Sivers moments are small. However, the results are not small, as shown in Fig. 5.47. Therefore, the first order expansion approximation is not reliable, and the second or even the third order expansion should be considered.

It is difficult to solve the equations analytically if the expansion goes to more than  $2^{nd}$  order. Fortunately, we can apply the numerical calculation method to get the precise results.

The procedure is the following:

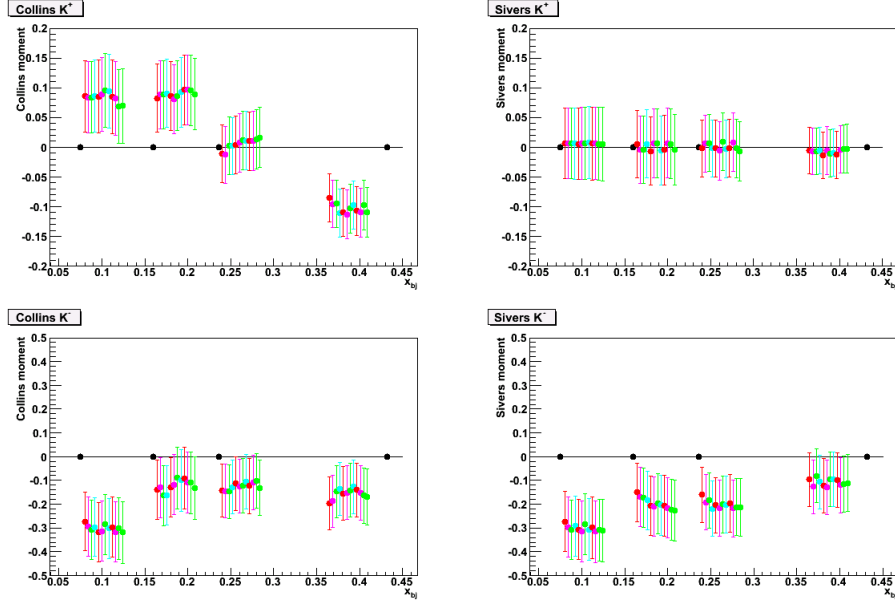


Figure 5.50: The upleft panel is for  $K^+$  Collins moment, the upright is for  $K^+$  Sivers moment, the downleft is for  $K^-$  Collins moment, the downright is for  $K^-$  Sivers moment. Under condition  $abs(CT.K.t) < 0.87$ , the different results are obtained with different cut combination of gas Cherenkov and aerogel Cherenkov.

The log-likelihood probability is:

$$\begin{aligned}
 L(\epsilon_i) &\equiv \log \left( \prod_{event} f_{i_{\pm}}(\phi_h, \phi_S) \right) \\
 &= \sum_{event} \log \left( 1 + P_{i_{T\pm}/V_{pm}} \sum_j \epsilon_j A_j(\phi_h, \phi_S) \right) - N \log Norm_{exp} + Const. \quad (5.106)
 \end{aligned}$$

We can simply calculate  $L(\epsilon_i)$  numerically for a range of the parameters and find the values of  $\epsilon_i$  which give the maximal value of  $L(\epsilon_i)$ . The uncertainty can then be determined from the  $1\sigma$  contour.

A simple program was written using C++ as follows:

```

Double_t a = -0.345, b = -0.345, A[342]=0, B[342]=0;
for(Int_t i=0; i<342; i++){A[i]= a + 0.001*i; B[i]= b+0.001*i;}
for (Int_t j=0; j<342; j++){ for(Int_t k=0; k<342; k++){substitute A[j], B[k] into formula Eq. 5.106 } }

```

And find the final results as following:

Fig. 5.51 shows the final kaon result of Collins and Sivers moments. The Sivers moment for  $K^+$  is consistent with zero, and the Collins moment and Sivers moment are negative for  $K^-$ .

It also can be shown in two dimension way as Fig. 5.52, and Fig. 5.53.

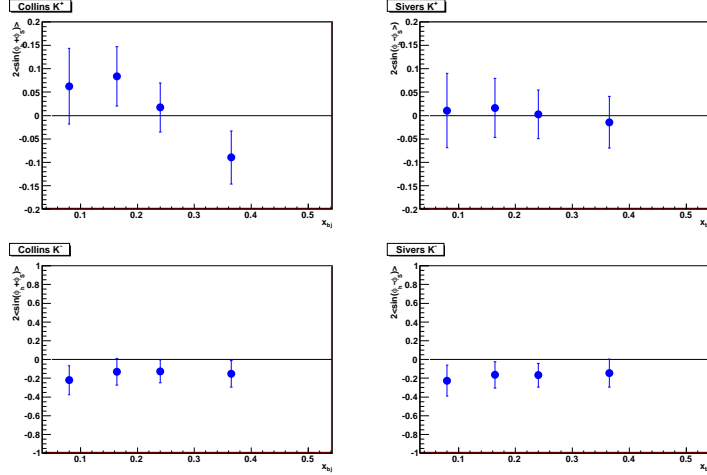


Figure 5.51: Result of kaon Collins moment and Sivers moment from numerical MLM analysis. Left up panel: Collins moment for  $K^+$ , right up panel: Sivers moment for  $K^+$ . Left down panel: Collins moment for  $K^-$ , right down panel: Sivers moment for  $K^-$ . The Sivers moment for  $K^+$  is consistent with zero, and the Collins moment and Sivers moment are negative for  $K^-$ .

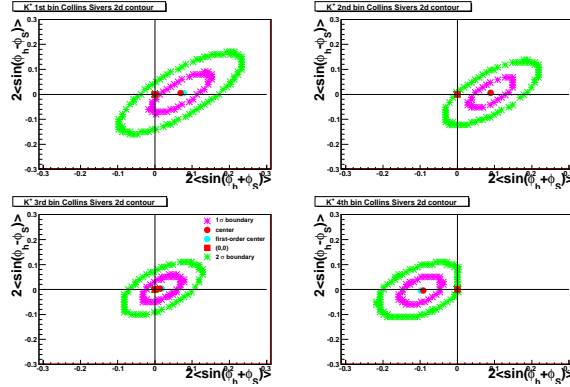


Figure 5.52: Collins moment versus Sivers moment for positive kaon.

Fig. 5.52 shows the two dimension at contours for numerical calculation in 4 bins for positive kaons. It shows the  $1\sigma$  and  $2\sigma$  contours, it also plots the central values for the first order calculation and the numerical calculation. The two values are very similar.

Fig. 5.53 shows the result for negative kaons. The central values obtained from the two calculations are significantly different. For the first bin, the central values of Collins moment go from -0.32 to -0.23, and the central values of Sivers moment go from -0.34 to -0.22 depending on the method used.

Figs. 5.54 and 5.55 are similar to Figs. 5.52 and 5.53, except that the  $1\sigma$  and  $2\sigma$  contours corresponding to the first-order MLM analysis are also included.

The results in Fig. 5.56 and Fig. 5.57 are very stable with respect to cuts and I choose the final results



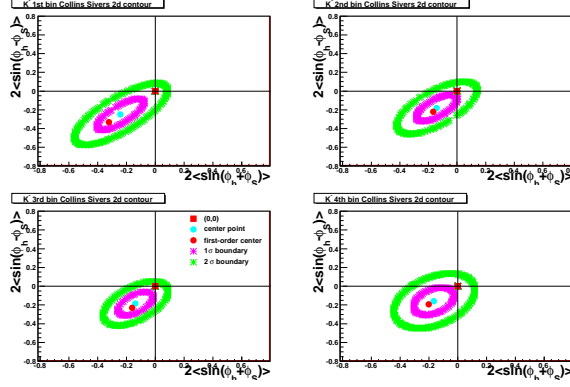


Figure 5.53: Collins moment versus Siverts moment for negative kaon.

with cut  $abs(CT.K.t) < 0.87$  &&  $L.cer.asum_c < 30.$  &&  $L.a1.asum_c < 125.$ , as already stated before.

## 5.5 Nitrogen Dilution Factor

As discussed in Sec. 4.5, due to the effect of depolarization of the emitted photons, about 1% nitrogen was filled in the polarized  $^3\text{He}$  target cell. Nitrogen can absorb a photon and end up into the nitrogen's rotational and vibrational states [126] to quench the emitted photons. Nitrogen ( $\text{N}_2$ ) consist of 7 protons and 7 neutrons with no net polarization. However, the SIDIS kaon electroproduction from nitrogen will dilute the  $^3\text{He}$  asymmetry:

$$A_{raw} = f \cdot P_{^3\text{He}} \cdot A_{^3\text{He}} \quad (5.107)$$

Where  $P_{^3\text{He}}$  is the polarization of  $^3\text{He}$ .  $A_{^3\text{He}}$  is the  $^3\text{He}$  asymmetry, and  $f$  is the dilution factor defined as:

$$f = \frac{N_{^3\text{He}}\sigma_{^3\text{He}}}{N_{^3\text{He}}\sigma_{^3\text{He}} + N_{\text{N}_2}\sigma_{\text{N}_2}} \quad (5.108)$$

Where  $N_{^3\text{He}}$  is the number of  $^3\text{He}$  atom in the target cell, and  $N_{\text{N}_2}$  is the number of  $\text{N}_2$  atoms in the target cell.  $\frac{\sigma_{\text{N}_2}}{\sigma_{^3\text{He}}}$  was measured through the reference cell runs filled with  $\text{N}_2$  or  $^3\text{He}$ . The density (or pressure) of  $\text{N}_2$  and  $^3\text{He}$  in the cell can be obtained by the filling density and cross-checked with data taken at the begining of the experiment. Table 5.7 lists the filling densities of all the three target cells provided by the target group. Also, the pressure curves of  $\text{N}_2$  and  $^3\text{He}$  are provided by target group.

Due to low statistics of kaons, especially for negative kaons, the dilution factor cannot be obtained bin by bin. There are three ways to estimate the  $\text{K}^-$  nitrogen dilution factor:

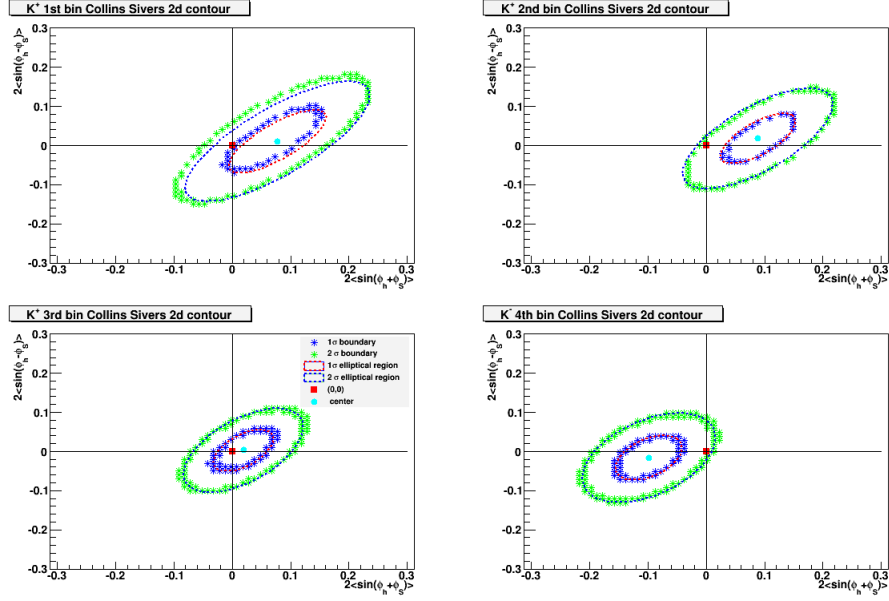


Figure 5.54: Positive kaon  $1\sigma$  and  $2\sigma$  Collins moment and Sivers moment contours for 4 bins. Aqua round point is the center point from numerical algorithm, the red round point is the central value from first order calculation. The pink and green curves are  $1\sigma$  and  $2\sigma$  Collins moment and Sivers moment contours from numerical algorithm, yet the red and blue curves are  $1\sigma$  and  $2\sigma$  contours from first order calculation.

Table 5.7: The filling densities of all three target cells. The “2% (relative)” represent the 2% of the listed density.

| Name    | ${}^3\text{He}$ (amg)     | $\text{N}_2$ (amg)         |
|---------|---------------------------|----------------------------|
| Astral  | $8.08 \pm 2\%$ (relative) | $0.11 \pm 5\%$ (relative)  |
| Maureen | $7.52 \pm 2\%$ (relative) | $0.106 \pm 5\%$ (relative) |
| Brady   | $7.87 \pm 2\%$ (relative) | $0.11 \pm 5\%$ (relative)  |

1. The first is directly from Eq. 5.108. Adding up all the kaons from the reference  $\text{N}_2$  cell with the proper weight, we obtained the result 0.92. For  $K^-$ , only 14 events were collected from reference  $\text{N}_2$  cell runs. This leads to a large statistical uncertainty for this method.
2. The second is to use the pion events from both  ${}^3\text{He}$  and  $\text{N}_2$ , and to estimate the dilution factor as 0.91.
3. The third method is to consider the quark content of  $K^-$ ,  $\bar{u}s$ , both of which are sea quarks. Since the sea quark distribution for proton and neutron are similar, one can assume that the  $K^-$  production cross section only depends on the total number of nucleons of the target. Therefore, the dilution factor can be calculated as 0.907, which is consistent with the other results.

For estimating the nitrogen dilution factor of  $K^+$ , there are also three methods:

1. One is directly from calculation from Eq. 5.108 (for all three cells), which are 0.914, 0.920, 0.918,

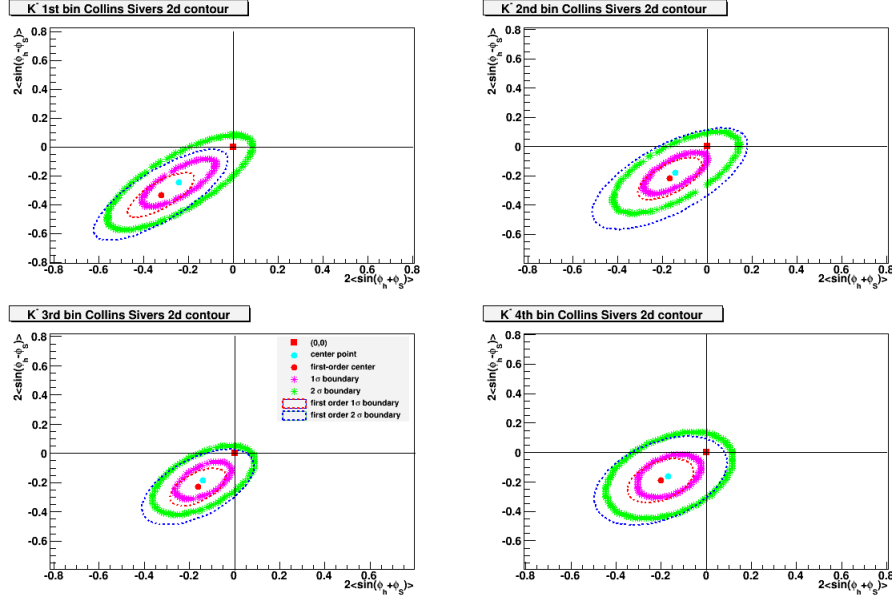


Figure 5.55: Negative kaon  $1\sigma$  and  $2\sigma$  Collins moment and Sivers moment contours for 4 bins. Aqua round point is the center point from numerical algorithm, the red round point is the central value from first order calculation. The pink and green curves are  $1\sigma$  and  $2\sigma$  Collins moment and Sivers moment contours from numerical algorithm, yet the red and blue curves are  $1\sigma$  and  $2\sigma$  contours from first order calculation.

0.916, and the relative uncertainties for  $N_2$  are 24%, 14%, 19%, 25% which corresponds to systematic uncertainties: 2.1%, 1.9%, 1.6%, 2.1%.

2. Similar to  $K^-$ , using the method comparing coincidence positive kaon events with coincidence positive pion events which have dilution factors of 0.915, 0.912, 0.917, 0.914.
3. The third method again considers the quark content of  $K^+$ ,  $u\bar{s}$ . Assuming that  $K^+$  is formed dominantly from the fragmentation of  $u$  quark, then the  $K^+$  production cross section should be proportional to the number of  $u$  quarks in the target nucleons. Since there are 5  $u$  quarks in  ${}^3\text{He}$  and 42  $u$  quarks in  ${}^{14}\text{N}$ , one can readily obtain the dilution factor as 0.916. Similar argument can also be applied to  $\pi^+$  and  $P$  production, and they should have the same dilution factor.

So it is roughly similar to  $\pi^+$  and proton.

## 5.6 Systematic Uncertainties

In this section, we will discuss various systematic uncertainties in extracting the Collins moment and Sivers moment of  ${}^3\text{He}$  from the experiment E06-010 data. In the previous section, we already discussed the systematic uncertainties in extracting nitrogen dilution factor.

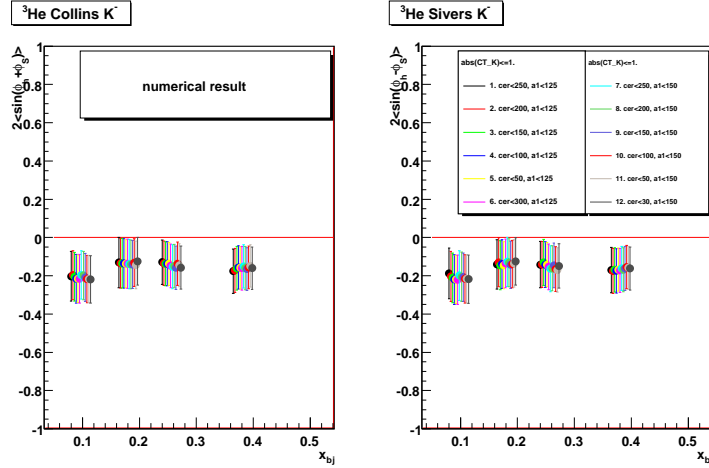


Figure 5.56: Collins moments and sivers Moments change under tof cut  $abs(CT.K.t) < 1.$  condition combining with the other different gas Cherenkov cuts and aerogel Cherenkov cuts for Negative kaon. The left panel is for  $K^-$  Collins moment, the right panel is for  $K^-$  Sivers moment. Under condition  $abs(CT.K.t) < 1.$ , the different results change with different cut combination of gas Cherenkov and aerogel Cherenkov. The fluctuation is reasonable enen for  $K^-$  at first bin, the central values of Collins moment for  $K^-$  at first bin are around  $-0.18 \sim -0.22$ , the central values of Sivers moment for  $K^-$  at first bin are around  $-0.18 \sim -0.22$ .

#### 1. Yield Drift Due to BigBite Preshower Radiation Damage

As discussed in Sec. 5.1.5, the light yield in the BigBite preshower was drifting in the experiment E06-010 due to radiation damage. The light yield was corrected in the offline analysis, however, since the preshower and shower energy deposit also played a role as trigger, some data in the lowest  $x$  bin, which corresponds to the lowest momentum, were lost. Drifts of coincidence electrons yield would lead to false asymmetries. Indeed, other slow drifts of the experimental conditions can also cause drifts of the yields.

Fortunately, the target spin was flipped regularly every 20 minutes throughout the entire experiment regardless of what happened on the detector side. So the target spin flip was independent of the yield drift. Thus, the effect of the false asymmetries would be mostly cancelled by the frequent target spin flip.

Since the yield drift is mainly due to BigBite preshower radiation damage, and affects the lowest  $x$  bin most, it is independent of the LHRS data. The central values of the extracted Collins and Sivers moments were changed on average 11% of the statistical uncertainties for the first  $x$  bin and 2% for the rest of the  $x$  bins for coincidence pions in LHRS. Since this systematic error should be independent of the hadron types detected in LHRS, the pion values are also used for the kaon systematic uncertainties due to the yield drift.

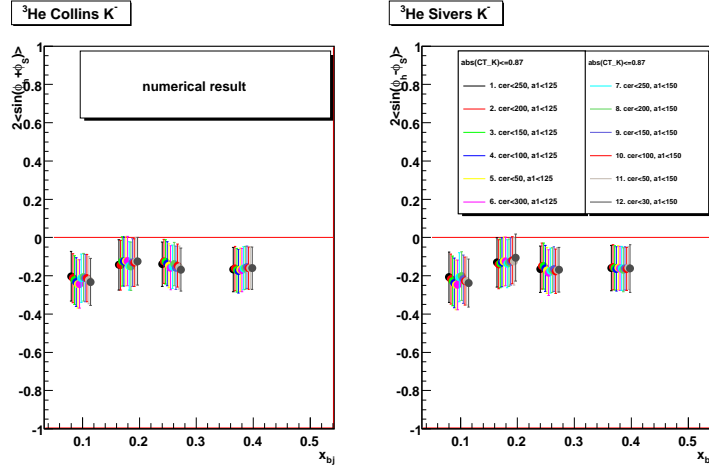


Figure 5.57: Collins moments and sivers Moments change under tof cut  $abs(CT.K.t) < 0.87$  condition combining with the other different gas Cherenkov cuts and aerogel Cherenkov cuts for Negative kaon. The left panel is for  $K^-$  Collins moment, the right panel is for  $K^-$  Sivers moment. Under condition  $abs(CT.K.t) < 0.87$ , the different results change with different cut combination of gas Cherenkov and aerogel Cherenkov. The fluctuation is reasonable even for  $K^-$  at first bin, the central values of Collins moment for  $K^-$  at first bin are around  $-0.20 \sim -0.23$ , the central values of Sivers moment for  $K^-$  at first bin are around  $-0.20 \sim -0.23$ .

## 2. Cut Stability Studies

For each cut in the analysis, we evaluated the associated systematic uncertainties. On the LHRS side, for the PID cuts, the systematic uncertainties are due to the contamination of pions in the coincidence kaons. Because the proton peak is far away from pion (kaon) peak, there is negligible contamination for coincidence proton event set. The systematic uncertainties from the pion contamination to the kaon sample will be discussed later.

On the BigBite side, for the PID cuts, the systematic uncertainties are due to the contamination in coincidence electrons (negative pion contamination and photon-induced electron contamination). The systematic uncertainties based on the negative pion contamination and photon-induced electron contamination to coincidence electron sample will be discussed later.

The acceptance cut on optics or pion rejectors in the LHRS side and acceptance cut on the charge, optics in BigBite side are quite strict and are expected to be negligible for asymmetry formation. There are two other types of cuts which are the coincidence timing cut and the vertex related cuts. For the coincidence timing cut, the systematic uncertainty is from random coincidence. The random coincidence background for  $K^-$  (contamination  $< 0.4\%$ ) and proton (contamination  $\sim 0.4\%$ ) are negligible ( $< 1\%$ ). The random coincidence background for  $K^+$  (contamination is  $\sim 2.7\%$ ) was subtracted (for coincidence proton sample, it was also subtracted, and the asymmetry is very close to zero).

For the vertex related cuts, the major source of the systematic uncertainties is associated with the BigBite target collimators. The target collimators were installed in experiment E06-010 on the BigBite side to block the high energy electrons and photons generated in the target endcaps. The target collimators significantly reduce the trigger rates and the background in the BigBite detectors. The effect of target collimators has been discussed in Sec. 4.6. In addition, for all the empty reference cell runs taken during the experiment, no coincidence kaons and protons were observed. So the target collimators are very effective, the electrons scattering from the  $^3\text{He}$  atoms near the endcaps may hit the edge of the target collimators and continue falling into the acceptance. For those kind of events, they are not likely to have a correct optics reconstruction. Therefore, they have a great chance not passing the various optics cuts and the coincidence vertex cut. The vertex cut for BigBite was between -0.14 and 0.14 meters, and it will lose 4% statistics for coincidence kaons and 5% for coincidence protons, corresponding to systematic uncertainties of about 13% of the statistics uncertainties for coincidence kaons and 15% for coincidence protons.

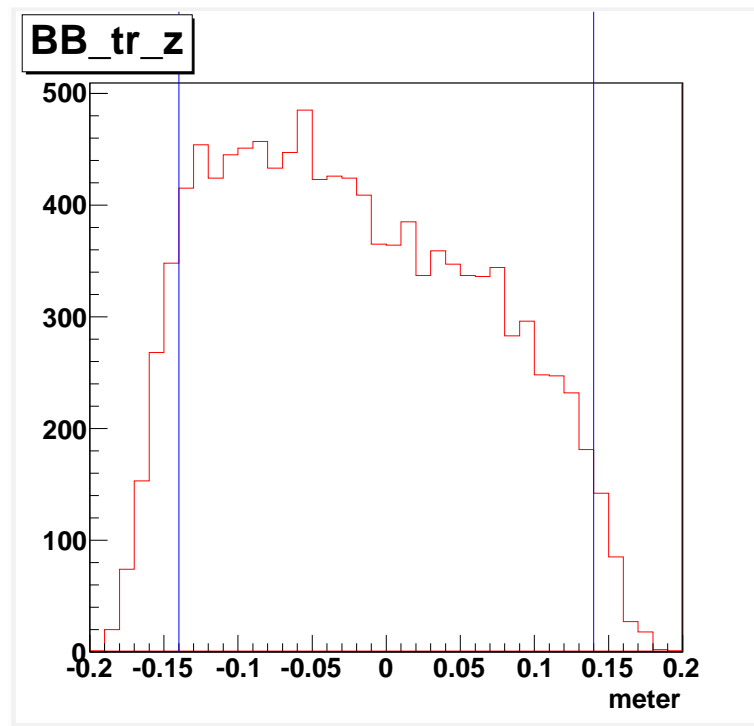


Figure 5.58: A tight BigBite vertex cut was used to study the systematic uncertainties.

### 3. BigBite negative pion contamination and Photon-induced Electron Contamination

In Sec. 5.2.2, we discussed the negative pion contamination into the coincidence electron sample is about 1-3% for coincidence with  $K^+$ , 0-1.5% for  $K^-$ , 1-6% for proton, and the photon-induced electron

contamination in the coincidence electron sample is about 0-16% for coincidence with  $K^+$ , 0-19% for  $K^-$ , 1-22% for proton. Therefore, the asymmetries of coincidence  $\pi^- K^\pm$ ,  $\pi^- p$  and photon-induced  $eK^\pm$ ,  $ep$  channel would cause false asymmetries for the SIDIS coincidence  $e\pi^\pm$ ,  $ep$  channel. In order to study these effects, we selected  $\pi^-$  in the BigBite with coincidence  $K^\pm$  or proton in LHRS, and extracted the ‘‘Collins moment’’ and ‘‘Sivers moment’’ by assuming they are coincidence electron events. The difference between the central values of the  $\pi^- K^\pm$ ,  $\pi^- p$  ‘‘Collins moment’’ and ‘‘Sivers moment’’ and the central values of  $eK^\pm$ ,  $ep$  ‘‘Collins’’ and ‘‘Sivers’’ moments are treated as the systematic uncertainties after weighting the corresponding contamination number. The effect is about 0.1-2.2%, varying bin by bin, of the corresponding statistical uncertainties. The same procedure was used to evaluate the false asymmetry due to the photon-induced electron  $eK^\pm$ ,  $ep$  contamination. In this situation, we selected the positron events in the BigBite in the production runs under the assumption that the photon-induced electron and positron have the same kinematics and same asymmetries. The effect is mainly for the lower  $x$  bins. The systematic uncertainties due to photon-induced electrons are about 22%, 13%, 4%, 4% for coincidence  $K^+$  of the corresponding statistical uncertainties, 18%, 11%, 3%, 3% for coincidence  $K^-$  of the corresponding statistical uncertainties, and 12%, 7%, 3%, 3% for coincidence proton of the corresponding statistical uncertainties.

#### 4. Pion Contamination

We discussed the pion contamination to coincidence kaon sample in LHRS in Sec. 5.2.3. In order to get pure kaons from huge background of pions, we used strict cuts for identifying kaons. The pion contamination to coincidence kaon sample is less than 1% for coincidence  $K^+$ , and less than 5% for coincidence  $K^-$ . For proton, due to the large separation between the proton peak and pion peak, the pion contamination to proton sample is negligible. The random background was already subtracted in the calculation. Due to small ‘‘Collins moment’’ and ‘‘Sivers moment’’ of coincidence pion (shown as Fig. 5.59) and the small ratio of the pion contamination to coincidence kaon sample, the systematic uncertainties from the pion contamination to kaon sample is about 1% for coincidence  $K^+$ , and 3% for coincidence  $K^-$ .

Fig. 5.59 shows the Collins moment and Sivers moment for coincidence pions. The values are relative small.

#### 5. Bin Centering Correction

From raw asymmetry, if we shift the  $x$  bin, the central values of the asymmetry can change accordingly. We have studied the effect of shift in  $x$  bin on the central values of the ‘‘Collins moment’’ and ‘‘Sivers

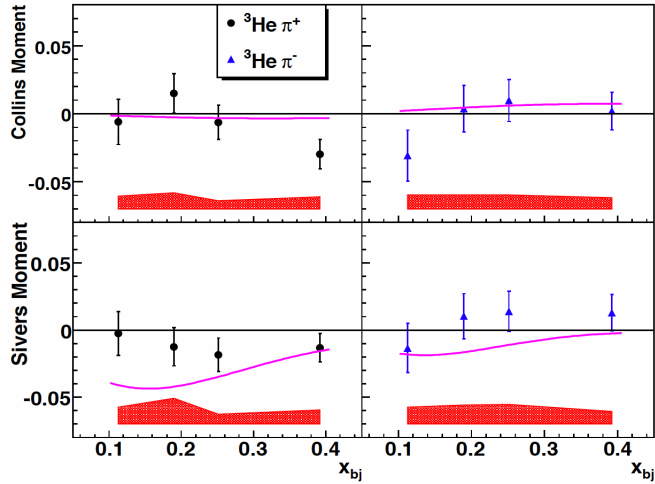


Figure 5.59: The Collins moment and Sivers moment for coincidence pions. The values are relative small.

moment”. The systematic uncertainty of the 2nd bin for coincidence  $K^-$  is 15% of the statistical uncertainty, and 11% for the 2nd bin for coincidence  $K^+$ . The systematic uncertainties of the other bins are roughly 7% of statistical uncertainties.

#### 6. Target Density Fluctuation

The target group analysed the target density fluctuation due to the change of the temperatures, as discussed in Sec. 5.1.1. This introduces a systematic uncertainty about 2.1% of the statistical uncertainties.

#### 7. Systematic Uncertainties due to Other Angular Dependent Terms

The other angular dependent terms would influence the two terms  $\langle \sin(\phi_h + \phi_S) \rangle$  and  $\langle \sin(\phi_h - \phi_S) \rangle$ . However, it is very difficult to estimate the effect due to low statistics of kaons. This will be discussed later.

Other sources of systematic uncertainties are identical to the pion data [111]. They include:

8. Target Polarization: about 5% relative to the central value of asymmetries.
9. Left HRS single-track cut: about 1.5% of the statistical uncertainties.
10. BigBite Tracking Quality cut: about 1.5% of the statistical uncertainties.
11. Livetime Correction: about 1.5% of the statistical uncertainties for the HRS negative polarity only.
12. W and W' cut: only influence the highest bin, about 8% of the statistical uncertainties for the fourth bin.



| Source                        | Systematic Uncertainties for $K^+/(K^-)$ | Type     |
|-------------------------------|--|----------|
| $N_2$ dilution                | 1.5-2.1% (0.4-2.5%)                      | relative |
| Yield Drift                   | 11%, 2%, 2%, 2% (11%, 2%, 2%, 2%)        | absolute |
| BigBite Vertex Cut            | 13% (13%)                                | absolute |
| BigBite $\pi^-$ conta         | 0.1-2.2%(0.1-2.2%)                       | absolute |
| Photon-induced electron cont. | 22%, 13%, 4%, 4% (18%, 11%, 2%, 3%)      | absolute |
| HRS Pion Contamination        | 1% (3%)                                  | absolute |
| Bin Centering                 | 7%, 11%, 7%, 7% (7%, 15%, 7%, 7%)        | absolute |
| Target Density                | 2.1%(2.1%)                               | absolute |
| Target polarization           | 5% (5%)                                  | absolute |
| LHRS Single Track             | 1.5% (1.5%)                              | absolute |
| BigBite Tracking Quality      | 1.5% (1.5%)                              | absolute |
| Livetime Correction           | 1.5%                                     | absolute |
| w & w' cut                    | -(-,-,8%)                                | absolute |
| Related cuts                  | 37%/36%, 25%/29%, 18%/19%, 17%/20%       |          |

Table 5.8: Summary of the systematic uncertainties in the coincidence  ${}^3\text{He}(e,e'K^\pm)X$  channel. Here “relative” represents the uncertainties are relative to the central value of the asymmetries. The “absolute” represents that the uncertainties are absolute, and presented in the unit of the statistical uncertainties.

Table 5.8 shows the systematic uncertainties from various sources for coincidence  $K^+(K^-)$ , the percent is relative to statistical uncertainties. The Table does not include uncertainties from other angular modulations, the radiative correction and the diffractive  $\rho$  production.

#### Systematic Uncertainties due to Other Angular Dependent Terms

In principle, we can use Maximum likeli-hood method to get multiple term fit. However, due to the low statistics for kaons, the two term Collins and Sivers moment fit already resulted in large statistical uncertainties. The method I have adopted is the following. First, for each additional angular dependent term, I perform a single-term MLM fit to find out the central values of this term for the 4 bins. Then I perform a three-term fit including the Collins and Sivers terms as well as the additional angular dependent term. However, the values of the additional term is taken from the previous single-term fit. The new central values of the systematic uncertainty caused by the neglect of this additional angular dependent term. This procedure is repeated for all additional angular dependent terms.

The following is the detailed information for the systematic uncertainties due to other angular momentum terms for  $K^+$  and  $K^-$ .

$K^+$ : Influences due to other angular momentum terms as table 5.9

$K^-$ : Influences due to other angular momentum terms as table 5.10

The final systematic uncertainties for  $K^+/K^-$  are in the following table 5.11:

Table 5.9: Influences due to other angular momentum terms for  $K^+$ 

| Angular modulation                   | bin1   | bin2   | bin3   | bin4    |
|--------------------------------------|--------|--------|--------|---------|
| Pretzlocity $\sin(3\phi_h - \phi_S)$ | -0.043 | -0.095 | -0.001 | -0.029  |
| Lmax                                 | 0.5927 | 4.8314 | 0.3062 | 2.358   |
| Collin                               | 0.0960 | 0.1487 | 0.0200 | -0.0895 |
| Sivers                               | 0      | 0.0620 | 0.0841 | 0.0242  |
| $\sin(2\phi_h - \phi_S)$             | -0.001 | 0.011  | -0.012 | -0.006  |
| Lmax                                 | 0.086  | 2.132  | 0.306  | 2.296   |
| Collins                              | 0.0721 | 0.0943 | 0.0141 | -0.1015 |
| Sivers                               | 0.0061 | 0.0079 | 0.0181 | -0.0061 |
| $\sin(\phi_S)$                       | -0.014 | -0.071 | 0.016  | -0.004  |
| Lmax                                 | 0.0902 | 2.144  | 0.307  | 2.300   |
| Collins                              | 0.0662 | 0.0943 | 0.0123 | -0.0955 |
| Sivers                               | 0.0058 | 0.0081 | 0.0362 | -0.0051 |
| Cahn ( $\cos(\phi_S)$ )              | small  | small  | small  | small   |
| Boer_mulder ( $\cos(2\phi_h)$ )      | small  | small  | small  | small   |

Table 5.10: Influences due to other angular momentum terms for  $K^-$ 

| Angular modulation                   | bin1   | bin2   | bin3   | bin4   |
|--------------------------------------|--------|--------|--------|--------|
| Pretzlocity $\sin(3\phi_h - \phi_S)$ | -0.096 | -0.073 | -0.047 | -0.13  |
| Lmax                                 | 1.474  | 1.318  | 1.220  | 1.636  |
| Collin                               | -0.166 | -0.105 | -0.113 | -0.125 |
| Sivers                               | -0.143 | -0.121 | -0.131 | -0.086 |
| $\sin(2\phi_h - \phi_S)$             | -0.004 | -0.013 | -0.003 | 0.013  |
| Lmax                                 | 2.107  | 2.007  | 1.694  | 1.834  |
| Collins                              | -0.246 | -0.145 | -0.143 | -0.165 |
| Sivers                               | -0.253 | -0.181 | -0.191 | -0.156 |
| $\sin(\phi_S)$                       | -0.016 | -0.165 | -0.107 | -0.001 |
| Lmax                                 | 2.115  | 2.245  | 1.784  | 1.834  |
| Collins                              | -0.256 | -0.235 | -0.203 | -0.165 |
| Sivers                               | -0.243 | -0.091 | -0.131 | -0.156 |
| For Cahn ( $\cos(\phi_S)$ )          | small  | small  | small  | small  |
| Boer_mulder ( $\cos(2\phi_h)$ )      | small  | small  | small  | small  |

Table 5.11: Summary of the final systematic uncertainties in the coincidence  ${}^3\text{He}(e,e'K^\pm)X$  channel.

| Sources of systematic uncertainties | Systematic Uncertainties $K^+/(K^-)$       |
|-------------------------------------|--|
| Target and cuts                     | 37%/36%, 25%/29%, 18%/19%, 17%/20%         |
| Pretzlocity Collins                 | 32%/31%, 32%/31%, 32%/31%, 32%/31%         |
| Pretzlocity Sivers                  | 52%/48%, 52%/48%, 52%/48%, 52%/48%         |
| $\sin(2\phi_h - \phi_S)$ Collins    | 5.1%/3.3%, 5.1%/3.3%, 5.1%/3.3%, 5.1%/3.3% |
| $\sin(2\phi_h - \phi_S)$ Sivers     | 2.4%/2.5%, 2.4%/2.5%, 2.4%/2.5%, 2.4%/2.5% |
| $\sin(\phi_S)$ Collins              | 4.7%/5.3%, 4.7%/5.3%, 4.7%/5.3%, 4.7%/5.3% |
| $\sin(\phi_S)$ Sivers               | 2.6%/4.1%, 2.6%/4.1%, 2.6%/4.1%, 2.6%/4.1% |
| Cahn $\cos(\phi_h)$ Collins         | 3.2%/1.7%, 3.2%/1.7%, 3.2%/1.7%, 3.2%/1.7% |
| Cahn $\cos(\phi_h)$ Sivers          | 2.2%/3.1%, 2.2%/3.1%, 2.2%/3.1%, 2.2%/3.1% |
| Boer_mulder $\cos(2\phi_h)$ Collins | 1.9%/3.1%, 1.9%/3.1%, 1.9%/3.1%, 1.9%/3.1% |
| Boer_mulder $\cos(2\phi_h)$ Sivers  | 2.2%/2.3%, 2.2%/2.3%, 2.2%/2.3%, 2.2%/2.3% |

13. Systematic uncertainties due to incomplete acceptance:

For the setup of the transversity experiment, the spin directions were set up in four directions (left/right in transver\_in\_plane and up/down in vertical), the azimuthal angles  $\phi_h$  and  $\phi_S$  are not complete  $2\pi$  coverage, for the larger statistics, the incomplete acceptance has less effects to the extracted Collins and Sivers moments. But for smaller statistics, the incomplete acceptance has big effects. That causes big systematic uncertainties.

Here, three plots of sub group kaons and pions plots for Collins and Sivers moments are showing in Fig. 5.61, Fig. 5.60. The fluctuation for small statistics are bigger, the systematic uncertainties due to incomplete acceptance is from the maximum difference between the central values from sub group results to the final central values with real data comparing with the statistical uncertainties. For negative kaon, the total real events are around 2000 events, the 1000 events sub group negative kaon and 2000 events positive kaon situations are selected as the comparison. For the positive kaon, the total real events are around 11500 events, so the positive kaon sub 5750 events and negative pions 11500 events and positive pions 11500 events are listed as comparison.

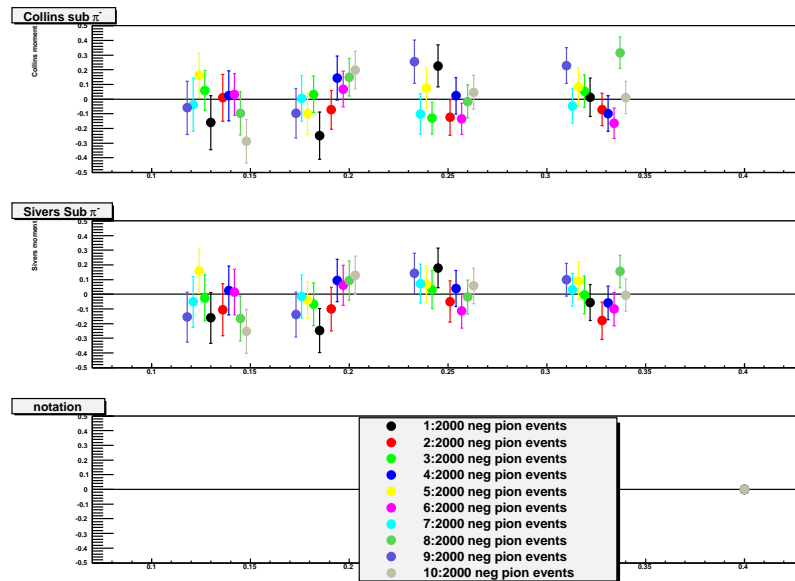


Figure 5.60: The Collins and Sivers moments of random sub group negative pion on Transversely  $^3\text{He}$  target are shown. The fluctuation is bigger, but it is reasonable for the total pion results.

For small statistics, there are some correlation between Collins and Sivers moments, which mostly due to incomplete acceptance, meanwhile, with low statistics, there will randomly have false correlation between different independent variables, both of them influence the final results, they are counted as systematic uncertainties.

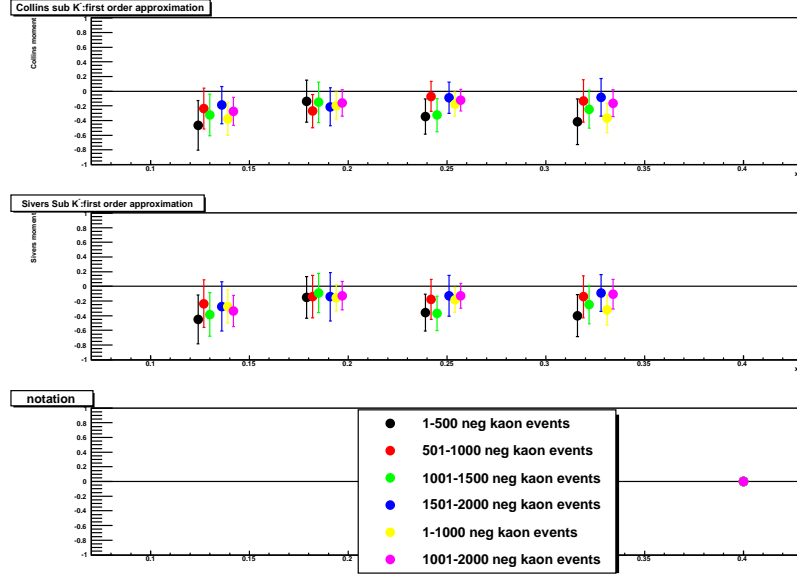


Figure 5.61: The Collins and Sivers moments of sub group negative kaon on transversely  $^3\text{He}$  target are shown. The fluctuation is bigger, but it is reasonable for the total negative kaon results.

Table 5.12: Sources of systematic uncertainties for  $K^+/(K^-)$  due to incomplete acceptance

|               | bin1 | bin2 | bin3 | bin4 |
|---------------|------|------|------|------|
| $K^+$ Collins | 18%  | 9%   | 9%   | 13%  |
| $K^+$ Sivers  | 16%  | 9%   | 8%   | 13%  |
| $K^-$ Collins | 38%  | 27%  | 31%  | 48%  |
| $K^-$ Sivers  | 24%  | 31%  | 25%  | 36%  |

The total systematic uncertainties due to incomplete acceptance for  $K^+/K^-$  are showing in the following table 5.12:

The final systematic uncertainties is listed in the following table 5.13:

## 5.7 $^3\text{He}$ Results

After considering nitrogen dilution and systematic uncertainties, we obtained the results of Collins and Sivers moments of coincidence  $K^\pm$  on transversely polarized  $^3\text{He}$  target, as shown in Fig. 5.62.

So far, we have presented the result on Collins and Sivers moments as a function of  $x$ . It is of interest to analyse the data as a function of other kinematic variables, such as  $Q^2$ ,  $P_T$  and  $z$ . Due to the limited

Table 5.13: Final systematic uncertainties for  $K^+/(K^-)$

|                    | bin1    | bin2    | bin3    | bin4    |
|--------------------|---------|---------|---------|---------|
| Tot_sys_uncert_Col | 51%/59% | 41%/49% | 37%/46% | 37%/59% |
| Tot_sys_uncert_Siv | 65%/63% | 57%/63% | 55%/57% | 55%/63% |

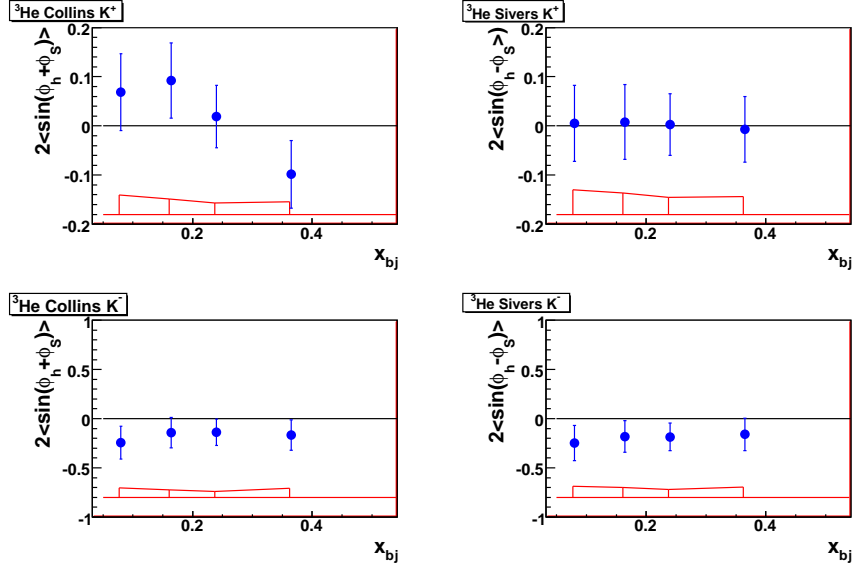


Figure 5.62: The results of Collins and Sivers moments of kaon on transversely polarized  ${}^3\text{He}$  target. The error bars represent the statistical uncertainties only. The systematic uncertainties are shown in the bottom.

spectrometer acceptance, the different kinematic variables could be highly correlated. To investigate possible correlations between various kinematic variables, we show in Figs. 5.63 and 5.64 the correlations for  $Q^2$  versus  $x$ ,  $P_T$  versus  $x$ , and  $z$  versus  $x$ , respectively, for all hadrons. We find that  $Q^2$  is strongly correlated with  $x$ , Therefore it is not necessary to analyse the Collins and Sivers moments as a function of  $Q^2$ , since we already have the result for  $x$ . On the other hand, Figs. 5.63 and 5.64 show that the correlations between  $P_T$  and  $x$  and between  $z$  and  $x$  are not very strong. Therefore, I have repeated the analysis with data binned as a function of  $P_T$  and  $z$ . The results of such analysis are shown in Figs. 5.65 and 5.66.

## 5.8 Nuclear Correction: From ${}^3\text{He}$ to Neutron

As we know, the spin dependent cross section of  ${}^3\text{He}$  can be written as the sum of spin dependent cross section of proton and neutron using the effective nucleon polarization:

$$\sigma_T^{3He} = P_n \sigma_T^n + 2P_p \sigma_T^p \quad (5.109)$$

For unpolarized cross section, we have

$$\sigma_U^{3He} = \sigma_U^n + 2\sigma_U^p \quad (5.110)$$

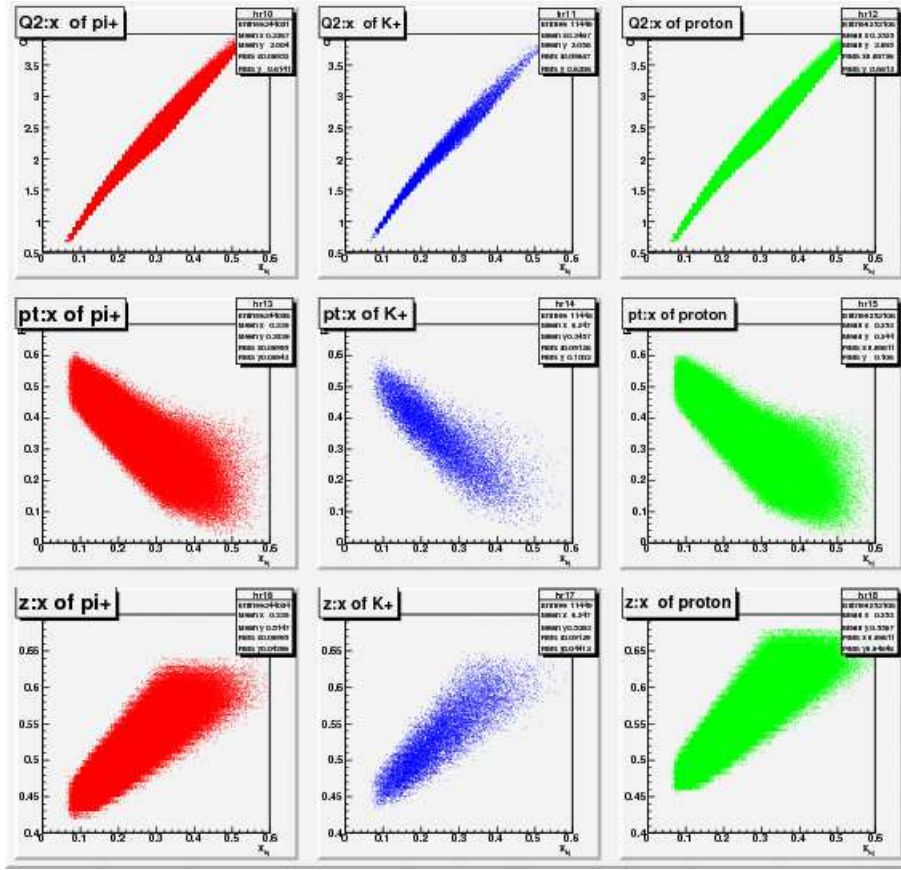


Figure 5.63: The two dimensional correlations between  $Q^2$  vs  $x$ ,  $p_t$  vs  $x$  and  $z$  vs  $x$ , the left column is for  $\pi^+$ , the middle column is for  $K^+$ , the right column is for proton. The first row is for  $Q^2$  vs  $x$ , which has strong correlations. The second row is for  $p_t$  vs  $x$ , which shows some correlations, so it is worth showing Collins and Sivers moments as a function of  $p_t$ , the third row is for  $z$  vs  $x$ , which shows some corrections.

With the following definition:

$$A_p = \frac{\sigma_T^p}{\sigma_U^p}, A_n = \frac{\sigma_T^n}{\sigma_U^n}, f_{H_2} = \frac{\sigma_U^n}{\sigma_U^n + 2\sigma_U^p} \quad (5.111)$$

Then,

$$A_n = \frac{A_{3He} - (1 - f_{H_2})P_p A_p}{f_{H_2} P_n} \quad (5.112)$$

From ref [128] [129] [130], the effective nucleon polarization  $P_p$  and  $P_n$  can be obtained as follows:

$$P_n = 0.86_{-0.02}^{+0.036}, P_p = -0.028_{-0.004}^{+0.0094}. \quad (5.113)$$

If  $f_{H_2}$  and  $A_p$  are available, the result on neutron asymmetry can be obtained from the measured asymmetry on  $^3\text{He}$ .

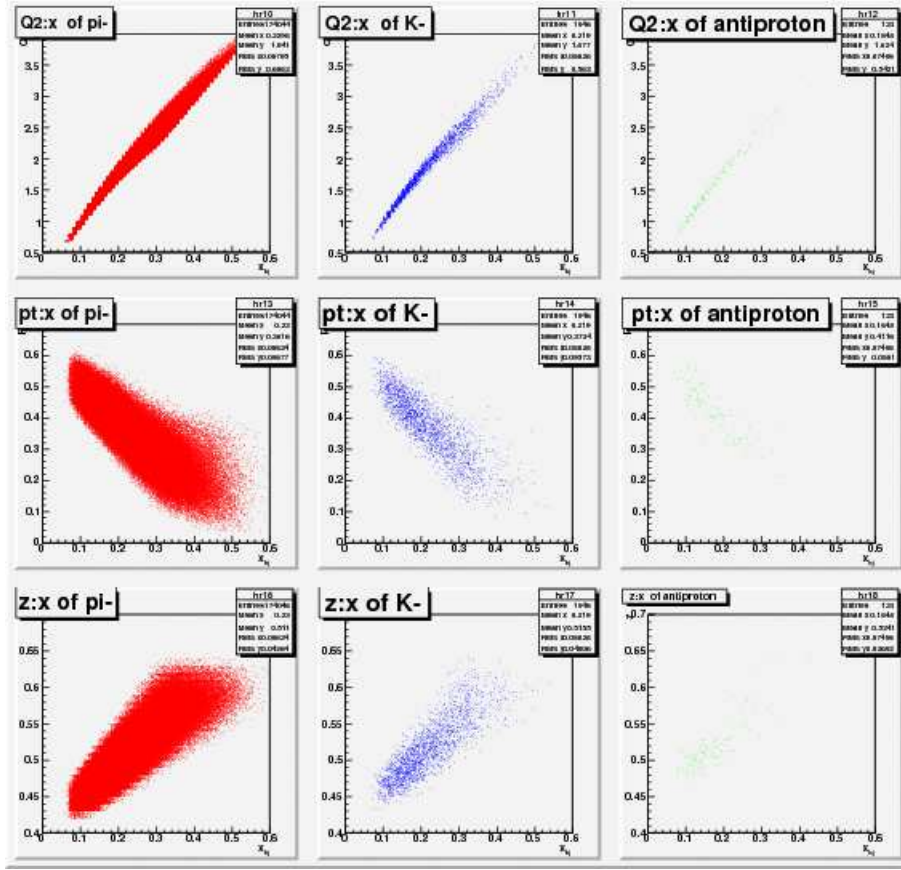


Figure 5.64: The two dimensional correlations between  $Q^2$  vs  $x$ ,  $p_t$  vs  $x$  and  $z$  vs  $x$ , the left column is for  $\pi^-$ , the middle column is for  $K^-$ , the right column is for anti-proton. The first row is for  $Q^2$  vs  $x$ , which has strong correlations. The second row is for  $p_t$  vs  $x$ , which shows some correlations, so it is worth showing Collins and Sivers moments as a function of  $p_t$ , the third row is for  $z$  vs  $x$ , which shows some corrections.

In principle, we can determined  $f_{H_2}$  from the  $H_2$  reference data. Indeed, this can be done for  $K^+$ , as shown in Fig. 5.67. However, the low statistics for  $K^-$  makes it very difficult to obtain  $f_{H_2}$  with any accuracy. The top panel in Fig. 5.67 shows the result when all  $K^-$  data are combined into a single bin (the statistical error bars are shown for all four bins). Clearly, we have to use other methods for estimating  $f_{H_2}$ .

As discussed earlier, when we considered the dilution factor for  $N_2$ , we can assume that the production of  $K^-(\bar{u}s)$  is only from the DIS on sea quarks which subsequently hadronize into a  $K^-$ . Therefore, the dilution factor  $f_{H_2}$  should be  $\sim \frac{1}{3}$  for  $K^-$  production, since there are three nucleons in  ${}^3\text{He}$  versus a single nucleon for neutron. One can also assume that the production of  $K^+(u\bar{s})$  is dominated by DIS on u quark. Since there are 5 u quarks in  ${}^3\text{He}$  and only one u quark in neutron, one expects the dilution factor for  $K^+$  to be roughly  $\frac{1}{5}$ . It is interesting that these simple estimate are in qualitative agreement with the data shown in Fig. 5.67.

Using these values for the  $K^+$  and  $K^-$  dilution factors, we can know obtain the Collins and Sivers

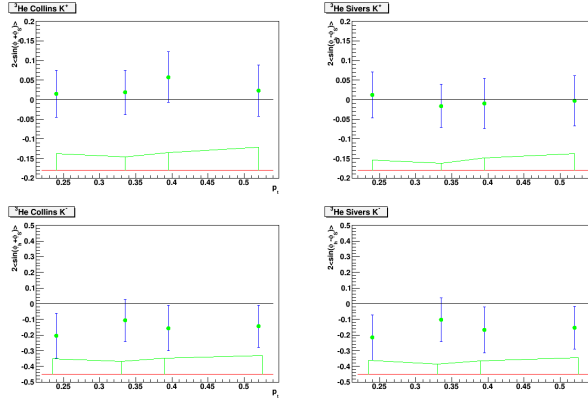


Figure 5.65: Collins and Sivers moments of kaons versus  $p_t$ . Upleft panel: Collins moment of  $K^+$ , upright panel: Sivers moment of  $K^+$ . Downleft panel: Collins of  $K^-$ , downright panel: Sivers moment of  $K^-$ . The Collins and Sivers moments of  $K^-$  are negative, the Sivers moment of  $K^+$  is consistent with zero.

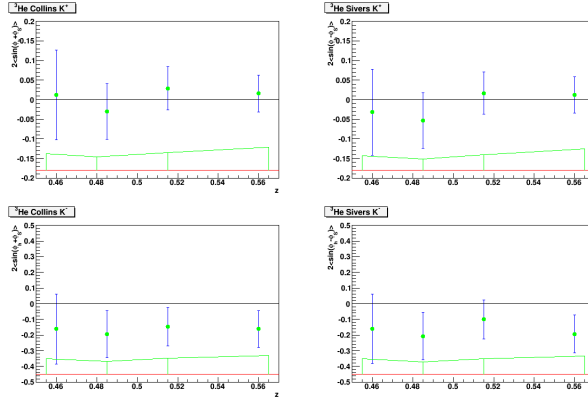


Figure 5.66: Collins and Sivers moments of kaons versus  $z$ . Upleft panel: Collins moment of  $K^+$ , upright panel: Sivers moment of  $K^+$ . Downleft panel: Collins of  $K^-$ , downright panel: Sivers moment of  $K^-$ . The Collins and Sivers moments of  $K^-$  are negative, the Sivers moment of  $K^+$  is consistent with zero.

moments for neutron. The results are shown in Fig. 5.68. Fig. 5.69 compares our results on the Sivers moment with the theoretical predictions by Anselmino *et al.* [131] based on their global fits to existing HERMES and COMPASS data. While the  $K^+$  data are consistent with the prediction, the  $K^-$  data on the Sivers moment are significantly more negative than the prediction. Unfortunately, the large experimental uncertainties do not allow a more definitive conclusion.



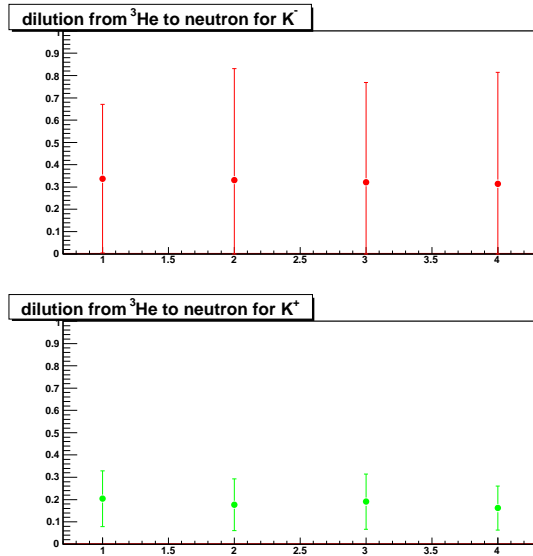


Figure 5.67: The  $^3\text{He}$  dilution factor for kaons from reference  $H_2$  data. The top panel is for  $\text{K}^-$  (assuming all bins to calculate the central value, and showing the statistical uncertainty for each bin), the bottom panel is for  $\text{K}^+$ .

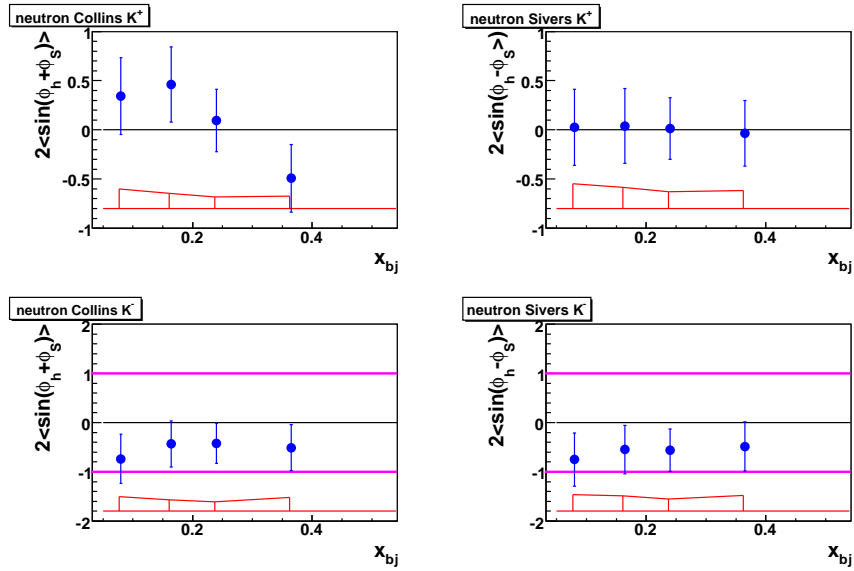


Figure 5.68: Results of Collins and Sivers moments of kaon on transversely polarized “neutron” target. The error bars represent the statistical uncertainties only. The systematic uncertainties are shown in bottom.

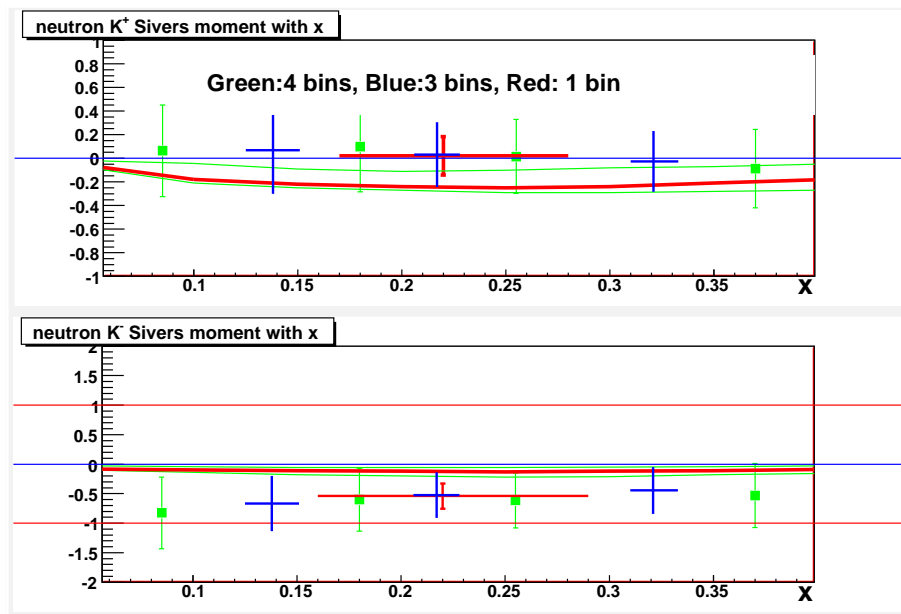


Figure 5.69: Comparison between the neutron Siverts moment data with theoretical predictions by Anselmino *et al.* [131]. The red curves are the central values of the prediction, and the green curves indicate the  $1\sigma$  range. The data points with different colors correspond to analysis using different number of bins in  $x$ . The top panel is for  $K^+$  and the bottom panel is for  $K^-$ .

# Chapter 6

## Results and Conclusion

As discussed in Chapter 5, the kaon Collins and Sivers moments had been extracted simultaneously using the Maximum Likelihood Method (MLM). The pion Collins and Sivers moments were already extracted as described in X. Qian's thesis [111]. We summarize the findings on the Collins and Sivers moments for both pions and kaons in this Chapter.

### 6.1 Pion Collins Moment and Sivers Moment

The pion results of Collins ( $2 \langle \sin(\phi_h + \phi_S) \rangle$ ) and Sivers ( $2 \langle \sin(\phi_h - \phi_S) \rangle$ ) moments on  ${}^3\text{He}$  are shown in Fig. 6.1.

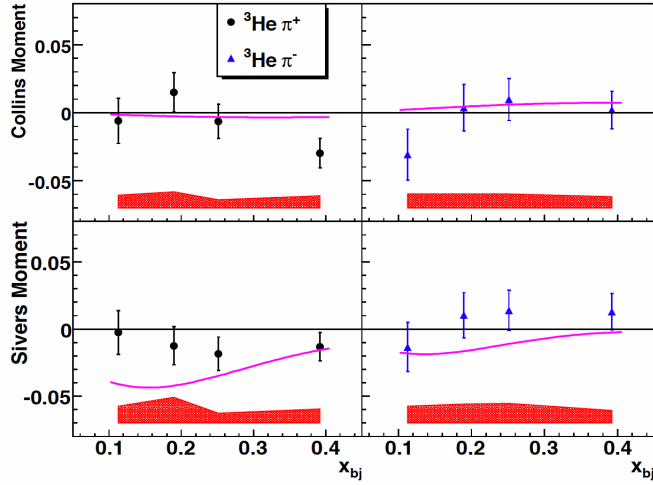


Figure 6.1: Final pion Collins moment and Sivers moment on neutron. Fig. is from [111]

The magenta curves are from Anselmino *et al.* [131] [132]. The black curves in Collins moments are from Ma *et al* [134]. The red curves are from Pasquini [111]. The blue curves and blue bands are from W. Vogelsang and F. Yuan [136] [137]. The observations of the preliminary neutron results <sup>1</sup> on Collins and Sivers moments are similar to those of  ${}^3\text{He}$ . They are:

<sup>1</sup>The final results will be presented in a future paper.

- Except for the fourth x bin of  $\pi^+$ , the rest of the extracted Collins moment are consistent with the theoretical predictions.
- Both the  $\pi^+$  and  $\pi^-$  Sivers moments are systematically higher than the predictions. For the  $\pi^-$  Sivers moment, our data suggest that the asymmetry favors a positive value, while the calculation suggests a negative value.
- The second and the fourth x bin of  $\pi^+$  show non-zero target spin asymmetries with more than two  $\sigma$  deviation from zero (stat. only).
- Our  $\pi^+$  Sivers moments do not favor large negative value. [111]

## 6.2 Kaon Collins and Sivers Moments

The preliminary kaon results of Collins ( $2 \langle \sin(\phi_h + \phi_S) \rangle$ ) and Sivers ( $2 \langle \sin(\phi_h - \phi_S) \rangle$ ) moments on  ${}^3\text{He}$  are shown in Fig. 6.2.

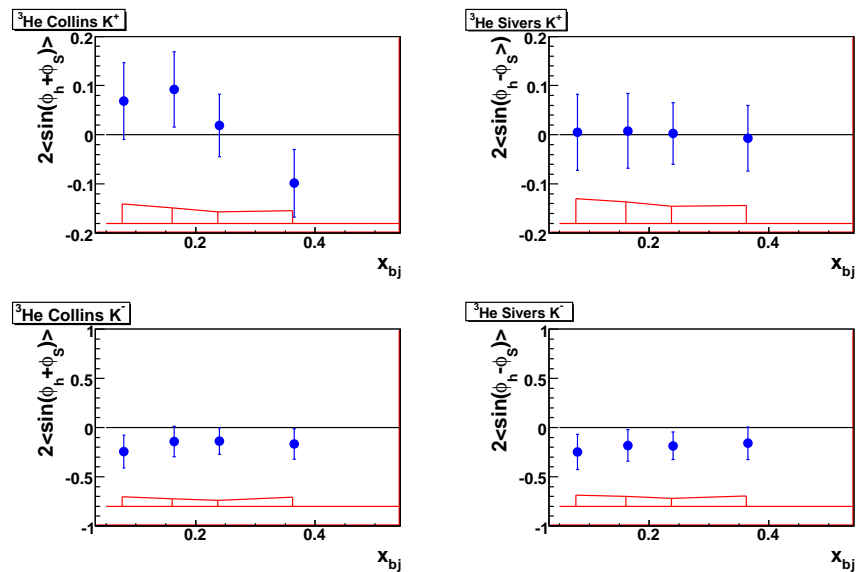


Figure 6.2: Final kaon Collins moment and Sivers moment on  ${}^3\text{He}$ .

Due to small kaon statistics and limited kaon information from literature, precise extraction of kaon Collins and Sivers moments on neutron is not trivial. In Chapter 5, we already show the neutron results based on the dilution factor assumption from  ${}^3\text{He}$  to neutron for both  $\text{K}^+$  and  $\text{K}^-$ . Here I only show the kaon results on  ${}^3\text{He}$ . The observations of the preliminary kaon results<sup>2</sup> on  ${}^3\text{He}$  are as following:

<sup>2</sup>The final results will be presented in a future paper.

- $K^+$  Sivers moments are consistent with zero.
- $K^-$  Collins and Sivers moments are both negative approximately 1 sigma away from zero.

### 6.3 Conclusion

In summary, we have presented preliminary kaon Collins and Sivers moments on  $^3\text{He}$  through the SIDIS SSA measurement. Experiment E06010 provides the first data in this channel with kinematic coverage  $x = 0.13 \sim 0.41$  and  $Q^2 = 1.31 \sim 3.1 \text{GeV}^2$ . Due to small kaon statistics and limited kaon information from literature, the extraction of kaon Collins and Sivers moments on neutron has large uncertainties. Yet we still can provide some information on neutron. These data would improve our knowledge on the transverse spin structure of neutron in the valence quark region. Together with other data, the transversity and Sivers distribution functions for strange quark could be extracted.

In the future, the investigation of quark transversity distribution, quark Sivers distribution and quark fragmentation will continue in JLab Hall A. Two new experiments have already been proposed to run after the 12 GeV upgrade is completed. One is experiment (PR09-018) which will use the BigBite spectrometer and a new large acceptance Super BigBite spectrometer as a hadron arm to measure the SSA in SIDIS reactions using a transversely polarized  $^3\text{He}$  target [138]. The other is experiment (PR12-09-014) which will use a solenoid detector (SoLID) with a full  $2\pi$  azimuthal angle coverage to measure the SSA on a transversely polarized  $^3\text{He}$  target [139]. These two experiments are expected to extract much more precise results of transversity and Sivers distribution functions.

The main accomplishment of this experiment, I believe, is the demonstration of the feasibility of measuring SSA using transversely polarized  $^3\text{He}$  target at the Jefferson laboratory. Hopefully, this experiment will lead to many future exciting results and possibly unexpected new findings.

# References

- [1] <http://cdms.berkeley.edu/Education/DMPages/essays/whyDM.shtml>
- [2] S. Dürr *etal.* *Science*, **322**:1224,2008.
- [3] M. Gell-Mann. A schematic model of baryons and mesons. *Phys.Lett.*, **8**:214, 1964.
- [4] G. Zweig, 1964. CERN Report TH 401.
- [5] R. P. Feynman, 1969, Proceeding of the 3rd Topical Conference on High Energy Collision of Hadrons, Stony Brook, N. Y.
- [6] J. D. Bjorken and F. A. Paschos. *Phys.Rev.*, **185**:1975, 1969.
- [7] M. Breidenbach *etal.* *Phys.Rev.Lett.*, **23**:935, 1969.
- [8] E. D. Bloom *etal.* *Phys.Rev.Lett.*, **23**:930,1969.
- [9] M. Y. Han and Y. Nambu. *Phys.Rev.*, **139**:1006, 1965.
- [10] O. W. Greenberg. Spin and unitary spin independence in a paraquark model of baryons and mesons, *Phys.Rev.Lett.*, **13**:598, 1964.
- [11] P.L.Anthony *etal.* (E155 Collaboration), Measurements of the  $Q^2$  dependence of the proton and neutron spin structure function  $g_1^p$  and  $g_1^n$ , *Phys.Lett.*, **B493**, 19-28(2000).
- [12] P.L.Anthony *etal.* (E155 Collaboration), Precision measurement of the proton and deuteron spin structure functions  $g_2$  and asymmetries  $A_2$ , *Phys.Lett.*, **B553**, 18-24(2003).
- [13] J.P.Ralston and D. E. Soper, *Nucl.Phys.*, **B152**, 109 (1979).
- [14] X.Artru and M. Mekhfi, *Z.Phys.*, **C45**, 669 (1990). *Nucl. Phys.* B152, 109 (1979)
- [15] P. Schweitzer *etal.*, *PhysRev.*, **D64**, 034013(2001).
- [16] B. Q. Ma, I. Schmidt and J. J. Yang, *Phys.Rev.*, **D65**, 034010(2002),and B. Q. Ma private communications, 2005.
- [17] J.C.Collins, *Nucl.Phys.*, **B396**,161 (1993).
- [18] A. Airapetian *etal.*, (HERMES), *Phys.Rev.Lett.*, **84**, 4047 (2002);
- [19] A. Airapetian *etal.*, (HERMES), *Phys.Rev.*, **D64**,097101 (2001);
- [20] A. Airapetian *etal.*, (HERMES), *Phys.Lett.*, **B562**, 182 (2003).
- [21] The COMPASS Collaboration, *Phys.Rev.Lett.*, **94**, 202002 (2005).
- [22] R. Seidl (Belle Collaboration), to be published in the proceedings of SPIN 2004 (Trieste).
- [23] D. Sivers, *Phys.Rev.*, **D43**, 261 (1991).

- [24] S. J. Brodsky, D. S. Hwang and I. Schmidt, *Phys.Lett.*, **B530**, 99 (2002);
- [25] S. J. Brodsky, D. S. Hwang and I. Schmidt, *Nucl.Phys.*, **B642**, 344 (2002).
- [26] J. C. Collins, *Phys.*, **B536**, 43 (2002).
- [27] X. Ji and F. Yuan, *Phys.Lett.*, **B543**, 66 (2002);
- [28] A.V. Belitsky, X. Ji and F. Yuan, *Nucl.Phys.*, **B656**, 165 (2002).
- [29] Hall A Transversity Experiment (E-06-010/E-06-011, update of E-03-004).  
<http://hallweb.jlab.org/experiment/transversity/>
- [30] M. Anselmino *etal.*, A. Efremov and E. Leader, *Phys.Rept.* **261**, 1-124(1995).
- [31] S. Chekanov *etal.* [ZEUS Collaboration], arXiv:hep-ex/0208023.
- [32] A. D. Martin et al. *Eur. Phys. J. C* **23** (2002) 73.
- [33] J. Pumplin et al. [CTEQ Collaboration], *JHEP* 0207 (2002) 012.
- [34] Particle Data Group, *Phys.Lett.* **B 667**, 1 (2008).
- [35] M. Burkardt, A Miller and W-D Nowak, arXiv:0812.2208v2, [hep-ph], 2009.
- [36] P. L. Anthony *etal.* (E155 Collaboration), *Phys.Lett.* **B553**, 18-24(2003).
- [37] J.D. Björken, *Phys.Rev.* **179**, 1547 (1969).
- [38] J.D. Björken and E.A. Paschos *Phys.Rev.* **185**, 1975(1969)
- [39] R. Feynman, *Phys.Rev.Lett.* **23**, 1415 (1969).
- [40] M. Gell-Mann, *Phys.Lett.* **8**, 214 (1964).
- [41] G. Zweig, “An SU(3) model for strong interaction symmetry and its breaking”, CERN preprints **TH-401**, **TH-412** (1964).
- [42] V. Barone, A. Drago and P.G. Ratcliffe, *Phys.Rep.* **359**, 1-168 (2002).
- [43] R. L. Jaffe, arXiv:hep-ph/9602236 (1996).
- [44] J. Soffer, *Phys.Rev.Let.* **74**, 1292 (1995).
- [45] S. Kretzer, *Phys.Rev* **D62**, 054001 (2000).
- [46] Alessandro Bacchetta, Umberto D’Álesio, Markus Diehl, C. Andy Miller, *Phys.Rev.* **D70**, 117504 (2004).
- [47] A. Bacchetta *etal.*, arXiv:hep-ph/0707.3372v1 (2007).
- [48] A. Bacchetta, A. Metz, J. Yang, arXiv:hep-ph/0307282 (2003).
- [49] L. L. Pappalardo, Ph. D thesis, Università degli Studi di Ferrara, 2008.
- [50] A. Airapetian et al. (HERMES), *Phys.Rev.Lett.* **94**, 012002 (2005).
- [51] M. Dieffenthaler et al., hep-ex/0507013, (2005).
- [52] The COMPASS Collaboration, *Phys. Rev. Lett.* **94**,202002 (2005).
- [53] M. Dieffenthaler (on behalf of the HERMES collaboration), hep-ex/07062242v2, (2007).
- [54] The COMPASS Collaboration, CERN\_PHEP/2008-002, hep-ex/08022160v2, (2009).

- [55] M. Anselmino et al., Phys. Rev. **D71**, 074006 (2005).
- [56] M. Anselmino et al., Phys. Rev. **D72**, 094007 (2005).
- [57] W. Vogelsang and F. Yuan, Phys. Rev. **D72**, 054028 (2005).
- [58] M. Anselmino et al., The Sivers Function From SIDIS Data, hep-ph/0807.0166v1, 2008.
- [59] M. Anselmino et al. Transversity and Collins functions from SIDIS and  $e^+e^-$  data, hep-ph/07010063v3, 2007.
- [60] M. Anselmino et al., Sivers Effect for Pion and Kaon Production in Semi-Inclusive Deep Inelastic Scattering. hep-ph/0805.2677v1, 2008.
- [61] A. Martin, talk in DIS 2010 (2010).
- [62] H. Wollny, COMPASS collabration, Transverse Spin Effects at COMPASS. hep-ex/0902.0519v2, 2009.
- [63] A. Airapetian et al. Observation of the Naive-T-odd Sivers Effect in Deep-Inelastic Scattering. hep-ex/09063918v2, 2009.
- [64] M. Anselmino et al., Phys. Rev. **D75**, 054032 (2007).
- [65] M. Anselmino et al., Transversity and Collins Fragmentation Functions: Towards a New Global Analysis. hep-ph/0807.0173v1, 2008.
- [66] Y. Qiang, Ph.D. Thesis, MIT, 2007
- [67] J. Alcorn et al., Nucl. Instrum. Meth. **A522**, 294(2004).
- [68] Hall A Beam and Polarimeters webpage, <http://hallweb.jlab.org/equipment/beam.html>.
- [69] X. Zheng, Ph. D. Thesis, MIT, 2002
- [70] P. H. Solvignon, Ph.D. thesis, Temple University, 2006
- [71] JLab Hall A General Operations Manual
- [72] K. Unser. IEEE Trans. Nucl. Sci., NS28:2344,1981
- [73] B. Humensky, "General exam advanced project", Princiton University(1999).
- [74] [http://hallweb.jlab.org/experiment/HAPPEX/HAPPEXII/parity\\_daq.html](http://hallweb.jlab.org/experiment/HAPPEX/HAPPEXII/parity_daq.html)
- [75] C. Yan, Technical Report, Hall C Raster System-The Second Generation, Jefferson Lab, (unpublished), (1997).
- [76] Particle Data Group' Review of Particle Physics 2006.
- [77] J.-P. Chen, Hall A Polarized  $^3\text{He}$  Target System, [http://hallweb.jlab.org/equipment/targets/polhe3\\_tgt.html](http://hallweb.jlab.org/equipment/targets/polhe3_tgt.html).
- [78] F.D.Colegrove, L.D.Shearer, and G.K.Walters, Phys. Rev. **132**, 2561(1963).
- [79] M. V. Romalis, Ph. D. thesis, Princeton University, Princeton, New Jersey (1998).
- [80] JLAB E94-010, G. D. Cates, Z.-E. Meziani et al., <http://www.jlab.org/e94010/>
- [81] [http://hallweb.jlab.org/targets/polhe3/polhe3\\_tgt.html](http://hallweb.jlab.org/targets/polhe3/polhe3_tgt.html); and tech notes in <http://www.jlab.org/e94010>
- [82] Online Spin Flip, [https://hallweb.jlab.org/wiki/index.php/Online\\_Spin\\_Flip](https://hallweb.jlab.org/wiki/index.php/Online_Spin_Flip)



- [83] Feng Xiong, Ph.D thesis, Massachusetts Institute of Technology(MIT), 2002.
- [84] A. S. Barton, N. R. Newbury, G. D. Cates, B. Driehuys, H. Middleton, and B. Saam, *Phys. Rev. A* **49**, 2766 (1994).
- [85] T. E. Chupp *etal.*, *Phys. Rev. C*, **36** 2244 (1987).
- [86] M. V. Romalis, Ph. D thesis, Princeton University, Princeton, New Jersey (1998).
- [87] E. Babcock, *etal.*, *Phys. Rev. Lett.* 91, 123003(2003).
- [88] J. Alcorn et al. Basic instrumentation for Hall A at Jefferson Lab. *Nucl.Instr.andMeth.*, A522:294, 2004.
- [89] W. Bertozzi *etal.*, *Nucl.Instrum.andMeth.*, **191**, 957 (1977).
- [90] N. Liyanage, Ph. D. thesis, Massachusetts Institute of Technology, Cambridge, Massachusetts (1999).
- [91] B. D. Anderson *etal.*, <http://hallaweb.jlab.org/equipment/NIM.ps>
- [92] [https://hallaweb.jlab.org/wiki/index.php/Left\\_S2M\\_scintillators](https://hallaweb.jlab.org/wiki/index.php/Left_S2M_scintillators)
- [93] Vincent Sulkosky, <http://www.jlab.org/vasulk/s2m/docs/XP2282.pdf>.
- [94] P. A. Čerenkov. *Phys.Rev.*, 52:378, 1937.
- [95] E. Fermi. *Phys.Rev.*, 57:485, 1940.
- [96] DuPont<sup>TM</sup> Tedlar PVF Film. <http://www.dupont.com/tedlar>
- [97] A. Deur. TJNAF E94-010 Technical Note E94010-TN-03.
- [98] B. Wojtsekhowski *etal.* High Performance Threshold Aerogel Counters. *Nucl.Instr.Instr.andMeth.*
- [99] Lingyan Zhu, Particle Identification with A1/A2, JLAB-FIU-MIT-PHOTONIS, 2001.
- [100] R. Perrino *etal.**Nucl.Instr.andMeth.*, A457:571, 2001.
- [101] L. Lagamda *etal**Nucl.Instr.andMeth.*, A471:325, 2001.
- [102] R. Iommi *etal.* Test and Development of a Cherenkov diffusion detector prototye using Airglass aerogel at TJNAF, JLab-TN-00-010. 2000.
- [103] ALICE Collaboration, Technical Design Report of the High Momentum Particle Identification Detector,CERN/LHCC98-19, Alice TDR 1, 1998.
- [104] F. Garibaldi *etal.* High Resolution 1p-Shell Hypernuclear Spectroscopy. JLab Experiment E94-107, 1994.
- [105] RICH Detector part, <http://hallaweb.jlab.org/publications/AnnualReports/StatusReport2001.pdf>
- [106] C. Grupen, Particle Detectors, Cambridge University Press, (1996).
- [107] B. D. Anderson *etal.*, <http://hallaweb.jlab.org/equipment/NIM.ps>
- [108] CODA, CEBAF Online Data Aquisition System, <https://coda.jlab.org>.
- [109] J. Huang, Polarized 3He target spin-flip system, [https://hallaweb.jlab.org/wiki/index.php/Online\\_Spin\\_Flip](https://hallaweb.jlab.org/wiki/index.php/Online_Spin_Flip).
- [110] target polarization table, ID=252, <http://hallaweb.jlab.org/experiment/transversity/>
- [111] X. Qian, Ph.D Thesis, Duke, 2010.

- [112] Lingyan Zhu, Particle Identification with Aerogel Chrenkov Detector A1/A2, JLab, 2001.
- [113] C. Dutta, Ph.D. thesis, University of Kentucky, 2010.
- [114] Jin Huang, MIT, <http://hallaweb.jlab.org/experiment/transversity/>, Transversity ELOG, id=221.
- [115] P. R. Bevington and D. K. Robinson, "Data reduction and error analysis for the physical sciences", The McGraw-Hill Companies Inc. 1992.
- [116] K. de Jager and G. R. (Editors), Hall- A Annual Report 2009, <http://hallaweb.jlab.org/publications/AnnualReports/AnnualReport2009.pdf>.
- [117] J. Huang, Private communication.
- [118] Luciano Libero Pappalardo, Ph.D Thesis,"Transverse spin effects in polarized semi inclusive deep inelastic scattering", Universita' deli Studi di Ferrara, 2008.
- [119] F. James and M. Roos, "'MINUIT' A System for Function Minimization and Analysis of the Parameter Errors and Correlations", *Comput. Phys. Commun.* **10**,343(1975).
- [120] <http://hallaweb.jlab.org/experiment/transversity/> Pion- transversity [E-06-010]: Spokespersons:Jianping Chen, Xiaodong Jiang (contact), Jen-Chieh Peng Pion+ transversity [E-06-011]: Spokespersons:Evaristo Cisbani, Haiyan Gao, Xiaodong Jiang (contact)
- [121] J. Huang, Y. Qiang, Maximum Likelihood Estimation of Asymmetry and Angular Modulation for Transversity. v1.00, 2010.
- [122] A. Bacchetta et al., *JHEP* **200702**, 093, (2007).
- [123] The Jefferson Lab Hall A E06010 Collaboration
- [124] X. Qian et al. (Blue Team), Transversity Analysis ELog, #267
- [125] Individual kaon event with all the variables, <http://hallaweb.jlab.org/experiment/transversity/ID=375>.
- [126] W. Happer, *Rev.Mod.Phys.*, 44:169,1972.
- [127] <http://en.wikipedia.org/wiki/Pion>
- [128] F.Bissey *et al.*, *Phys. Rev.* **C64**, 024004(2001).
- [129] F. Bissey *et al.*, *Phys. Rev.* **C65**, 064317 (2002); e-Print: hep-ph/0109069.
- [130] A. Nogga, Ph.D thesis, Ruhr-Universität Bochum, Bochum, Germany (2001).
- [131] M. Anselmino, *et al.*, arXiv:0805.2677v2, [hep-ph], 2009.
- [132] M. Anselmino *et al.* *Phys. Rev.*, **D75**:054032, 2007.
- [133] M. Anselmino *et al.* *Phys. Rev.*, **D71**:074006, 2005.
- [134] B.-Q. Ma and I. Schmidt. *J. Phys.*, **G24**:L71, 1998.
- [135] S. Boffi, A. V. Efremov, B. Pasquini and P. Schweitzer, *Phys. Rev.* **D79**, 094012 (2009). arXiv:0903.1271.
- [136] W. Vogelsang and F. Yuan. *Phys. Rev.*, **D72**:054028,2005.
- [137] W. Vogelsang and F. Yuan, private communication.
- [138] B. Wojtsekhowski, E. Cisbani, G. Cates, and G. Franklin, JLAB approved experiment E09-018.
- [139] J.-P. Chen, H. Gao, X. Jiang, J.-C. Peng, and X. Qian, JLAB approved experiment E10-006.

# Vita

1. Name: Youcai Wang
2. Birth day: Jun 29, 1966
3. Birth place:Fuyang County, Zhejiang Province, China
4. M. A. degree in Physics, (UIUC)(2006)
5. M. A. degree in Computer Science and Physics (1989)
6. B. S. degree in Physics (1987)

## References

1. Name: Evaristo Cisbani  
Title: PhD in Physics

Institute: Italian National Institute of Health  
Address: via Regina Elena 299 - 0016 -Rome -Italy  
Phone: +39 06 4990 2847  
Email: evaristo.cisbani@iss.infn.it

2. Name: Jian-Ping Chen  
Title: PhD in Physics, JLab scientist staff  
Address: Jefferson Lab, Hall A  
12000 Jefferson Ave. MS 12H  
Newport News, VA, 23606 (USA)  
Phone: 001(757)269-7413  
Email: jpchen@jlab.org

3. Name: Alan M Nathan  
Title: Physics Professor  
Address: 403 Loomis Laboratory  
1110 W. Green  
Urbana, IL 61801  
University of Illinois  
Phone :001(217)3330965  
Email: a-nathan@illinois.edu

4. Name: Jen-Chieh Peng  
Title: Physics Professor, Director of dissertation research  
Address: 409 Loomis Laboratory  
1110 W. Green  
Urbana, IL 61801  
University of Illinois  
Phone : 001(217)2246039  
Email: jcpeng@illinois.edu